Modeling the seismic response of a two-storey calcium silicate brick masonry structure with nonlinear pushover and time-history analyses

by

Tianqi Xu

to obtain the degree of Master of Science in Civil Engineering at Delft University of Technology.



Modeling the seismic response of a two-storey calcium silicate brick masonry structure with nonlinear pushover and time-history analyses

by

Tianqi Xu

to obtain the degree of Master of Science in Civil Engineering at Delft University of Technology, to be defended publicly on Friday November 23, 2018 at 16:00 PM.

Student number: 4592875

Project duration: January, 2018 – November, 2018

Thesis committee: Prof. dr. ir. J.G. Rots, TU Delft, chairman

Dr. ir. F. Messali, TU Delft, daily supervisor

Dr. ir. G.J.P. Ravenshorst, TU Delft

An electronic version of this thesis is available at http://repository.tudelft.nl/.



Abstract

In the recent years, increasing induced seismic activities have been observed in the northern part of the Netherlands due to gas extraction. These seismic events may cause severe damages to the building stock in this area, which is mainly composed of unreinforced masonry (URM) buildings not designed to withstand seismic loads.

An extensive experimental campaign has been carried out at the Stevin II laboratory of Delft University of Technology to characterize the seismic responses of these URM structures. In this framework, a quasi-static cyclic pushover test on a full-scale masonry assemblage has been performed. The two-storey assemblage is composed of calcium silicate masonry walls and concrete floors, representing the load-bearing parts of a typical Dutch terraced house built in the period 1960-1980.

In this treatise, the seismic behavior of the tested masonry assemblage is modeled and analyzed via finite element analyses. The validation against the experimental results is achieved through nonlinear pushover analyses on a well-built model of the assemblage. Moreover, as the pushover method used in the aforementioned studies is based on static loading, its efficiency for the masonry structures under dynamic conditions needs to be evaluated. The evaluation is achieved by performing nonlinear time-history analyses on the model as well to obtain accurate seismic response of the structure. The objectives of this thesis project are summarized as follows:

- Create a valid finite element model representative of the tested masonry assemblage.
- Investigate its seismic response through both nonlinear pushover and time-history analyses.
- Validate the accuracy and applicability of pushover method to evaluate the behavior of the masonry assemblage under lateral loads.

All numerical analyses are carried out in the commercial software DIANA FEA 10.2. The recently developed Engineering Masonry model implemented in DIANA FEA 10.2 that includes the anisotropic property of masonry is adopted. A single masonry pier is first modeled to assess the suitability of this constitutive model to replicate the experimental behavior of calcium silicate masonry walls under cyclic lateral loading. The results are then compared with those obtained using a traditional isotropic material constitutive law (the total strain crack model). In both monotonic and cyclic pushover analyses of the masonry pier, the engineering masonry model is capable of capturing its structural behavior more comprehensively, while the previously used total strain crack model leads to divergence problems at an early stage.

The finite element model of the masonry assemblage is then created to simulate the specimen

properly under pushover analysis. Curved shell elements are used for both masonry walls and concrete floors. The pushover load is applied using a displacement controlled strategy. A special auxiliary loading system with rigid beams is attached to the house model to keep equal forces on the two floors during the loading history. Both monotonic and cyclic pushover analyses are carried out and the cyclic loading scheme is designed to fit the experimental loading protocol. Numerical results of the pushover analyses are compared to the experimental results mainly in terms of capacity curves (hysteresis loops), crack evolution and failure mechanisms.

The nonlinear pushover analyses reproduce the test results properly, showing similar maximum base shear forces and asymmetric capacity curves. In both experimental and numerical analyses, cracks start to form at the top and bottom of the masonry piers due to rocking mechanism and the failure of the structure is governed by damages of the wide piers. However, the numerical analyses are not able to reproduce neatly the diagonal crack failure in the wide piers. Besides, the numerical analyses show a more ductile behavior, with reduced softening, especially along the positive loading direction.

A sensitivity study based on the monotonic pushover analysis is conducted to investigate the influence of the most relevant masonry properties on the behavior of the model. The results show that the post-peak behavior of the model is directly related to the masonry compressive strength.

Finally, a series of nonlinear time-history analyses is performed. A horizontal ground motion representative of the earthquakes in the Groningen province is applied at the base of the structure. The incremental dynamic analysis method (IDA) is applied. The time-history analysis results are compared to the nonlinear pushover analysis results to validate the accuracy and applicability of the pushover method to evaluate the seismic behavior for this type of masonry structure. The incremental dynamic analysis provides similar base shear capacity and failure mechanisms as the nonlinear pushover analysis. However, the maximum displacement is smaller in both loading directions and a more distributed crack pattern is observed. Overall, for the studied masonry house, the pushover method is capable of properly estimating the base shear capacity but the deformation capacity might be overestimated.

It is recommended that further research focus on more thorough sensitivity studies and more comprehensive modeling strategies for the details of the house. Performing IDA with multiple different earthquake signals and getting the average IDA results is also recommended since the earthquake characteristics may influence the seismic response of the structure. Other variations of nonlinear pushover analysis and time-history analysis could be performed as well. A similar procedure can be adopted to study other building typologies, or for the same typologies with different details (e.g. connection at corners or type of masonry).

Acknowledgements

I would like to express my special thanks to the people who gave me their support during the thesis work:

My daily supervisor, Dr. ir. Francesco Messali, for his patient guidance over the entire duration of my thesis. Thank you for always being available to discuss my project and answer any question I had with thoughtful consideration.

Prof. dr. ir. Jan Rots, for providing me the opportunity to work on this interesting and challenging project. Your critical thoughts and invaluable suggestions deepen my understanding of this topic and steer me in the right direction.

Dr. ir. Geert Ravenshorst, for the constructive feedback during the committee meetings, and for giving me continuous encouragement in the research work.

Dr. Valentina Mariani and Manimaran Pari for helpful suggestions on the research approaches and modeling strategies.

My partner Erik, for his continuous support and meticulous proofreading of my work.

Finally, I would like to thank my parents and my friends for their encouragement throughout my study.

Tianqi Xu Delft, November 2018

Contents

Al	bstrac	et		iii
A	cknov	vledgem	nents	v
Li	st of l	Figures		xi
Li	st of '	Fables		XV
1	INT	RODU	CTION	1
	1.1	Object	tive and Scope	. 2
	1.2	Synop	osis	. 2
2	LIT	ERATU	URE STUDY	5
	2.1	Mecha	anical Properties of Masonry	. 5
		2.1.1	Properties of unit and mortar	. 5
		2.1.2	Properties of unit-mortar interface	. 6
		2.1.3	Properties of the composite material	. 7
	2.2	Structi	ural Behavior of Masonry Components	. 10
		2.2.1	In-plane response	. 10
		2.2.2	Out-of-plane response	. 11
	2.3	Nume	rical Modeling of Masonry	. 12
		2.3.1	Numerical approaches	
		2.3.2	Constitutive models	. 13
	2.4	Seism	ic Analysis and Assessment	
		2.4.1	Eigenvalue analysis	
		2.4.2	Nonlinear Pushover (NLPO) analysis	
		2.4.3	Nonlinear Time-history (NLTH) analysis	
		2.4.4	Seismic assessment of structures	. 21
3	FEA	OF M	ASONRY PIER TUD_COMP-20	23
	3.1	Descri	iption of the Test	. 23
	3.2	FE Mo	odel of Masonry Pier TUD_COMP-20	. 24
		3.2.1	Geometry of the model	. 24
		3.2.2	Finite element discretization	. 24
		3.2.3	Constitutive laws	. 26
	3.3	Nonlir	near Pushover Analysis	. 30
		3 3 1	Loading method	30

viii CONTENTS

		3.3.2 An	alysis procedure	1
	3.4		the Pushover Analysis	
			onotonic pushover results	
			clic pushover results	4
	3.5		n between Experimental and Numerical Results	5
			pacity curves	5
			ergy dissipation	6
			llure modes and crack patterns	
	3.6		Model and Results	7
			dated FE model	7
		_	merical results and assessment	8
4	FE N	MODEL OF	TUD_MASONRY_HOUSE-1 4	3
	4.1	Geometry of	of the Model	4
		•	ıll-to-wall connections	5
			ıll-to-floor connections	5
			mmetry	6
	4.2	•	nent Discretization	7
			ement type and properties	7
			nnection details	0
	4.3		e Laws	2
			asonry properties	2
			ncrete properties	3
			erface properties	3
	4.4	Modal Para	ameters Identification	5
5	NON	NLINEAR I	PUSHOVER ANALYSIS OF TUD_HOUSE-1 5	7
	5.1		ishover Load	
	3.1	* *	ading method	
			ading scheme	
	5.2		Pushover Analysis	
	5.3			
	0.0		pacity curves	
		-	ack evolution	
		5.3.3 Dri		
	5.4		Study	
		•	mpressive strength	
			mpressive fracture energy	
			tial shear strength	
6	NON	NLINEAR T	FIME HISTORY ANALYSIS OF TUD_HOUSE-1 8	1
J	6.1	Input Signa		
		1 0	Time History Analysis	
	0.7			
	6.2		·	
	6.3	Results in -	+X Direction	4
		Results in - 6.3.1 Hy	·	4 4

CONTENTS	ix

	6.4	Results in -X Direction	91
		6.4.1 Hysteresis curves	
		6.4.2 Crack evolution	
		6.4.3 Drifts	
7	COI	IPARISON AND DISCUSSION	99
	7.1	Structural Capacity	99
	7.2	Failure Mechanism	
8	CO	CLUSIONS AND RECOMMENDATIONS 1	.03
	8.1	Conclusions	03
	8.2	Recommendations	
Re	feren	ces 1	07
Αŗ	pend	ces 1	09
A	Resu	lts of the Masonry Pier 1	11
В	Geo	netrically Nonlinear Effect on Pushover Results	13
C	Resu	lts of Nonlinear Pushover Analysis	15
D			27
	D.1	+x direction	27
	D.2	-x direction	33

X CONTENTS

List of Figures

1.1	Induced seismicity (> 1.5) of the Groningen field in time sorted by magnitude vs. the annual production ("Groningen gasfield", 2016)	1
2.1	Typical tensile bond stress-crack displacement results for solid clay brick masonry:	-
2.2	Envelop of three tests (R. Van der Pluijm, 1992).	6
2.2	Typical shear bond stress-crack displacement results for solid clay brick masonry: Envelop of three tests (R. Van der Pluijm, 1992).	7
2.3	Typical experimental stress-displacement diagrams of solid soft mud brick (Binda,	
	Fontana, and Frigerio, 1988)	8
2.4	Tensile stress-displacement diagrams in the direction perpendicular to the head-	
	joint (Backes, 1985): (a) stepped cracks through joints; (b) vertically crack through	
	unit and head-joint	9
2.5	Failure modes of solid clay brick masonry under biaxial loading (Dhanasekar,	
	Page, and Kleeman, 1985)	9
2.6	Typical in-plane failure modes of masonry piers: (a) rocking; (b) sliding shear	
	failure; (c) diagonal cracking (Calderini, Cattari, and Lagomarsino, 2009)	10
2.7	Laterally loaded masonry wall with oblique and horizontal yield-lines (Brincker,	
	1984)	11
2.8	Out-of-plane failure mechanism (a)-(f) Overturing failures; (g)-(h) Failures based	
	on arch effect (D'Ayala and Speranza, 2003)	12
2.9	Modeling strategies for masonry structures: (a) detailed micro-modeling; (b) sim-	
	plified micro-modeling; (c) macro-modeling. (Lourenço, 2002)	13
2.10	Pre-defined axes in the engineering masonry model	14
2.11	Tensile stress-strain curve in engineering masonry model	15
	Compressive stress-strain curve in engineering masonry model	
2.13	In-plane shear stress-strain curve in engineering masonry model	17
2.14	Mechanical model for dynamic time history analysis	20
3.1	Quasi-static in-plane pushover test on TUD_COMP-20 (Esposito and Ravenshorst,	
3.1	2017)	23
3.2	FE model of the masonry pier TUD_COMP-20	
3.3	8-noded plane stress element: CQ16M	
3.4	Simplification of steel beam cross-section	
3.5	Stress-strain relation in the total strain crack model	
3.6	Stress-strain relation in the engineering masonry model	
3.7	Cyclic pushover loading scheme	
3.8	Capacity curves of the masonry pier in monotonic pushover analysis	34
-		

xii LIST OF FIGURES

3.9	Capacity curves of the masonry pier in cyclic pushover analysis	
3.10	Comparison of the numerical and experimental capacity curves	35
3.11	Energy dissipation of the masonry pier	36
3.12	Crack width of the pier model in cyclic pushover analysis: (a)-(e) at loading cycle	
	C2, C4, C6, C8 and C10 in positive direction; (f)-(j) at loading cycle C2, C4, C6,	
	C8 and C10 in negative direction	37
3.13	Capacity curve of wall TUD_COMP-20	39
	Energy dissipation for masonry pier TUD_COMP-20	40
	Crack width of the updated pier model in cyclic pushover analysis: (a)-(f) at load-	
	ing cycle C2, C4, C6, C8, C10 and C12 in positive direction; (g)-(l) at loading	
	cycle C2, C4, C6, C8, C10 and C12 in negative direction	41
3.16	Maximum vertical versus horizontal displacement of TUD_COMP-20	
	Crushing at the corners of TUD_COMP-20	42
	Sliding of TUD_COMP-20	42
4.1	TUD CS brick masonry assemblage (Ravenshorst et al., 2016)	44
4.2	Examples of the masonry wall details ("Types of Masonry Wall", 2017)	44
4.3	FE model of the masonry assemblage	
4.4	Details of connections: First floor (Ravenshorst et al., 2016)	
4.5	Details of connections: Second floor (Ravenshorst et al., 2016)	46
4.6	Symmetry of the assemblage model	
4.7	8-node curved shell element: CQ40S	
4.8	House model with generated mesh	
4.9	Full connections (red lines) in the house model	
4.10	6-node 3D line interface element: CL24I	
4.11	Interface elements (red lines) in the house model	
4.12	Mode shapes of the house model	56
5.1	Location of steel beams	59
5.2	Cyclic loading scheme in numerical pushover analysis	60
5.3	Capacity curve of the house model (cyclic pushover analysis)	
5.4	Hysteresis curves at each stage	62
5.5	Capacity curves of the CS brick masonry house	64
5.6	Analysis of the crack evolution	65
5.7	Results at the end of initial stage	66
5.8	Results at cycle 8 (positive direction)	66
5.9	Results at cycle 8 (negative direction)	67
5.10	Results at cycle 15 (positive direction)	68
5.11	Results at cycle 18 (negative direction)	69
5.12	Results at cycle 22 (positive direction)	70
5.13	Results at cycle 22 (negative direction)	71
5.14	Results at cycle 27 (positive direction)	72
5.15	Results at cycle 27 (negative direction)	73
	Interstory drift	74
5.17	Capacity curves and compressive stress distributions	77
5.18	Capacity curves with different compressive fracture energy	78
5.19	Crack widths at step 50 in the positive direction (+21.4 mm)	79

LIST OF FIGURES	xiii
Zisi of fiderias	7111

6.1	Location of applied ground accelerations	
6.2	Input seismic signal	
6.3	Full scheme of applied accelerogram	
6.4	Full scheme of mirrored accelerogram	
6.5	Resulted relative displacement at the second floor	
6.6	Resulted base shear force of the house	
6.7	Hysteresis curves of the house model with time-history analysis	
6.8	Crack width at the maximum displacement of run 1 to run 4	
6.9	Crack width at the maximum displacement of run 5 and run 6	
6.10	Crack width at the maximum displacement of run 7 and run 8	
6.11	Crack width at the maximum displacement of run 9, 10 and 11 90	
6.12	Maximum drifts of the two floors in each run	
	Resulted relative displacement at the second floor	
6.14	Resulted base shear force of the house	
6.15	Hysteresis curves of the house model with time-history analysis	
6.16	Crack width at the maximum displacement of run 1 to run 4	
	Crack width at the maximum displacement of run 5 and run 6	
	Crack width at the maximum displacement of run 7 and run 8	
6.19	Crack width at the maximum displacement of run 9 (0.40 g), displacement -77.50	
	mm	
6.20	Maximum drifts of the two floors in each run	
7.1	Time-history hysteresis curves vs. Pushover backbone curve	
7.1	Comparison of the capacity curves	
7.2	Comparison of crack patterns (same scale) at displacement +104 mm	
1.5	Comparison of crack patterns (same scale) at displacement 1104 mm 102	
A. 1	Capacity curves from monotonic pushover analysis	
A.2	Capacity curves from cyclic pushover analysis	
B.1	Capacity curves	
D.1	Capacity curves	
C .1	Crack widths at the end of pseudo-linear stage (Cycle 8, positive direction) 115	
C.2	Stress/strain at the end of pseudo-linear stage (Cycle 8, positive direction) 116	
C.3	Crack widths at the end of pseudo-linear stage (Cycle 8, negative direction) 116	
C.4	Stress/strain at the end of pseudo-linear stage (Cycle 8, negative direction) 117	
C.5	Crack widths at the peak base shear capacity (Cycle 15, positive direction) 117	
C.6	Crushing at the peak base shear capacity (Cycle 15, positive direction)	
C.7	Stress/strain at the peak base shear capacity (Cycle 15, positive direction) 118	
C.8	Crack widths at the peak base shear capacity (Cycle 18, negative direction) 119	
C.9	Crushing at the peak base shear capacity (Cycle 18, negative direction)	
C.10	Stress/strain at the peak base shear capacity (Cycle 18, negative direction) 120	
C.11	Crack widths at post-peak stage (Cycle 22, positive direction)	
C.12	Crushing at post-peak stage (Cycle 22, positive direction)	
	Stress/strain at post-peak stage (Cycle 22, positive direction)	
C.14	Crack widths at post-peak stage (Cycle 22, negative direction)	
	Crushing at post-peak stage (Cycle 22, negative direction)	
	Stress/strain at post-peak stage (Cycle 22, negative direction)	

xiv LIST OF FIGURES

C .17	Crack widths at the last loading cycle (Cycle 27, positive direction)
C .18	Crushing at the last loading cycle (Cycle 27, positive direction)
C.19	Stress/strain at the last loading cycle (Cycle 27, positive direction)
C.20	Crack widths at the last loading cycle (Cycle 27, negative direction)
C.21	Crushing at the last loading cycle (Cycle 27, negative direction)
C.22	Stress/strain at the last loading cycle (Cycle 27, negative direction)
	Results at run 1 (0.03 g, +2.16 mm)
	Results at run 2 (0.06 g, +3.51 mm)
D.3	Results at run 3 (0.10 g, +5.27 mm)
D.4	Results at run 4 (0.15 g, +10.40 mm)
D.5	Results at run 5 (0.20 g, +19.32 mm)
D.6	Results at run 6 (0.25 g, +36.11 mm)
	Results at run 7 (0.30 g, +48.48 mm)
	Results at run 8 (0.35 g, +65.60 mm)
	Results at run 9 (0.40 g, +71.90 mm)
	Results at run 10 (0.50 g, +87.10 mm)
	Results at run 11 (0.62 g, +103.90 mm)
	Results at run 1 (0.03 g, -1.15 mm)
	Results at run 2 (0.06 g, -3.29 mm)
	Results at run 3 (0.10 g, -6.66 mm)
	Results at run 4 (0.15 g, -12.82 mm)
	Results at run 5 (0.20 g, -19.94 mm)
	Results at run 6 (0.25 g, -31.82 mm)
	Results at run 7 (0.30 g, -38.07 mm)
	Results at run 8 (0.35 g, -50.73 mm)
	Results at run 9 (0.40 σ -77 50 mm)

List of Tables

3.1	Quasi-static cyclic in-plane tests performed on masonry pier	24
3.2	Finite elements used in the masonry pier model	26
3.3	Material properties of steel	27
3.4	Masonry properties in total strain crack model	28
3.5	Material properties in engineering masonry model	29
3.6	Target displacements in cyclic loading	
3.7	Monotonic pushover analysis procedure	33
3.8	Cyclic pushover analyses procedure	
3.9	Masonry properties in updated FE model	
3.10	Comparison of base shear force capacity of wall TUD_COMP-20	39
4.1	Finite elements used in the house components	50
4.2	Finite elements used in the shear connection	
4.3	Masonry properties in the FE model	53
4.4	Material properties of concrete	53
4.5	Material properties of interface	54
4.6	Eigenvalue analysis results	55
4.7	Comparison of eigenfrequencies	56
5.1	Applied target displacements for each cycle	59
5.2	Procedure of the cyclic pushover analysis	
5.3	Procedure of the monotonic pushover analysis	61
5.4	Comparison of the drifts at Cycle 27	75
5.5	Comparison of the drifts at Cycle 21	76
6.1	PGA value for each run	83
6.2	Procedure of the nonlinear time-history analysis	84
6.3		91
6.4		97

xvi LIST OF TABLES

Chapter 1

INTRODUCTION

Gas extraction in the northern part of the Netherlands has led to an increase in the number of induced earthquakes during recent years (Figure 1.1). The building stock in this area is mainly composed of unreinforced masonry (URM) buildings, which were not designed to resist seismic loads and may therefore be severely damaged in the case of seismic events.

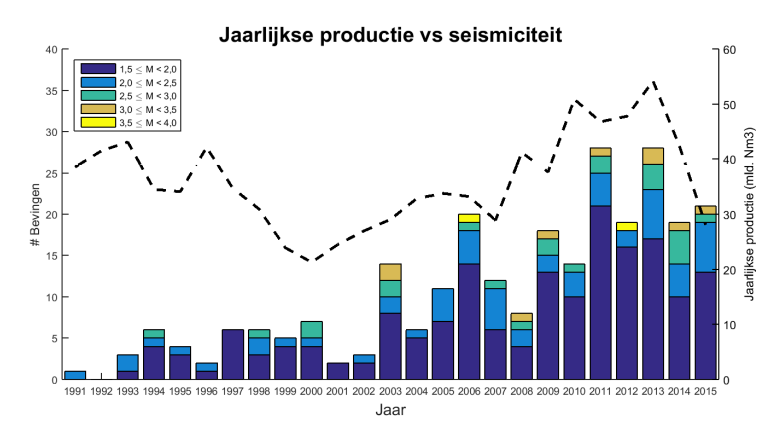


Figure 1.1: Induced seismicity (> 1.5) of the Groningen field in time sorted by magnitude vs. the annual production ("Groningen gasfield", 2016)

Various experimental and numerical studies have been conducted to assess the seismic performance of these masonry buildings. A quasi-static cyclic pushover test was carried out on a full-scale masonry assemblage at TU Delft. The specimen represents the load-bearing parts of a typical two-story Dutch terraced house built in the period 1960-1980, with slender piers and limited connections between floor and piers.

The pushover method used in the aforementioned study is a powerful tool to investigate structural performance under seismic loading, and has been adopted by many earthquake performance-design codes (e.g. Eurocode 8, FEMA 356). It provides good estimates for structures that vibrate primarily in the fundamental mode (Krawinkler and Seneviratna, 1998).

However, the pushover method is based on static loading. Therefore, it may lead to inaccurate predictions for the masonry structures in dynamic conditions (Krawinkler and Seneviratna, 1998).

Moreover, as the invariant lateral load pattern is used during the pushover test, some important deformation modes of the structure might be ignored, especially for masonry houses with slender piers where higher mode effects may occur.

1.1 Objective and Scope

Due to the reasons stated before, the accuracy and applicability of the pushover method on this type of masonry structures need to be validated. The evaluation is achieved by performing both nonlinear pushover analyses and nonlinear time history analyses on the finite element model of the masonry assemblage. The nonlinear time history analysis is considered capable of providing accurate seismic behaviors of the structure, as the structural response is directly calculated under real seismic inputs.

Therefore, the objectives of this research are summarized as follows:

- Create a valid finite element model representative of the tested masonry assemblage.
- Investigate its seismic response through both nonlinear pushover and time-history analyses.
- Validate the accuracy and applicability of pushover method to evaluate the behavior of the masonry assemblage under lateral loads.

This research is conducted based on the quasi-static pushover test of a calcium silicate (CS) brick masonry assemblage at TU Delft. Numerical modeling of the tested specimen is carried out in the commercial software DIANA FEA 10.2.

The new Engineering Masonry model implemented in DIANA FEA 10.2 that includes the anisotropic property of masonry is used to model the CS brick masonry. The finite element model of the masonry assemblage is built in such a way that it can simulate the specimen properly under pushover analysis. Results of the nonlinear pushover and time history analyses of the house model are then compared to evaluate the efficiency of the pushover method. The main aspects to investigate and compare the seismic behaviors are capacity curves (hysteresis loops), crack patterns and failure mechanisms.

1.2 Synopsis

The research work starts with a literature study on the material and structural properties of masonry, its numerical approaches, and the seismic analysis and assessment methods (Chapter 2).

To get acquainted with modeling masonry structures in DIANA FEA 10.2, and to verify the advantages of using the Engineering Masonry model, a single masonry pier is first modeled and analyzed with the pushover method (Chapter 3).

Then, the finite element model of the masonry assemblage (Chapter 4), the performed nonlinear pushover analysis (Chapter 5) and nonlinear time-history analysis (Chapter 6) are presented in detail.

1.2. SYNOPSIS 3

Thereafter, a comparison between the results of nonlinear pushover and time-history analyses is presented (Chapter 7).

Finally, conclusions are drawn and recommendations for further research are outlined (Chapter 8).

Chapter 2

LITERATURE STUDY

Masonry is one of the oldest materials that is still in use today. Here, its properties are discussed at the material and structural level in Section 2.1 and 2.2, respectively. Section 2.3 presents the existing numerical modeling methods of masonry. Additionally, two common seismic analysis methods (i.e. monotonic/cyclic pushover analysis and dynamic time-history analysis) and the corresponding assessment ways are presented in Section 2.4.

2.1 Mechanical Properties of Masonry

The mechanical properties of masonry may vary a lot among different types. This section focuses on the unreinforced brick masonry that was widely used in the northern part of the Netherlands, consisting of brick units and general mortar joints. The mechanical properties of masonry are highly dependent on the properties of its constituents.

2.1.1 Properties of unit and mortar

The masonry unit is a quasi-brittle material that behaves much stronger under compression than tension, like concrete. EN-1996-1-1 (2005) defines f_b as the normalized compressive strength of a $100 \times 100 \times 100$ mm cubic masonry unit specimen, which considers the restraint effect of the platens in the standard test. However, the normalized compressive strength is not representative of the true strength of masonry units (Lourenco, 1996). Additionally, the brittle nature of masonry units makes it difficult to capture the post-peak behavior experimentally. As a result, it is very difficult to estimate the real compressive fracture energy G_{fc} .

The tensile strength of masonry units is not directly related to their compressive strength. Rather, it depends on the shapes, used materials and perforation ratios of the units (Lourenco, 1996). Normally, uniaxial, splitting and flexural tensile tests can be conducted to obtain the tensile parameters of masonry units.

The compressive strength of the mortar, f_{mo} , can be obtained through the standard tests with mortar prisms casted in steel molds. The disadvantage of this test is that it does not consider the effect of water absorption by the units, thus the result can not represent the mortar behavior in masonry composites (Lourenco, 1996). To overcome this drawback, Stockl, Bierwirth, and Kupfer (1994)

performed the tests on the mortar specimen extracted from a masonry bed-joint. Results show a three times higher mortar strength than the value obtained from the standard test.

2.1.2 Properties of unit-mortar interface

The interfaces between masonry units and mortar may be considered the weakest part in masonry composites. The weak interfaces usually crack first at low stresses, leading to a highly nonlinear response. Two failure modes are distinguished at these interfaces. Mode I is related to tensile failure and Mode II is related to shear failure.

Mode I Failure

Deformation controlled tensile bond tests for solid clay and calcium-silicate brick masonry were conducted by R. Van der Pluijm (1992). Results from these tests showed an exponential tension softening curve for the tensile bond strength with respect to the crack width, as shown in Figure 2.1.

Defining the fracture energy as the energy needed to form a unit area of crack, a low mode I fracture energy G_f^I was found in the tests, with a range from 0.005 to 0.02 [Nmm/mm²], for a tensile bond strength varying from 0.3 to 0.9 [N/mm²] (Lourenco, 1996). Moreover, a reduced area of bond surface is found in the cracked specimens, which might be due to shrinkage of the mortar or the construction process of masonry.

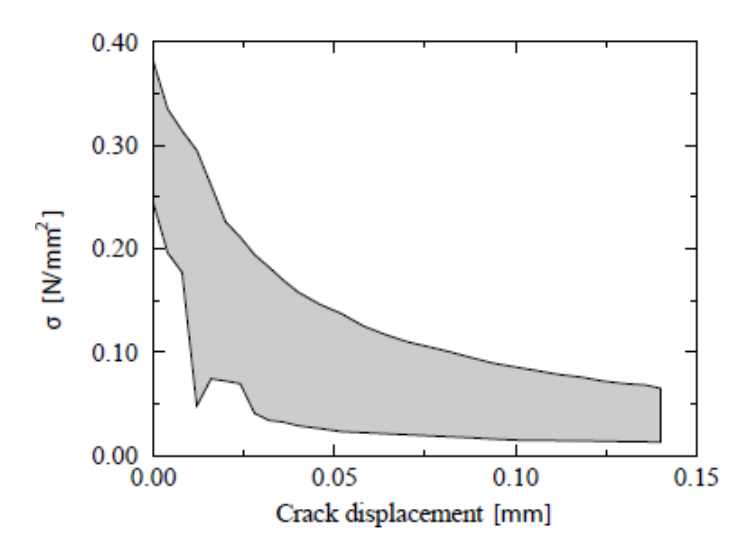


Figure 2.1: Typical tensile bond stress-crack displacement results for solid clay brick masonry: Envelop of three tests (R. Van der Pluijm, 1992).

MODE II FAILURE

Researches have designed tests that provide a uniform stress state in the joints to investigate the Mode II failure mechanism. A representative shear test for the solid clay and calcium-silicate brick masonry was performed by Rob Van der Pluijm, Hamid, and Harris (1993). Like in the tensile test, an exponential softening relation was found. As expected, residual stresses due to dry friction remained after the peak strength (Figure 2.2). The mode II fracture energy G_f^{II} - defined as the un-

derneath area of the stress-displacement curve, ranges from 0.01 to 0.25 [Nmm/mm²] for an initial cohesion c varying from 0.1 to 1.8 [N/mm²] (Lourenco, 1996).

Additionally, it is found that a higher compressive stress level resulted in an increase of the fracture energy. The shear behavior of the interface can be described by a Coulomb friction model. The initial internal friction angle ϕ_0 and the residual internal friction angle ϕ_r can be measured by $\tan \phi_0$ and $\tan \phi_r$, respectively. The residual internal friction angle was found to be approximately constant (Lourenco, 1996) and it determines the residual dry friction level.

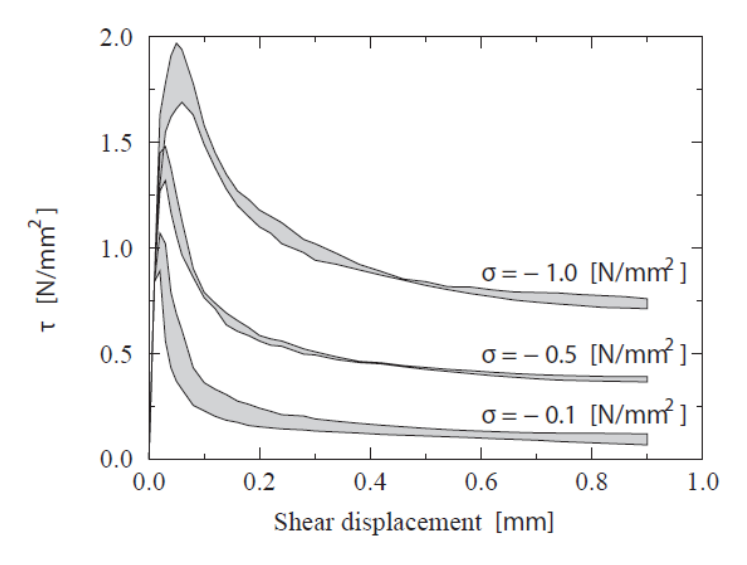


Figure 2.2: Typical shear bond stress-crack displacement results for solid clay brick masonry: Envelop of three tests (R. Van der Pluijm, 1992).

2.1.3 Properties of the composite material

The mechanical properties of masonry as a composite material are presented here. Because of the interaction between the masonry units and mortar, the properties of the individual masonry constituents are not sufficient to represent the composite behavior. Rather, uniaxial and biaxial tests are normally performed to obtain the mechanical properties of a masonry composite.

UNIAXIAL COMPRESSIVE BEHAVIOR

The masonry composite is an anisotropic material due to the geometry of units and joints. The uniaxial behavior of masonry is determined in two local axes: perpendicular to the bed-joints and perpendicular to the head-joints.

The RILEM test (Wesche and Ilantzis, 1980) is normally performed to get the compressive strength of masonry perpendicular to the bed-joints. A typical stress-displacement relation extracted from experiments can be seen in Figure 2.3. A clear quasi-brittle behavior of masonry under compression can be observed and the increasing strength results in a more brittle behavior (Lourenco, 1996). The compressive behavior of masonry perpendicular to the head-joints may have an effect on its capacity, especially for masonry with high perforation units.

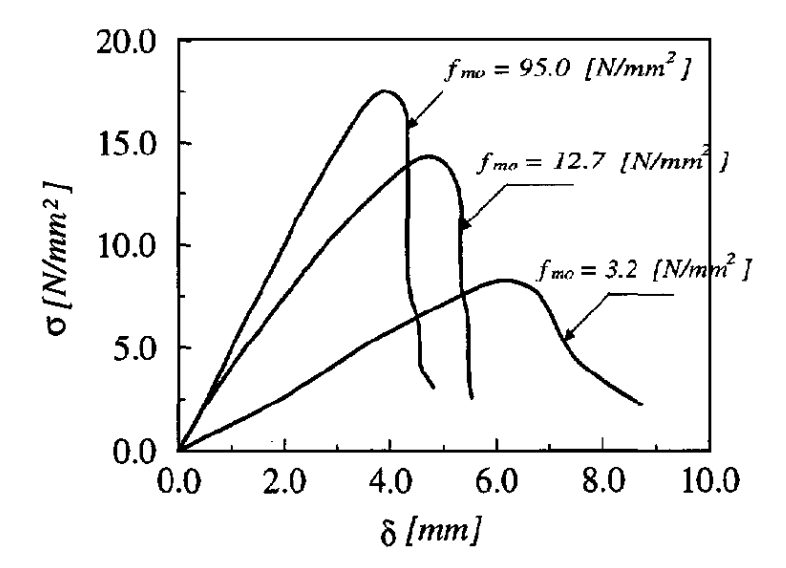


Figure 2.3: Typical experimental stress-displacement diagrams of solid soft mud brick (Binda, Fontana, and Frigerio, 1988).

The elastic moduli of masonry perpendicular to the bed-joints and head-joints are obtained from the compressive tests. It is accepted to obtain the elastic modulus of masonry at 1/3 of the maximum compressive stress from the stress-strain curve, as the behavior of masonry can be considered quasi-linear until this load.

UNIAXIAL TENSILE BEHAVIOR

The interfaces between the units and mortar joints are normally the weakest parts which lead to a failure when masonry is loaded in tension perpendicular to the bed-joints. Thus, the masonry tensile strength normal to the bed-joints can be roughly equal to the tensile bond strength between the units and joints (Lourenco, 1996). However, for special types of masonry with weak units and a high tensile bond strength, failure might be governed by the tensile strength of the units instead.

For the tensile test perpendicular to the head-joints, two different failure modes are often found: stepped cracks through head and bed-joints and vertical crack through head-joints and units. Figure 2.4 gives the typical experimental stress-displacement curves in tension for these two failure modes.

BIAXIAL BEHAVIOR

Several studies (Dhanasekar, Page, and Kleeman, 1985) have investigated the behavior of masonry under biaxial stress states in order to better understand its performance under different load combinations. Figure 2.5 presents the different failure modes of masonry under biaxial loading. The influence of principal stress rotation with respect to the axis parallel to the bed-joints and principal stress ratio on the failure modes is clearly illustrated.

It should be noted that the failure modes and strength envelopes of masonry under biaxial loading may differ when using different unit materials (e.g. clay and calcium-silicate), unit shapes (e.g. solid and perforation) and unit-mortar geometries.

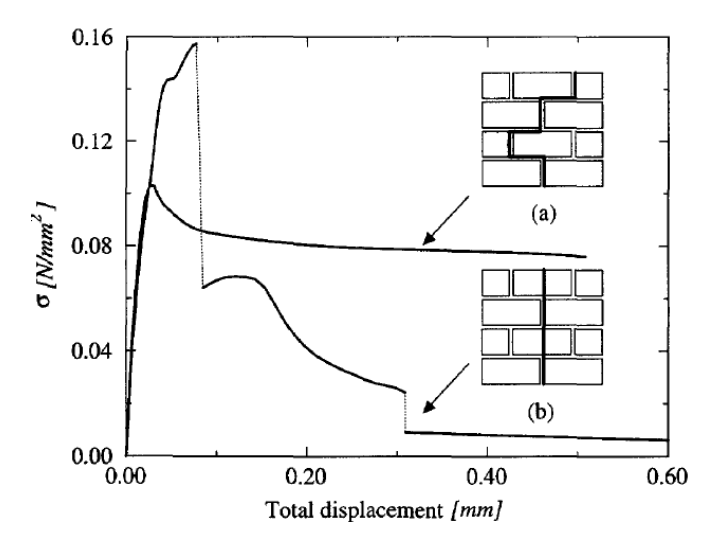


Figure 2.4: Tensile stress-displacement diagrams in the direction perpendicular to the head-joint (Backes, 1985): (a) stepped cracks through joints; (b) vertically crack through unit and head-joint.

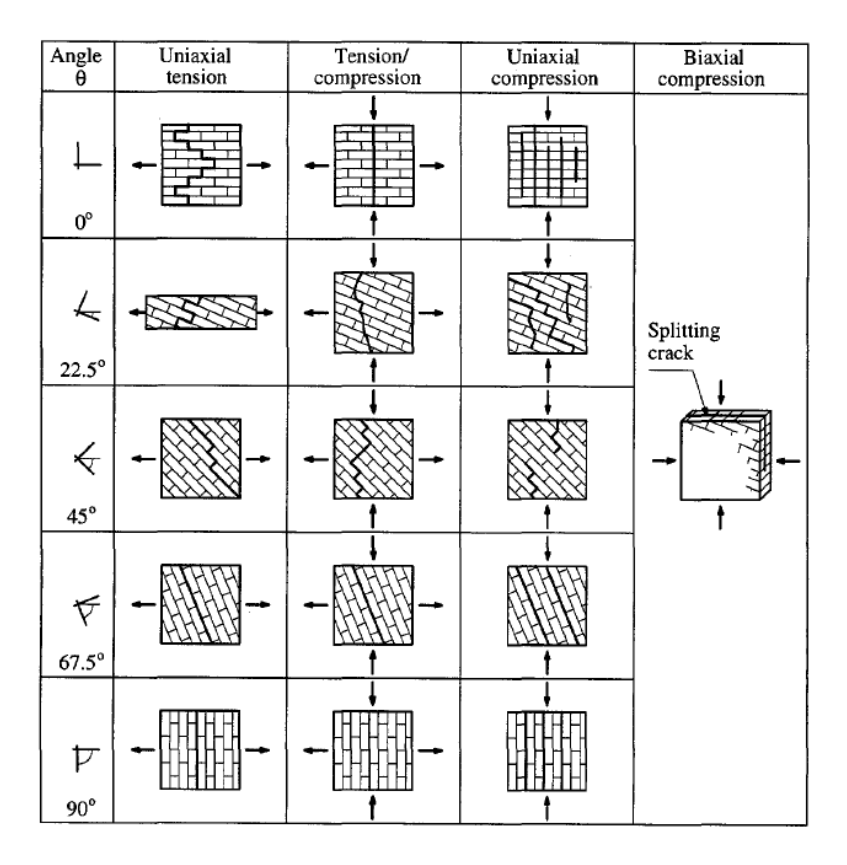


Figure 2.5: Failure modes of solid clay brick masonry under biaxial loading (Dhanasekar, Page, and Kleeman, 1985).

2.2 Structural Behavior of Masonry Components

The structural behavior of masonry components is studied here. Subsection 2.2.1 and 2.2.2 discuss the in-plane and out-of-plane responses of typical unreinforced masonry walls under seismic loading, respectively.

2.2.1 In-plane response

Experimental tests on masonry walls showed that it has three typical failure modes under in-plane loading: rocking failure due to flexure, sliding failure due to shear and diagonal cracking due to shear.

- *Rocking* Figure 2.6 (a) shows the damage pattern of the masonry pier associated with rocking failure. In this mode, the lateral load causes tensile cracks at the corner of the pier, which starts to behave as a nearly rigid body rotating about the toe (Calderini, Cattari, and Lagomarsino, 2009). If the applied compressive load on the wall is relatively high compared to the masonry compressive strength, sub-cracks may occur around the compressed corner. The failure of the masonry pier is then governed by *toe crushing*.
- *Sliding shear failure* This failure mode is marked by the occurrence of a horizontal sliding plane along bed-joint, as shown in Figure 2.6 (b). Because of the lateral load, horizontal tensile cracks starts to form at the interface between the bed-joint and unit. When the friction coefficient of the interface is small and there is low compressive load on the pier, sliding shear failure might occur.
- *Diagonal cracking* If the diagonal cracking mechanism governs the failure of a masonry pier, a clear damage pattern with a diagonal crack forming at the center and towards the corners is usually observed (Figure 2.6 (c)). Depending on the properties of masonry constituents, the crack may go through the head-joints and bed-joints, or through the units (Calderini et al., 2009).

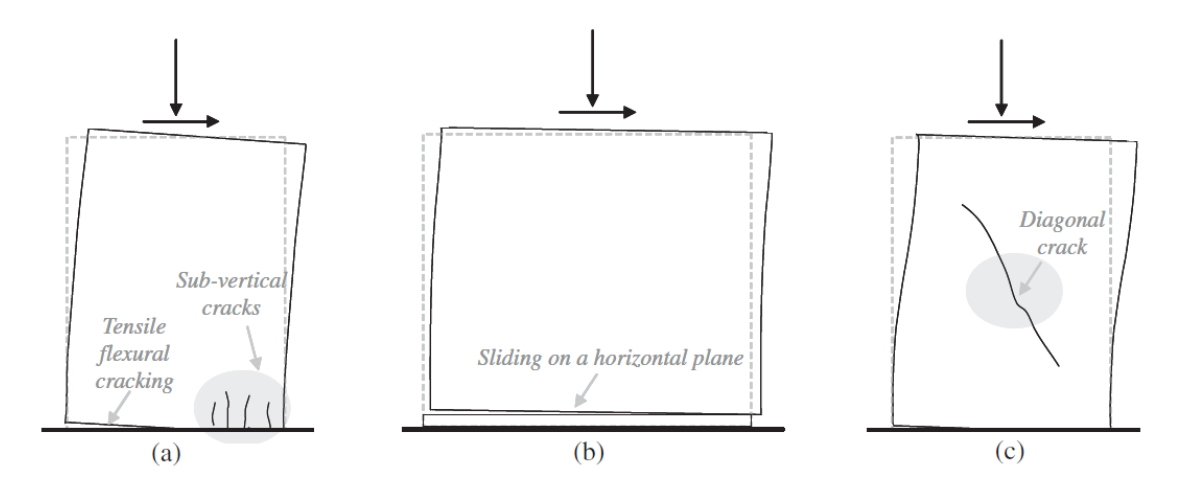


Figure 2.6: Typical in-plane failure modes of masonry piers: (a) rocking; (b) sliding shear failure; (c) diagonal cracking (Calderini, Cattari, and Lagomarsino, 2009).

2.2.2 Out-of-plane response

Masonry structures under seismic events are often subject to in-plane and out-of-plane loads simultaneously. Various research have been done to investigate the out-of-plane responses of unreinforced masonry walls.

Brincker (1984) conducted several tests on the unreinforced masonry walls under the load combination of out-of-plane lateral forces and in-plane pressures. The test results show that the masonry walls subject to out-of-plane loading have ductile properties and the yield line theory can be applied as a design method for the laterally loaded masonry walls.

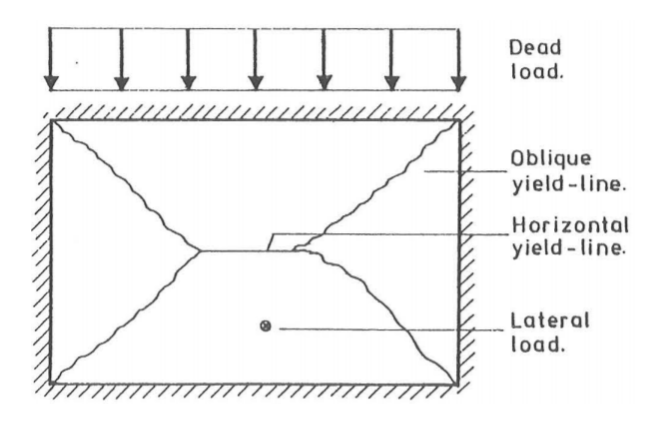
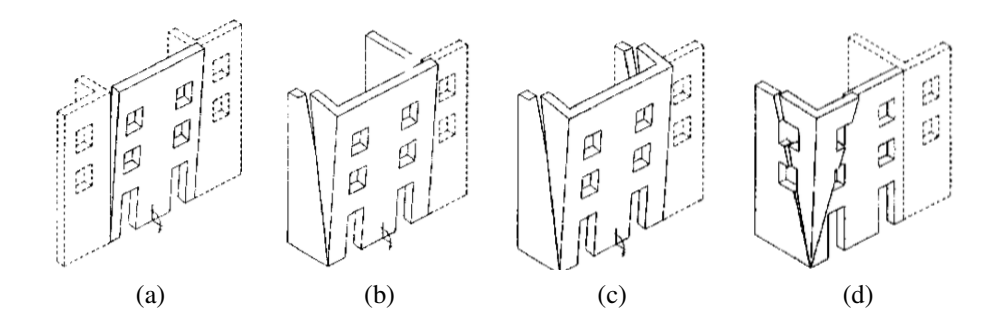


Figure 2.7: Laterally loaded masonry wall with oblique and horizontal yield-lines (Brincker, 1984)

D'Ayala and Speranza (2003) studied the out-of-plane mechanisms of masonry walls with different layouts in the masonry buildings. The development of their out-of-plane mechanisms are found directly related to the quality and strength of the connections with other elements of the structure. For non-strengthened walls, the out-of-plane overturing failure normally occurs and different failure modes can be detected as shown in Figure 2.8 (a)-(f). On the other hand, when the the masonry wall is well connected to other structural components, the overturing mechanism is generally avoided. Instead, the failure is governed by the so-called arch effect, as shown in Figure 2.8 (g)-(h).

Meisl, Elwood, and Ventura (2007) performed shaking table tests on four full-scale unreinforced masonry walls to investigate the sensitivity of out-of-plane responses to the type of ground motion and the quality of the wall connections. Both parameters do not show a big influence on the peak response of the walls. However, for high amplitude tests, a negative slope is observed in the force-displacement curve for the wall while no instability occurred in the system.



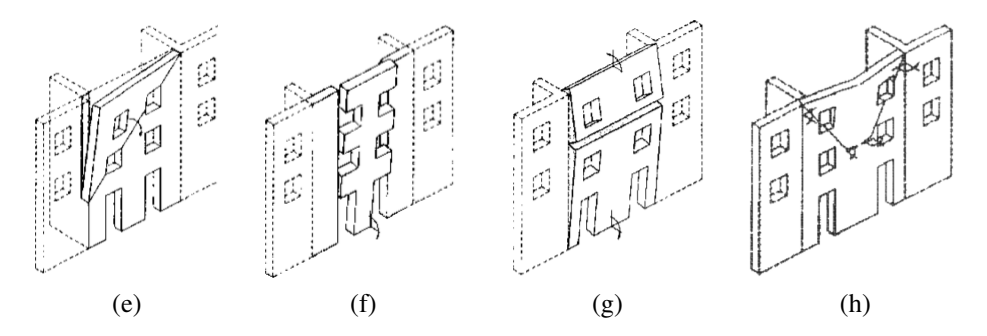


Figure 2.8: Out-of-plane failure mechanism (a)-(f) Overturing failures; (g)-(h) Failures based on arch effect (D'Ayala and Speranza, 2003)

2.3 Numerical Modeling of Masonry

Numerical modeling is a useful tool to validate experimental results and to understand the complex nonlinear behavior of structures. Numerous modeling methods have been developed to simulate the structural behavior of masonry structures. First, this section briefly describes the main numerical approaches used nowadays. Then, two material models that can be employed for masonry in DIANA FEA 10.2 are discussed.

2.3.1 Numerical approaches

Numerous numerical modeling approaches have been applied to masonry. With respect to the solution process, mainly the Discrete Element Method (DEM) and Finite Element Method (FEM) can be categorized. Meanwhile, different modeling methods to represent the structure are adopted, like the equivalent frame models where the piers and spandrels are represented through beam elements with calibrated properties, and the plane-stress/shell representations which models the masonry structural components directly (Rots, Messali, Esposito, Jafari, and Mariani, 2016). In this subsection, only the FEM approaches that will be implemented for this research are discussed in detail.

Generally, the FEM approaches for masonry can be divided into micro-scale modeling of the individual components, i.e. unit, mortar and interface between the unit and mortar, or macro-scale modeling which considers masonry as a composite (Rots, 1991). Figure 2.9 shows the three general approaches to model masonry: (a) detailed micro-modeling, (b) simplified micro-modeling, and (c) macro-modeling.

• *Detailed micro-modeling* uses continuum elements to model the units and mortar. The interface between them is also included and modeled with discontinuous elements.

Both elastic and inelastic material properties of unit and mortar can be included in the continuum elements. The unit-mortar interface represents the potential crack/slip plane, and initial dummy stiffness is required for the interface to avoid interpenetration of the continuum elements (Lourenco, 1996).

• Simplified micro-modeling simplifies the modeling by representing the joints, including mortar and unit-mortar interface, as discontinuous elements. In this way, masonry is modeled

as a bench of units bonded by potential fracture/slip interfaces along the joints (Lourenco, 1996).

• *Macro-modeling* considers masonry as a homogeneous material, with units, mortar and joints smeared out in the continuum elements. No distinction is made between the individual units and joints of the masonry.

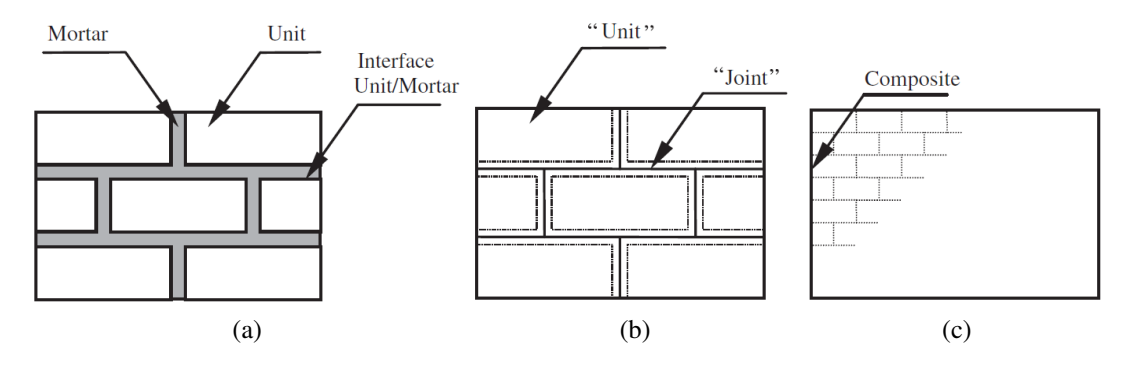


Figure 2.9: Modeling strategies for masonry structures: (a) detailed micro-modeling; (b) simplified micro-modeling; (c) macro-modeling. (Lourenço, 2002)

None of these three modeling approaches is better than the other. Rather, the choice of method depends on the needed accuracy level and simulation requirements.

Micro-modeling is suitable for studying structural behavior of single masonry components and when local effects need to be taken into account. Simplified micro-modeling method saves calculation time and effort, compared to the detailed micro-modeling. Nonetheless the Poisson's effect of mortar is not included in this approach, which may lower the accuracy level of results.

Macro-modeling requires much less computational effort and can be constructed easily. This type of modeling is highly practical when the aim is to capture the global behavior of a structure composed of solid walls with sufficiently large dimensions (Lourenco, 1996). As such, this type of modeling is used in this research.

2.3.2 Constitutive models

Macro-modeling of masonry requires proper constitutive models to simulate its nonlinear behavior, especially under seismic loading in this project. The two constitutive models which can be used for masonry in DIANA FEA 10.2 are discussed below.

2.3.2.1 Total strain crack model

Feenstra, Rots, Arnesen, Teigen, and Hoiseth (1998) first developed the total strain based crack model for concrete in the FEM software DIANA FEA. This constitutive model follows the smeared approach. It requires the following inputs: a) elastic properties: Young's modulus and Poisson's ratio; and b) parameters related to the tensile, compressive and shear behavior.

The tensile stress-strain relation in the model is characterized by a predefined tensile softening curve and corresponding tensile parameters. The compressive behavior is characterized by a compressive function and corresponding compressive parameters. The available tension softening functions and compressive functions can be found in DIANA FEA User's Manual (Manie, 2017).

However, employing this model to masonry may lead to inaccurate results. It does not include the anisotropic property of masonry and highly underestimates the energy dissipation under cyclic loading. Furthermore, this model does not distinguish tensile cracks and shear cracks, thus it fails to simulate the different failure modes of masonry.

2.3.2.2 Engineering Masonry Model

In order to overcome the disadvantages of using the total strain crack model for masonry, an updated model also based on smeared total strain formulation was developed in DIANA FEA 10.2; namely, the engineering masonry model (Schreppers, Garofano, Messali, and Rots, 2017).

This model includes the anisotropic property of masonry by introducing different values of elastic and inelastic parameters in two orthogonal directions (local x- and y-direction). The local x-axis of each element is normal to the head-joints and the local y-axis is normal to the bed-joints (Figure 2.10).

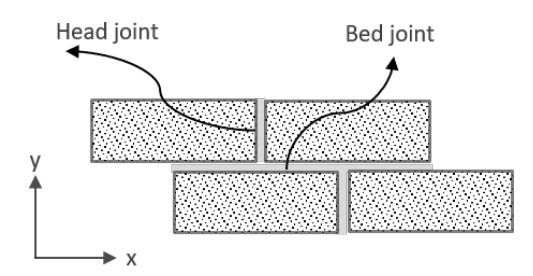


Figure 2.10: Pre-defined axes in the engineering masonry model

The constitutive model is described by its elastic, tensile, compressive and in-plane shear behaviors.

ELASTIC BEHAVIOR

Different values of elastic moduli of masonry are defined along the local x- and y-axis. To improve the stability of the numerical calculations, it is assumed that there is no coupling between neither the normal nor the shear stiffnesses in the model (Rots et al., 2016).

Poisson's ratio is also set to zero in the elastic stage to simplify the model. These assumptions are accurate enough for Dutch brick Masonry, which is characterized by small values of Poisson's ratio (Esposito, Jafari, Ravenshorst, Schipper, and Rots, 2018).

TENSILE BEHAVIOR

The tensile behavior can be defined in four crack planes in the engineering masonry model. Cracking occurs in all four directions normal to the crack planes. Two of the crack directions coincide with the local x- and y-axis, respectively. The other two crack directions are defined as the diagonal directions whose angle α is related to the pattern of brick units and mortar joints.

Along both the local x- and y-axis, the tensile stress-strain curve is determined by the Young's modulus E_i , tensile strength f_{ti} and cracking fracture energy G_{fti} , where i=1 and 2, is the index for the local x- and y-axis respectively. Linear tension softening is assumed in this model. The area under the tensile stress-strain curve is related to fracture energy G_{fti} and crack bandwidth h, which can be calculated from the area over which the the crack is smeared ($h = \sqrt{A}$, where A is the element area). The ultimate tensile strain ε_{uti} is defined when the crack is fully open, thus its value can be derived with a simple geometric relation:

$$\varepsilon_{uti} = 2f_{ti} \frac{G_{fti}}{h} \tag{2.1}$$

Secant unloading and reloading is assumed, which indicates that the stress and strain follow a straight path to and from the origin as shown in Figure 2.11.

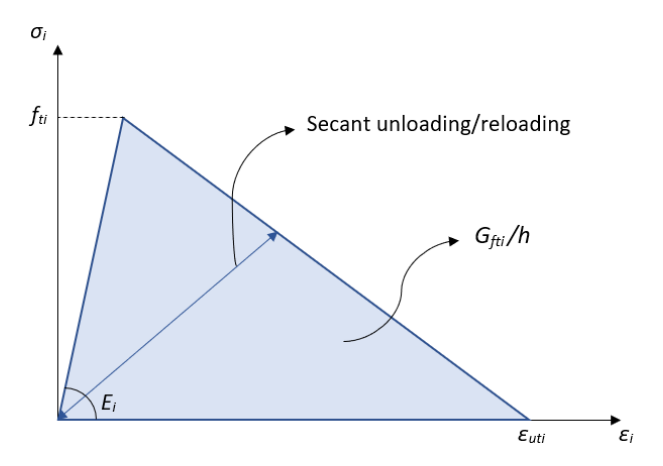


Figure 2.11: Tensile stress-strain curve in engineering masonry model

The tensile parameters normal to the bed-joint (tensile strength f_{ty} and crack fracture energy G_{fty}) are necessary to detect the masonry tensile failure. Therefore, they are fixed inputs in the engineering masonry model. To consider cracking in the other two directions, i.e. normal to the head-joint and diagonally, DIANA FEA 10.2 provides four options (Schreppers et al., 2017):

- head-joint failure not considered (headtp=none);
- direct input head-joint tensile strength (headtp=explic);
- diagonal stair-case cracks (headtp=diagon);
- tensile strength head-joint defined by friction (headtp=fricti).

HEADTP=NONE Head-joint failure is not considered in this option. The tensile strength f_t and cracking fracture energy G_{ft} are only defined in the direction perpendicular to the bed-joint (local

y-axis).

HEADTP=EXPLIC Cracking along bed-joints and head-joints is evaluated in this case. An additional input value for the tensile strength normal to the head-joints (f_{tx}) is required. However, the defined cracking fracture energy (G_{ft}) is used for the tensile stress-strain curves in both directions.

HEADTP=DIAGON Diagonal cracks are activated in this mode, together with cracking along the bed-joint and head-joint. The diagonal tensile strength $f_{t\alpha}$ is calculated from the tensile strength normal to the head-joints and bed-joints, with a pre-defined diagonal angle α :

$$f_{t\alpha} = \frac{f_{tx} \cdot f_{ty}}{\sqrt{(f_{tx} \cos \alpha)^2 + (f_{ty} \cos \alpha)^2}}$$
(2.2)

The value of $f_{t\alpha}$ is automatically calculated by DIANA FEA. In this case, the tensile strength normal to the head-joint (f_{tx}) is evaluated with the masonry shear sliding mechanism that the shear slip occurs along the bed-joint, thus its value depends on the limit shear stress $(f_{tx} = \tau_{max}/\tan\alpha)$. The direct inputs for this option include the tensile strength normal to the bed-joints f_{ty} , the diagonal angle α and the cracking fracture energy G_{ft} .

HEADTP=FRICTI Cracking along the bed-joints and head-joints is evaluated in this mode. Head-joint cracking may occur due to the two mechanisms: a) shear slip along the bed-joints; b) tensile failure of the masonry units. The tensile strength normal to the head-joints (f_{tx}) is derived from the shear strength τ_{max} and a pre-defined diagonal angle α ($f_{tx} = \tau_{max}/\tan \alpha$). A minimum head-joint tensile strength may be specified to include the second failure mechanism.

COMPRESSIVE BEHAVIOR

The compressive behavior of masonry in the engineering masonry model is mainly characterized by the Young's modulus (E_i) , compressive strength (f_{ci}) , compressive fracture energy (G_{fci}) and a factor n_i which considers the deformation capacity of masonry beyond the elastic limit:

$$n_i = (E_i \varepsilon_{pi}) / f_{ci} \tag{2.3}$$

where ε_{pi} is the masonry strain at the compressive strength f_{ci} .

The same compressive stress-strain relation is applied along the local x- and y-axis. The predefined curve (Figure 2.12) consists of a third order and a parabolic curve up to the compressive strength, then a linear softening curve is assumed until the residual stress is at 10% of the compressive strength. The ultimate compressive strain (ε_{uci}) is defined as the strain when the linear softening curve would reach zero stress. The value of ε_{uci} can be derived from the compressive fracture energy G_{fci} and crack bandwidth h (Rots et al., 2016).

Unlike the secant unloading defined in the total strain crack model, a bilinear unloading relation is adopted here. This bilinear unloading curve is built with a linear unloading with stiffness E_i , followed by a secant unloading. An unloading factor λ ($0 \le \lambda \le 1$) is defined to determine the bilinear point, as shown in Figure 2.12. It is easy to conclude that $\lambda = 0$ indicates a linear

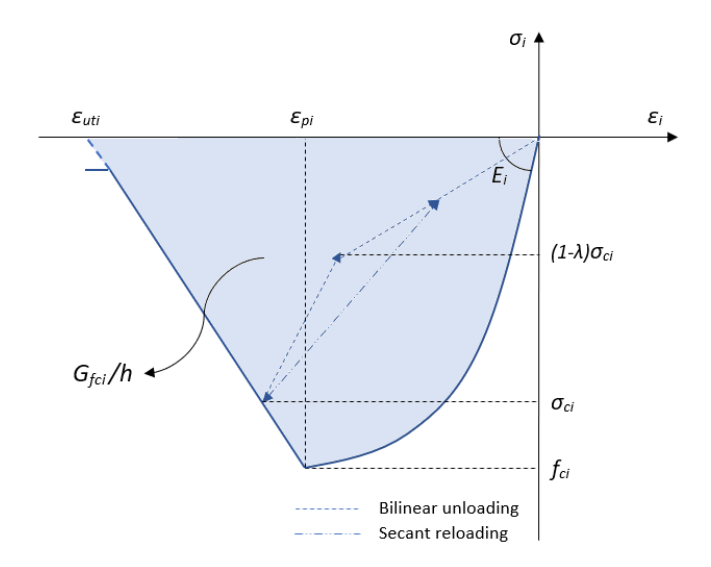


Figure 2.12: Compressive stress-strain curve in engineering masonry model

unloading to zero stress level with the initial stiffness E_i and $\lambda = 1$ represents the secant unloading (Rots et al., 2016). With this definition, the energy dissipation of masonry under the cyclic loading can be modeled properly.

SHEAR BEHAVIOR

The in-plane shear behavior of masonry is evaluated by the standard Coulomb friction criterion (Figure 2.13). The elastic shear stress-strain curve is characterized by the initial shear stiffness (*G*) and shear stress limit (τ_{max}). The shear stress limit τ_{max} is defined by the cohesion *c* and the friction angle ϕ :

$$\tau_{max} = \max(0; c - \sigma_{yy} \tan \phi)$$
 (2.4)

where σ_{yy} is the stress normal to bed-joints.

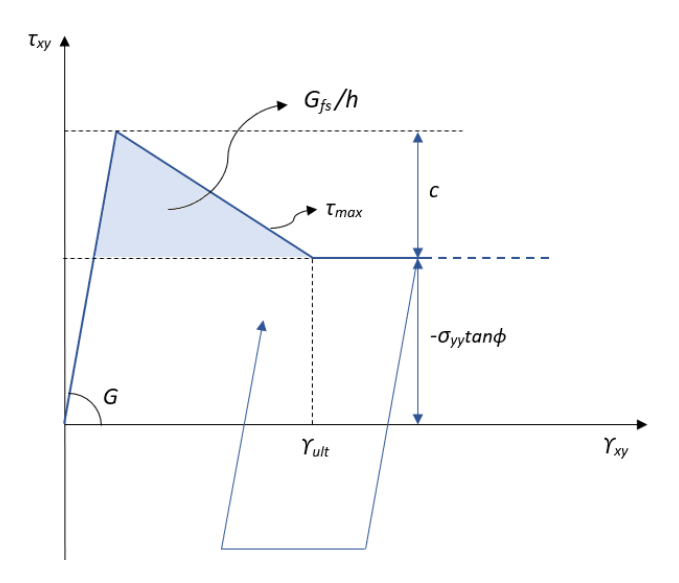


Figure 2.13: In-plane shear stress-strain curve in engineering masonry model

2.4 Seismic Analysis and Assessment

Seismic analyses for non-linear systems can be achieved through different methods, among which two main types are: nonlinear static pushover analysis (NLPO) and nonlinear dynamic time history analysis (NLTH). This section gives a brief description of these two methods theoretically. Both methods are powerful tools to capture the structural seismic response from the initial elastic phase and cracking formation to the final collapse. Meanwhile, it is important to recognize the dynamic properties (i.e. modal parameters) of the studied structure. For this, an eigenvalue analysis is required and also discussed in this section.

2.4.1 Eigenvalue analysis

The eigenvalue analysis is conducted by solving the equations of motion of the structure under free vibration. It is often implemented as the first step when performing structural dynamic analyses to determine the natural frequencies and mode shapes. These parameters give a direct observation of the structural dynamic properties, and are useful for the subsequent analyses.

For a multi degree-of-freedom (MDOF) and undamped system, the governing equations of free vibration can be written in matrix form as:

$$\mathbf{M}\ddot{\mathbf{u}} + \mathbf{K}\mathbf{u} = \mathbf{0} \tag{2.5}$$

The characteristic equation of the above eigenvalue problem is derived as:

$$\mathbf{K}\phi_i = \omega_i^2 \mathbf{M}\phi_i \tag{2.6}$$

where,

 ω_i = i-th circular eigenfrequency, i=1,2...n;

 ϕ_i = i-th eigenvector, i=1,2...n;

 $\mathbf{K} = \text{stiffness matrix};$

M = mass matrix.

For each natural frequency f_i and eigenvector ϕ_i , the corresponding generalized mass m_{ii} can be defined as $m_{ii} = \phi_i^T \mathbf{M} \phi_i$. With the eigenvectors ϕ_i normalized such that $m_{ii} = 1$, the effective mass percentage $m_{eff,i}$ which indicates the contribution of the i-th mode can be calculated using the following equations:

$$m_{eff,i,x} = \frac{(\phi_i^T \mathbf{M} r_x)^2}{m_{ii}}$$

$$m_{eff,i,y} = \frac{(\phi_i^T \mathbf{M} r_y)^2}{m_{ii}}$$

$$m_{eff,i,z} = \frac{(\phi_i^T \mathbf{M} r_z)^2}{m_{ii}}$$
(2.7)

where $m_{eff,i,x}$, $m_{eff,i,y}$ and $m_{eff,i,z}$ are the effective mass percentages for the translational degrees of freedom in global X, Y and Z directions. r_x , r_y and r_z are the influence vectors which represent the displacements resulting from a static unit ground displacement in the direction of the corresponding translational degree of freedom (Manie, 2017).

2.4.2 Nonlinear Pushover (NLPO) analysis

Nonlinear pushover analysis is a static approach to evaluate the seismic performance of structures. It is based on the assumption that the analyzed structure can be generalized as an equivalent single degree-of-freedom (SDOF) system with respect to its seismic response. A basic requirement to perform this equivalent analysis is that the seismic response of the structure is dominated by a single mode (Krawinkler and Seneviratna, 1998).

The inertia forces caused by the ground motion are approximately represented by a lateral load pattern on the structure. Implementing a pushover analysis consists of applying the gravity load and lateral loads in a predefined pattern (possible patterns are described hereinafter), and pushing the structure under the load pattern to a target displacement. The target displacement is determined based on the studied performance level. Depending on the application method of the lateral loads, the pushover analysis can be classified as monotonic or cyclic.

2.4.2.1 Monotonic Pushover Analysis

In monotonic pushover analyses, lateral loads are monotonically increased until the structure reaches the target displacement. Normally, a fixed lateral load pattern is used. It is clearly a rough estimation and only valid when the distribution of inertia forces is reasonably constant throughout the earthquake and the obtained maximum deformations under the load pattern are comparable to those expected in the earthquake. Therefore, the fixed load pattern pushover analysis is mainly suitable for structures that are not heavily affected by higher modes or those that only have a single failure mechanism that can be detected by the fixed lateral load pattern (Krawinkler and Seneviratna, 1998).

With respect to the design of the fixed lateral load pattern, the pushover analysis can be classified as: mass proportional, mode proportional and mode-mass proportional.

- Mass proportional: the lateral force distribution is proportional to the mass distribution of the structure;
- Mode proportional: the lateral force distribution is proportional to the most relevant mode shape of the structure;
- Mode-mass proportional: the lateral force distribution is obtained by multiplying the most relevant mode shape with the mass distribution.¹

The mass proportional pushover analysis is more focused on the structural behavior of lower stories since more forces are distributed at the lower part of the structure than in reality. Moreover, the mass proportional pushover analysis magnifies the relative importance of the story shear forces compared to the overturning moments (Krawinkler and Seneviratna, 1998). On the other hand, the mode proportional pushover analysis usually predicts more damage in the higher part of the structure.

However, pushover analyses with fixed load pattern may lead to inaccurate results, because the

¹Here the mode shape refers to the normalized eigenvector obtained from the eigenvalue analysis of the structure.

real distribution of inertia forces varies with time during seismic loading and redistribution of these forces probably occurs due to local failure mechanisms. The idea of applying adaptive load patterns that can follow the variant distribution of inertia forces provides a solution to overcome these drawbacks. A possible strategy for performing adaptive pushover analyses is to use the lateral forces proportional to the story shear resistance at the previous step (Bracci, Kunnath, and Reinhorn, 1997).

Monotonic pushover analyses yield force-displacement curves which are referred to as capacity curves or pushover curves. Typically, the base shear force is plotted against the top displacement of building structures.

2.4.2.2 Cyclic Pushover Analysis

Due to the cyclic nature of earthquake loading, damage accumulates and leads to a degradation in stiffness and strength. Thus, monotonic pushover analyses may overestimate the strength and deformation capacity of structures. To overcome this disadvantage, the quasi-static cyclic pushover analysis is more commonly adopted both experimentally and numerically in seismic analyses.

Cyclic pushover analyses are carried out by performing a sequence of pushover analyses in the positive and negative loading directions. The target displacement for each cycle is properly designed to capture the complete behavior of the structure.². The same methods are used to determine the lateral load pattern as in the monotonic pushover analysis, but limited to the invariant mass proportional or the mode proportional patterns

The results obtained from cyclic pushover analyses are hysteresis curves that present the force-displacement relationship under the complete cyclic loading. It is possible to build a backbone curve with the peak force-displacement points from each cycle. The backbone curve is similar in form - and thus comparable - to the monotonic pushover curve (Panyakapo, 2014).

2.4.3 Nonlinear Time-history (NLTH) analysis

Nonlinear time history analysis is an accurate method to study the seismic performance of structures. Real seismic signals are typically used as inputs. They vary arbitrarily with time. The response of the system (i.e. relative displacements) is directly calculated via numerical methods.

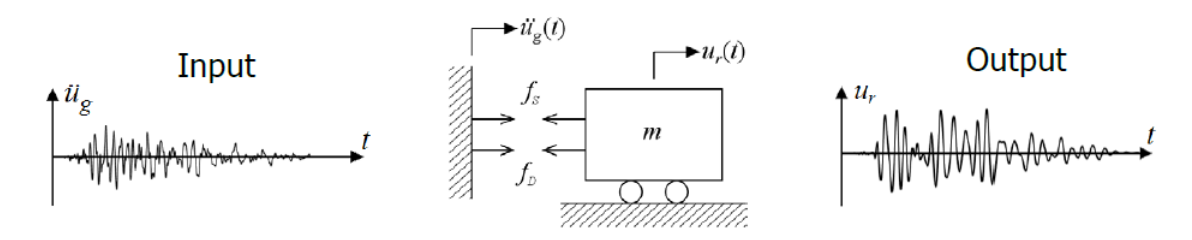


Figure 2.14: Mechanical model for dynamic time history analysis

²Normally one cycle is composed of a monotonic pushover analysis in the positive loading direction and a monotonic pushover analysis in the negative loading direction.

Figure 2.14 shows a simple mechanical model for the dynamic time history analysis of a SDOF system. The corresponding equation of motion is derived as:

$$m\ddot{u}_r(t) + f_D + f_S = -m\ddot{u}_g(t) \tag{2.8}$$

where f_D is the damping force and $f_S = f(u_r, sgn(u_r))$ is the restoring force which includes non-linearity.

The procedure for implementing a nonlinear time history analysis is briefly stated as:

- calculate u_r^{i+1} at time step t_{i+1} based on the displacement at previous time step u_r^i (e.g. through Newmark-beta method);
- calculate force f_S at time step t_{i+1} : $f_S^{i+1} = f_S^i + k^T (u_r^{i+1} u_r^i)$;
- find convergence of the time step t_{i+1} through iterations (e.g. Newton-Raphson method).

Incremental Dynamical Analysis (IDA)

Based on the dynamic time history analysis, the incremental dynamic analysis method was developed to estimate more thoroughly the seismic behavior of structures. This method applies a set of ground motion signals to the analyzed structure, and each signal is scaled to certain level of intensity (Vamvatsikos and Cornell, 2002). With a well-defined intensity scheme, the seismic response of the structure can be captured comprehensively.

Results of such analyses are usually presented using IDA curves, plotting the damage measure (DM) against the intensity measure (IM). Damage measure characterizes the structural behavior of the model; for instance, the maximum base shear, maximum interstorey drift ratio and so on. The intensity measure represents the intensity of a ground motion; for instance, the peak ground acceleration (PGA), peak ground velocity (PGV) and spectrum acceleration at the structure's fundamental period with 5% damping ($S_a(T_1,5\%)$)(Vamvatsikos and Cornell, 2002).

2.4.4 Seismic assessment of structures

In both nonlinear pushover and time history analyses, the main aspects to assess the structural performance under seismic events include: interstorey drifts, hysteresis loops, seismic capacity, crack patterns and failure mechanisms.

The interstorey drifts are defined as the ratio of the relative floor displacement and the interstorey height. It can be a key factor to assess the deformation and ductility distribution of the structure.

The hysteresis loops are presented by the base shear forces against the roof/floor relative displacements of the structure under seismic loads, which can be obtained through the dynamic time history analysis and quasi-static pushover analysis. The capacity curve from monotonic pushover analysis gives an estimation of the backbone curve of the hysteresis loops.

The seismic capacity of the structure can be evaluated with different assessment methods. The Capacity Spectrum Method (CSM) advised in Dutch standard NPR 9998 and N2 method adopted

in Eurocode 8 are mostly used in the pushover analyses while the IDA curves are used in dynamic time history analyses. Detailed procedures of these assessment methods can be found in P. Fajfar (1999,2000) and Vamvatsikos and Cornell (2002).

Chapter 3

FEA OF MASONRY PIER TUD_COMP-20

The numerical pushover analysis of a masonry pier was conducted first to get acquainted with modeling masonry, and to validate the Engineering Masonry model in the Finite Element software DIANA FEA 10.2. The finite element model is constructed on the basis of the specimen TUD_COMP-20 tested at TU Delft. Section 3.1 gives a brief description of the test and Section 3.2 explains the constructed finite element pier model in detail. The numerical pushover analyses procedures and results are presented in Section 3.3. Comparison between the numerical and experimental results are shown in Section 3.4. Based on this comparison, the finite element model is calibrated to fit experimental behaviors better. The updated pier model and numerical results are discussed in Section 3.5.

3.1 Description of the Test

Several masonry wall components and full-scale masonry assemblages were tested at TU Delft to investigate the structural behavior of Dutch masonry houses under seismic events. The slender pier TUD_COMP-20 was made of calcium silicate (CS) bricks, with unit dimensions of $210 \times 102 \times 71$ mm. A quasi-static in-plane pushover test was conducted on the specimen to investigate its seismic responses. Figure 3.1 (a) shows the overview of the specimen.

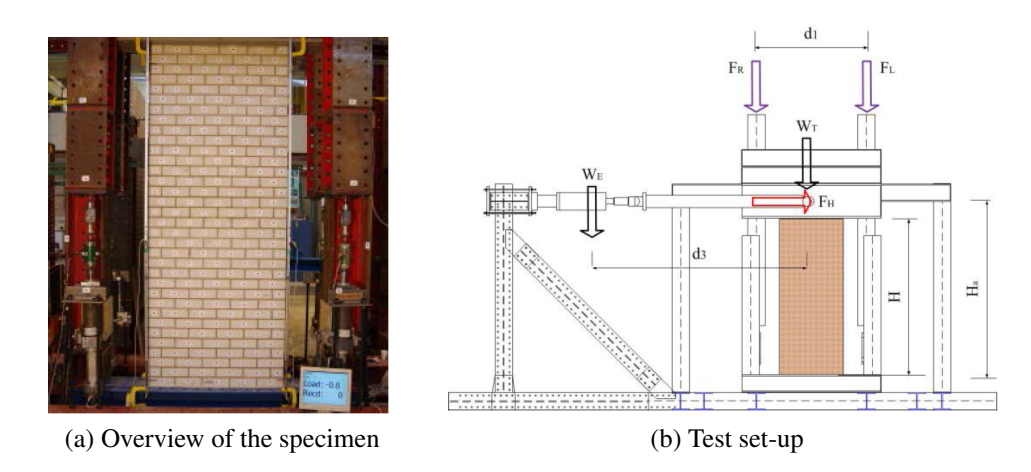


Figure 3.1: Quasi-static in-plane pushover test on TUD_COMP-20 (Esposito and Ravenshorst, 2017)

Table 3.1 lists the general information about the specimen and test conditions.

Specimen Name	Unit Type	L_w	H_w	t_w	σ_{v}	Boundary Conditions
		mm	mm	mm	MPa	
TUD_COMP-20	CS bricks	1110	2778	102	0.63	Cantilever

Table 3.1: Quasi-static cyclic in-plane tests performed on masonry pier

The masonry pier TUD_COMP-20 was tested in a cantilever configuration, with dimensions of approximately 1.3×2.7 m. The test set-up consists of a steel-frame assembling system with horizontal and vertical actuators. Figure 3.1 (b) shows the test set-up. The specimen was glued to the bottom steel beam to prevent sliding between the masonry and supporting beam. The top steel beam is used to introduce both horizontal and vertical loads to the masonry pier: the horizontal actuator connected to the center of top beam introduces a cyclic pushover load and the vertical actuator introduces a pre-compression load (σ_v). More detailed descriptions of the test can be found in Esposito and Ravenshorst (2017).

3.2 FE Model of Masonry Pier TUD_COMP-20

The finite element model of the masonry pier TUD_COMP-20 is built in DIANA FEA 10.2, based on the test conditions described in the previous section. The properties of the model and adopted assumptions are discussed in this section. Contents are arranged in the order of construction of the model, starting from its geometry and mesh, to applied constitutive laws and loading procedures.

3.2.1 Geometry of the model

The masonry pier and top steel beam of the set-up are included in the constructed finite element model (Figure 3.2). The pier is 1110 mm in width and 2778 mm in height, just as the test specimen. The top steel beam is fully connected to the masonry pier, so there is no sliding between these two components.

In the test, the horizontal actuator is connected to the center of the steel beam HEB600. To simplify the modeling, a steel beam with a rectangular cross-section (102 mm \times 300 mm) is used instead. The length of the beam is the same as the short edge of the masonry pier (1110 mm).

The specimen was tested under cantilever configuration, and the same boundary conditions are applied in the finite element model by fixing its base line. Additionally, to apply prescribed deformation at the loading point (node 823), DIANA FEA requires adding the constraint of displacement in the loading direction (x-direction). These attached supports are indicated in Figure 3.2.

3.2.2 Finite element discretization

Plane stress elements are considered to be suitable to model the structural behavior of the masonry pier, because its out-of-plane stress is zero ($\sigma_{zz} = 0$) under the loading conditions. Moreover, in

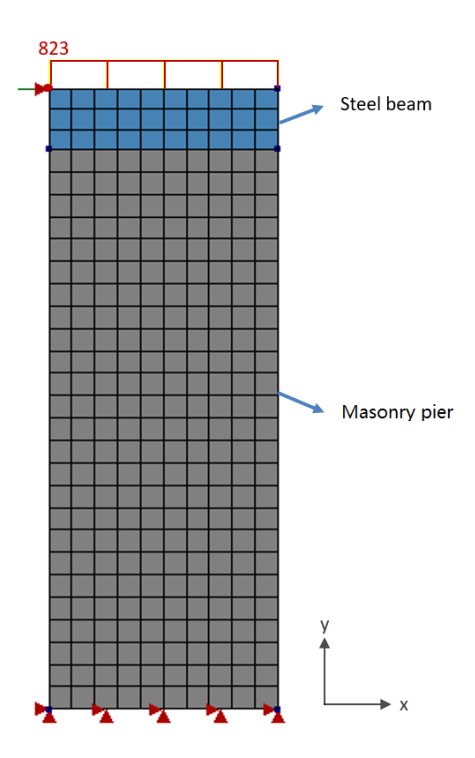


Figure 3.2: FE model of the masonry pier TUD_COMP-20

the analyses of the masonry pier, we would like to validate the engineering masonry model built in DIANA FEA 10.2, which is only applicable to plane stress elements and shell elements.¹

Therefore, the 8-node quadrilateral plane stress elements (CQ16M in DIANA FEA 10.2) are chosen to model the masonry pier. For compatibility, the top steel beam is also modeled with this element. CQ16M elements possess quadratic shape function (Figure 3.3) and two degrees of freedom per node (u_x and u_y). The chosen integration scheme is 2×2 Gauss integration.

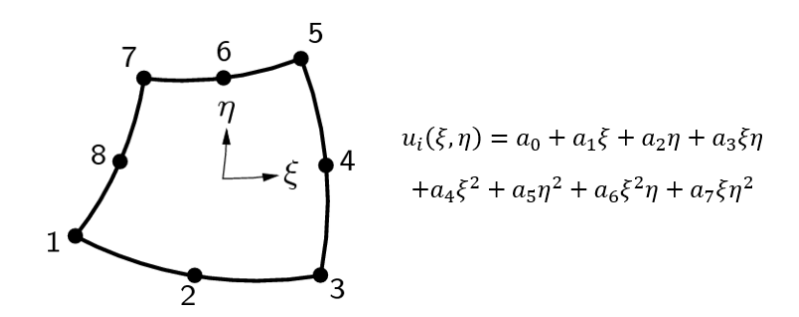


Figure 3.3: 8-noded plane stress element: CQ16M

The thickness of the applied finite elements is 102 mm. A mesh size of 111 mm is chosen, which is close to its thickness and proportional to the width of the masonry pier. A summary of the used finite elements for both structural parts is presented in Table 3.2, including the number of elements for each component and the total number of nodes in the model.

¹Shell elements are not used in the model because there is no out-of-plane behavior.

	Masonry pier	Steel beam	
Element type	regular plane stress	regular plane stress	
Element type	(CQ16M)	(CQ16M)	
Integration	Gauss integration	Gauss integration	
Integration	(2×2)	(2×2)	
Mesh size	111 mm	111 mm	
Element geometry	102 mm	102 mm	
(thickness)	102 111111	102 11111	
Number of	250	30	
elements	230	30	
Total number	917		
of nodes	917		

Table 3.2: Finite elements used in the masonry pier model

3.2.3 Constitutive laws

The focus of this research is the non-linear behavior of masonry. Two different smeared crack models of masonry are discussed and applied to the model. Steel is assumed much stiffer than masonry, so yielding does not occur. Thus, it is modeled as a linear-elastic material.

STEEL PROPERTIES

In the finite element model, the HEB600 steel beam on top of the masonry pier is modeled with a rectangular cross-section beam (see Figure 3.4).

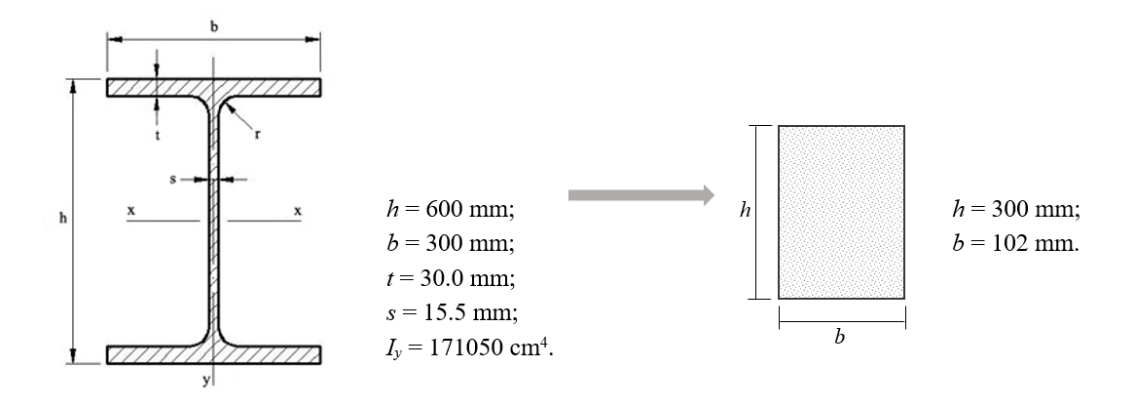


Figure 3.4: Simplification of steel beam cross-section

The true structural behavior of the HEB600 beam is simulated by modifying the Young's modulus of the simplified beam. The modified modulus (E'_s) is derived from a simple formula equaling the bending stiffness of HEB600 and the simplified beam.

$$E_s' \cdot \frac{1}{12} t_{beam} h_{beam}^3 = (EI)_{HEB600}$$
 (3.1)

where t_{beam} and h_{beam} are the thickness and height of the steel beam, and E_s is the modulus of steel ($E_s = 210$ GPa). The material properties of the steel in the model are presented in Table 3.3.

PropertyParameterUnitValueLinear elasticYoung's modulus E_s MPa1564706Poisson's ratiov0.3

Table 3.3: Material properties of steel

MASONRY PROPERTIES

Two different constitutive models are used for the masonry, namely the Total Strain Crack model and the Engineering Masonry model. Both material models are included in DIANA FEA 10.2. The adopted stress-strain relationships and relevant material parameters are described here. The difference of these two material models on the numerical results are discussed in section 3.3.

Total strain crack model

ELASTIC PROPERTIES First, the Young's modulus E, Poission's ratio v and mass density ρ of the CS brick masonry are defined in the total strain crack model. Six material tests were carried out to determine its mass density, Poission's ratio and elastic modulus in the direction perpendicular to the bed joint.² The average value of the results are used as inputs in the material model (see Table 3.4). Young's modulus are evaluated at 1/3 of the maximum compressive stress.

TENSILE BEHAVIOR A linear tension softening curve based on fracture energy is applied. Values of the two required input parameters (tensile strength f_t and Mode-I fracture energy G_{ft}) are presented in Table 3.4. f_t is obtained based on the averaged value of the flexural bond strength of the CS brick masonry through seven material tests. G_{ft} cannot be directly tested and is estimated through the following empirical equation (Schreppers et al., 2017):

$$G_{ft} = 0.025(2f_t)^{0.7} (3.2)$$

COMPRESSIVE BEHAVIOR The compressive strength of the CS brick masonry is much larger than its tensile strength. a Thorenfeldt compression curve is applied in this case. The only input is the compressive strength f_c of the CS brick masonry, which is extracted from the average value of f_c tested in the direction perpendicular to bed joint.

Figure 3.5 shows the adopted tensile and compressive stress-strain curves in the total strain crack model. Table 3.4 lists the input material parameters of the CS brick masonry.

Engineering Masonry Model

ELASTIC PROPERTIES Elastic modulus in the direction normal to head-joint and bed-joint of masonry (E_x and E_y), and the shear modulus (G_{xy}) are defined separately in the engineering masonry

²Results of the material properties test of the CS brick masonry can refer to Esposito, Messali, and Rots (2016)

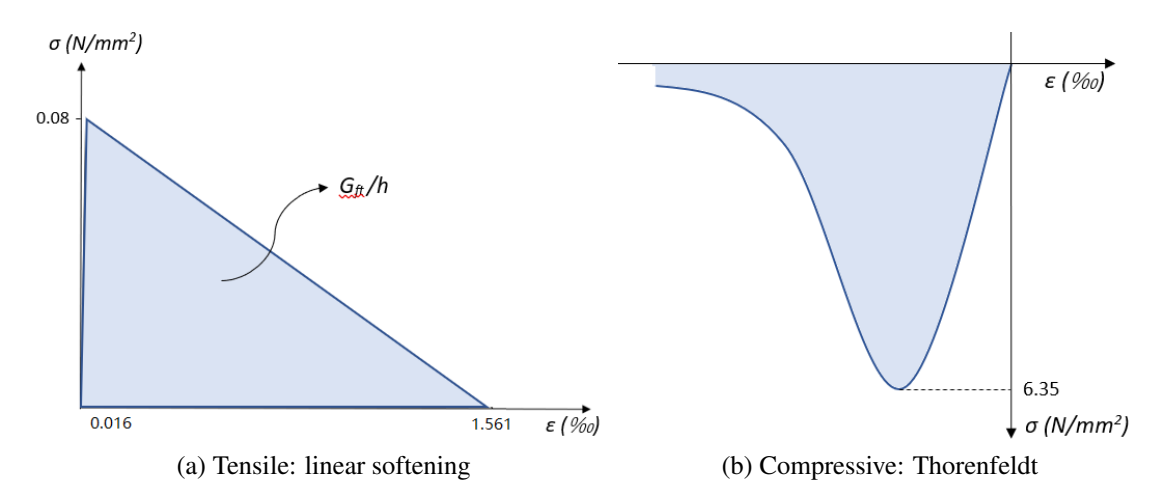


Figure 3.5: Stress-strain relation in the total strain crack model

Property	Parameter		Unit	Value
Linear	Young's modulus	E	MPa	4972
properties	Poisson's ratio	ν	MPa	0.16
properties	Mass density	ρ	kg/m ³	1805
	Tensile curve			Linear-crack
Tensile	Tensile cui ve			energy
behavior	Tensile strength	f_t	MPa	0.08
Deliavioi	Mode-I tensile	C.	N/mm	0.00693
	fracture energy	acture energy G_{ft}		0.00033
	Crack bandwidth			Rots
Compression	Compressive curve			Thorenfeldt
behavior	Compressive strength	f_c	MPa	6.35
	Crack orientation			Rotating

Table 3.4: Masonry properties in total strain crack model

model. Among them, E_y can be obtained from the standard compressive tests in the direction perpendicular to bed joints. The tested value of E_x is not available, therefore, an empirical relation is applied: $E_y/E_x = 1.5$. Similarly, G_{xy} is estimated via $G_{xy} = 0.4E_y$ (Schreppers et al., 2017). The elastic parameters used in the model are listed in Table 3.5.

TENSILE BEHAVIOR As discussed in section 2.3.2, four potential crack planes are provided in the engineering masonry model, associated with four head-joint failure options. Each option is tested in the masonry pier model. Their influences on the numerical results are evaluated. All the adopted tensile parameters are listed in Table 3.5. f_{ty} and G_{ft} are obtained with the same way as described before. Diagonal angle α is calculated according to the brick layout and mortar joint patterns. A minimum tensile strength normal to the head-joint (f_{tx}) is estimated via $f_{ty}/f_{tx} = 0.5$ from literature (Schreppers et al., 2017).

COMPRESSIVE BEHAVIOR The same compressive stress-strain curve is defined for both bed-joint and head-joint directions regardless of the head-joint failure choice in the engineering masonry model. The input values of compressive strength f_c and compressive fracture energy G_{fc} are extracted from standard compressive test of the CS brick masonry in the direction perpendicular to bed joints (Esposito et al., 2016). A linear unloading is chosen to simulate the highly nonlinear behavior of masonry under cyclic loading, which gives $\lambda = 0$. All compressive parameters of the model are listed in Table 3.5 as well.

SHEAR BEHAVIOR The standard Coulomb friction criterion is adopted to describe shear behavior in the engineering masonry model. The value of cohesion c and friction angle ϕ are obtained from the shear test of masonry (Esposito et al., 2016).

Figure 3.6 shows the adopted tensile and compressive stress-strain curves and Table 3.5 summarizes the input material parameters of the CS brick masonry in the engineering masonry model.

Table 3.5: Material properties in engineering masonry model

Property	Parame	ter		Unit	Value
	Young's modulus	Perpendicular to head joints	E_{x}	MPa	3315
Elasticity		Perpendicular to bed joints	E_{y}	MPa	4972
	Shear modulus		G_{xy}	MPa	1989
	Mass density		ρ	kg/m ³	1805
	Tensile strength	Bed joint	f_{ty}		0.08
Cracking	Tensile strength	Head joint (minimum)	f_{tx}	MPa	0.16
	Tensile fracture energy		G_{ft}	N/mm	0.00693
	Angle between stepped diagonal crack and bed joint		α	rad	0.792
	Compressive strength		f_c	MPa	6.35
Crushing	Fracture energy in compression		G_{fc}	N/mm	20
	Factor to strain at compressive strength		n		5
	Unloading factor		λ		0
Shear	Friction angle		φ	rad	0.464
failure	Cohesion		f_{vo}	MPa	0.13

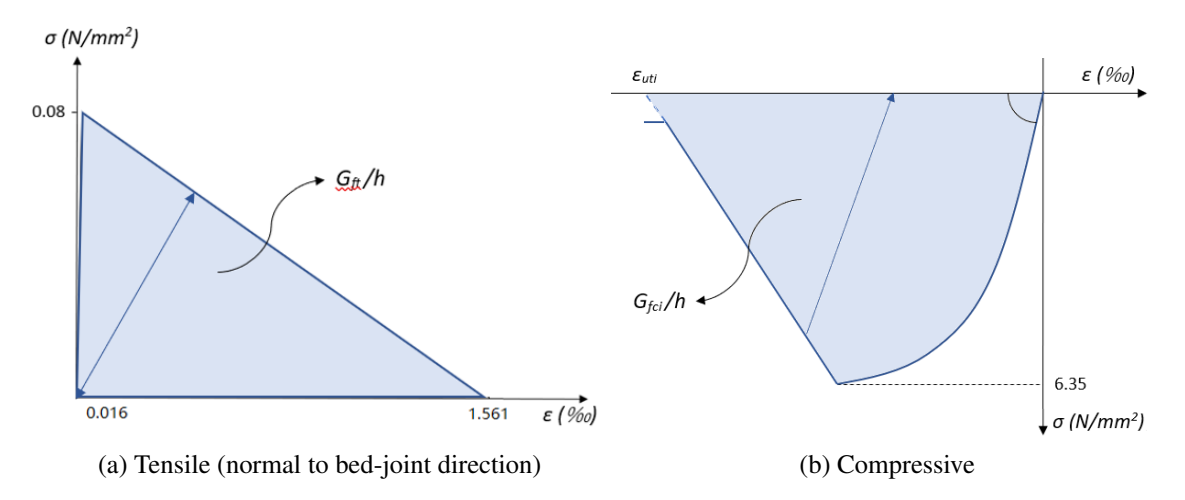


Figure 3.6: Stress-strain relation in the engineering masonry model

3.3 Nonlinear Pushover Analysis

The nonlinear pushover analysis is conducted on the built masonry pier model. This section discussed the loads and corresponding load application methods on the model, as well as the procedure to perform the pushover analyses.

3.3.1 Loading method

In total, three load types are applied to the model: self-weight of the masonry pier, the precompression load on the top steel beam and the pushover load.

Self-weight

The self-weight of the masonry pier is applied first to the model. Note that the self-weight of steel beam is included in the pre-compression load (σ_{ν}), thus only the masonry self-weight is considered here.

Pre-compression load

The pre-compression load consists of an applied vertical force and the additional weight of the steel frame system. During the test, the compressive load ($\sigma_v = 0.63\,$ MPa) was applied and kept constant through the two vertical actuators on the top steel beam. Thanks to the adopted cantilever boundary condition, forces in the two vertical actuators remained constant as well.

In the finite element model, the compressive forces are modeled as distributed forces along the top edge of the steel beam. This is considered reasonable as the steel beam is much stiffer than the masonry pier. The distributed force (f_v) is indicated with red lines in Figure 3.2. The value of this force is easily calculated through the beam width and the predefined compressive load σ_v , as:

$$f_v = w_{beam} \cdot \sigma_v = 102 \text{ mm} \times 0.63 \text{ MPa} = 64.26 \text{ N/mm}$$
 (3.3)

where w_{beam} is the width of the top steel beam, i.e. the thickness of the beam elements.

Pushover load

In the test, the horizontal pushover load was applied through an actuator connected to the center of the HEB600 steel beam. In the FE model, the top steel beam is simplified into a rectangular beam with a height of 300 mm. The horizontal load is thus applied at the top of the simplified beam in order to represent the moment arm from the experiment. Since the beam is very stiff compared to the masonry pier, the loading point is set at the top left corner of the steel beam (node 823), as shown in Figure 3.2.

The pushover load is applied with displacement control to obtain the post-peak behavior of the masonry pier. Therefore, a prescribed displacement is applied to the loading point (node 823) in the horizontal direction.

The loading history of masonry may influence the structure's behavior. Given the cyclic nature of earthquake, cracks can close and open again before new cracks occur. To take into account this influence, both monotonic and cyclic pushover analysis are performed on the model. The detailed loading schemes for both analysis are explained as follows.

MONOTONIC PUSHOVER The prescribed displacement in monotonic loading is set to be 90 mm. As the maximum displacement that the masonry pier was subjected to in the cyclic pushover test is 87 mm, the chosen target displacement makes it possible to compare these two results.

CYCLIC PUSHOVER The cyclic loading scheme is designed to resemble the loading history during the test. In the quasi-static cyclic pushover test, the pier was subject to a cyclically applied horizontal displacement. Fourteen cycles were applied in total, and each cycle was composed of three identical runs. In every run, the desired horizontal target displacement was applied in both directions (+x/-x directions) starting and ending at the initial position of the pier (zero displacement position) (Esposito and Ravenshorst, 2017).

The target horizontal displacements for each cycle are present in Table 3.6. A time dependent factor is added to each load step to realize the cyclic loading with constant rate. The cyclic loading scheme can be seen in Figure 3.7.

3.3.2 Analysis procedure

Nonlinear monotonic and cyclic pushover analyses are performed on the model. Physically nonlinear effects are included in both analyses. Two masonry pier models are built with total stain crack model and engineering masonry model, respectively. The same analysis procedures (i.e. iteration method and convergence criteria) are employed on both models.

Table 3.7 shows the numerical procedure in the monotonic pushover analysis.³ The lateral load is applied in 100 steps up to the target displacement (90 mm). Full Newton-Raphson method is applied, and the maximum number of iterations per load step is 20. Additionally, the line search

³Note the monotonic pushover analysis of the model is only carried out in the +x direction, because the masonry pier is symmetric in the loading plane.

Cycle	Net displacement (test)			splacement erical)
	m	m	n	ım
C1	-0.67	0.47	-0.45	0.45
C2	-1.58	1.14	-0.90	0.90
C3	-2.70	2.19	-1.80	1.80
C4	-3.88	3.34	-3.60	3.60
C5	-8.77	8.10	-8.10	8.10
C6	-18.63	17.84	-18.0	18.0
C7	-28.75	27.62	-27.0	27.0
C8	-38.86	37.35	-36.0	36.0
C9	-48.73	47.18	-45.0	45.0
C10	-58.66	56.93	-54.0	54.0
C11	-68.95	68.13	-63.0	63.0
C12	-80.13	78.53	-72.0	72.0
C13	-86.87	86.33	-81.0	81.0
C14	-86.39	87.06	-90.0	90.0

Table 3.6: Target displacements in cyclic loading

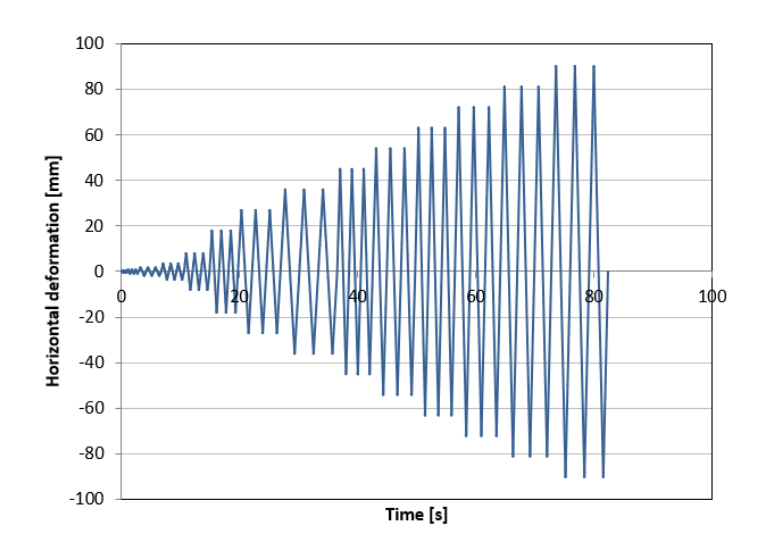


Figure 3.7: Cyclic pushover loading scheme

and continuation iteration techniques are activated to seek for a better convergence. The numerical calculation is considered convergent when both the displacement norm and force norm are satisfied.

Similarly, Table 3.8 gives the analysis parameters in the cyclic pushover analysis. In total 4116 time steps are used to perform the fourteen cycles of pushover loading in both +x and -x directions. The regular Newton-Raphson iteration method is adopted and the number of iteration per step is limited to 100. Line search is used here as well. Like in the monotonic pushover analyses, the numerical calculation reaches convergence when both the displacement norm and force norm are satisfied.

Load	Self-weight	1		
steps	Pre-compression	1		
steps	Pushover	0.01(100)		
	Max. number of iterations	20		
Iteration	Iteration method	Regular Newton-Raphson		
method	Line search	Yes		
	Continuation iteration	Yes		
Convergence	Satisfy both displacement norm (tolerance 0.01)			
criteria	and force norm (tolerance 0.01)			

Table 3.7: Monotonic pushover analysis procedure

Table 3.8: Cyclic pushover analyses procedure

Load	Self-weight	1	
steps	Pre-compression	1	
steps	Pushover	4116 time steps	
Iteration	Max. number of iterations	100	
method	Iteration method	Regular Newton-Raphson	
method	Line search	Yes	
Convergence	Satisfy both displacement norm (tolerance 0.01)		
criteria	and force norm (tolerance 0.01)		

3.4 Results of the Pushover Analysis

The results of monotonic and cyclic pushover analyses on the masonry pier model are discussed in section 3.4.1 and 3.4.2. In both sections, the pushover results of total strain crack model and engineering masonry model are compared in terms of capacity curves. The advantages of using the engineering masonry model to simulate seismic response of masonry are clearly shown.

3.4.1 Monotonic pushover results

Figure 3.8 (a) shows the capacity curve using the total strain crack model. The analysis divergent at a horizontal displacement of 48.6 mm. While using the engineering masonry model, we succeed to get results for all the steps, as shown in Figure 3.8 (b). However, when the model is pushed to a displacement of 60.3 mm, the numerical calculation dose not converge within the defined maximum 100 iterations and a sudden reduction in base shear force is observed in this step.

Note the capacity curve presented in Figure 3.8 (b) is based on the engineering masonry model with the first head-joint option (headtp=none) in which the head-joint failure is not considered, results with other head-joint options can be found in the Appendix A. Divergence occurred in the engineering masonry model with the third option (headtp=diagon), while models with the other three head-joint options give very similar results.

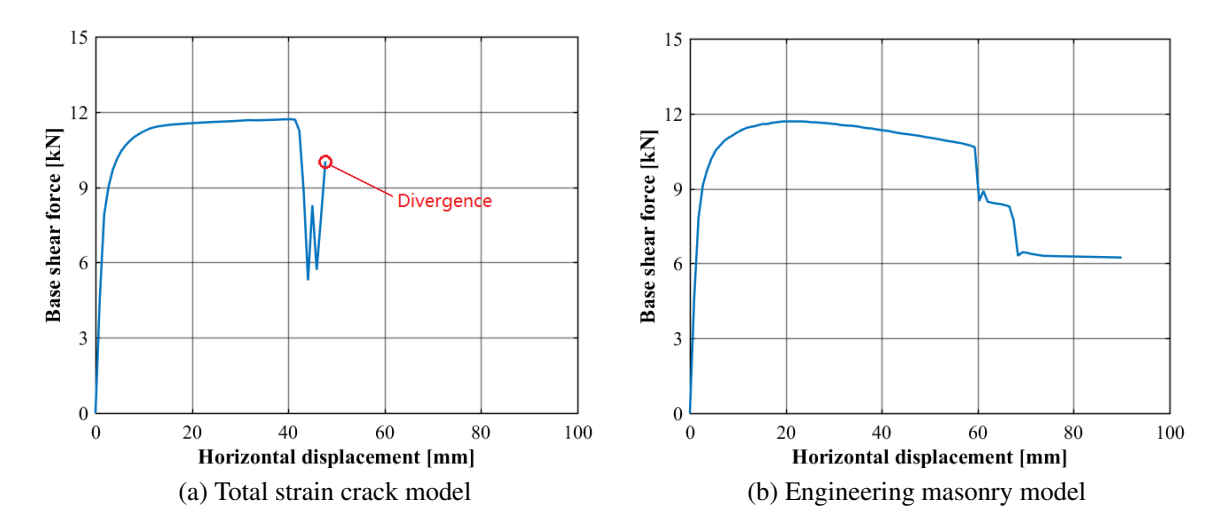


Figure 3.8: Capacity curves of the masonry pier in monotonic pushover analysis

3.4.2 Cyclic pushover results

Figure 3.9 gives the hysteresis curves resulted from the cyclic pushover analyses on the two models. Divergence occurred at the first run of cycle 9 (target displacement: ± 45 mm) in the total strain crack model (see Figure 3.9 (a)).

The resulting curves using engineering masonry model is shown in Figure 3.9 (b). Like for the monotonic pushover results, the presented curve is from the model with the first head-joint option (head-joint failure not considered) in DIANA FEA 10.2. Results from the other head-joint options can be found in the Appendix A. Divergence occurred at an early stage in the engineering masonry model with the third option (headtp=diagon), while models with the other three head-joint options give very similar results.

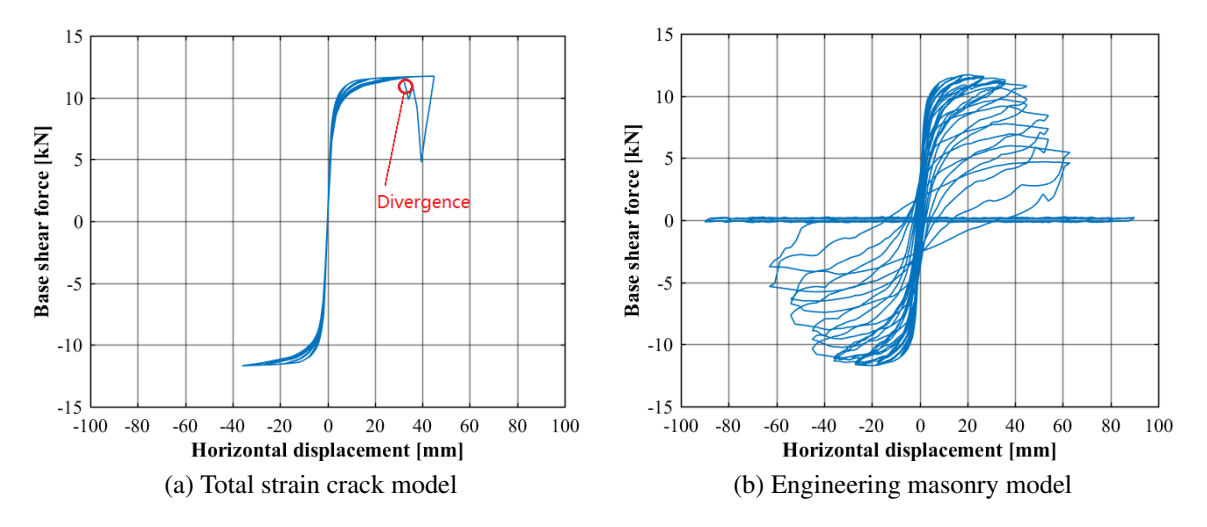


Figure 3.9: Capacity curves of the masonry pier in cyclic pushover analysis

It can be observed from Figure 3.9 that the engineering masonry model is more suitable to simulate the structural behavior of TUD_COMP-20 under cyclic loading. The energy dissipation during the

cyclic pushover loading process can not be illustrated using the traditional total strain crack model. The advantages of the engineering masonry model in simulating the seismic behavior of masonry are verified. Therefore, the following research work is based on the engineering masonry model.

3.5 Comparison between Experimental and Numerical Results

To validate the simulation of the masonry pier TUD_COMP-20, the obtained numerical cyclic pushover results are interpreted and compared to the experimental results in terms of capacity curves (section 3.4.1), energy dissipation (section 3.4.2), failure mechanisms and crack patterns (section 3.4.3).

3.5.1 Capacity curves

The capacity curves of TUD_COMP-20 under cyclic loading from experiment and numerical analysis are compared in Figure 3.10.

In the quasi-static cyclic pushover test, the pier TUD_COMP-20 was subjected to a maximum displacement of 87 mm in both positive and negative loading directions, corresponding to a drift 3.1%, until collapse occurred. The maximum base shear force in the positive and negative direction during loading history are +15.4 and -14.8 kN, respectively. In both directions, the base shear force reduced gradually with substantial energy dissipation after reaching the peak value. A 20% reduction in the force was observed at a displacement of +68.1 and -69.1 mm for positive and negative loading direction, respectively (Esposito and Ravenshorst, 2017).

Numerical results show a smaller value of the maximum base shear force in both positive and negative loading directions, which are +11.7 and -11.7 kN respectively. The 20% reduction of the force occurs at a displacement of +49 and -48 mm approximately. Energy dissipation during the cyclic loading can be observed in the capacity curve. However the numerical results show the masonry pier already collapses at the fist run of Cycle 12 (target displacement: ± 72 mm).

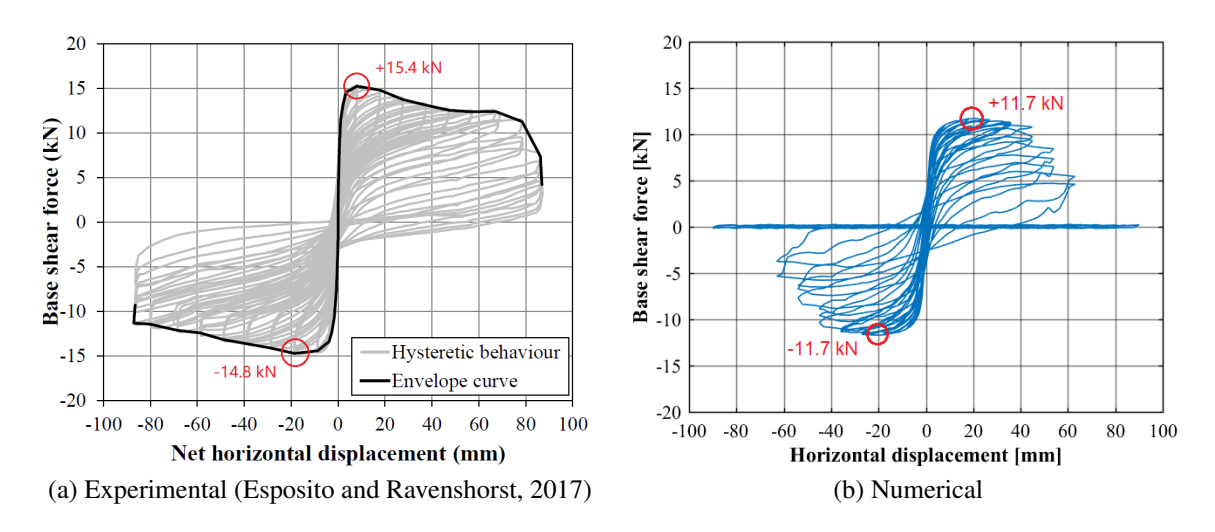


Figure 3.10: Comparison of the numerical and experimental capacity curves

3.5.2 Energy dissipation

In addition to the capacity curves, the energy dissipation in each cycle during the test and numerical loading are also plotted and compared (Figure 3.11). The horizontal axis indicates the displacement of the masonry pier in the loading direction per cycle, and vertical axis gives corresponding energy dissipation, which is calculated through the area of hysteresis loop for each loading cycle. The amount of dissipated energy in numerical analysis is much lower (around 60%) than the amount during the test.

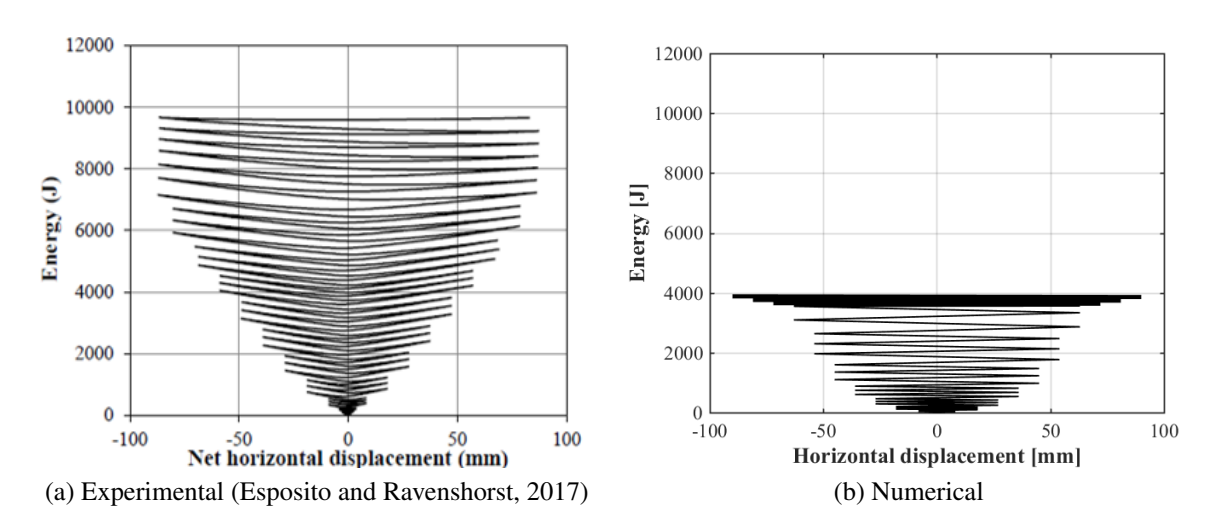


Figure 3.11: Energy dissipation of the masonry pier

3.5.3 Failure modes and crack patterns

The masonry pier specimen was governed by the rocking and crushing failure modes during the quasi-static pushover test. With the increment of the loading displacement, horizontal cracks developed gradually in three layers of mortar bed joints at the bottom of the pier. Moreover, splitting cracks at both bottom sides of the pier occurred at large displacements. Toe crushing was observed during the last two loading cycles (C13 and C14), which finally resulted in the collapse of the specimen (Esposito and Ravenshorst, 2017).

Similar mechanisms can be found in the numerical analysis. The damage also concentrates at the bottom of the masonry pier. Horizontal cracks are found around the position of three mortar joints from the bottom. The phenomenon of toe crushing occurred with large displacements, and fully developed along the bottom layer of bricks of the pier, leading to collapse of the pier model at cycle C12. Crack pattern evolution of the model is shown in Figure 3.12.

In general, the numerical model shares the same failure mechanism (rocking and crushing) and crack patter evolution with test specimen. However, the maximum base shear force in both loading directions are slightly underestimated. Additionally, the energy dissipation is much lower than that in the test. Calibration of the finite element model of the masonry pier is then required, which is discussed in the following section.

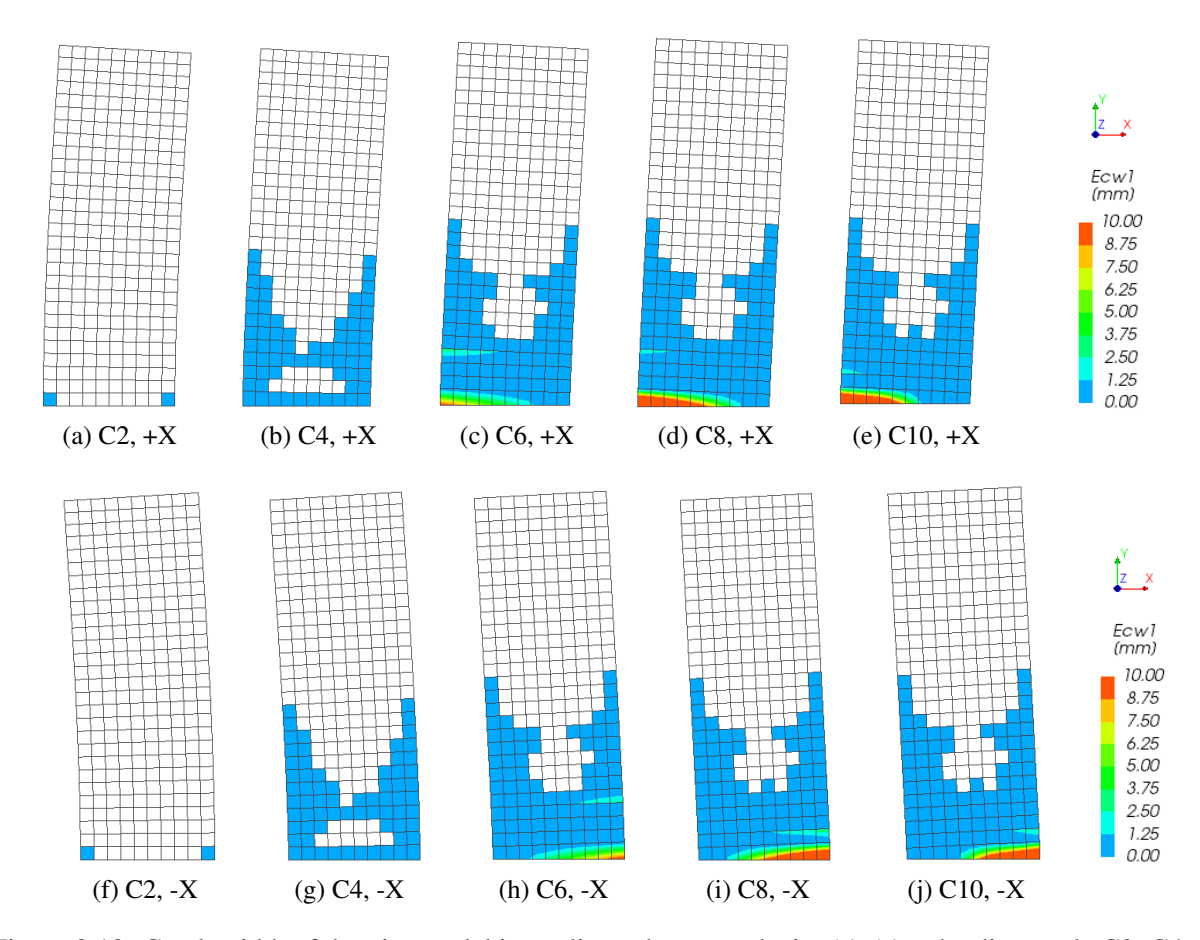


Figure 3.12: Crack width of the pier model in cyclic pushover analysis: (a)-(e) at loading cycle C2, C4, C6, C8 and C10 in positive direction; (f)-(j) at loading cycle C2, C4, C6, C8 and C10 in negative direction.

3.6 Calibrated Model and Results

A parametric study was performed to calibrate the masonry pier model. In particular, in order to better estimate the energy dissipation of TUD_COMP-20. Parameters related to the crushing of masonry were selected.

Among the crushing parameters in the engineering masonry model, the unloading factor λ has already been set as zero, which indicates linear unloading, to consider the energy absorption. Therefore, the compressive strength f_c , compression fracture energy G_{fc} and strain factor n are modified to update the FE model.

3.6.1 Updated FE model

In total 27 models were built with different values of f_c , G_{fc} and n.⁴ All other material parameters, loading scheme and iteration methods remain unchanged from the original FE model.

⁴Values of 80% and 120% of the original f_c and G_{fc} are chosen, and n varies in 4, 5 and 6.

The capacity curves and energy dissipation for each model are plotted and compared to the experimental results. Among all the FE models for masonry pier TUD_COMP-20, results of the model with masonry compressive strength $f_c = 8.89\,$ MPa, compression fracture energy $G_{fc} = 27\,$ N/mm and compressive strain factor n=5 matches the experimental curves best. Masonry properties of the updated FE model are summarized in Table 3.9. The modified parameter values are marked in red.

Property	Parame	ter		Unit	Value
	Young's modulus	Perpendicular to head joints	E_x	MPa	3315
Elasticity		Perpendicular to bed joints	E_{y}	MPa	4972
	Shear modulus		G_{xy}	MPa	1989
	Mass density		ρ	kg/m^3	1805
	Tensile strength	Bed joint	f_{ty}		0.08
Cracking	_	Head joint (minimum)	f_{tx}	MPa	0.16
	Tensile fracture energy		G_{ft}	N/mm	0.00693
	Angle between stepped diagonal crack and bed joint		θ	rad	0.792
	Compressive strength		f_c	MPa	8.89
Crushing	Fracture energy in compression		G_{fc}	N/mm	27
	Factor to strain				
	at compressive		n		5
	strength				
	Unloading factor		λ		0
Shear	Friction angle		φ	rad	0.464
failure	Cohesion		f_{vo}	MPa	0.13

Table 3.9: Masonry properties in updated FE model

3.6.2 Numerical results and assessment

Figure 3.13 shows the base shear force - horizontal displacement curve of the update FE model, with a comparison to the experimental curves. The maximum base shear force in positive and negative loading direction increased to +12.1 kN and -12.1 kN, respectively, compared to +11.7 kN and -11.7 kN in the original numerical results.

Analytical calculations of the force capacity of the masonry pier are also available according to Eurocode 8 and NPR 9998. For the masonry pier TUD_COMP-20 which shows a flexural type

failure, the estimate in Eurocode 8 gives a base shear force capacity of 12.9 kN, and the formulation proposed by NPR 9998 predicts a premature toe-crushing failure with base shear force of 12.0 kN (Esposito and Ravenshorst, 2017).

Table 3.10 summarizes the maximum base shear force of TUD_COMP-20 obtained from experiment, numerical modeling and analytical calculations. Errors in the numerical and analytical estimation of the base shear force capacity are listed in Table 3.10 as well.

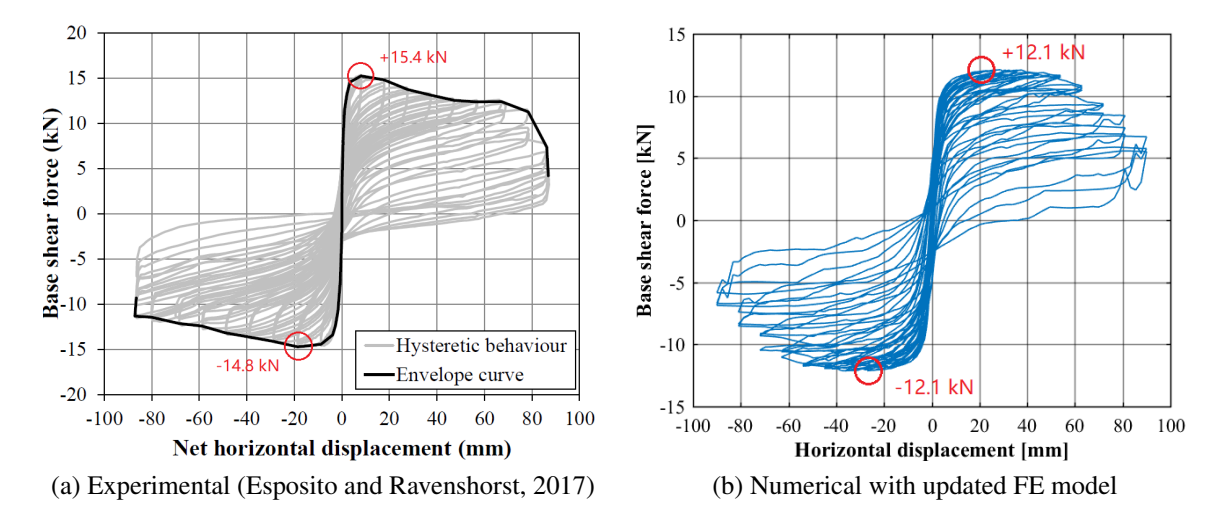


Figure 3.13: Capacity curve of wall TUD_COMP-20

Table 3.10:	Comparison	of base shear	force capacity	of wall TUD.	COMP-20

Analysis	Positive loading direction(+X)		Negative lo directio (-X)	Failure mode		
	Max. base shear force	Error	Max. base shear force	Error	mode	
	kN		kN			
Experimental	+15.4		-14.8		Rocking and	
results	+13.4	_	-14.0	_	toe crushing	
Numerical	+12.1	-0.21	-12.1	-0.18	Rocking and	
results	+12.1	-0.21	-12.1	-0.16	toe crushing	
Eurocode 8	+12.9	-0.16	-12.9	-0.12	Rocking	
NDD 0008	112.0	0.22	-12.0	-0.19	Premature	
INF IX 9990	NPR 9998 +12.0 -0.22 -1	+12.0 -0.22		-12.0	-0.19	toe crushing

In addition to the capacity curves, the energy dissipation of the updated masonry pier model is compared to the experimental results, as shown in Figure 3.14. It can be seen that compared to the results obtained in the original model (Figure 3.11), the amount of dissipated energy in the updated FE model is much closer to the experimental results.

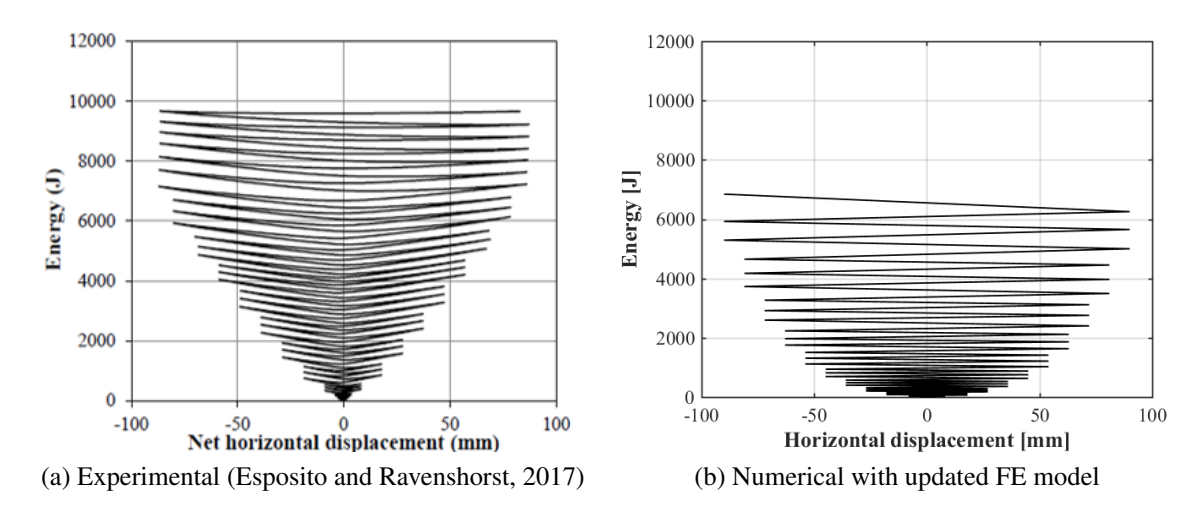


Figure 3.14: Energy dissipation for masonry pier TUD_COMP-20

Rocking and toe crushing failure mode is also observed in the updated masonry pier model. Small horizontal cracks at the right and left bottom sides of the pier start to develop from the second cycle, and the crack width keeps increasing with the pushover load in both directions. Toe crushing occurred at large displacements. The crack width evolution is shown in Figure 3.15.

Besides comparing the structural capacities and crack patterns, the relation between the vertical and horizontal displacement, and the amount of local deformation are also assessed for the updated FE model.

The curves of vertical versus horizontal displacement at the top left and right corners of the pier (Figure 3.16). The amount of crushing at the four corners of TUD_COMP-20 are also similar in the test and numerical analysis (Figure 3.17). Evaluation of the crushing is achieved by measuring the vertical displacement over 4 bricks at the four corners of the pier both experimentally and numerically. Sliding of the pier is calculated through the horizontal displacement between the first and the second brick layer at the top and bottom of the pier. Numerical results show similarity with the experimental results, but slightly more sliding at the top at large displacements (Figure 3.18).

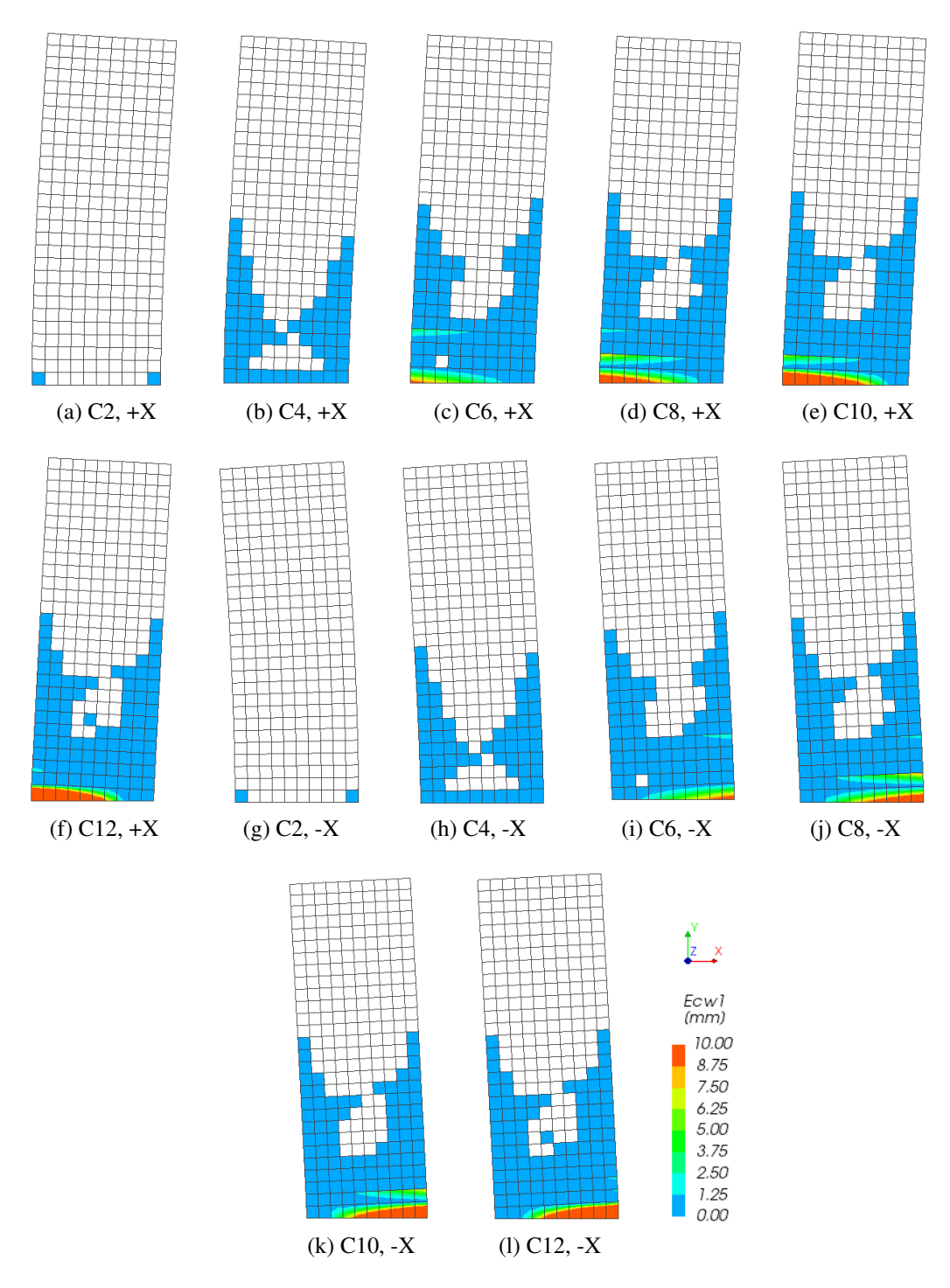


Figure 3.15: Crack width of the updated pier model in cyclic pushover analysis: (a)-(f) at loading cycle C2, C4, C6, C8, C10 and C12 in positive direction; (g)-(l) at loading cycle C2, C4, C6, C8, C10 and C12 in negative direction.

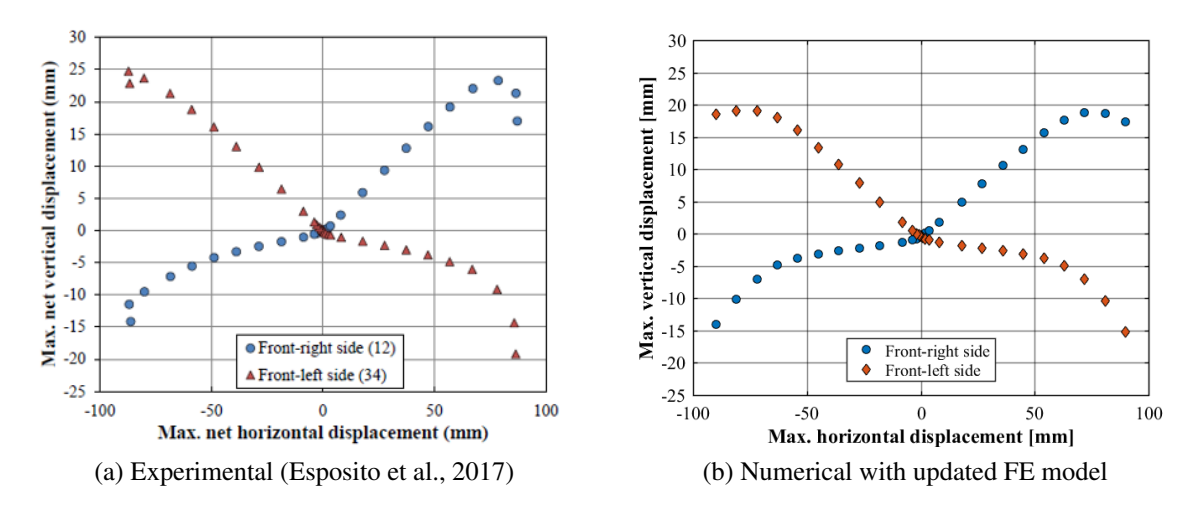


Figure 3.16: Maximum vertical versus horizontal displacement of TUD_COMP-20

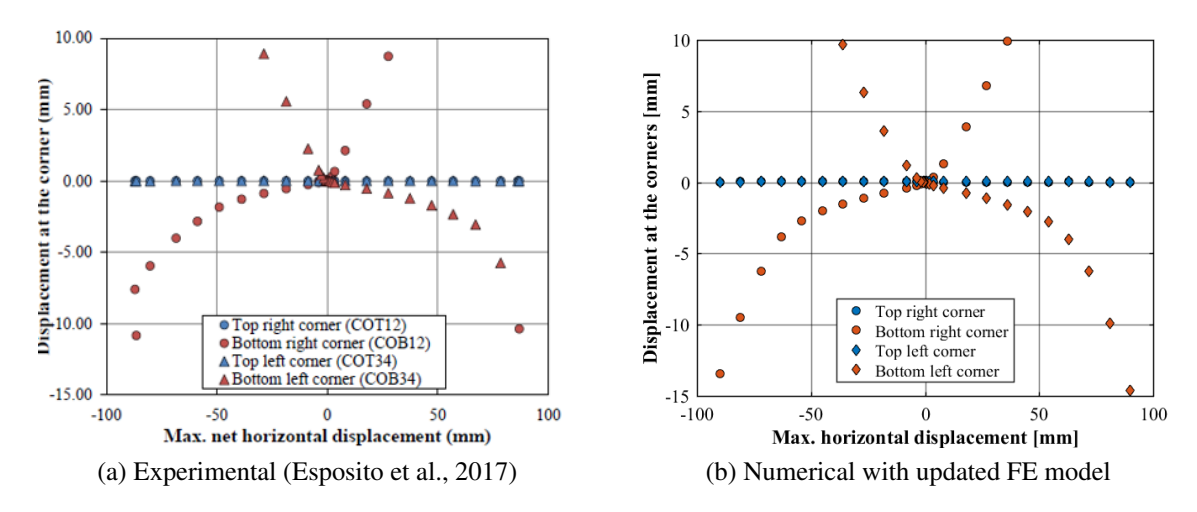


Figure 3.17: Crushing at the corners of TUD_COMP-20

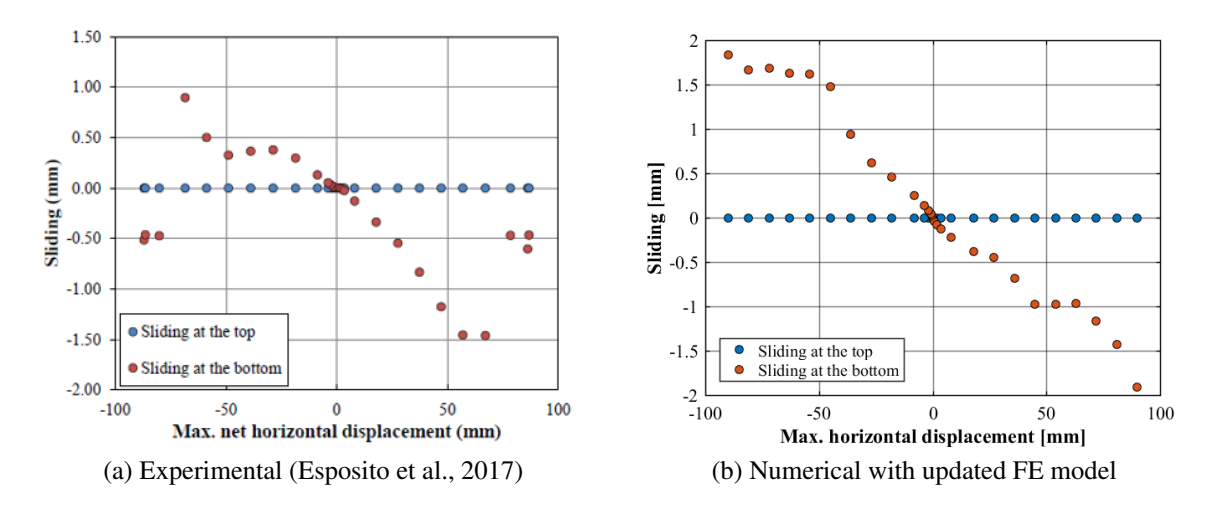


Figure 3.18: Sliding of TUD_COMP-20

Chapter 4

FE MODEL OF TUD MASONRY HOUSE-1

This chapter discusses the finite element model of a masonry house. This house model is based on the CS brick masonry assemblage tested at TU Delft, which resembles the typology of typical Dutch terraced houses built in the years 1960-1980. These terraced houses are normally two-story high buildings made of unreinforced masonry. They are characterized by the use of cavity walls and large openings in the facades. The inner leaf and outer leaf of the cavity walls are generally connected by steel ties, and CS brick masonry is commonly used to build the inner loadbearing part of the cavity walls.

The tested masonry assemblage is composed of CS brick masonry walls (inner leaf) and concrete floors (see Figure 4.1). The following features of the masonry terraced houses are included in the design of the specimen and thus also in the finite element model:

- Slender piers due to the large openings in the facades;
- Running bond to connect the long transversal walls to the facades (Figure 4.2);
- Limited connection between the masonry piers and concrete floors.

To simplify the performed quasi-static pushover test and to reduce the computational burden in numerical analyses, the specimen and the built house model do not include:

- Soil and upper structure interaction;
- Spandrels connecting the masonry piers and openings;
- Outer leaf of the cavity walls.

Section 4.1 and 4.2 discuss the geometry and finite element discretization of the house model. Section 4.3 then describes the relevant constitutive laws. Finally, section 4.4 presents the necessary dynamic properties of the house model to investigate its seismic behavior.

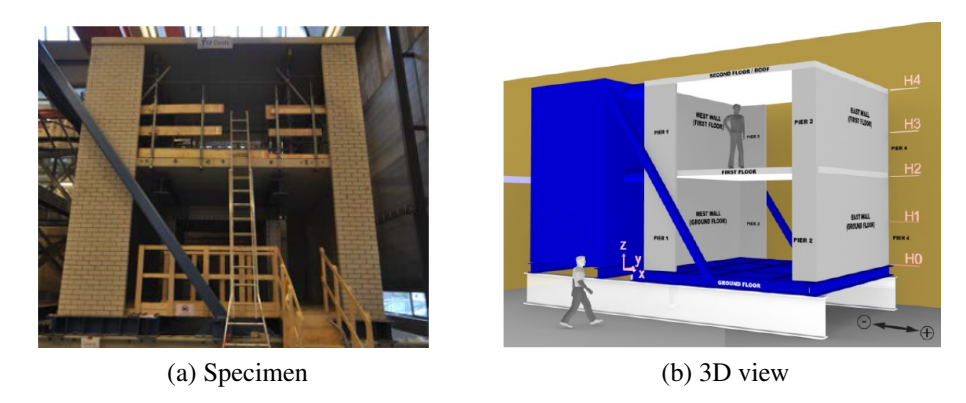


Figure 4.1: TUD CS brick masonry assemblage (Ravenshorst et al., 2016)

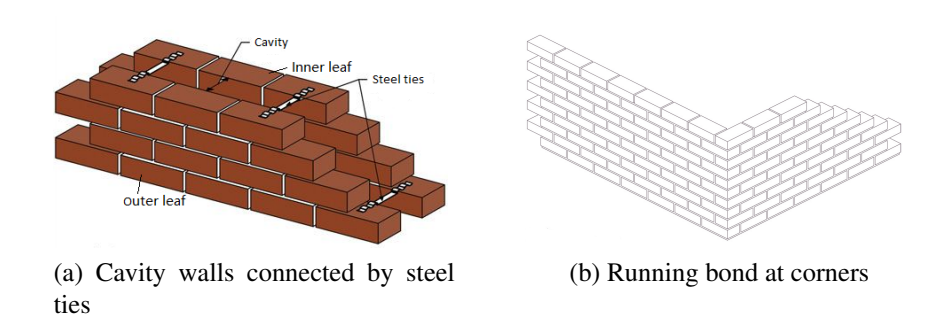


Figure 4.2: Examples of the masonry wall details ("Types of Masonry Wall", 2017)

4.1 Geometry of the Model

Like the assembled structure in the test, the finite element model only represents the loadbearing parts of the terraced house unit. The geometry of the house model is shown in Figure 4.3. Two loadbearing walls expand along the transverse direction (global y-direction) on the west and east side, respectively, with a length equals 5.2 m. The south and north facades are identical and composed of two piers connected to the transversal walls. The two piers on the same side of facade have different sizes: the piers connected to the western wall (Pier 1 and Pier 3) have a width of 1.1 m, while the piers on the eastern side (Pier 2 and Pier 4) have a width of 0.6 m. The total height of the assemblage model is 5.3 m, with a height of 2.7 m for the first layer and 2.6 m for the second layer.¹

As shown in Figure 4.1 (b), the masonry assemblage is built on a steel substructure (blue parts) in the lab, and the first layer of masonry was glued on the steel foundation to avoid sliding of the masonry at the bottom. The steel substructure is not included in the numerical model as it does not influence the structural behavior of the assembled structure. In fact, all degrees of freedom at the base of the house model are fixed to simulate the test condition. The tying function in DIANA FEA simplifies the model construction. The chosen master node (node 4 in Figure 4.3) is fully constrained and all other nodes along the base are selected as slave nodes with equal displacement as node 4.

¹Simplifications are made on the dimensions of the finite element model with respect to the specimen.

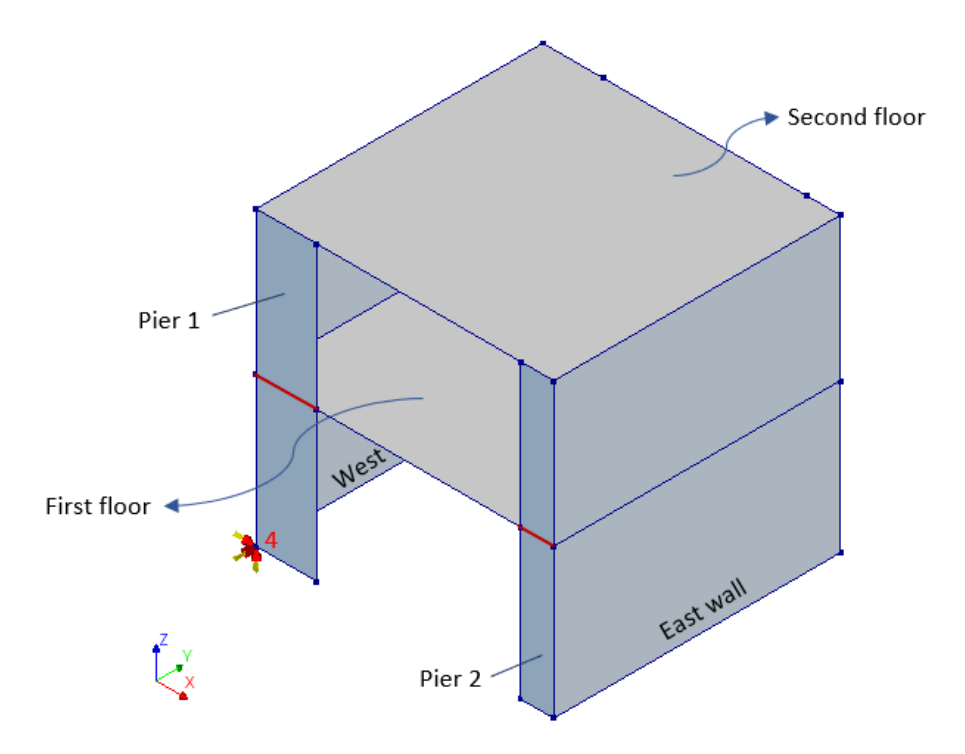


Figure 4.3: FE model of the masonry assemblage

Besides the boundary conditions discussed above, the connections between the masonry transversal walls and piers, as well as the connections between the masonry walls and concrete floors should be properly modeled.² Different consideration and modeling methods are applied on these connections, which are discussed in sections 4.1.1 and 4.1.2.

4.1.1 Wall-to-wall connections

The running bond was used for the masonry bricks at the corner of the transversal walls and the piers of the assemblage specimen, as shown in Figure 4.2 (b). Application of this technique causes the interlocking of the bricks, thus the connections between the transversal walls and piers can be modeled with shared nodes.

4.1.2 Wall-to-floor connections

The connections between the masonry walls and concrete floors differ at both floor levels. The connection details adopted in the assembled specimen and finite element model are described below.

FIRST FLOOR LEVEL

Figure 4.4 shows the details of connections at the first floor level in the assembled structure. In the construction of the specimen, the concrete floor is first laid up on the two loadbearing walls in the transversal direction and subsequently filled by mortar (Figure 4.4 (b)). This connection can be

²The concrete floor consists of two separated slabs is modeled as a monolithic floor due to the application of reinforced concrete dowels connection.

considered relatively stiff, thus it is modeled fully connected with shared nodes.

Horizontal anchors are used to connect the floor to the piers per Figure 4.4 (a). All the anchors are cast in the floor and masoned in the piers. These anchors are mainly designed as shear connectors to assist the shear force between the piers and floor in the horizontal direction (global x-direction), and almost no forces can be transferred through the anchors in the transversal and vertical directions (global y- and z-directions)(Ravenshorst et al., 2016). These features are simulated by means of interface elements along the intersection lines of the floor and piers (red lines in Figure 4.3).

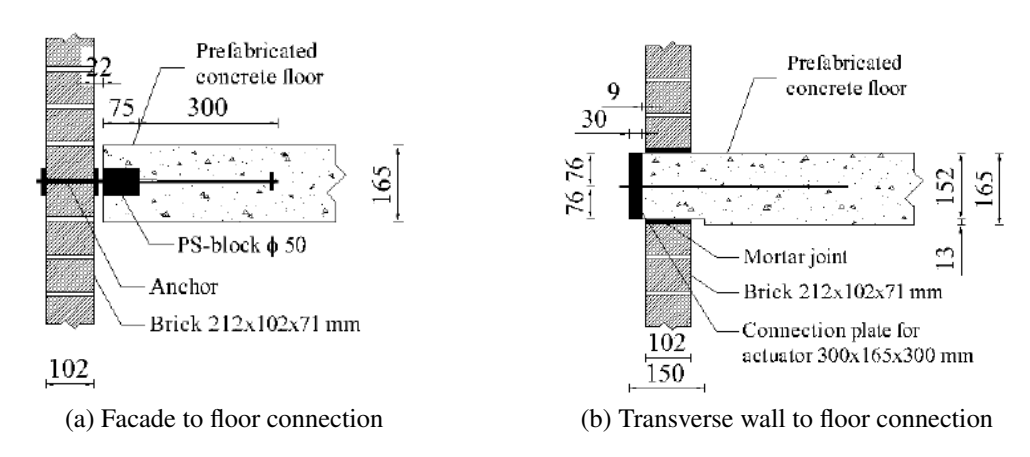


Figure 4.4: Details of connections: First floor (Ravenshorst et al., 2016)

SECOND FLOOR LEVEL

Figure 4.5 shows the connection details at the second floor. It can be seen that the floor is laid connected to the top of the transversal walls and piers via mortar joints. Therefore, shared nodes are adopted to build the connections between the second floor and masonry walls (piers).

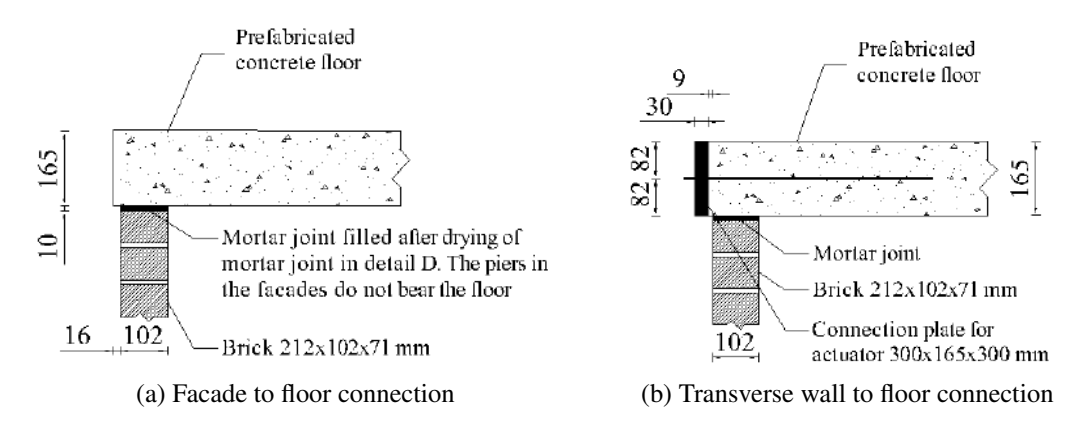


Figure 4.5: Details of connections: Second floor (Ravenshorst et al., 2016)

4.1.3 Symmetry

The symmetry of studied assemblage can be used to further simplify the numerical modeling. The geometry of the model is symmetric along the global y-direction. Additionally, in this research

project, the house is only loaded in the global x-direction. Thus the house is also symmetrically loaded in the y-direction.

Using these features, a half model of the masonry assemblage was built, as shown in Figure 4.6. Since the masonry assemblage is loaded along the x-direction, the symmetric plane should have no movement in the y-direction. The displacements along y-direction in the symmetry plane (specified with dashed lines in the full house model) are thus constrained in the half model.

Using the half model largely reduces the computational time in DIANA FEA, especially in nonlinear time-history analyses. In this research work, the half model is verified to represent the whole structure through monotonic pushover analysis, and both the nonlinear pushover and time-history analyses presented in Chapter 5 and 6 are based on the half model.

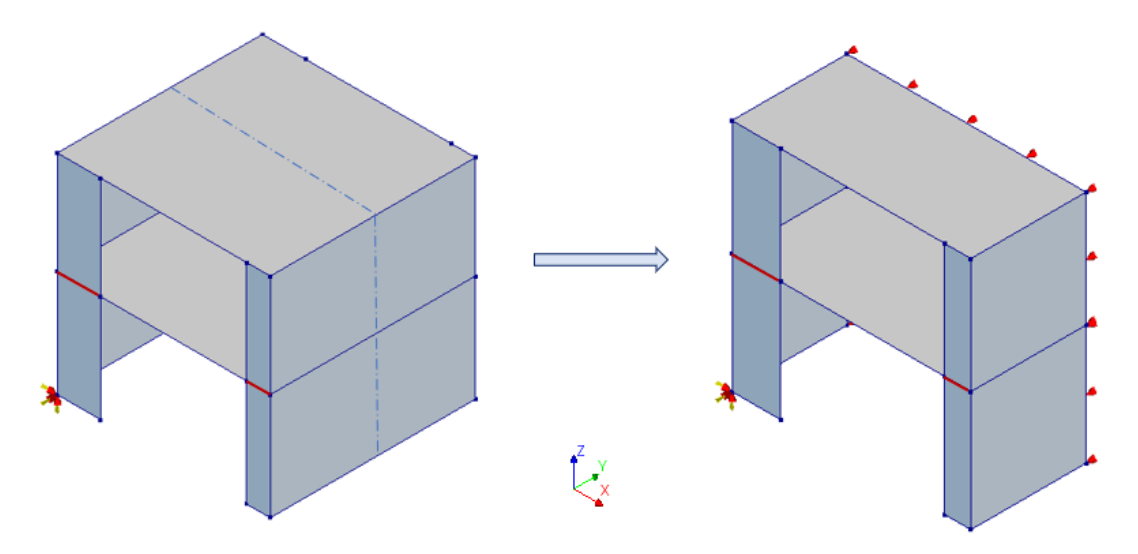


Figure 4.6: Symmetry of the assemblage model

4.2 Finite Element Discretization

Although the house is three-dimensional, the thickness to width and height ratios of the walls and the floors allow the use of elements whose typology is two-dimensional. The finite element discretization of the built house model is explained in terms of element types, mesh properties and connection details in the following sections.

4.2.1 Element type and properties

Shell elements are appropriate to model the walls and floors of the house. They accurately represent both in-plane and out-of-plane deformations. Additionally, they can be used together with the engineering masonry material model.

The 8-node curved shell element (CQ40S) has quadratic shape function and a reduced 2×2 Gauss

integration scheme.³ A 3-point Simpson integration scheme is used over the thickness by default. To better show the out-of-plane deformation and cracks of the transversal walls, model with a 7-point integration scheme over the element thickness is built.

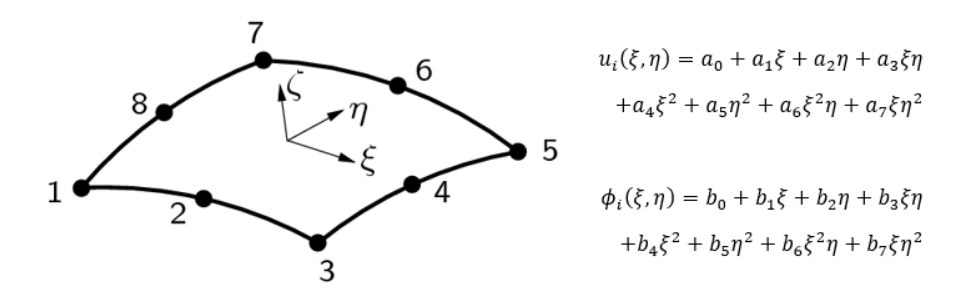


Figure 4.7: 8-node curved shell element: CQ40S

DIANA FEA adopts the Mindlin-Reissner hypotheses, which posits that lines normal to the midplane remain straight but not necessarily perpendicular after deformation.

Five degrees of freedom are defined in each node of the curved shell element: three translations and two rotations. In the thickness direction of the shell elements, the in-plane strains ε_{xx} , ε_{yy} and γ_{xy} vary linearly, while the transverse shear strains γ_{xz} and γ_{yz} are constant. For the chosen quadratic element, the strain ε_{xx} , membrane force n_{xx} and shear force q_{xz} vary linearly in x-direction and quadratically in y-direction. Similarly, the strain ε_{yy} , membrane force n_{yy} and shear force q_{yz} vary linearly in y-direction and quadratically in x-direction.

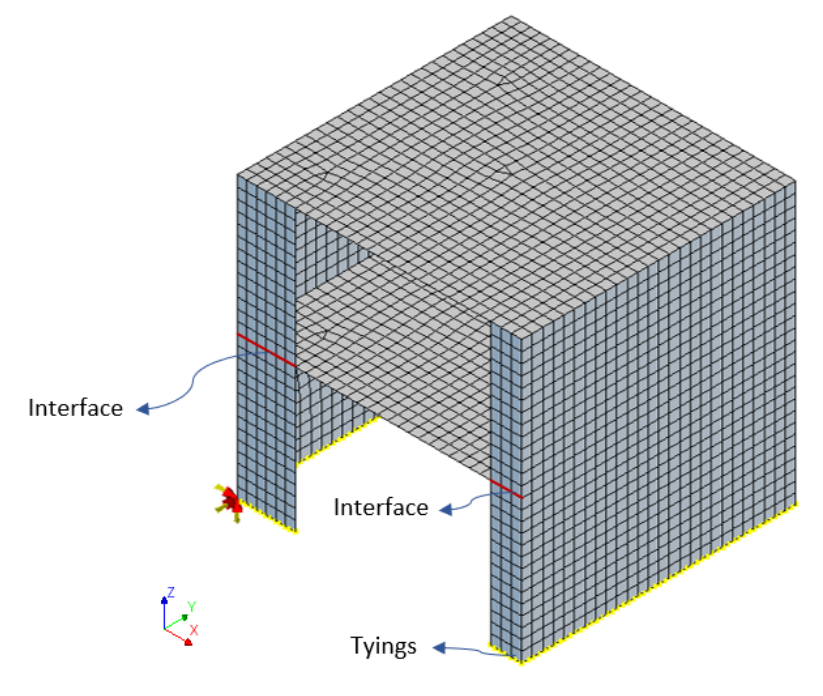
Triangular curved shell elements are avoided, as they may cause shear locking, and lead to inaccurate results. For this purpose, and taking into account the units dimension of the used CS brick masonry $(210 \times 71 \times 102 \text{ mm})$, a mesh size of 200 mm is applied.

Both the full and half model with generated mesh are shown in Figure 4.8. The interfaces between the piers and floor are indicated with red lines at the first floor level. Additional attention is required on the element geometries when constructing the house model. Because the anisotropic material property of masonry is considered in the model, the local coordinates of the masonry walls need to be specified properly. The local x-direction of both transversal walls and piers should coincide with the bed-joints of the CS brick masonry. Thus, different local coordinates are adopted in the walls in global x- and y-direction, which are indicated in Figure 4.8 as well.

The element properties, number of elements per component and the total number of nodes in both models are summarized in Table 4.1. As mentioned in the Section 4.1, different connections between the masonry walls and concrete floors are used in the model. Detailed explanation of the meshes along these connections are presented in section 4.2.2.

³The 2×2 Gauss integration scheme is used to avoid membrane and shear locking.

⁴The mentioned strains and forces are defined in the local coordinate of the shell elements.



(a) Full house model

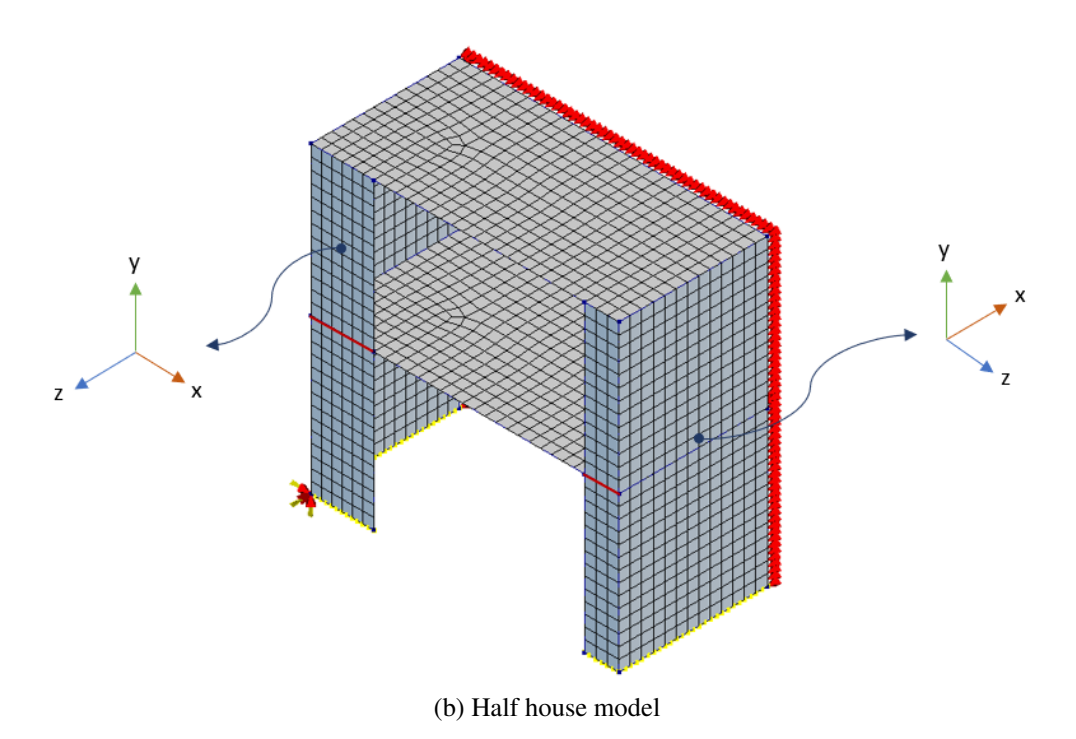


Figure 4.8: House model with generated mesh

	Masonr	y wall	Concrete floor		
Floment type	curved shel	l element	curved shell element		
Element type	(CQ4	0S)	(CQ40S)		
Integration	2×2	× 7	$2 \times 2 \times 7$		
Mesh size	200 n	nm	200 mm		
Element	102		165		
thickness	102 n	nm	165 mm		
Element	ah ayya in E	: 1 Q	some as alabal as andinata		
coordinates	shown in F	igure 4.8	same as global coordinate		
	Full House Model				
	Piers	Transversal walls	Floors		
Number of	$162 \times 2 + 81 \times 2$	2 711 + 702	727 + 727		
elements	102 \ 2 \ + 01 \ \ 2	/11 + /02	121 + 121		
Total number		1032	7		
of nodes		1032	1		
	Half	House Model			
	Piers	Transversal walls	Floors		
Number of elements	162 + 81 378 + 351		365 + 365		
Total number of nodes	5353				

Table 4.1: Finite elements used in the house components

4.2.2 Connection details

As discussed in Section 4.1, different methods are applied to model the connections of the masonry house. These are fulfilled with different mesh properties along the connections.

Generally, two different connections are adopted in the assemblage model:

- Rigid connections: applied between floor and transversal walls at the first floor level, between the floor and masonry walls at the second floor level, and between the masonry transversal walls and piers;
- Shear connections: applied between the floor and masonry piers at the first floor level.

The rigid connections are modeled via shared nodes, as shown in Figure 4.9. The red lines indicate the positions of rigid connections. DIANA FEA automatically merges the nodes at the same positions after meshing.

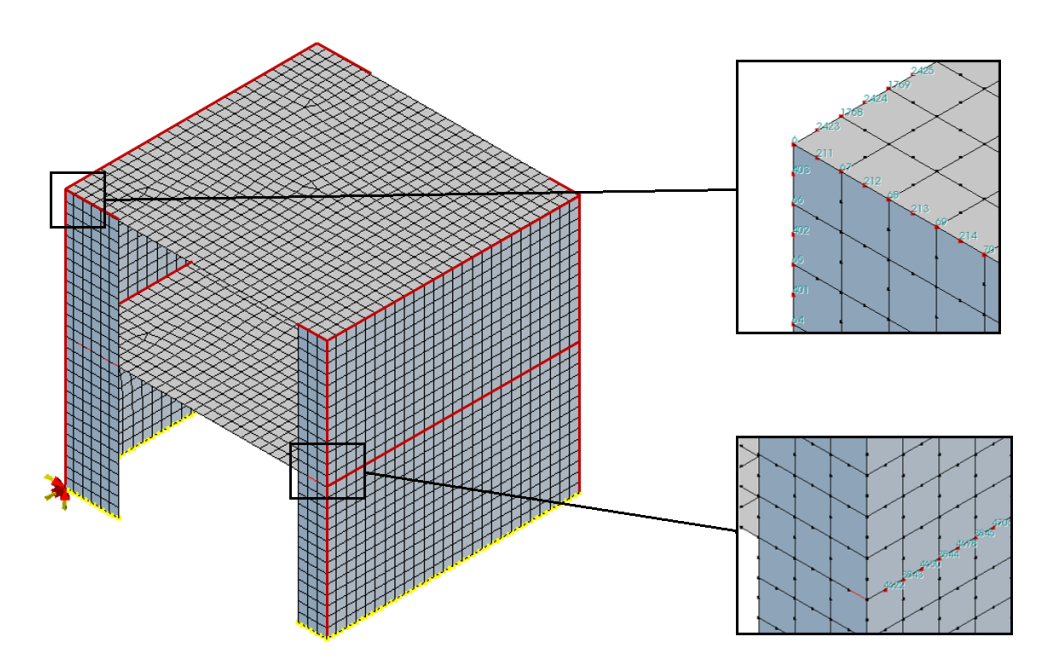


Figure 4.9: Full connections (red lines) in the house model

The shear connections at the first floor level are modeled with 3D line interface elements. The chosen interface element is the 6-node line interface element between two lines in a curved shell configuration (CL24I in DIANA FEA). Figure 4.10 shows its topology and the corresponding degrees of freedom. Its properties are summarized in Table 4.2.

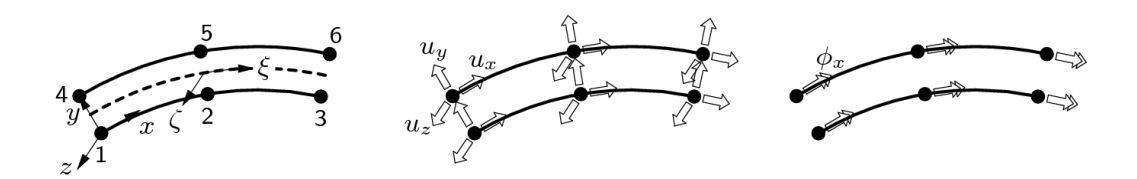


Figure 4.10: 6-node 3D line interface element: CL24I

Table 4.2: Finite elements used in the shear connection

	Shear connection (Interface)		
Element type	6-node 3D line interface (CL24I)		
Interpolation	quadratic		
Integration	3+3		
Mesh size	200 mm		
Element thickness	165 mm		
Element shape	flat		
Element coordinate	shown in Figure		
Total	Total 18 (full model)		
number of elements	9 (half model)		

In the house model, there is no gap between the concrete floor and the masonry walls. That is, the two rows of nodes in the interface element are overlapped in terms of coordinates. However, one row of nodes is attached to the masonry wall elements while the other row is attached to the concrete floor elements. Figure 4.11 presents a schematic diagram of the position of the interface element.

As the shear connections between concrete floor and masonry piers only assist the shear forces in the global x-direction, for the adopted 3D line interface, only the shear stiffness in x-direction is specified. The normal stiffness in y-direction and the shear stiffness in z-direction should be zero. The material properties of the interface are discussed in Section 4.3 later in detail.

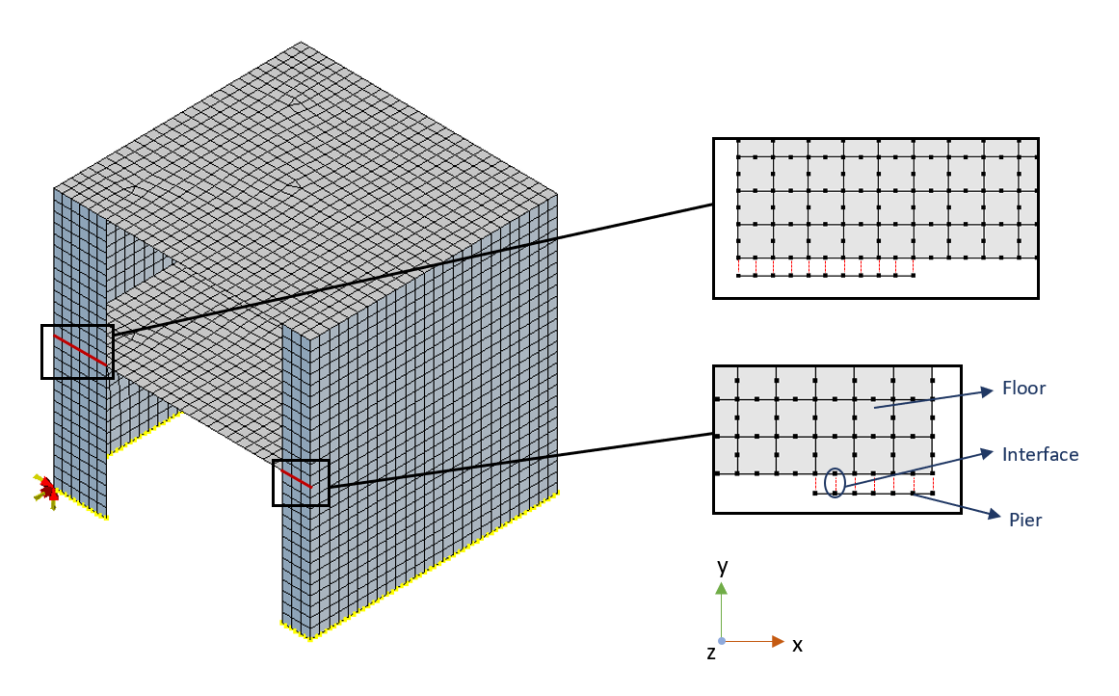


Figure 4.11: Interface elements (red lines) in the house model

4.3 Constitutive Laws

The properties of materials used in the house model are discussed in this section. These materials are: masonry for the transversal walls and piers, and concrete for the two floors. An additional material is specified for the interface elements.

4.3.1 Masonry properties

The Engineering Masonry model is adopted in this house model. Its tensile, compressive and shear stress-strain relations are described in section 2.3.2.

The values of the input material parameters are summarized in Table 4.3. The Young's modulus in both head-joint and bed-joint directions (E_x and E_y), compressive strength (f_c) and shear properties (ϕ and f_{v0}) of the CS brick masonry are obtained from the material tests on the components. Other input values are derived from experimental equations, in the same way as explained

in section 3.2.3.

Property Parameter Unit Value Perpendicular **MPa** 2212 E_x Young's modulus to head joints **Elasticity** Perpendicular MPa E_{y} 3264 to bed joints Shear modulus G_{xy} MPa 1306 Mass density kg/m^3 1805 ρ Tensile strength Normal to bed joint f_{ty} MPa 0.19 Tensile **Cracking** N/mm 0.0127 G_{ft} fracture energy Angle between stepped diagonal θ 0.792 rad crack and bed joint Compressive MPa 5.84 f_c strength **Crushing** Fracture energy 17.39 G_{fc} N/mm in compression Factor to strain at compressive 5 n strength Unloading factor λ 0

Table 4.3: Masonry properties in the FE model

4.3.2 Concrete properties

Friction angle

Cohesion

Shear

failure

The focus of the research is to assess the masonry wall damage under seismic loading. Thus, the concrete in the model is assumed to behave linear-elastically. The reinforced concrete slab of the house specimen has the strength class C53/65. The necessary input are shown in Table 4.4.

φ

 f_{vo}

rad

MPa

0.406

0.14

Property	Parameter		Unit	Value
Linear elastic	Young's modulus	E_s	MPa	35500
	Poisson's ratio	ν		0.2
	Mass density	ρ	kg/m^3	2400

Table 4.4: Material properties of concrete

4.3.3 Interface properties

As discussed in section 4.2.2, 3D line interface elements are used between the first concrete floor and masonry piers to simulate the shear connections between these two components. The chosen interface element in DIANA FEA has linear material properties. Normal stiffness in y-direction,

two shear stiffness in x- and z-direction are required.

The shear connectors between the concrete floor and masonry piers only transfer force along the global x-direction. Therefore, the applied interface elements only has stiffness in the x-direction. The normal stiffness modulus in y-direction and shear stiffness modulus in z-direction are set zero. Shear stiffness of the interface is estimated with the following equation:

$$E_t = \frac{1}{10} E_n = \frac{100 \cdot E}{l_{adj}} \tag{4.1}$$

where E_n is the normal stiffness of the interface element, E is the stiffness of the connected elements, l_{adj} is the length of the adjacent element.

At the floor and piers connections, the estimation of the stiffness of interface is based on the stiffness of masonry ($E_y = 3264$ MPa, see in Table 4.3) because the shear strength of masonry is weaker than concrete. The length of adjacent element is 200 mm as specified before. The calculated shear stiffness of the interface is presented in Table 4.5.

Table 4.5: Material properties of interface

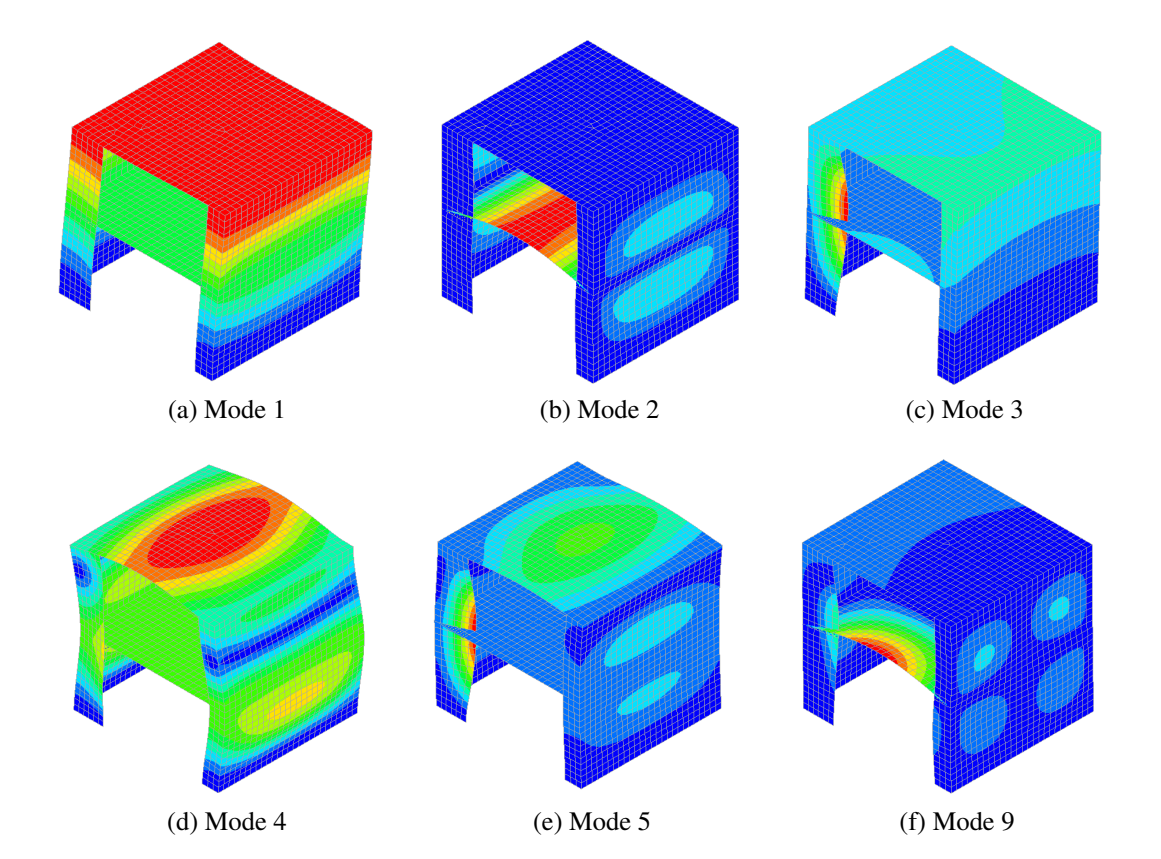
Property	Parameter		Unit	Value
Linear	Normal stiffness	$E_{n,y}$	MPa	0
	Shear stiffness	$E_{t,x}$	MPa	1632
		$E_{t,z}$	MPa	0

4.4 Modal Parameters Identification

The dynamic properties (modal parameters) of the model are identified through an eigenvalue analysis. The first 50 eigenfrequencies and their corresponding modal shapes are determined. For each calculated frequency f_i , DIANA normalized the eigenvector ϕ_i so that the generalized mass $m_{ii} = 1$ ($m_{ii} = \phi_i^T M \phi_i$). The corresponding effective masses $m_{eff,i}$ for the translational degrees of freedom in global x-, y- and z-direction are calculated. The modes contribute most in terms of the effective mass percentage are listed in Table 4.6, and the corresponding mode shapes are shown in Figure 4.12.

Mode	Frequency [Hz]	Effective mass percentage [%]		
		x-direction	y-direction	z-direction
1	3.617	79.71	0.00	0.02
3	13.152	0.00	70.51	0.00
42	51.254	0.01	0.00	31.53
2	10.732	0.02	0.00	26.31
4	13.313	9.72	0.00	11.22
5	14.523	3.44	0.00	15.74
32	41.333	0.00	9.03	0.00
9	18.066	0.00	5.53	0.00

Table 4.6: Eigenvalue analysis results



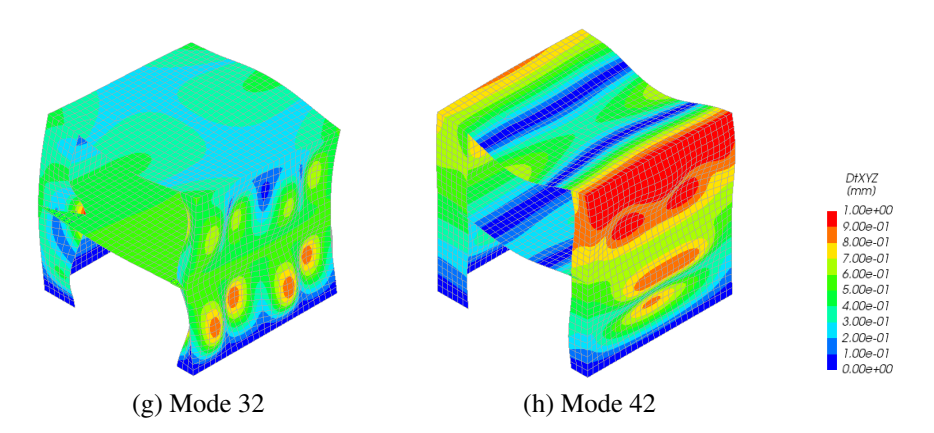


Figure 4.12: Mode shapes of the house model

The fundamental mode shows the vibration of the whole structure in x-direction. Mode 2 and mode 4 present the first order bending of the first floor and second floor in z-direction, respectively. These three modes of the assemblage specimen were identified as well in the TU Delft test. The eigenfrequencies from numerical eigenvalue analysis and dynamic identification test are compared in Table 4.7.

Table 4.7: Comparison of eigenfrequencies

Mode	Numerical	Experimental
	[Hz]	[Hz]
First mode in the x-direction of the structure	3.62	4.05
First mode in the z-direction of the first floor	10.73	11.75
First mode in the z-direction of the second floor	13.31	14.34

Chapter 5

NONLINEAR PUSHOVER ANALYSIS OF TUD HOUSE-1

A nonlinear pushover analysis is performed on the built masonry house model to evaluate its seismic behavior under the lateral loads in x-direction. Section 5.1 introduces the applied lateral loads and corresponding loading method. The procedure for performing the nonlinear pushover analysis in DIANA FEA is presented in Section 5.2. The results of the pushover analysis are discussed and compared to the experimental results in Section 5.3. A sensitivity study is presented in Section 5.4, to investigate the influence of certain material properties on the behavior of the house model.

5.1 Applied Pushover Load

In the quasi-static pushover test, a steel frame was built to apply the lateral load on the CS brick masonry assemblage (Figure 4.1). A prescribed displacement was imposed through two actuators at the second floor level. These were coupled with another two actuators at the first floor level to keep the applied forces at both levels equal (Ravenshorst et al., 2016).

The same mass proportional pushover loading is applied in the numerical analysis.¹ Section 5.1.1 presents a method to apply equal forces on both floor levels while prescribing a displacement-controlled loading. Moreover, a similar lateral loading scheme is adopted on the numerical model to compare the numerical and experimental results. This scheme is presented in section 5.1.2.

5.1.1 Loading method

A displacement-controlled loading scheme is necessary to track the post-peak response of the house model up to the maximum specified displacements. However, for this house model with identical floors, the mass proportional pushover analysis also requires that the equivalent forces on both floors be the same.

This problem is solved by using a loading system consisting of two vertical rigid steel beams connected to both floors through rigid links (Figure 5.1 (a)). The positions of the steel beams are determined based on the positions of actuators in the test, at 1.1 meter inwards from the facades at

¹In both experiment and numerical analyses, the mass is assumed to be lumped at floor levels.

both sides.

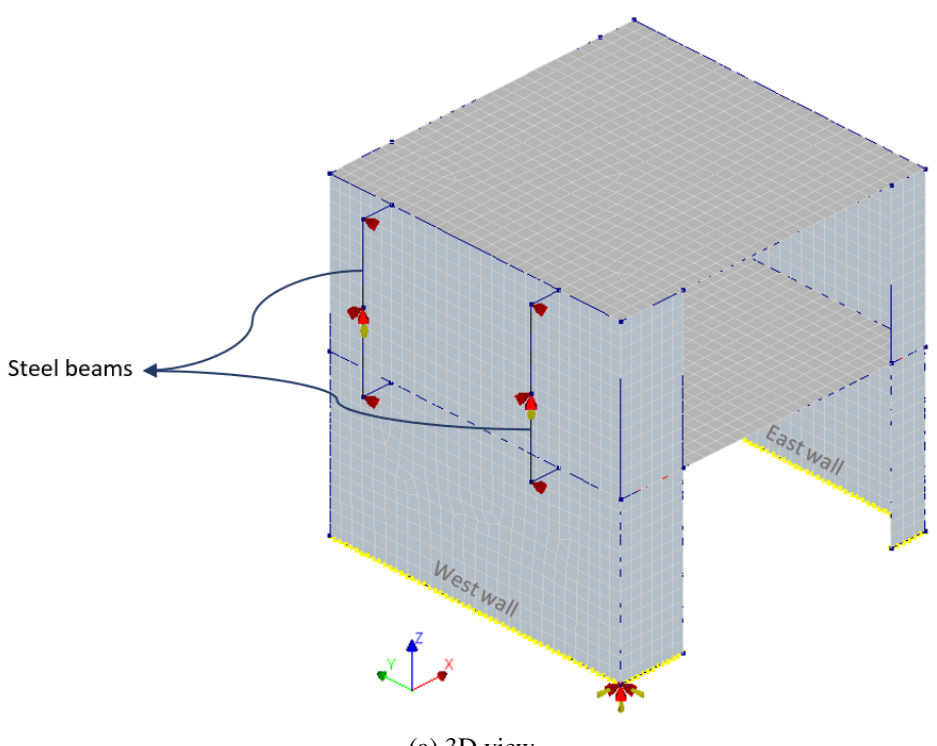
The loading points are set at the mid-points of the two steel beams, and the same prescribed displacement is applied on both nodes in the x-direction. Under the lateral loading, the rigid beam can rotate around the middle point and two equal forces are generated at both ends connected to the two floors ($F_1 = F_2$, $F_3 = F_4$ in Figure 5.1 (b)).

The boundary conditions of the steel beams are shown in Figure 5.1. The translations of the loading nodes (middle points) are constrained in x-direction due to the prescribed displacement loading in DIANA FEA, and along the z-axis to prevent the beams from moving vertically. A rotational restraint is also added at these two nodes to prevent torsion of the beams. Additionally, the two ends of the steel beams are constrained in y-direction, thus the beams can only rotate in the xz-plane around the displaced middle points.

Considering the relatively high stiffness of the masonry assemblage with respect to the steel frame, the forces on the northern (F_1, F_2) and southern (F_3, F_4) side of the model might differ. However, this difference has a limited influence on the stress distribution in the masonry house model due to the high torsional stiffness of the concrete floors and the transversal walls (Ravenshorst et al., 2016).

5.1.2 Loading scheme

The loading scheme applied to the house model is designed based on the loading conditions in the quasi-static pushover test on the assemblage.



(a) 3D view

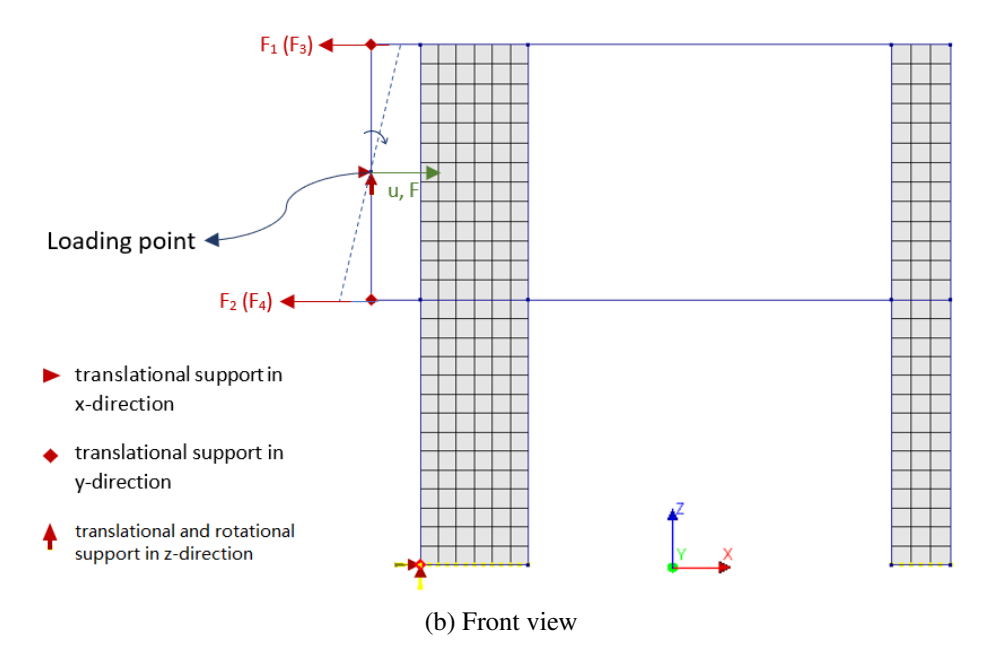


Figure 5.1: Location of steel beams

The maximum target displacement is set to be 150% of that observed in the test, to capture the structural behavior beyond the experimental limitation. Therefore, a total of 27 cycles are applied, among which the first 22 cycles are identical to the experimental ones and the following 5 cycles have been added to investigate the structural behavior in case the test was further conducted. Each cycle consists of 3 runs and each run reaches the given target displacements in the positive (+x) and negative (-x) directions, starting and ending at zero. The applied target displacements are increased gradually for each next cycle, listing in Table 5.1.²

Cycle	u _{min}	u _{max}	Cycle	u _{min}	u _{max}	Cycle	u _{min}	u _{max}
	mm	mm		mm	mm		mm	mm
C1	-0.22	0.15	C12	-6.77	6.77	C23	-75.94	78.20
C2	-0.30	0.45	C13	-9.02	9.02	C24	-83.46	85.71
C3	-0.83	0.68	C14	-11.28	11.28	C25	-90.98	93.23
C4	-1.16	0.95	C15	-15.76	16.57	C26	-98.50	100.75
C5	-1.45	1.34	C16	-19.42	20.42	C27	-106.02	108.27
C6	-1.76	1.62	C17	-28.37	29.53			
C7	-2.11	1.95	C18	-36.47	37.96			
C8	-2.42	2.24	C19	-45.12	45.85			
C9	-2.58	2.38	C20	-52.47	55.05			
C10	-3.28	2.96	C21	-61.63	63.19			
C11	-4.66	4.21	C22	-69.05	70.80			

Table 5.1: Applied target displacements for each cycle

Like in the test, the loading time for each cycle remains constant. Thus, the deformation velocity

²Note that the target displacement in the test is defined at the second floor, while in the numerical analysis it is defined at the loading point of the rigid beam.

increases per cycle due to the increasing amplitude. The loading scheme of the cyclic pushover analysis is shown graphically in Figure 5.2.

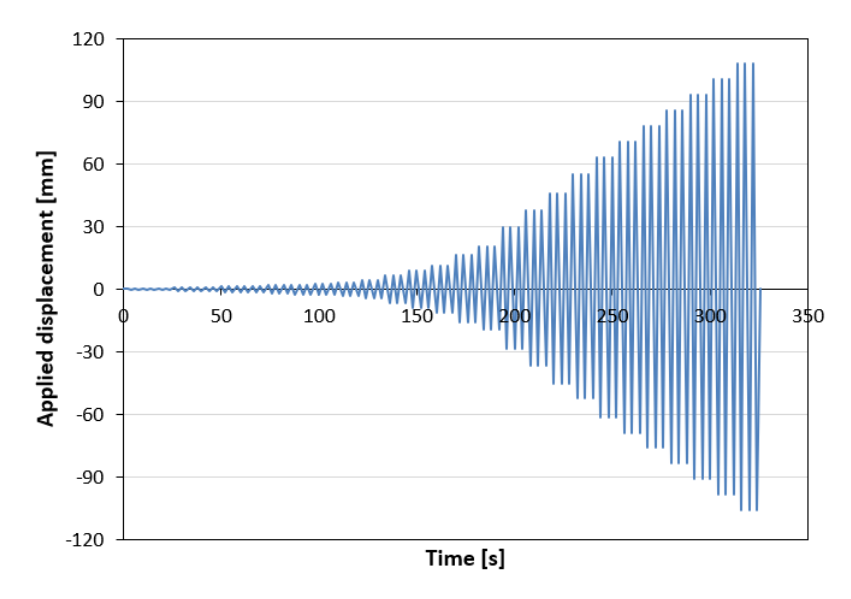


Figure 5.2: Cyclic loading scheme in numerical pushover analysis

5.2 Nonlinear Pushover Analysis

The nonlinear pushover analysis is performed in DIANA FEA. First, the self-weight of the masonry house is applied. The cyclic lateral load is then applied per Table 5.1 with the defined time dependent factors for each step. Both physical and geometrical nonlinearities are accounted for in the numerical analysis.

The regular Newton-Raphson iteration method with line search is chosen and the number of iterations per step is limited to 100. Each step is considered convergent when either the displacement norm or force norm gets smaller than the tolerance of 0.01. The satisfaction of both the norms is not required here because of the impractical computational time. Furthermore, a validation based on the monotonic pushover analysis shows that employing these two criteria provides the same results. The analysis parameters are summarized in Table 5.2.

Load	Self-weight	10	
steps	Cyclic pushover	14600 time steps (see Figure 5.2)	
Iteration	Max. number of iterations	100	
method	Iteration method	Regular Newton-Raphson	
memou	Line search	Line search Yes	
Convergence	Satisfy either displacement norm (tolerance 0.01)		
criteria	or force norm (tolerance 0.01)		

Table 5.2: Procedure of the cyclic pushover analysis

A monotonic pushover analysis is also performed on the built house model, as an upper threshold

for the results of the cyclic pushover analysis. A prescribed deformation is applied on the loading nodes of the rigid beams, up to the largest target displacement of the cyclic load in both positive (+x) and negative (-x) directions. This monotonic lateral load is applied in 300 load steps (0.35 mm per step) and up to 105 mm for both directions. The same iteration method and convergence norms as in the cyclic pushover analysis (see Table 5.3) are used. Both physically and geometrically nonlinear effects are included.³

Load	Self-weight	10	
steps	Monotonic pushover	300 steps (0.35 mm per step)	
Iteration	Max. number of iterations	100	
method	Iteration method	Regular Newton-Raphson	
memou	Line search Yes		
Convergence	Satisfy either displacement norm (tolerance 0.01)		
criteria	or force norm (tolerance 0.01)		

Table 5.3: Procedure of the monotonic pushover analysis

5.3 Results

The results of the cyclic and monotonic nonlinear pushover analyses on the half house model are shown here. Section 5.3.1 discusses the seismic behavior of the masonry house in terms of its capacity curves. Then, section 5.3.2 presents the crack evolution of the house under the cyclic pushover load. Finally, the deformation and drifts of the structure are analyzed in section 5.3.3. Comparisons between these numerical results and the corresponding experimental results are also discussed here.

5.3.1 Capacity curves

In this research, the response of the house model during the cyclic pushover analysis is divided into the following four stages:

- 1. Initial stage (gravity load)
- 2. Pseudo-linear stage (cycles 1-8)
- 3. Pre-peak stage (cycles 9-18)
- 4. Post-peak stage (cycles 19-27)

Figure 5.3 shows the hysteresis and backbone curves of the house model in terms of base shear force versus displacement at the second floor level. The base shear force of the full house model is equal to the sum of the reaction forces at the two loading points of the steel beams. For the half house model, the base shear force is calculated by doubling the reaction force at the loading nodes.

³The influence of including/excluding geometrically nonlinear based on the monotonic pushover analysis is presented in Appendix B.

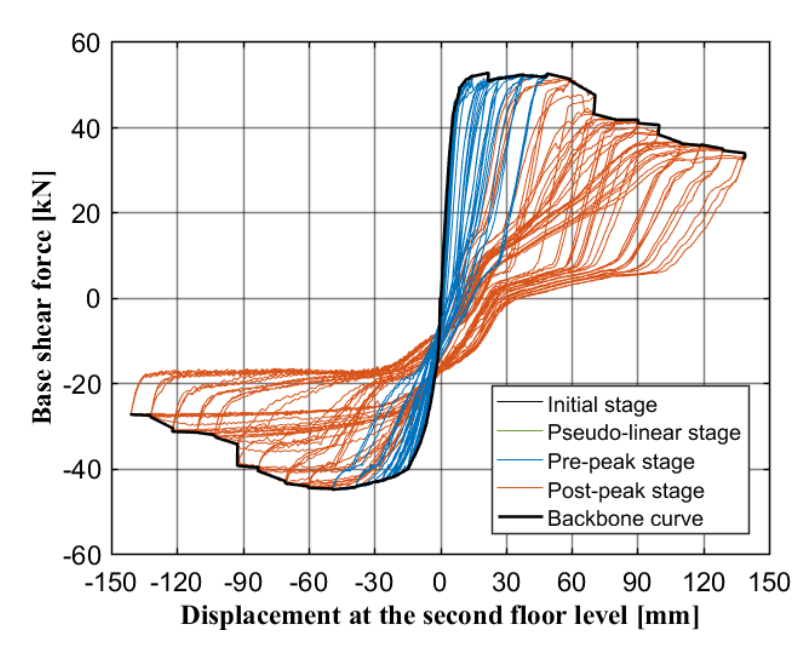


Figure 5.3: Capacity curve of the house model (cyclic pushover analysis)

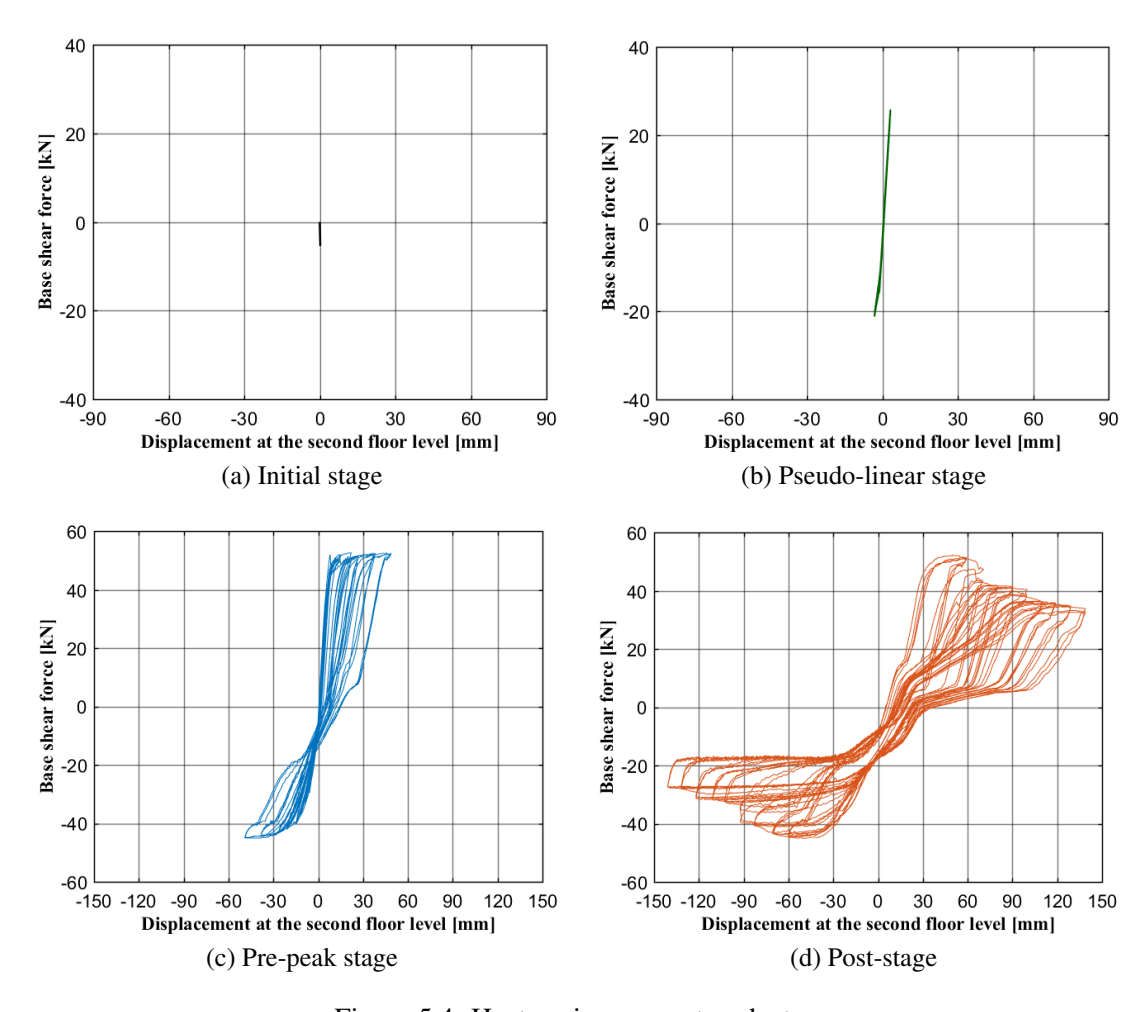


Figure 5.4: Hysteresis curves at each stage

The displacement is extracted from the node on the second floor, which connects to the rigid links.

INITIAL STAGE

Only gravity load is applied to the house model in the initial stage. A small base shear force (-4 kN) is observed under this compressive loading (Figure 5.4 (a)). The shear force along -x direction is generated due to the asymmetry of the piers. The western facade with wider pier is stiffer than the eastern side, therefore it deforms less under the gravity.

PSEUDO-LINEAR STAGE

The hysteresis curves during the pseudo-linear stage shows an almost linear relation in both loading directions (Figure 5.4 (b)). The stiffness of the house model at this stage is almost the same as that of the assemblage specimen.

The maximum second floor displacements reached during this stage are +3.18 mm and -3.18 mm in the positive and negative directions, respectively. The associated maximum base shear forces are +25.4 kN and -21.2 kN. These results closely match the experimental ones.

PRE-PEAK STAGE

The peak base shear forces in +x direction and -x direction are +52.6 kN (Cycle 15) and -45.0 kN (Cycle 18), respectively. It is also observed that the base shear force in the positive direction remains almost constant at the peak value from Cycle 15 to Cycle 18, thus the pre-peak stage is defined until Cycle 18. Overall, the base shear capacities in both directions are slightly larger than the maximum forces obtained during the test, which are around +48 kN in the positive direction and -40 kN in the negative direction.

Unlike the pseudo-linear stage, the hysteresis curves at this stage clearly show the nonlinearity of masonry. Energy dissipation is observed under the cyclic loading and a positive residual displacement at the second floor level starts to accumulate with the increasing cyclic loading, as observed in the experimental curves.

POST-PEAK STAGE

After reaching the peak value, the base shear force of the house model gradually decreases. A maximum displacement of +139 mm and -141 mm in the positive and negative directions at the second floor level is reached at the last cycle.

During the post-peak stage, a reduction of 20% in base shear force is achieved at a displacement of +80.3 mm (Cycle 21) in the positive direction, while in the negative direction it occurs at a displacement of -92.4 mm (Cycle 22). The base shear force decreases slower than in the experiment, especially in the positive loading direction. Relatively large energy dissipation can be observed from the hysteresis curve at this stage ((Figure 5.4 (d)). An increased residual displacement in +x direction is also shown in the figure.

Monotonic pushover curve

Figure 5.5 compares the monotonic pushover curve to the backbone curves from the cyclic pushover analysis and the experiment on the assemblage specimen. Notice again that the house model is pushed to 150% of the maximum displacements in the test.

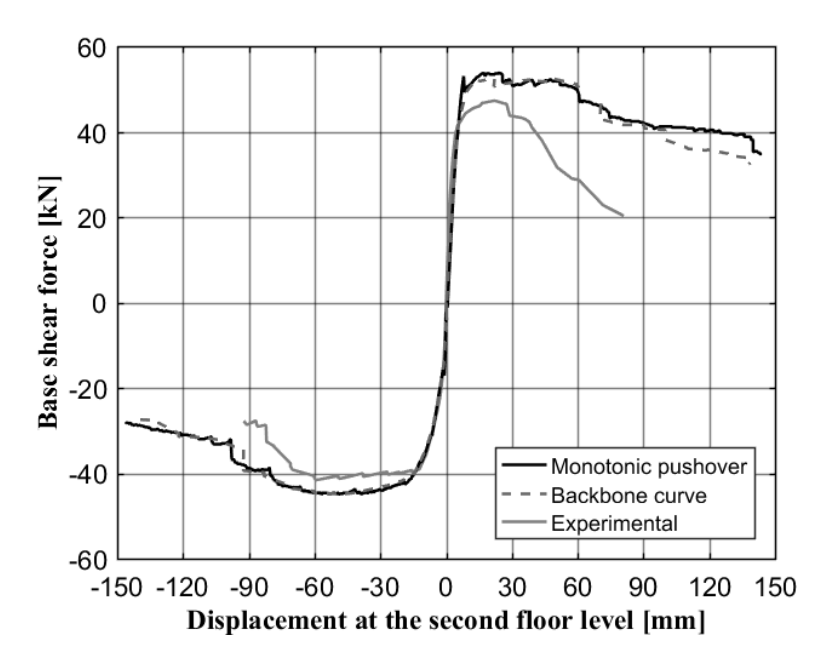


Figure 5.5: Capacity curves of the CS brick masonry house

Figure 5.5 shows that the monotonic pushover curve and the backbone curve of cyclic hysteresis loops agree very closely. Only a slightly bigger base shear force is observed at the monotonic pushover curve when the house experiences a large displacement in the +x direction. Overall, the monotonic pushover analysis presents a very accurate upper bound for the backbone curve of the cyclic pushover analysis. This observation is consistent with the formulation of the adopted engineering masonry model, in which cyclic damage is not considered.

However, both the monotonic and the cyclic pushover analyses overestimate the maximum base shear force of the house, when compared to the experimental ones. Furthermore, a slower reduction of the base shear force is obtained in the numerical modeling which indicates a more ductile structural behavior, especially in the positive loading (+x) direction.

5.3.2 Crack evolution

The crack evolution of the half house model is discussed in this section, mainly in terms of the crack widths of the masonry walls at each stage. Cracks with a width larger than 0.13 mm are considered fully open. This value is estimated through the defined masonry ultimate tensile strain.

Figure 5.6 (a) indicates the representative positions where the crack patterns are analyzed. These positions are as follows:

• the end of the initial stage;

- the end of the pseudo-linear stage (Cycle 8);⁴
- the position of the peak base shear force (Cycle 15/18);⁵
- the position after 20% reduction of the peak base shear force has been reached for both directions (Cycle 22), which is also the last cycle in the test;
- and the end of the pushover analysis (Cycle 27).

Crushing of masonry might occur as well under large displacement loading, e.g. at the post-peak stage. The crushing patterns of the house model are also presented when it is detected.

Note that the masonry wall cracks might vary along the thickness of the elements. Here, cracking and crushing are presented at their minimum layers. More detailed crack and crush patterns of the maximum layers and stress/strain conditions of the house model can be found in Appendix C.

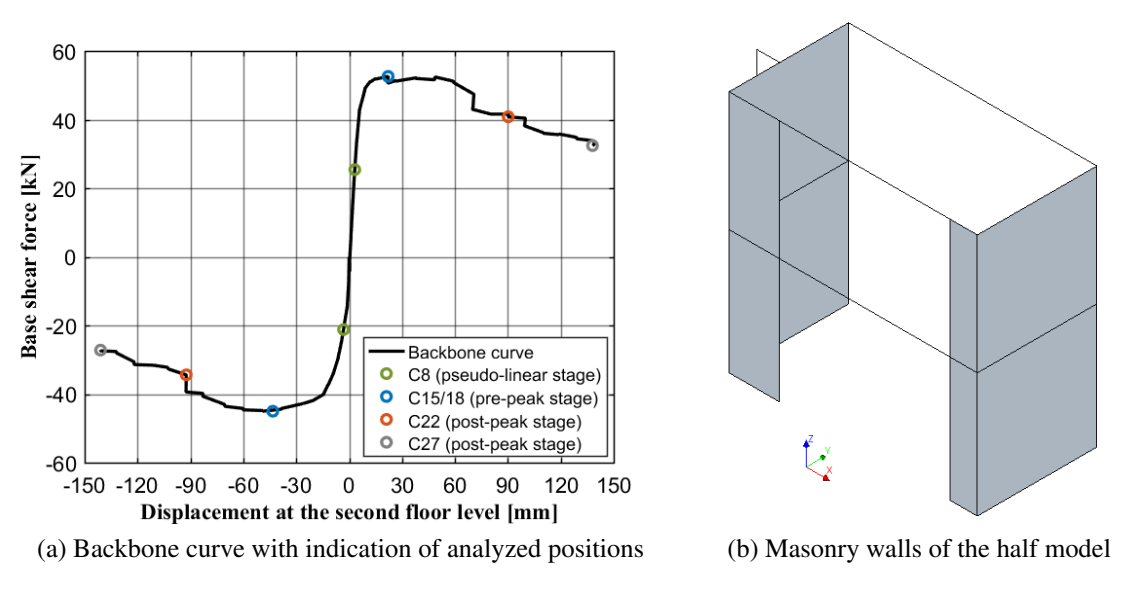


Figure 5.6: Analysis of the crack evolution

INITIAL STAGE

Only gravity is activated in the initial stage. Deformation of the house due to self-weight can be seen in Figure 5.7 (a). Gravity load leads to cracks along the rigid connections between the masonry walls and concrete floors. However, these cracks are less than 0.1 mm as shown in Figure 5.7 (b): they are not visible to the naked eye.

These cracks form because the two concrete floors tend to deflect under gravity but are constrained at the connections. Additionally, due to the asymmetric geometry of the model, the narrow pier deforms more. As a result, a small crack is found in the narrow pier side at the second floor level.

⁴Crack patterns are presented at the maximum displacement of each analyzed cycle.

⁵The peak base shear force occurs at Cycle 15 in the positive direction and Cycle 18 in the negative direction.

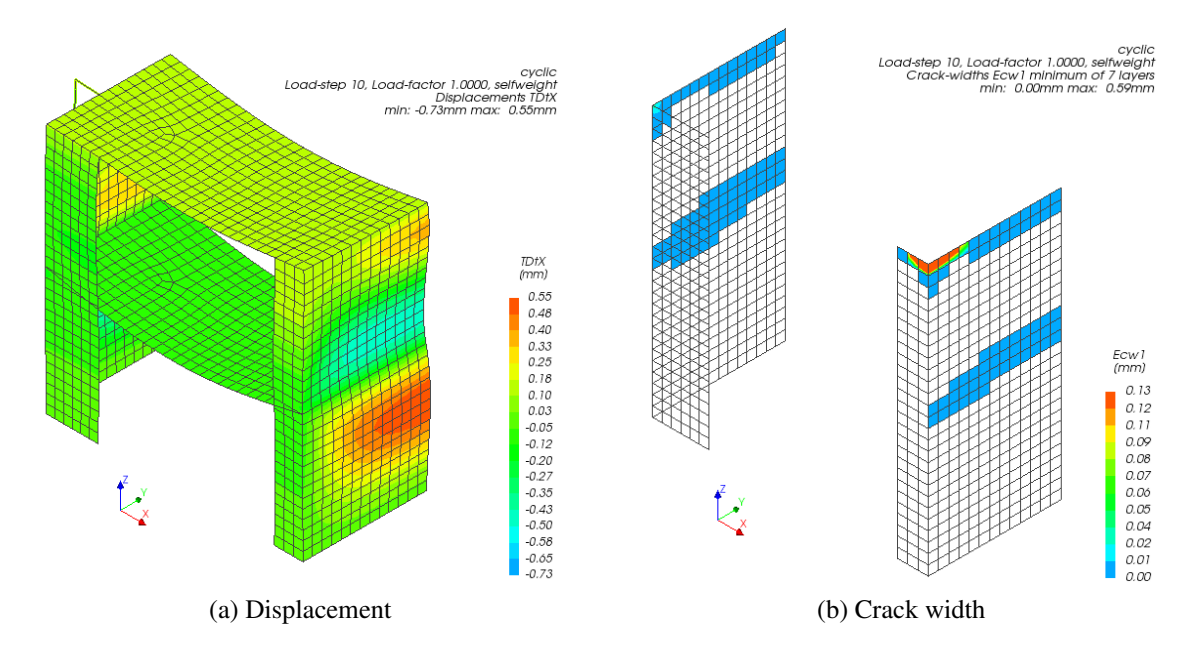


Figure 5.7: Results at the end of initial stage

PSEUDO-LINEAR STAGE

During the pseudo-linear stage, horizontal cracks start to develop at the bottom of the masonry piers. The previous cracks along the rigid connections also develop further. The formation of these cracks shows that the structural behavior is actually nonlinear.

Figure 5.8 provides the displacement and crack patterns of the half model loaded in the positive

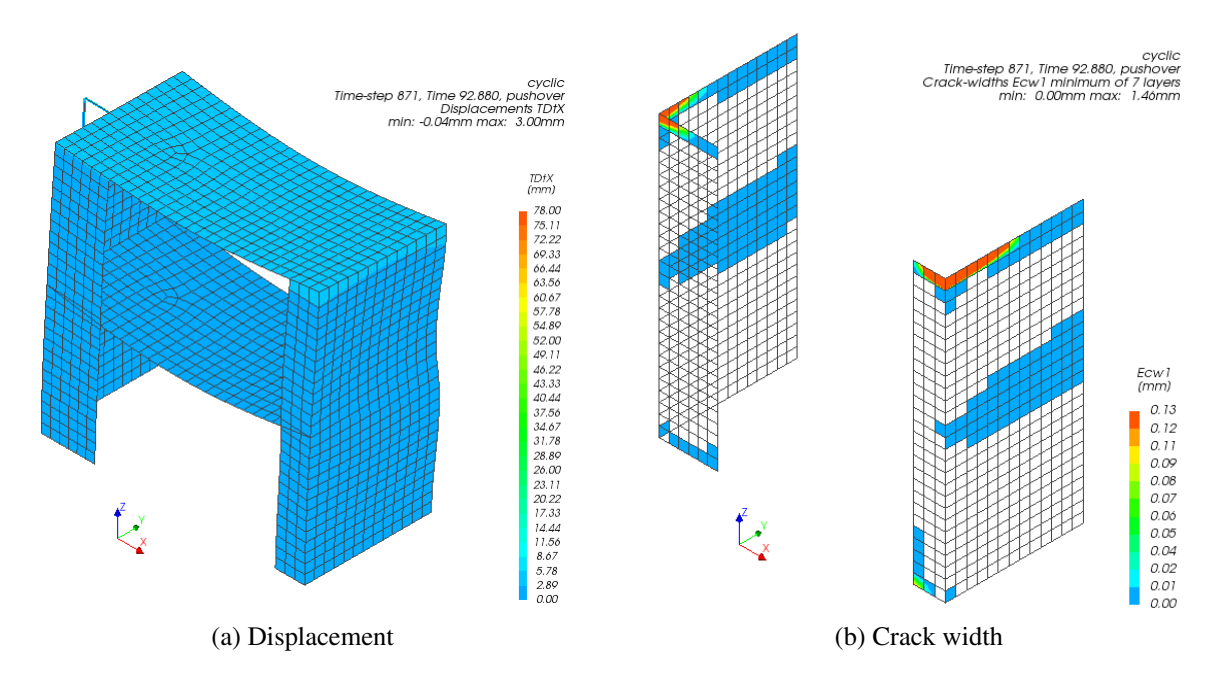


Figure 5.8: Results at cycle 8 (positive direction)

direction at Cycle 8. Besides the cracks caused by gravity, there are new horizontal cracks at the bottom of the masonry piers due to the cyclic lateral loading. When loading in the positive direction, cracks in the wide pier tend to close while cracks in the narrow pier are opening.

Conversely, cracks open in the wide pier and close in the narrow pier under negative loading (Figure 5.9). The wide pier displays a rocking mechanism with horizontal cracks at the tensile side of the bottom. A larger crack width is observed when loaded in the negative direction, which agrees with the asymmetric property of the capacity curves.

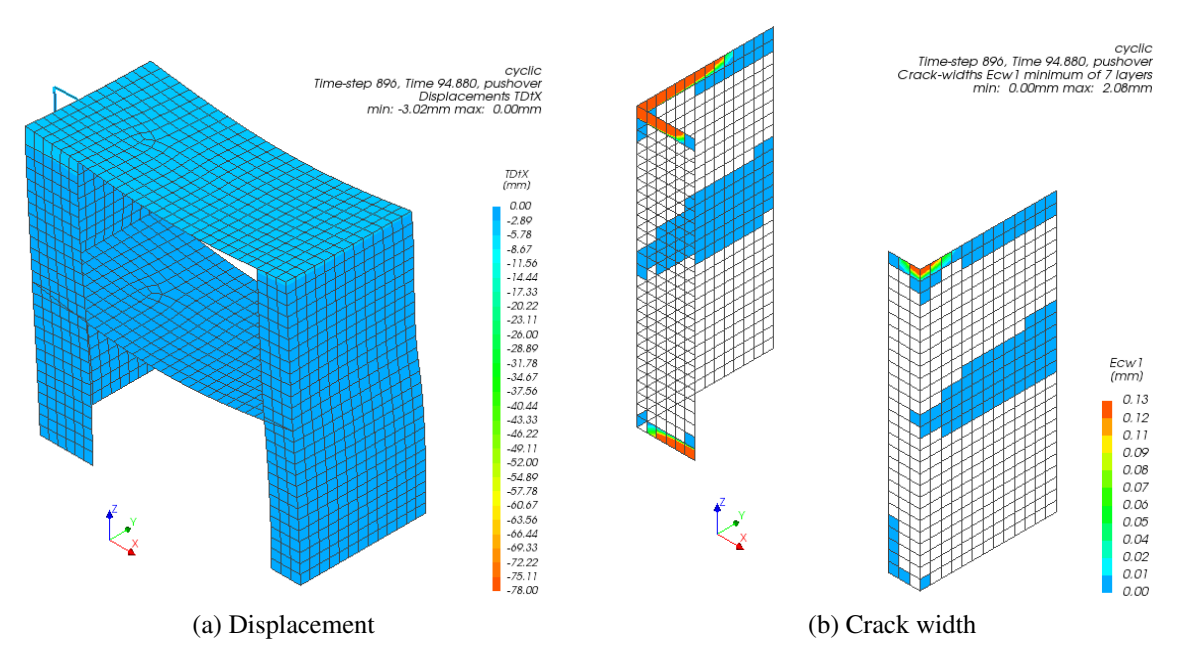


Figure 5.9: Results at cycle 8 (negative direction)

PRE-PEAK STAGE

The rocking mechanism is observed on both piers at the pre-peak stage, with horizontal cracks opening along the top and the bottom. The formation of these cracks leads to the decrease of the house stiffness, as seen in the backbone curve.

Figure 5.10 shows the crack patterns when the maximum base shear force in the positive loading direction is reached (displacement: +22.1 mm). Horizontal cracks due to rocking occur on both piers. Additionally, a second layer of horizontal crack appears as well on the tensile side of the piers under positive loading.

In addition, the crack openings are found in the transversal wall along the bottom and the connection with the first floor slab. The development of the crack at the first floor level might be the cause of the slight reduction in base shear force immediately after the peak value is reached. Moreover, small cracks are found around the connections between the masonry piers and transversal walls, especially at the ground floor. The formation of these cracks evidences the existence of a two-way out-of-plane mechanism of the transversal walls.

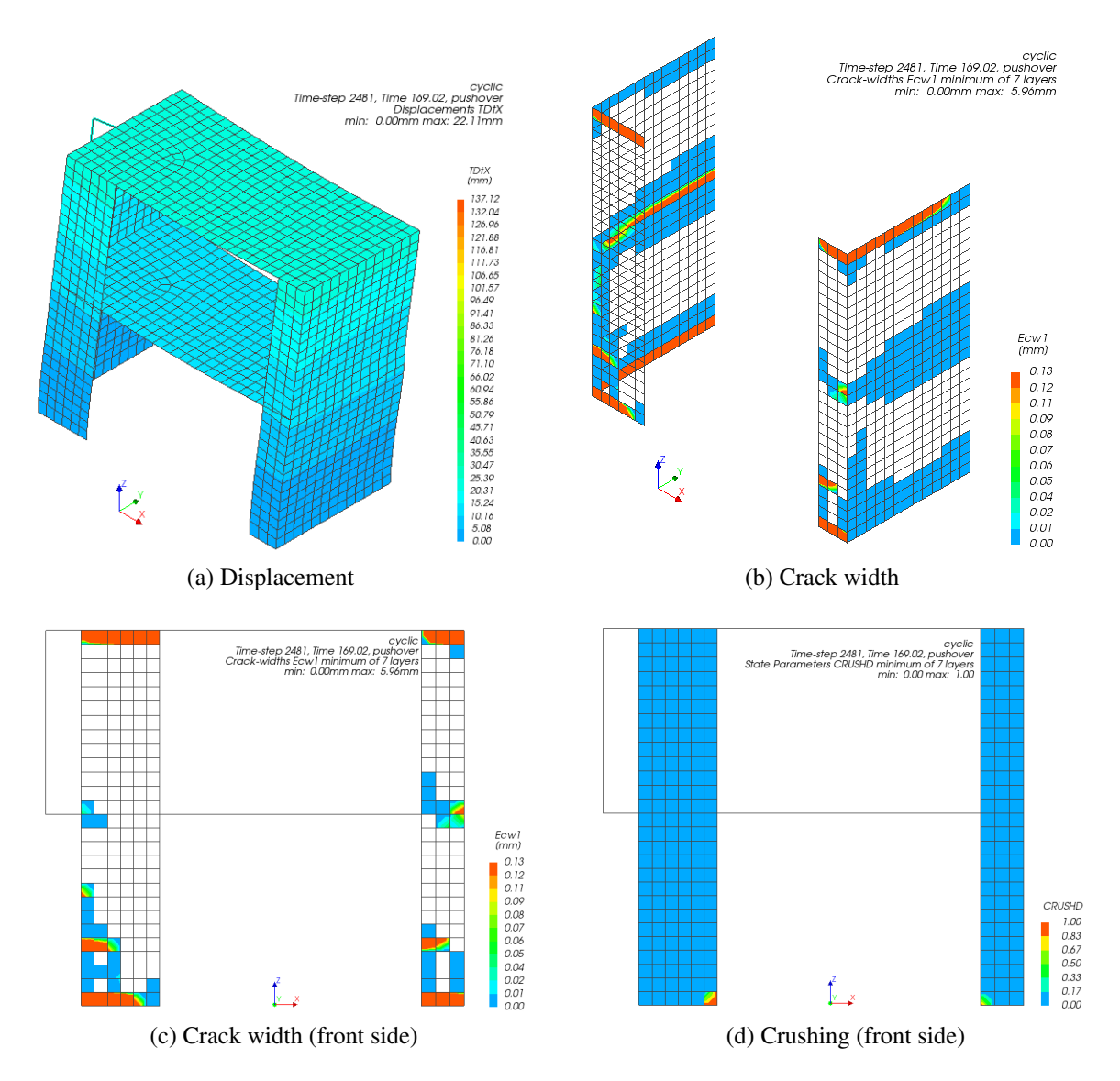


Figure 5.10: Results at cycle 15 (positive direction)

In the negative direction, a slow increase in base shear force is detected after Cycle 15 and the model finally reaches the maximum base shear force at Cycle 18 with a displacement of -34.6 mm.

Figure 5.11 shows the cracking behavior of the model in the negative direction at Cycle 18. The change of loading direction leads to closure of the cracks formed previously in the piers and the opening of new horizontal cracks at the other side. The main damage of the model is still localized at the bottom of the wide pier due to rocking, although more sub-cracks are formed in the pier under the increased load. Limited toe crushing is observed as well at the corners of both piers due to cyclic loading, as shown in Figure 5.11 (d).

The negative loading also leads to closure of the horizontal crack along the wall-to-floor connection at the first floor level. Flexural cracks in the transversal walls develop further at both floor levels, demonstrating a more clear trend of the two-way mechanism caused by the use of running bond between the masonry piers and walls.

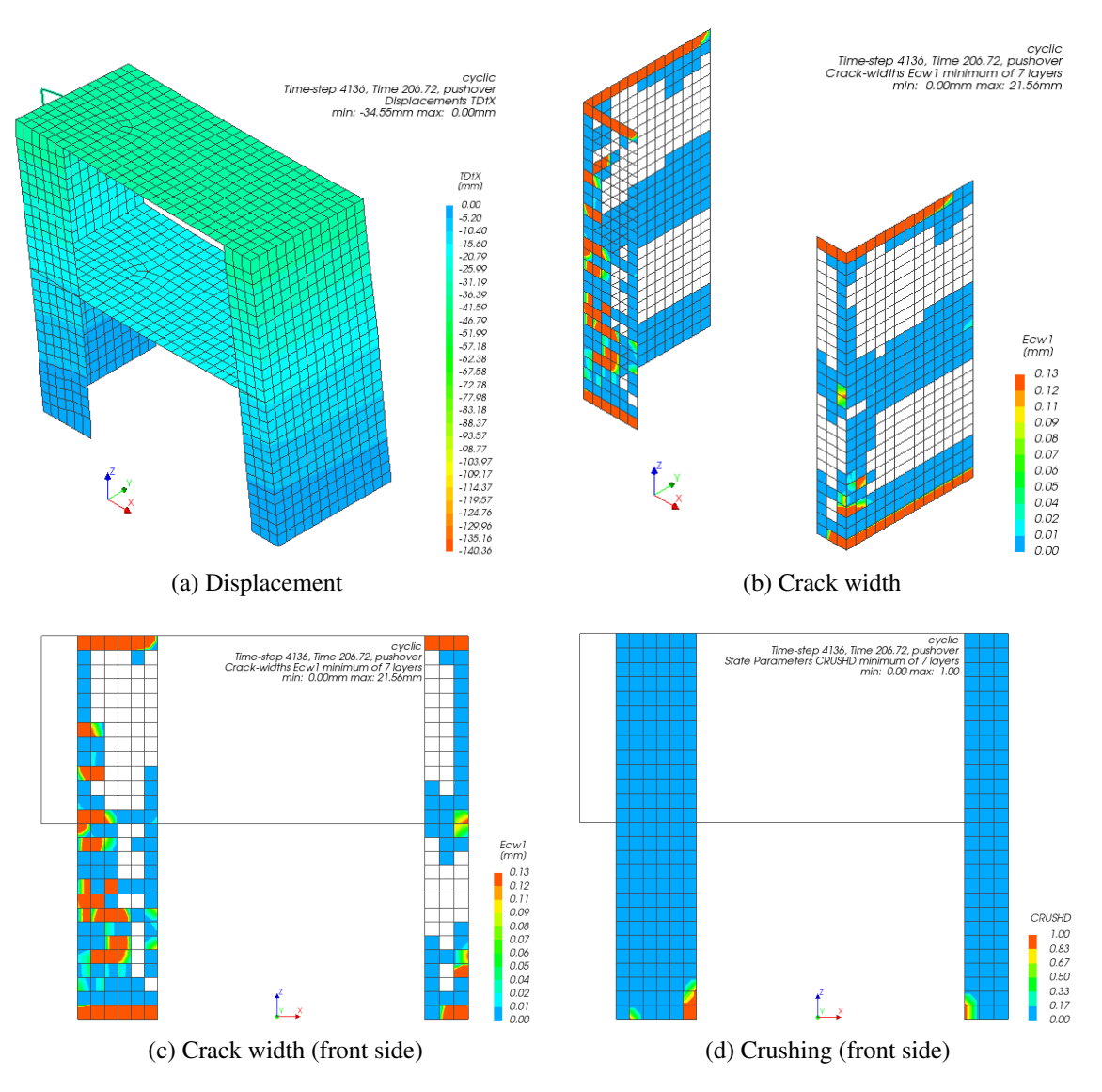


Figure 5.11: Results at cycle 18 (negative direction)

POST-PEAK STAGE (CYCLE 22)

The positions of main cracks remain constant in the post-peak stage. Cracks at the top and bottom of both piers continue widening under the increased lateral loading. Small sub-cracks keep forming on both piers as well.

Figure 5.12 shows the cracking and crushing behaviors of the model under pushover loading in the positive direction at Cycle 22. The most severe damage of the model is localized at the bottom of the narrow pier, then at the tensioned side of the wide pier. Cracks are also found along the top and bottom of the transversal walls due to rocking of the structure. Additionally, small cracks continue to form on both transversal walls and a two-way mechanism can be found although the clear diagonal crack patterns are not presented.

Crushing is found at compressive corners of both masonry piers under the cyclic loading. The

formation of the crushing damage within the wide pier influences the position of the compressive stress, resulting in a smaller level arm (Figure C.13 in Appendix C). This reduction then contributes to the decrease in base shear force of the house model at the post-peak stage.

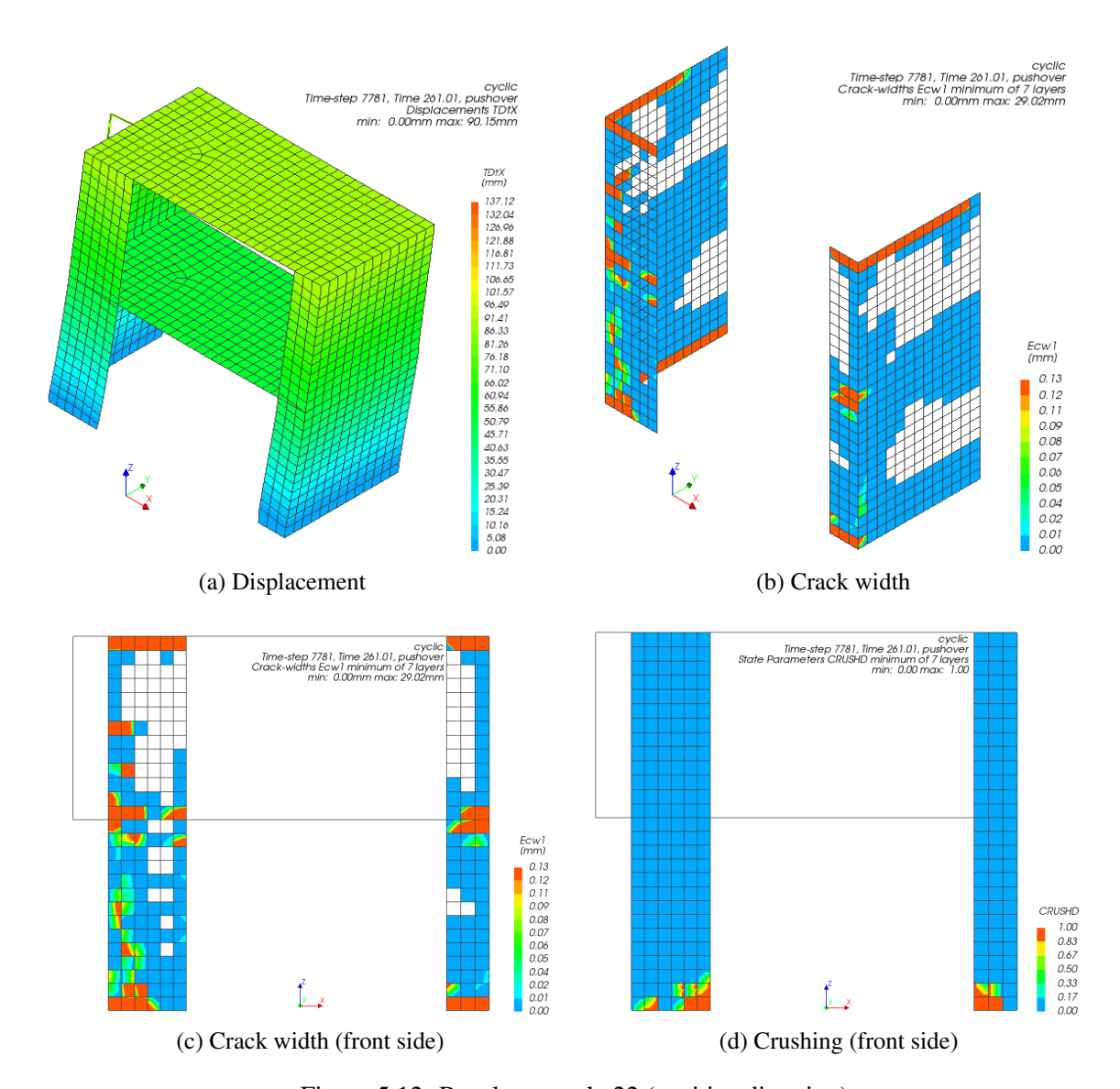


Figure 5.12: Results at cycle 22 (positive direction)

Similar cracking and crushing behaviors are found when the model reaches the maximum displacement in negative direction of this cycle (see Figure 5.13).

In the negative loading, the biggest crack is found along the bottom of the wide pier. Cracks along the connection at the top and bottom of the transversal walls also extend a lot due to the increased loading. Crushing occurs on both piers as discussed before. However, for negative loading the compressive side of the wide pier is supported by the interlocking with the transversal wall, leading to a slower reduction in the base shear force.

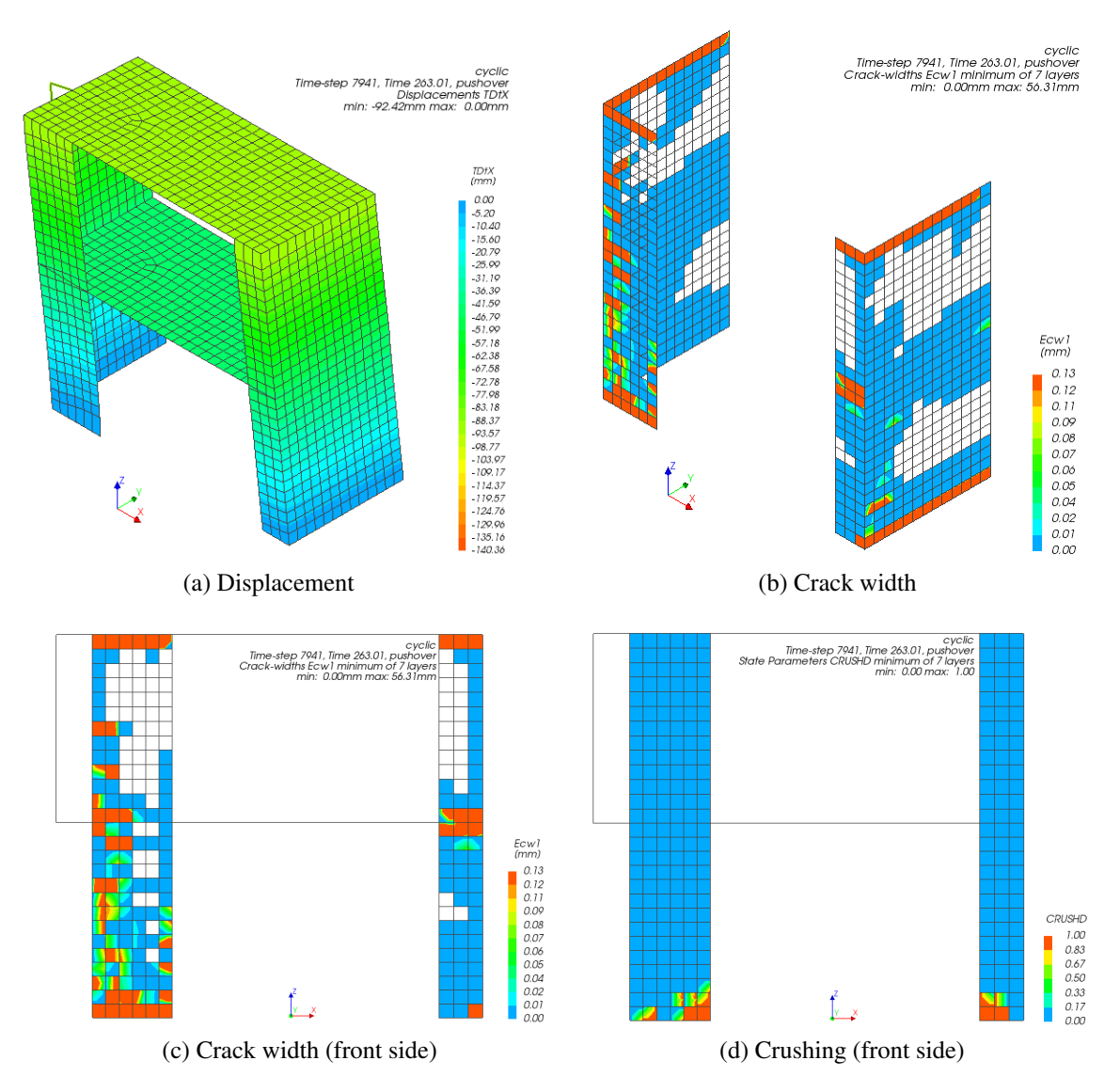


Figure 5.13: Results at cycle 22 (negative direction)

POST-PEAK STAGE (CYCLE 27)

Cracking and crushing patterns of the house model at the last loading cycle (Cycle 27) are also presented.

Figure 5.14 shows its behavior at the maximum displacement in positive direction. Very large deformations of the house are observed. The largest crack is localized along the bottom of the narrow pier. The cracks at the top and bottom of the transversal walls extend more as well, while the overall crack pattern of the transversal walls remain unchanged.

More severe crushing damage is detected in both masonry piers, as shown in Figure 5.14 (d). The progressive crushing damage in the wide pier causes the redistribution of compressive stress (see Figure C.19 in Appendix C), and therefore leads to the further reduction in base shear force of the model.

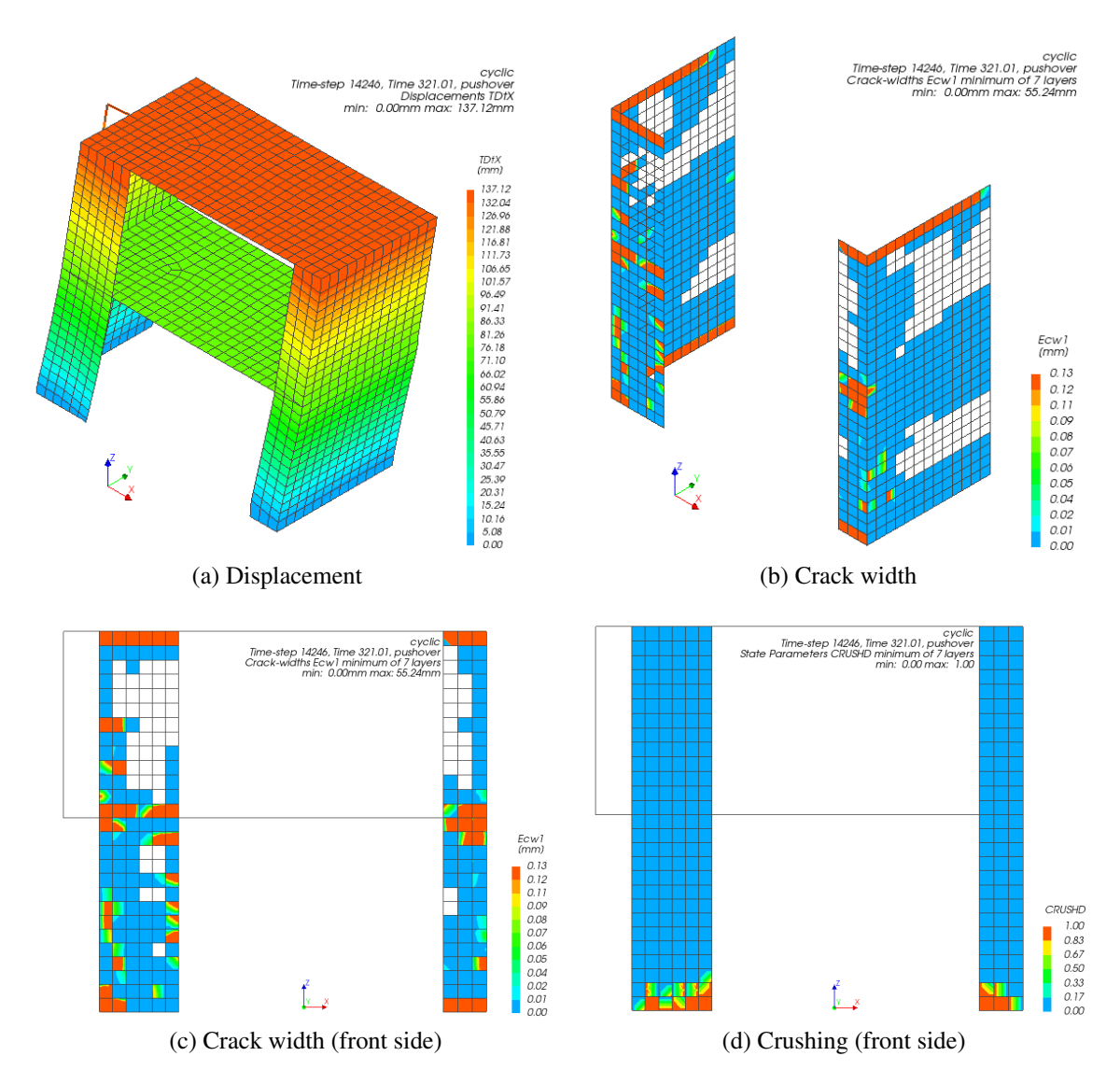


Figure 5.14: Results at cycle 27 (positive direction)

Figure 5.15 shows its behavior at the maximum displacement in negative direction.

The most severe damage is localized at the bottom of the wide pier with widely opened cracks. The cracks within the transversal walls almost remain the same as before while the cracks along their top open more. The crushing damage in both piers extends more, compared to that at Cycle 22, and results in the further decrease in base shear force of the model in the negative direction.

Crack evolution summarization

In conclusion, the structural behavior of the house model under cyclic pushover load is governed by the damage of the masonry piers, with a strong correlation between the crack evolution and capacity curve of the model.

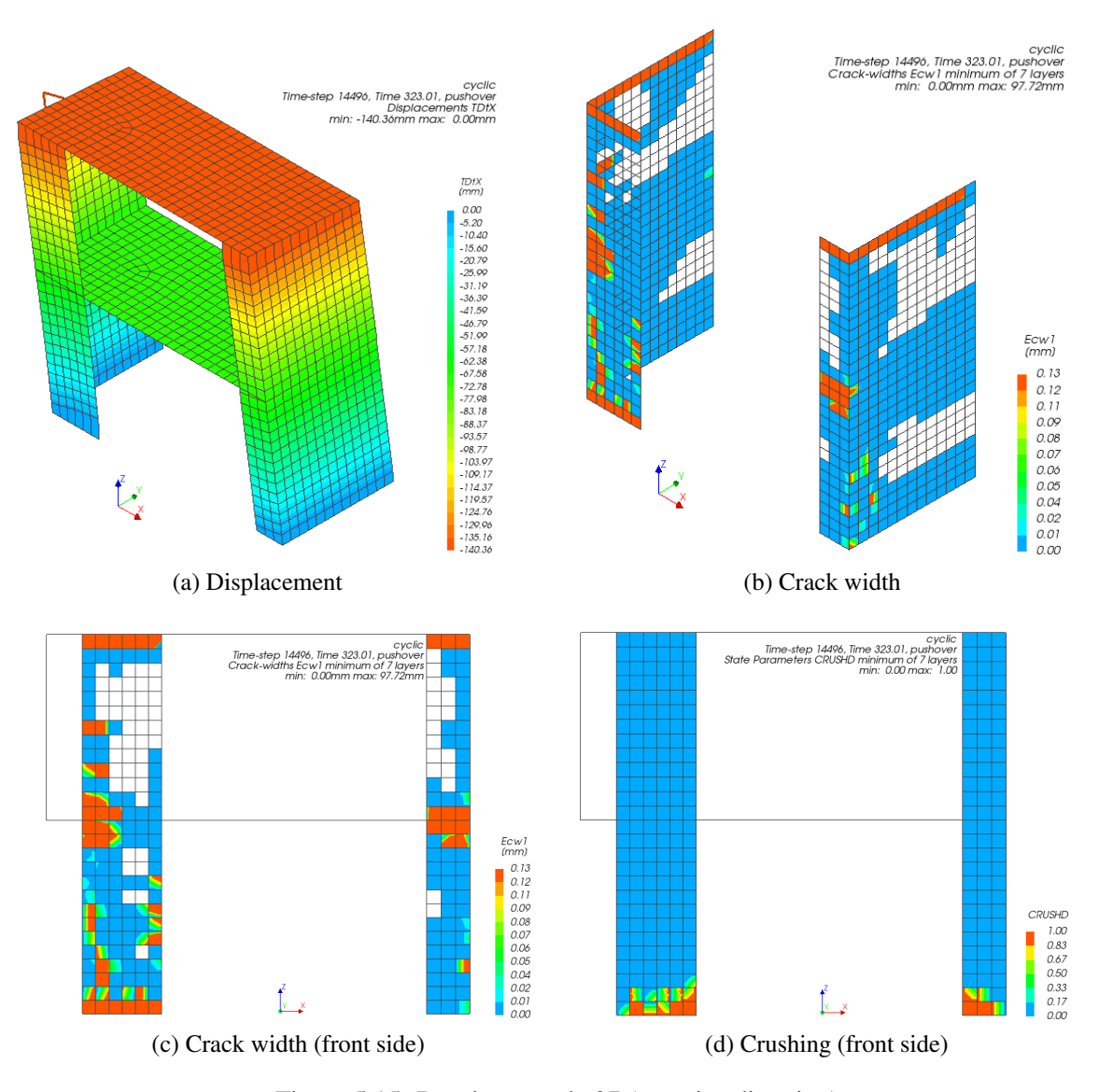


Figure 5.15: Results at cycle 27 (negative direction)

The numerical results agree well with the experiment at the pseudo-linear and pre-peak stage: the rocking mechanism associated with horizontal cracks at the top and bottom is observed on both masonry piers. These cracks reduce the stiffness before reaching the maximum base shear force in both directions. While no clear diagonal/vertical cracks were identified in the wide pier – as observed during the experiment – there was clear evidence of progressive damage of the pier panel during the post-peak stage. Furthermore, the occurrence of toe-crushing redistributes the compressive stress within the masonry piers, resulting in a smaller level arm and therefore a reduction in the base shear force. The post-peak behavior of the model is more related to the toe-crushing and this might explain the slower softening observed from the numerical capacity curves.

It is worth noting that the numerical model captured the asymmetric behavior of the house in terms of both capacity curve and crack patterns, as observed in the experiment. While both piers exhibit rocking mechanism with horizontal cracks and toe crushing, the narrow pier has a much smaller impact on the global stability of the structure due to its relatively small moment of inertia,

compared to the wide pier. Therefore, a lower base shear capacity and larger crack widths are observed in the negative direction and more damages are concentrated on the wide pier.

Additionally, the crack patterns in the transversal walls indicate the existence of a two-way out-of-plane mechanism, since the cracks not only form at the top, the intermediate height and the bottom of the walls but also develop diagonally from the wall edges.⁶ The formation of this mechanism is triggered by the use of running bond between the piers and the transversal walls, which are modeled as rigid connections. However, there is no clear diagonal crack patterns in the transversal walls, as observed in the experiment.

5.3.3 Drifts

In this section, the deformation of the house model is discussed in terms of interstory drifts. The drifts are calculated as the ratio of the relative floor displacement and interstory height, which is 2.7 m for the first floor level and 2.6 m for the second floor level in the model.

Figure 5.16 shows the calculated drifts at the maximum displacement of each loading cycle. A very small drift is found at the pseudo-linear stage (cycle 1 - 8) in both directions, and the drifts of the first floor and second floor are almost the same. During the pre-peak stage, the drifts of both floors become larger under the increased displacement loading. The first floor and second floor still show similar drifts, but a slightly larger drift of the second floor is observed at the last two cycles of this stage (cycle 17, 18) for both directions.

In the post-peak stage, a difference is observed between the drifts of the two floors in positive direction. The drift of the first floor is larger than second floor at each loading cycle and the difference between the drifts increases with the number of cycles. This could be a result from the more severe damage of the wide pier at the ground floor. In the negative direction, similar drift values are obtained for the two floors.

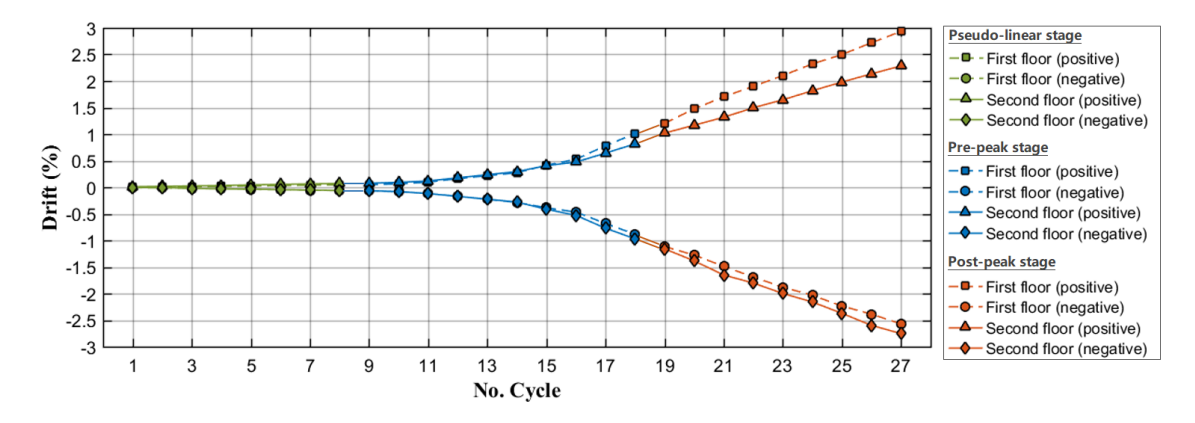


Figure 5.16: Interstory drift

A maximum drift of +2.3/-2.8% is found at the first floor level during the whole loading history, while the maximum drift at the second floor level is +2.9/-2.6%, in the positive and negative

⁶The described crack patterns are more clear seen at the maximum layer of the model, which can be found in Appendix C.

directions. For the primary seismic unreinforced masonry wall governed by rocking/toe crushing mechanism, Eurocode 8 gives analytical solutions to define its limit drifts. Two limit states are specified: 1) severe damage and 2) near collapse.

$$d_{r,SD} = 0.008 \frac{H_0}{D} \tag{5.1}$$

$$d_{r,NC} = \frac{4}{3}0.008 \frac{H_0}{D} \tag{5.2}$$

where $d_{r,SD}$ is the drift limit for the severe damage state and $d_{r,NC}$ is the drift limit for the near collapse state, H_0 is the height of the section where the flexural capacity is attained and the contraflexural point, and D is the in-plane horizontal dimension of the wall (EN-1998-3, 2005).

The numerical results are compared with calculated drift limits (Ravenshorst et al., 2016), and listed in Table 5.4. Given the estimated drift limits for the wide pier, the house model reaches the limit state of severe damage in both directions. The obtained drifts of the first floor and the second floor are 110% and 90% of the calculated value for near collapse limit state in the positive direction. In the negative direction, the obtained first floor and second floor drifts are 100% and 105% of the calculated value for near collapse limit state. Nevertheless, the drifts of both floors have not reached the estimated value for severe damage limit state of the narrow pier.

Therefore, it can be concluded that the limit state of near collapse of the model is reached at the last loading cycle, for both positive and negative directions. The structural behavior of the model under cyclic pushover loading is governed by the wide pier.

	Case	Drift (%)		
	Case	Wide piers	Narrow piers	
	First floor - positive		2.9	
Numerical	Second floor - positive	2.3		
(Cycle 27)	First floor - negative 2.6		2.6	
	Second floor - negative	2.8		
Eurocode 8	Limit state of severe damage	1.9	3.6	
	Limit state of near collapse	2.6	4.8	

Table 5.4: Comparison of the drifts at Cycle 27

To compare the obtained drifts in the numerical analysis with experimental results, the drifts of both floors at Cycle 21 are also examined⁷ (see Table 5.5). A clear difference is found between the numerical and experimental results in the negative direction.

In the numerical analysis, almost the same drift value is found on the first floor and second floor, which is 1.5% and 1.6%, respectively. However, in the test a drift of 2.2% is observed on the first floor and a relatively small drift of 1.0% is found on the second floor. The large drift of the first floor in the test is related to the reduction of the piers' cross-sections caused by diagonal/vertical cracks, which were not detected in the numerical analysis.

⁷Cycle 22 in the test is only composed by half a run in the negative loading direction.

Furthermore, it can also be concluded from Table 5.5 that the limit state of severe damage has not been reached at Cycle 21 of the numerical analysis for both directions.

Case		Drifts (%)	
		Wide piers	Narrow piers
	First floor - positive		1.7
Numerical	Second floor - positive	1.3	
(Cycle 21)	First floor - negative	1.5	
	Second floor - negative	1.6	
Experiments	Both floors - positive	1.5	
(Cycle 21)	First floor - negative 2.2		2.2
	Second floor - negative		1.0
Eurocode 8	Limit state of severe damage	1.9	3.6
	Limit state of near collapse	2.6	4.8

Table 5.5: Comparison of the drifts at Cycle 21

5.4 Sensitivity Study

A sensitivity study is carried out to investigate the influence of certain material parameters on the softening behavior of the model. All the studies presented herein are based on the monotonic pushover analysis. The seismic response of the models with different parameters are mainly discussed in terms of capacity curves.

As discussed in the previous section, the main difference between the numerical and experimental results occur during the post-peak stage. Generally, the numerical model displays slower softening and no clear diagonal/vertical cracks are detected in the wide pier of the model. Therefore, the influences of the compressive strength f_c , compressive fracture energy G_{fc} and initial shear strength f_{v0} of masonry are investigated.

5.4.1 Compressive strength

The original house model has a masonry compressive strength of 5.84 MPa. To obtain a softening behavior closer to the experiment, models with a masonry compressive strength of 75% and 50% of the original value were built. The corresponding compressive fracture energies were also scaled depending on the value of f_c . Figure 5.17 (a) compares the obtained capacity curves from these three models to the experimental curve.

It is observed that the model with a lower compressive strength shows a softening behavior that is closer to the experimental curve. Figure 5.17 (b)-(d) show the compressive stress distribution of the three models at the last step for positive loading. The decrease of masonry compressive strength leads to more severe crushing damage in the wide pier. The occurrence of this toe-crushing causes redistribution of the compressive stress and a reduction of level arm within the wide pier, as shown

in Figure 5.17 (b) and (c). It is clear that a smaller compressive strength leads to a larger decrease in the level arm of the pier, and therefore the corresponding model exhibits more reduction in the base shear force at the post-peak stage.

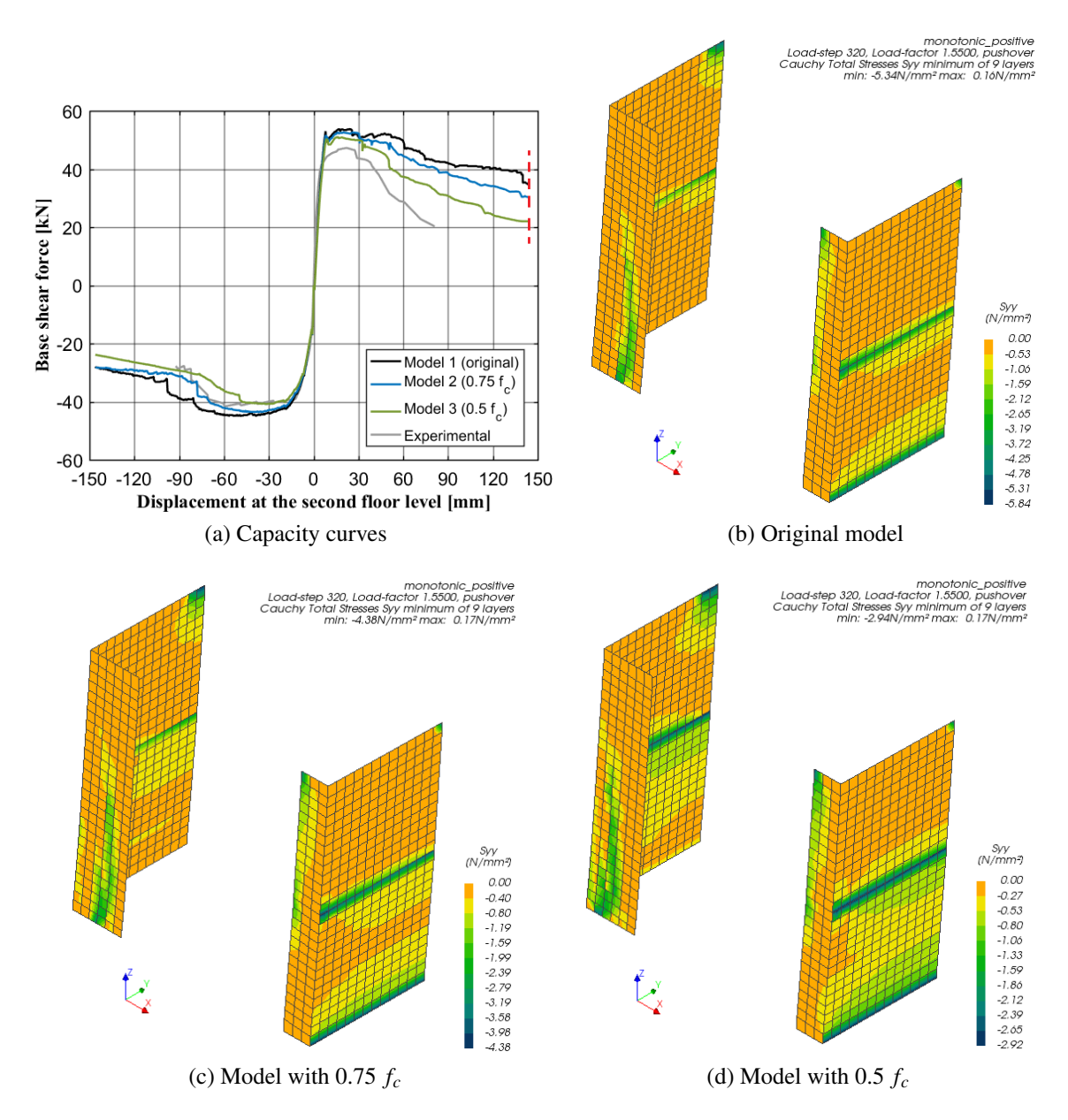


Figure 5.17: Capacity curves and compressive stress distributions

5.4.2 Compressive fracture energy

Similarly, models with reduced compressive fracture energies were analyzed. The original model has a compressive fracture energy of 17.39 N/mm. Two models with with 75% and 50% of the original compressive fracture energy were built and analyzed. All other material parameters stay unchanged. Figure 5.18 compares the capacity curves from these three models to the experimental one.

Changing the values of the compressive fracture energy only elicits changes in the post-peak behavior of the model. A slightly lower base shear force is found with the lower fracture energy model at the post-peak stage. However, the cracking and crushing patterns of the three models are very similar for each step. No distinct relation is found between the masonry compressive fracture energy and the structural behavior of the house model.

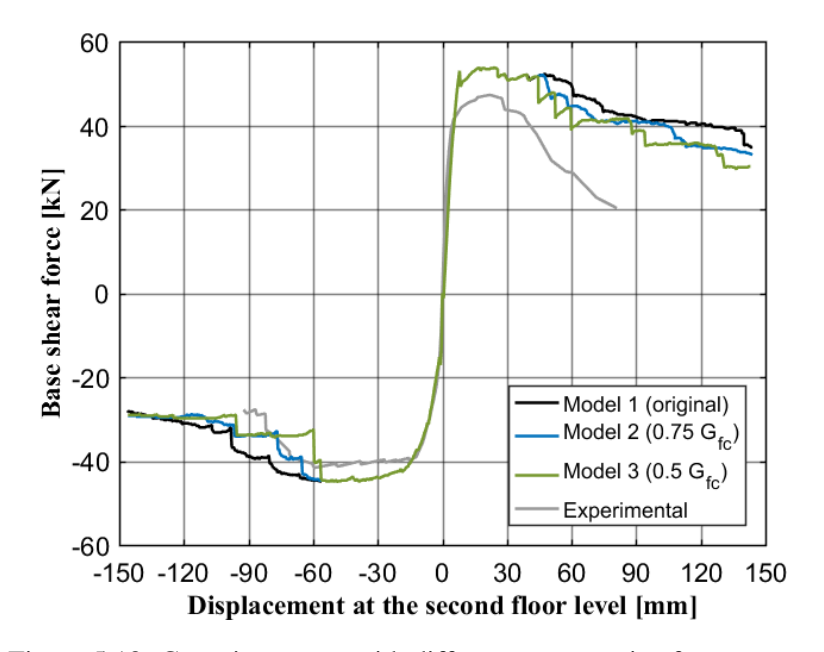


Figure 5.18: Capacity curves with different compressive fracture energy

5.4.3 Initial shear strength

The influence of the initial shear strength of masonry is also investigated. Two models are built with 75% and 50% of the original initial shear strength ($f_{v0} = 0.14$ MPa), respectively. Figure ?? (a) compares their capacity curves to the experimental one. The main differences are observed in the positive direction, with lower initial shear strengths leading to sudden reductions in the base shear force during the post-peak stage.

The crack patterns of these models at load step 50 in the positive direction (displacement: +21.4 mm) are examined, as shown in Figure 5.19 (b)-(d).

More sub-cracks are found in the wide pier of the model with a lower initial shear strength. Moreover, more severe damage associated with horizontal cracks are observed in the transversal walls, especially on the first floor. The formation of these cracks might cause the sudden reductions shown in the capacity curves, but these damage do not govern the collapse of the masonry house.

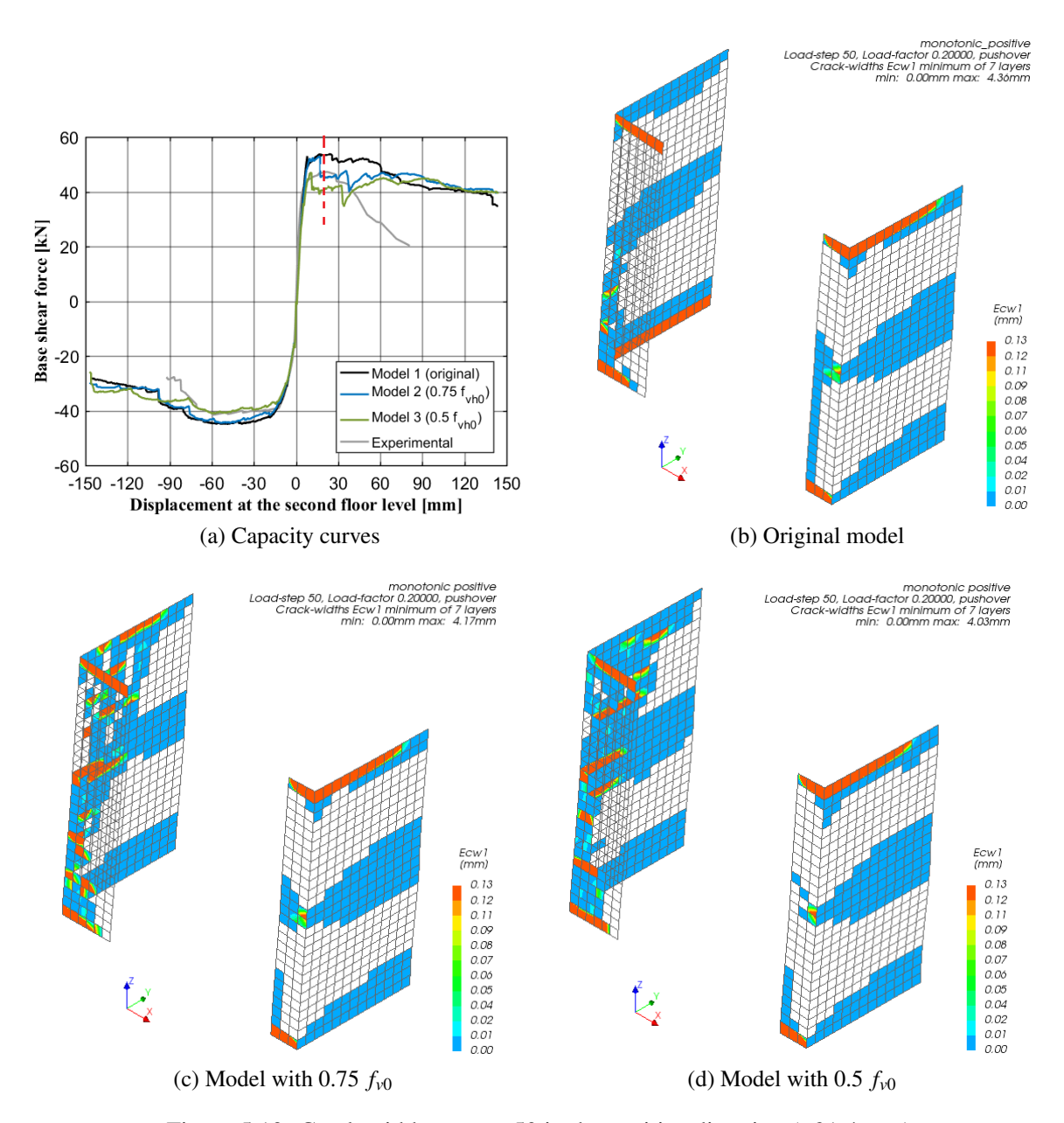


Figure 5.19: Crack widths at step 50 in the positive direction (+21.4 mm)

Chapter 6

NONLINEAR TIME HISTORY ANALYSIS OF TUD_HOUSE-1

The nonlinear time-history analysis is performed on the half house model to simulate its structural behavior under a real seismic event. The incremental dynamic analysis (IDA) method is used here to capture a more thorough seismic response. Section 6.1 presents the input signals used in this analysis. Then, Section 6.2 describes the analysis procedure in DIANA FEA. Finally, the results are discussed in Section 6.3.

6.1 Input Signals

The earthquake signals (i.e. ground accelerations in time history) are direct inputs in the nonlinear time-history analysis. Figure 6.1 shows the location of applied ground accelerations $(a_g(t))$ on the

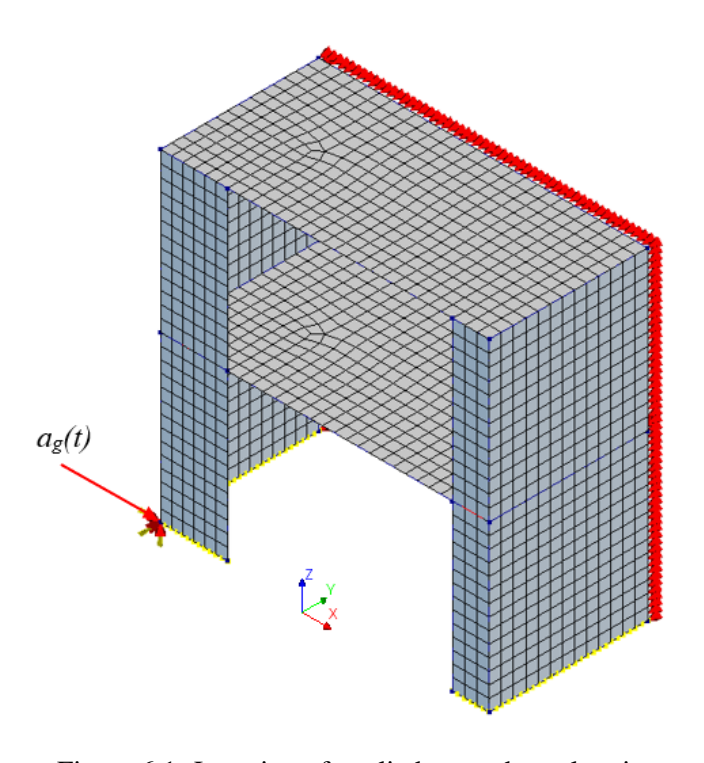


Figure 6.1: Location of applied ground accelerations

half house model.

The earthquake accelerogram is applied along the global x-axis of the model in order to compare the results to those from the cyclic pushover analysis and the experiment on the assembled specimen. Because soil-structure interaction is not considered in this research (as defined in Chapter 4), the input signal is applied directly to the base of the half house model. Thanks to the use of tying at the base of the model, the input acceleration is only applied to the master node of the base. The whole base of the model is subject to the same accelerations.

Figure 6.2 shows the input seismic signal. The applied accelerogram is consistent with the characteristics of induced seismic ground motions, and is similar to those used for shaking table tests on unreinforced masonry buildings at Eucentre (Graziotti, Tomassetti, Kallioras, Penna, and Magenes, 2017).

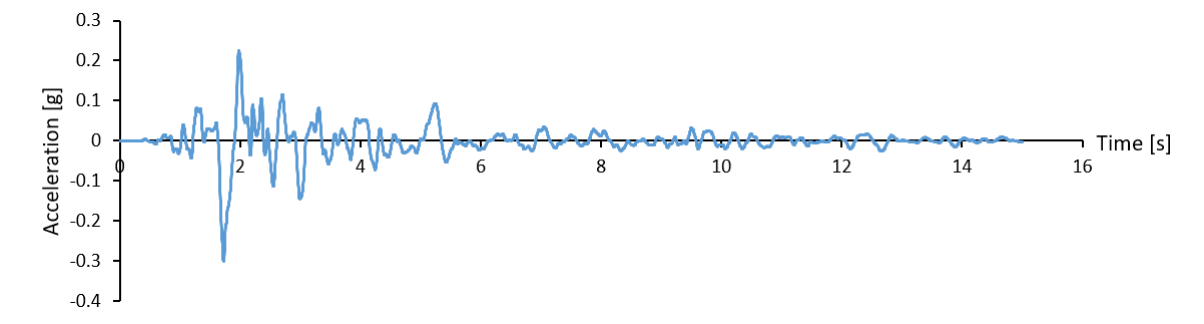


Figure 6.2: Input seismic signal

The above signal is scaled to twelve different levels of intensity to perform the incremental dynamic analysis. This set of 12 scaled signals is then applied to the house model. Each scaled signal is defined as one run of the whole loading history, thus there are 12 runs in total. Figure 6.3 shows the full scheme of the applied ground motion signals and Table 6.1 gives the value of peak ground acceleration (PGA) for each run.

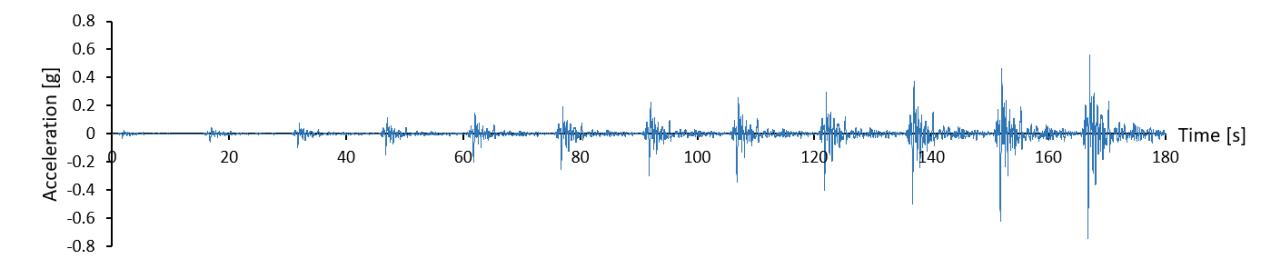


Figure 6.3: Full scheme of applied accelerogram

Additionally, it is noted that the features of the current accelerogram – in tandem with the asymmetric geometry of the house model – produce results which only capture the seismic behavior of the house in the positive (+x) direction properly. In order to compare with the results from cyclic pushover analysis in both positive and negative loading directions, the behavior of the model under dynamic loads along the -x direction is needed. Therefore, an incremental dynamic analysis with the mirrored accelerogram is also performed on the house model. Figure 6.4 shows the full scheme of the mirrored accelerogram.

Run	PGA value [g]
1	0.03
2	0.06
3	0.10
4	0.15
5	0.20
6	0.25
7	0.30
8	0.35
9	0.40
10	0.50
11	0.62
12	0.75

Table 6.1: PGA value for each run

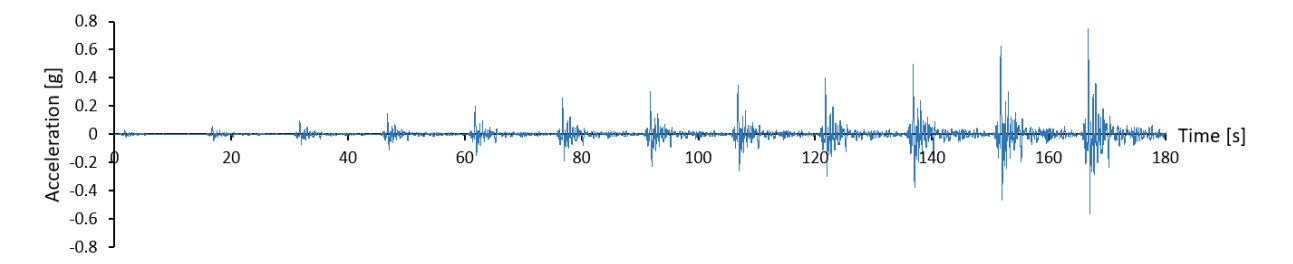


Figure 6.4: Full scheme of mirrored accelerogram

6.2 Nonlinear Time History Analysis

To perform the nonlinear time-history analysis in DIANA FEA, first the gravity load of the house is applied. Then, the earthquake accelerogram is applied by means of prescribed accelerations to the master node at the base. 3001 time steps are used for each run and the acceleration value for each step is added through a time dependent factor. Both physical and geometrical nonlinearities are included in the dynamic analysis.

Damping is included via Rayleigh damping coefficients derived from an eigenvalue analysis of the full house model. The coefficients for the mass matrix ($a = 2.0166 \text{ s}^{-1}$) and the stiffness matrix (b = 0.00049 s) are based on two vibration modes along the global x-axis, in agreement with the direction of the input seismic signal.

The secant iteration method, with line search and continuation iteration, is used in the nonlinear time-history analysis to achieve more stable numerical calculations. The number of iterations per step is limited to 100. Each step reaches convergence only when both the displacement and force norms are satisfied simultaneously. The detailed analysis parameters are summarized in Table 6.2.

Load	Self-weight 10		
steps	Ground acceleration 36012 time steps (1		
	Max. number of iterations	100	
Iteration	Iteration method	Secant (BFGS)	
method	First tangent	Previous iteration	
memou	Line search	Yes	
	Continuation iteration	Yes	
Convergence	Satisfy both displacement norm (tolerance 0.01)		
criteria	and force norm (tolerance 0.01)		

Table 6.2: Procedure of the nonlinear time-history analysis

Because the original accelerogram determines large deformations only in the positive direction, the nonlinear time-history analysis described above is performed twice on the house model. One analysis uses the original accelerogram (Figure 6.3) to get seismic responses of the house in +x direction, and the other one uses the mirrored accelerogram (Figure 6.4) to get the seismic responses in -x direction.

6.3 Results in +X Direction

The results of the nonlinear time-history analysis in the positive direction are discussed in this section. The house model is severely damaged after 11 runs and no valid numerical results are available for the last run, therefore only the results of the first 11 runs are presented here. First, the hysteresis curves (i.e. base shear force versus second floor displacement) are discussed in subsection 6.3.1. The crack patterns of the house model due to each run are then shown in subsection 6.3.2. Finally, subsection 6.3.3 describes the floor drifts observed during the analysis.

6.3.1 Hysteresis curves

Figure 6.5 and 6.6 present the resulting relative displacement at the second floor and the base shear force of the model in time histories. The maximum displacement at the second floor is found to increase in each run, while the maximum base shear force remains almost constant after run 4.

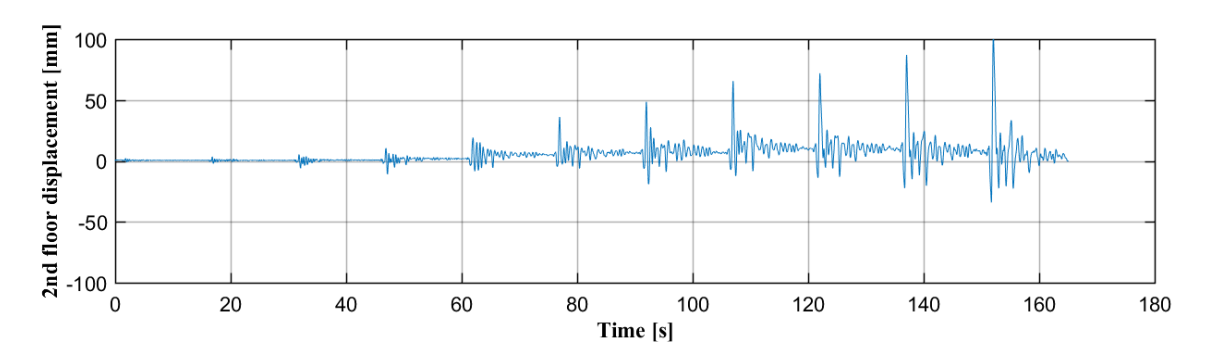


Figure 6.5: Resulted relative displacement at the second floor

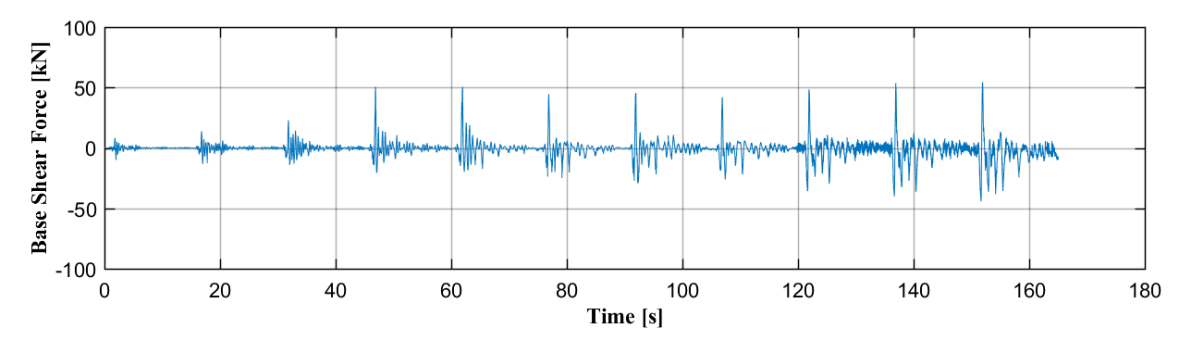
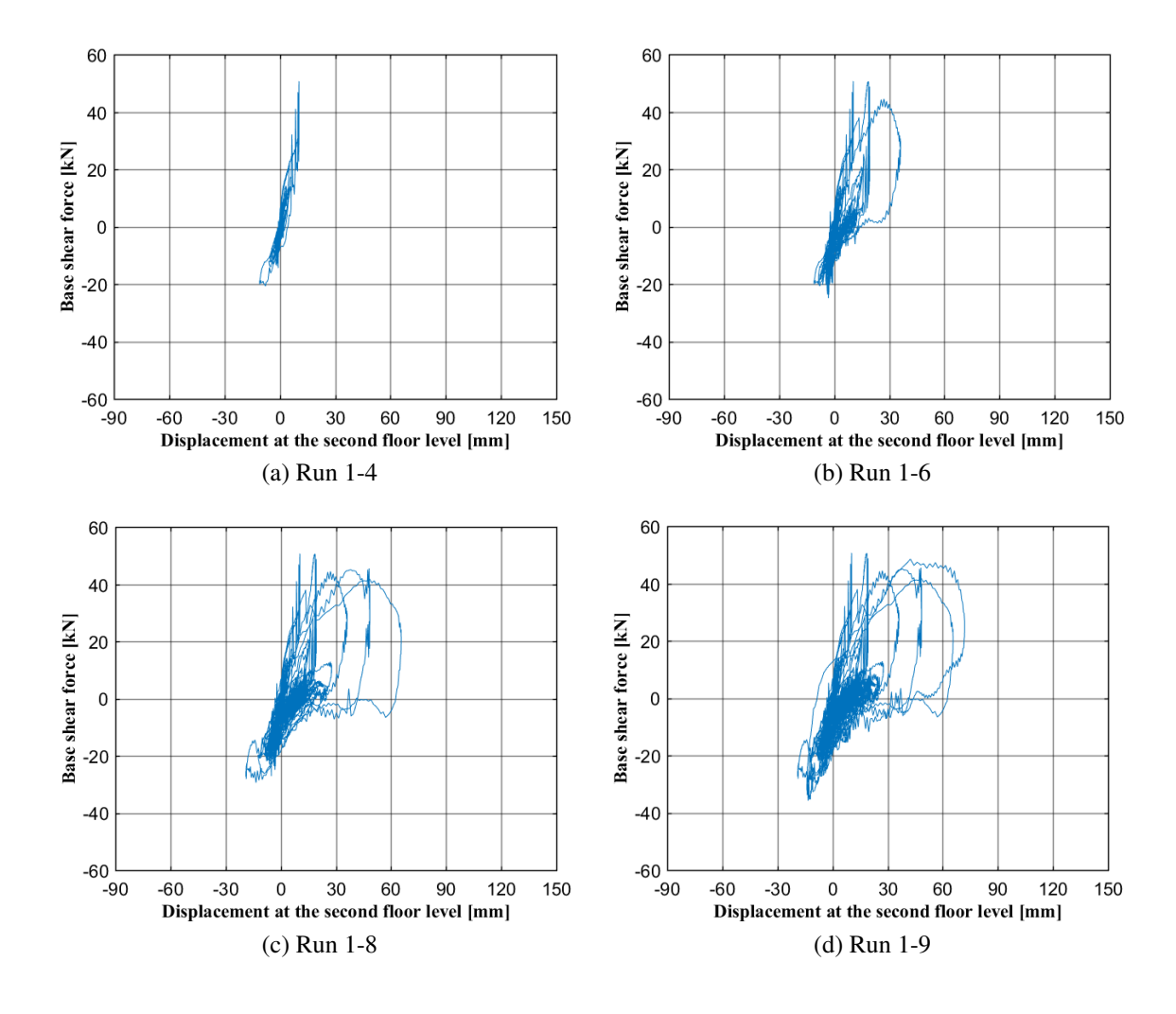


Figure 6.6: Resulted base shear force of the house

The hysteresis curves are graphed to investigate the relation between the base shear force and second floor displacement, as shown in Figure 6.7. To better show the seismic response of the model under the increased earthquake intensity, the curves are plotted at multiple representative stages during the whole loading history.

Run 1-4 (maximum: 0.15 g)

The hysteresis curves from run 1 to run 4 are shown in Figure 6.7 (a). A maximum base shear force of +50.68 kN is found in run 4 (0.15 g) at a displacement of +10.40 mm. Small energy dissipation



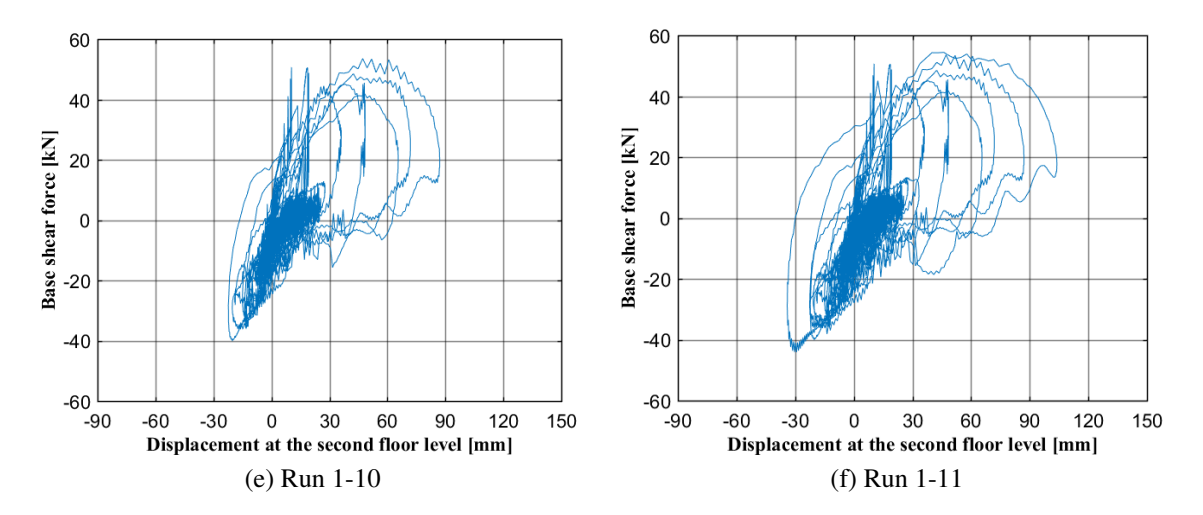


Figure 6.7: Hysteresis curves of the house model with time-history analysis

is observed under the seismic load of this intensity level.

Run 5 (0.20 g), Run 6 (0.25 g)

A severe stiffness degradation of the house model appears in run 5 (0.20 g), and more stiffness reduction can be observed in the hysteresis curves of run 6 (0.25g), as shown in Figure 6.7 (b). Run 5 yields the maximum base shear force of +50.64 kN at a displacement of +18.54 mm. In this run, the energy dissipation is still quite limited.

In contrast, run 6 yields a reduced base shear force of +44.52 kN with large energy dissipation. This indicates high nonlinearity due to severe damage of the house model. Additionally, the maximum displacement and maximum base shear force become decoupled; that is, they no longer occur simultaneously. This phenomenon might be related to the characteristics of the applied earthquake signal, and the contribution of higher modes when the model enters deep into the nonlinear range.

Run 7 (0.30 g), Run 8 (0.35 g)

During run 7, the house model moves further in the positive direction with a maximum displacement of +48.48 mm. However, the maximum base shear force remains similar to the previous run. More energy dissipation occurred and an accumulation of inelastic displacement is found in the positive direction.

In run 8, the maximum base shear force reduces to +41.88 kN while the dissipated energy and inelastic deformation in the positive direction keep increasing, as shown in Figure 6.7 (c).

Run 9 (0.40 g), Run 10 (0.50 g) and Run 11 (0.62 g)

Figure 6.7 (d) to (f) show the hysteresis curves from run 1 to run 9, 10 and 11. The maximum base shear forces are reached at similar displacements (around +47.0 mm) in these three runs, and their values are all around +50 kN. A maximum displacement of +103.90 mm is reached in run 11.

In all these three runs, the maximum displacement and maximum base shear force do not occur simultaneously.

Run 12 (0.75 g)

Like discussed before, the numerical results are heavily ill-behaved with impractical changes of forces at run 12 although no divergence is observed. Moreover, the model is found intensely damaged at the end of run 11 so it is assumed to be collapsed at the beginning of run 12.

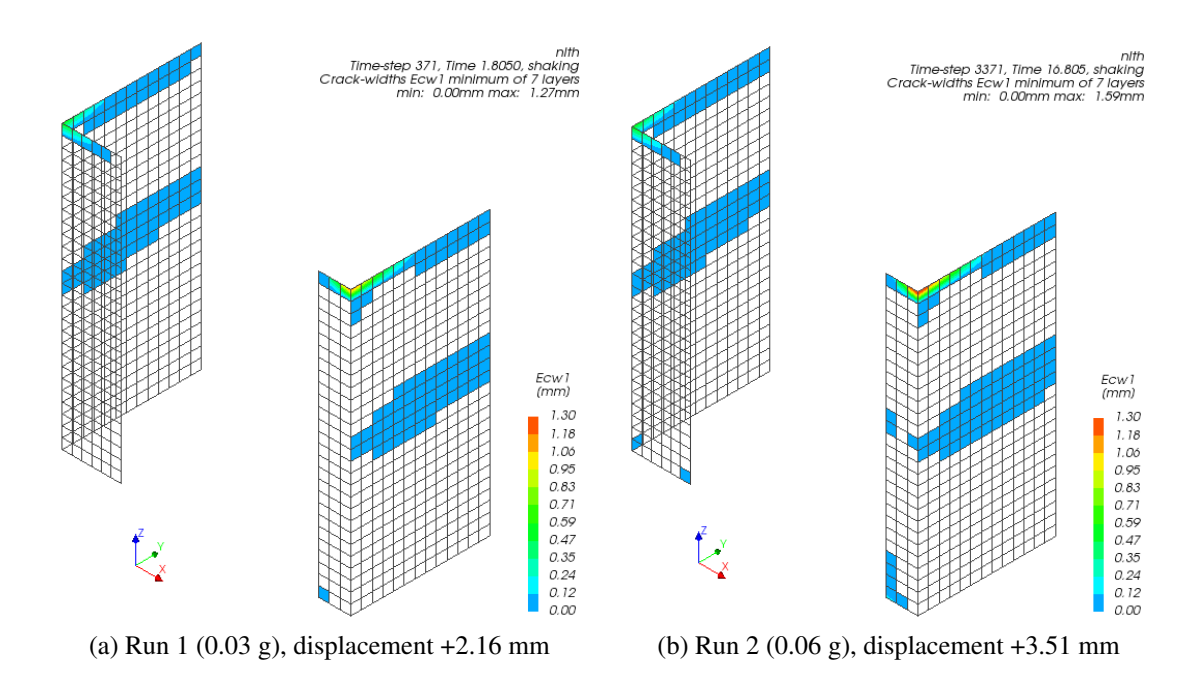
6.3.2 Crack evolution

The crack evolution is discussed in terms of the crack widths of the model at the maximum displacements of each run. Crack widths at the minimum layer over the element thickness are presented here. Corresponding crack patterns at the maximum layer can be found in Appendix D.

Run 1-4 (maximum: 0.15 g)

Figure 6.8 shows the obtained crack patterns from Run 1 to Run 4.

noindent Cracks along the rigid wall-to-floor connections are observed first, as shown in Figure 6.8 (a). The same rocking mechanism of the masonry piers is observed as in the pushover analysis. Both wide pier and narrow pier are activated, and horizontal cracks start to form at the bottom of both piers. Small flexural cracks also start to form in the transversal walls along the connection with the piers under the 0.15 g seismic load (Figure 6.8 (d)). The formation of these cracks might be a result of the use of running bond, which allows part of the transversal wall to act as a flange for the piers.



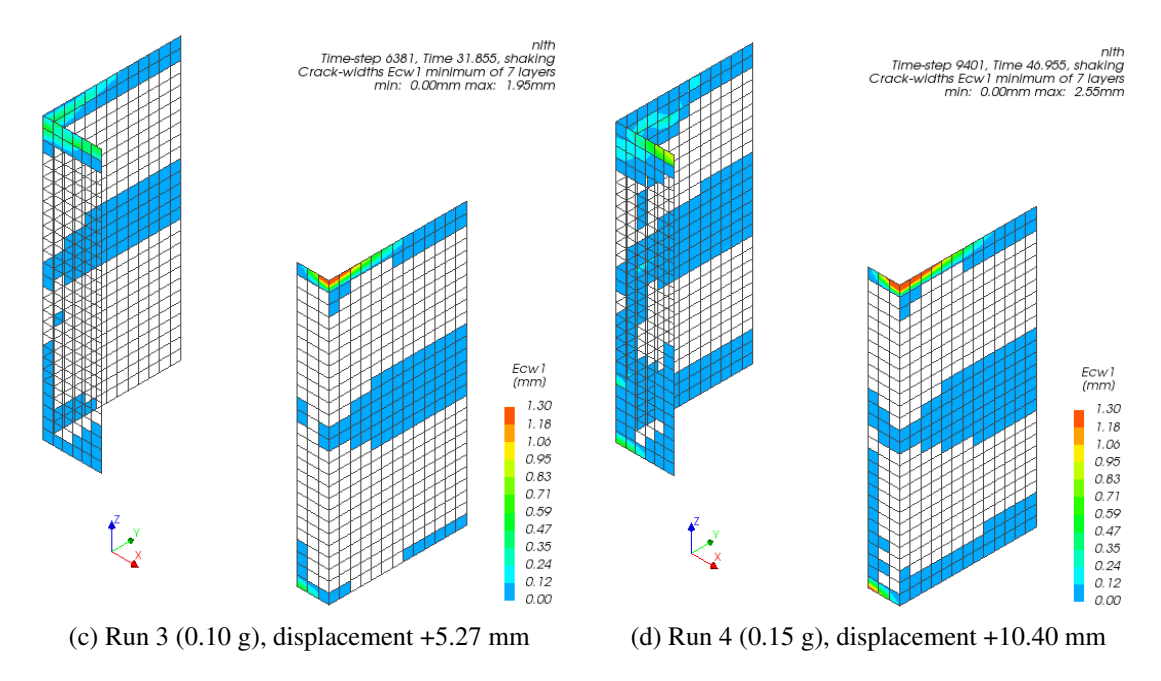


Figure 6.8: Crack width at the maximum displacement of run 1 to run 4

Run 5 (0.20 g), Run 6 (0.25 g)

Figure 6.9 (a) and (b) show the crack patterns at the maximum displacement of Run 5 and Run 6, respectively.

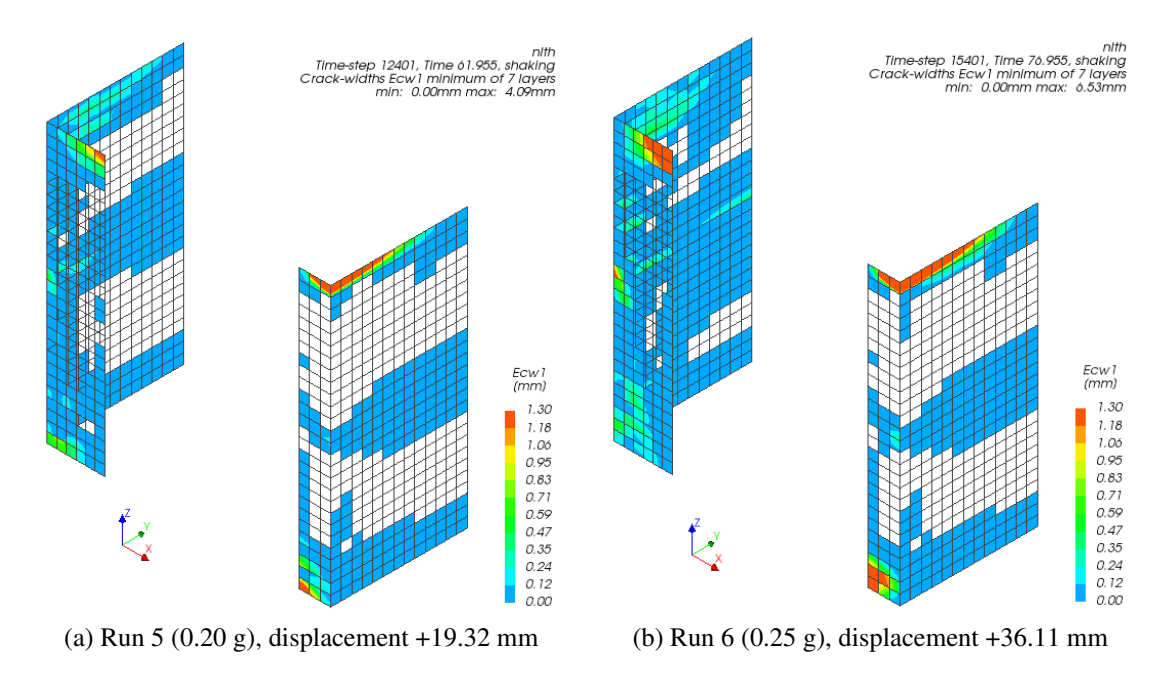


Figure 6.9: Crack width at the maximum displacement of run 5 and run 6

Figure 6.9 (a) shows that the cracks triggered by rocking of the piers keep developing in run 5. In run6, large cracks can be seen at the bottom of the narrow pier and the top of both piers (Figure 6.9

(b)). More sub-cracks are found in the wide pier at the ground floor level in this run, which leads to a reduction in the pier cross-section, and thus decreasing the maximum base shear force in the hysteresis curves.

Additionally, small cracks are observed over the transversal walls. Crack patterns at the maximum layer of the element show the cracks in the transversal walls are mostly located along the top, the intermediate height and the bottom of the walls (Figure D.5 and D.6 in Appendix D). However, the small cracks develop from the wall edges indicate the existence of a two-way mechanism.

Run 7 (0.30 g), Run 8 (0.35 g)

Figure 6.10 (a) and (b) show the crack patterns at the maximum displacement of Run 7 and Run 8, respectively.

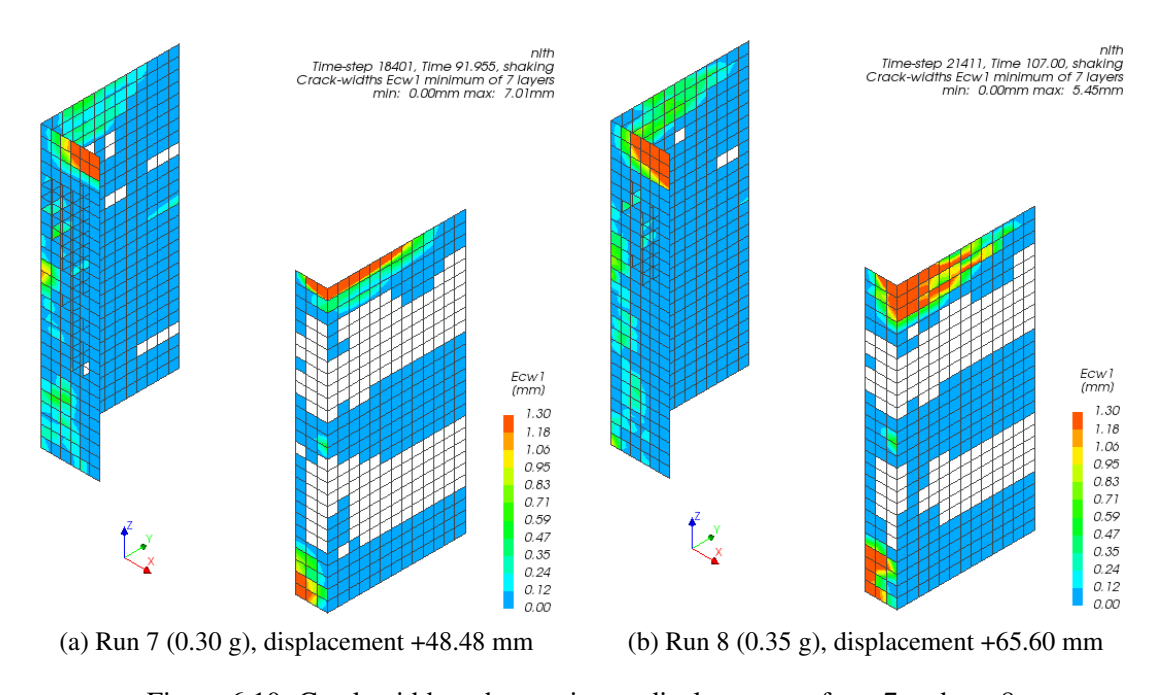


Figure 6.10: Crack width at the maximum displacement of run 7 and run 8

Cracks within both piers open more in run 7 (see Figure 6.10 (a)), leading to the degradation of the house strength. There is a large reduction in base shear force when the house model is loaded with 0.35 g in run 8. Figure 6.10 (b) shows widely opened cracks on narrow pier and cracks extending almost to the full height of the wide pier in this run. These cracks lead to a large reduction in the pier cross-section, and therefore result in the decrease in base shear force.

Run 9 (0.40 g), Run 10 (0.50 g), Run 11 (0.62 g)

Figure 6.10 (a) - (c) show the crack patterns at the maximum displacements of the last three runs.

The house model shows more severe damage when it reaches larger displacements in the last three runs. Besides the extension of cracks on the masonry piers, horizontal cracks start to form on the transversal walls at the ground floor level. At a displacement of +103.90 mm, multiple horizontal

cracks are found on the transversal wall which is connected to the wide pier, as shown in Figure 6.11 (c).

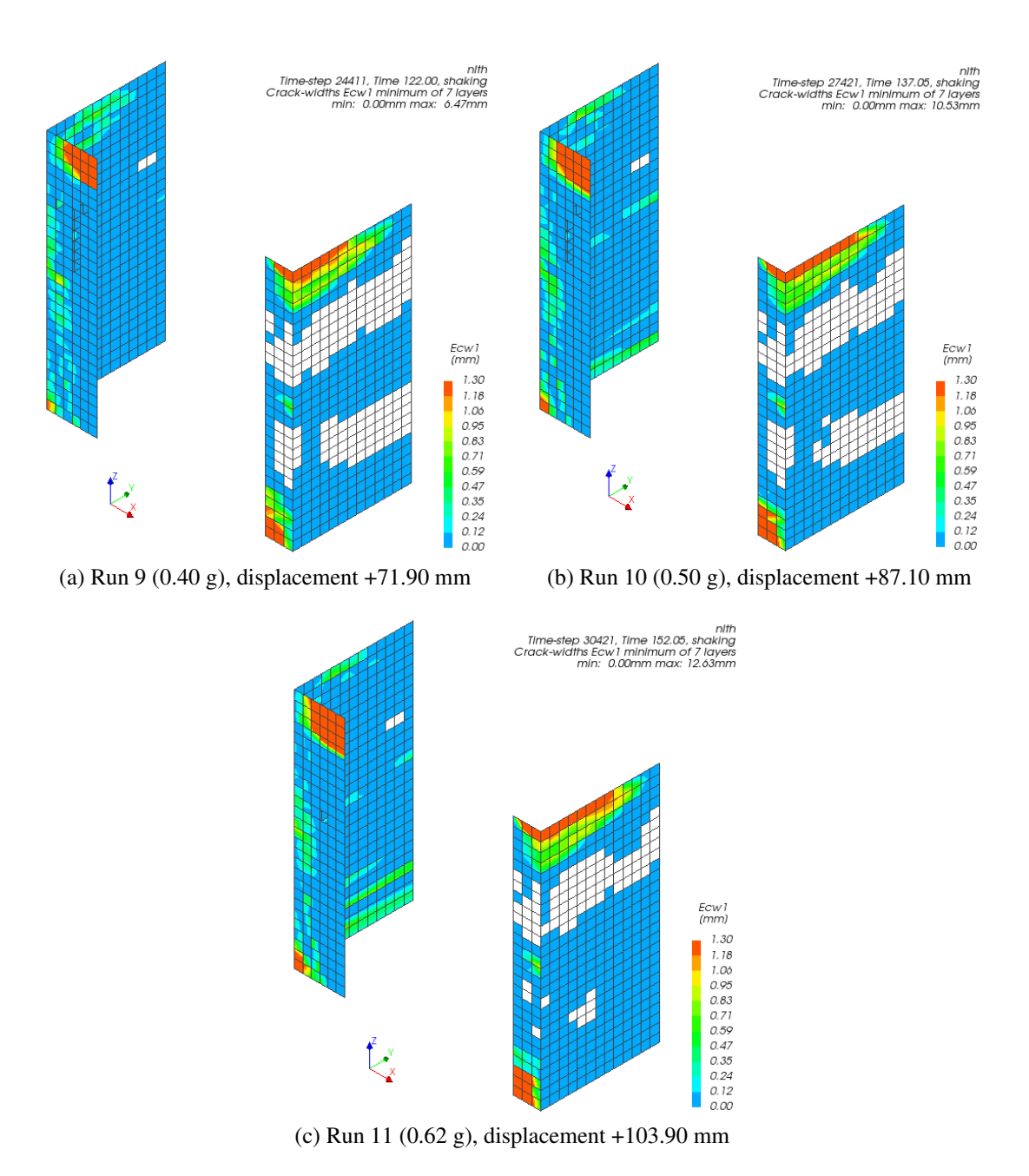


Figure 6.11: Crack width at the maximum displacement of run 9, 10 and 11

6.3.3 Drifts

The maximum drifts of the two floors in each run are calculated and shown in Figure 6.12. The drifts of the two floors are almost identical in the first five runs. However, a larger first floor drift is found since run 6 (0.25 g) due to the development of severe damage of the piers on the ground floor. The later-formed horizontal cracks on the transversal walls also contributes to the larger drift of the first floor.

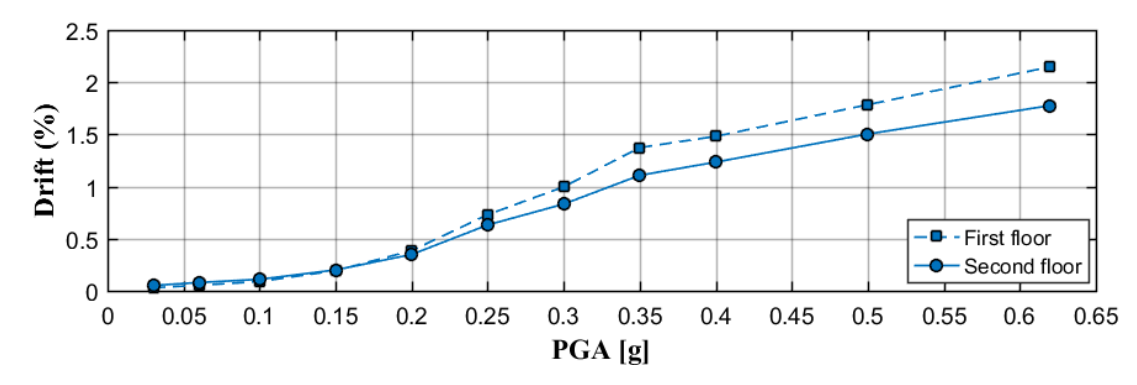


Figure 6.12: Maximum drifts of the two floors in each run

A maximum drift value of 2.2% at the first floor and 1.8% at the second floor are reached in run 11 (0.62 g). These values are compared to the drift limits per Eurocode 8, as discussed in section 5.3.3. Table 6.3 lists the numerical and analytical drifts. It can be concluded that the house model reached the limit state of severe damage in run 11 and the wide pier governs the structural response.

Case		Drift (%)	
		Wide piers	Narrow piers
Numerical	First floor - positive	2.2	
(0.62 g)	Second floor - positive	1.8	
Eurocode 8	Limit state of severe damage	1.9	3.6
	Limit state of near collapse	2.6	4.8

Table 6.3: Comparison of the drifts in Run 11 (positive direction)

6.4 Results in -X Direction

The seismic response of the house model in -x direction are obtained through the incremental dynamic analysis with the mirrored accelerogram. The results are discussed in terms of hysteresis curves, crack evolution and drifts. Only the results of the first 9 runs are presented here, as the model is severely damaged and no valid numerical results are available after run 9.

6.4.1 Hysteresis curves

Figure 6.13 and 6.14 show the time-histories of the relative displacement at the second floor and the base shear force.

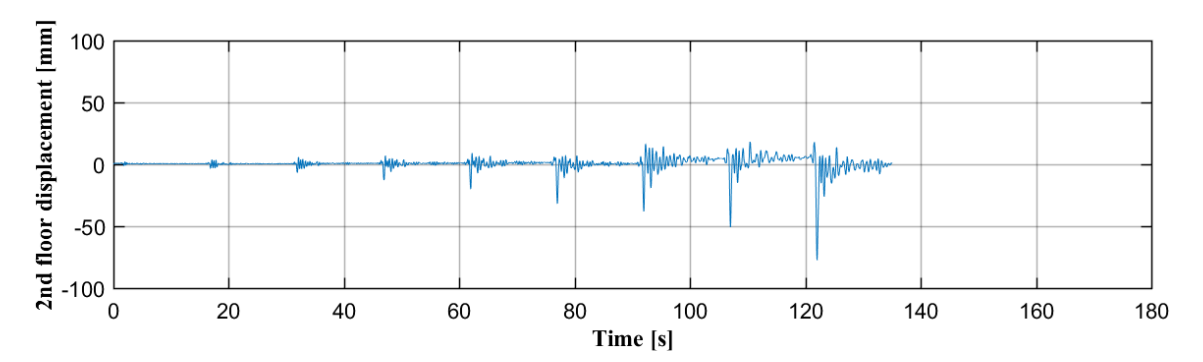


Figure 6.13: Resulted relative displacement at the second floor

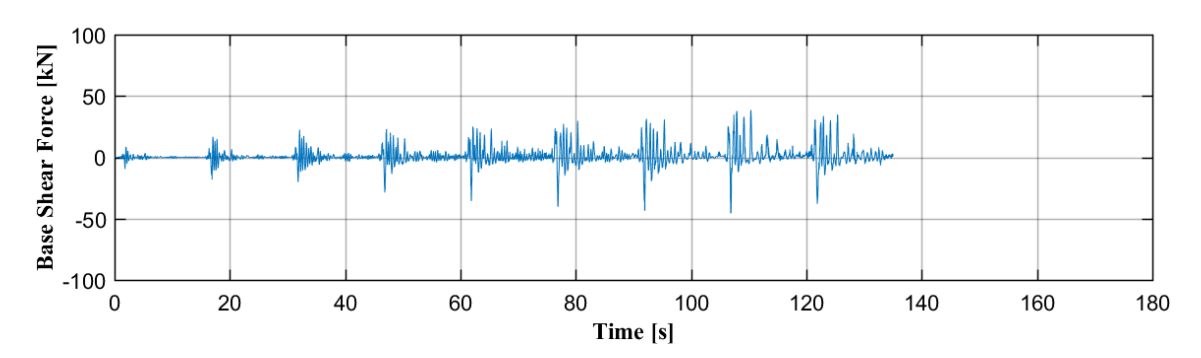
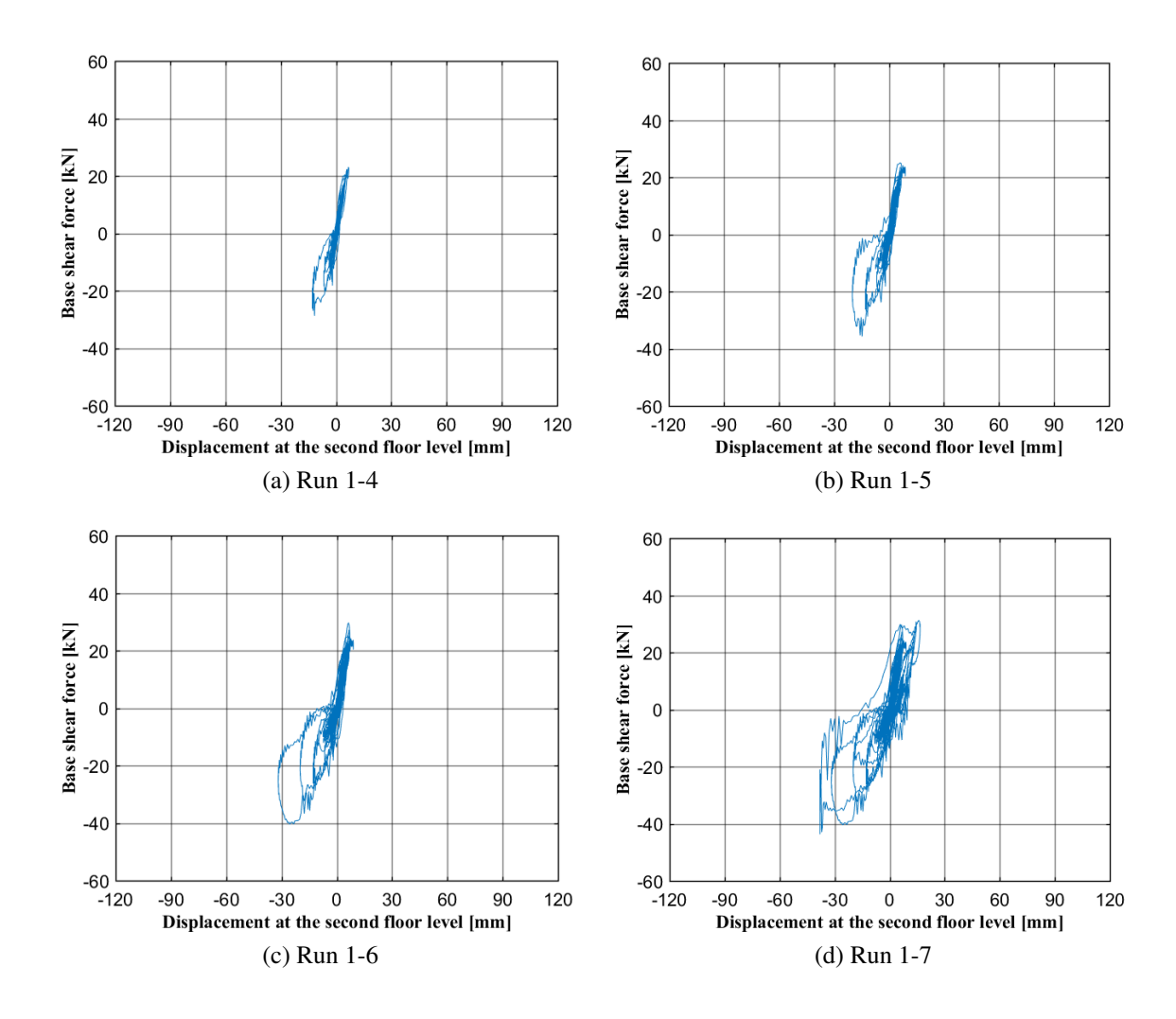


Figure 6.14: Resulted base shear force of the house

The maximum displacement in -x direction increases with the enhanced seismic intensity. A maximum displacement of -77.0 mm is reached in Run 9. The peak base shear force in each run also increases gradually, but an obvious reduction is captured in the last run.

The hysteresis curves are also plotted for multiple stages during the loading history, as shown in Figure 6.15.



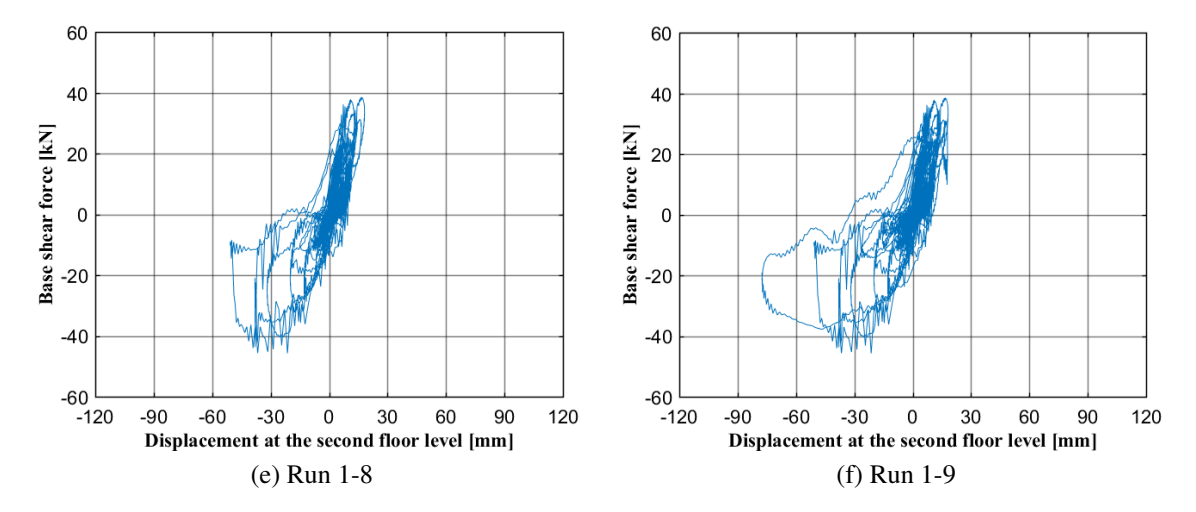


Figure 6.15: Hysteresis curves of the house model with time-history analysis

Run 1-4 (maximum: 0.15 g)

Figure 6.15 (a) gives the hysteresis curves from run 1 to run 4. Small displacements and base shear forces of the house are detected in the first three runs. The house stiffness does not yet show a clear reduction under these seismic intensities (0.10 g in run 3). However, a maximum base shear force of -28.71 kN in the negative direction is reached in run 4 (0.15 g), as well as some stiffness degradation and energy dissipation. This indicates the occurrence of damage in the model.

Run 5 (0.20 g), Run 6 (0.25 g)

Figure 6.15 (b) and (c) show the hysteresis curves from run 1 to run 5 and run 6, respectively. The maximum displacement and base shear force keep increasing in these two runs. The maximum displacements are -19.94 mm in run 5 and -31.82 mm in run 6. Likewise, the peak base shear force is -35.70 in run 5 kN and -40.42 kN in run 6.

Run 7 (0.30 g), Run 8 (0.35 g)

The hysteresis curves from run 1 to run 7 and 8 are shown in Figure 6.15 (d) and (e), respectively. Run 7 displays a more severe stiffness deterioration when the house reaches a displacement around -40.0 mm. As a result, the maximum base shear force increases more slowly in these two runs, reaching -45.69 kN in run 8 (0.35 g).

Run 9 (0.40 g)

A maximum displacement of -77.50 mm is reached in run 9, but the base shear capacity decreases to around -37 kN under the seismic load of this intensity, as shown in Figure 6.15 (f). Considerable energy dissipation is also observed from the hysteresis curves.

Run 10 (0.50 g), Run 11 (0.62 g) and Run 12 (0.75 g)

In the negative loading direction, the model shows severe damages after run 9 and the numerical results are already heavily ill-behaved in run 10. Therefore, the model is assumed to be collapsed

at the beginning of run 10.

6.4.2 Crack evolution

The crack patterns of the house model are presented at the maximum displacements of each run here, like for results in +x direction discussed in the section 6.3.2. Crack patterns at the maximum layer of element thickness can be found in Appendix D.

Run 1-4 (maximum: 0.15 g)

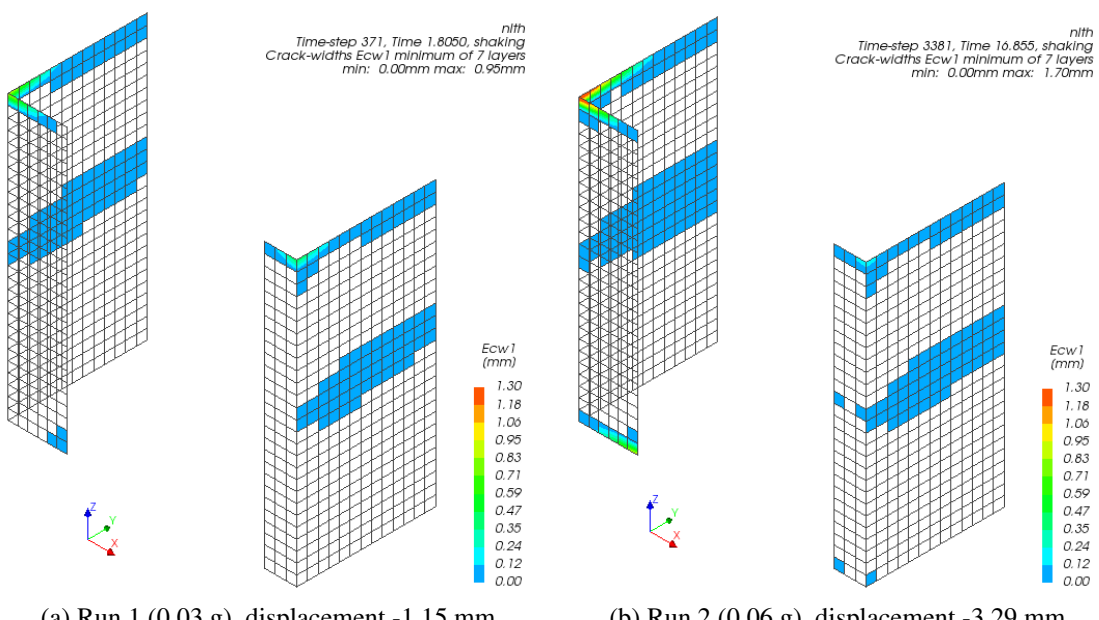
Figure 6.16 shows the crack patterns at the maximum displacements of run 1 to run 4.

Horizontal cracks form along the bottom of the wide pier due to rocking. These cracks develop further with the increased seismic load. At the maximum displacement in run 4 (0.15 g), a fully opened crack is observed at the bottom of wide pier. The rocking mechanism of the narrow pier is also active in this run. Additionally, small cracks develop on the transversal walls as well at the ground floor level.

Run 5 (0.20 g), Run 6 (0.25 g)

Figure 6.17 shows the obtained crack widths at Run 5 and 6.

The horizontal cracks formed previously at the bottom of the wide pier develop further. Larger cracks are also detected at the top of both piers. Flexural cracks triggered by a two-way out-ofplane mechanism are found in the transversal walls at the ground floor level. When reaching the displacement of -31.82 mm in run 6, relatively small cracks are observed along the bottom of right transversal wall, which is caused by rocking of the house model.



(a) Run 1 (0.03 g), displacement -1.15 mm

(b) Run 2 (0.06 g), displacement -3.29 mm

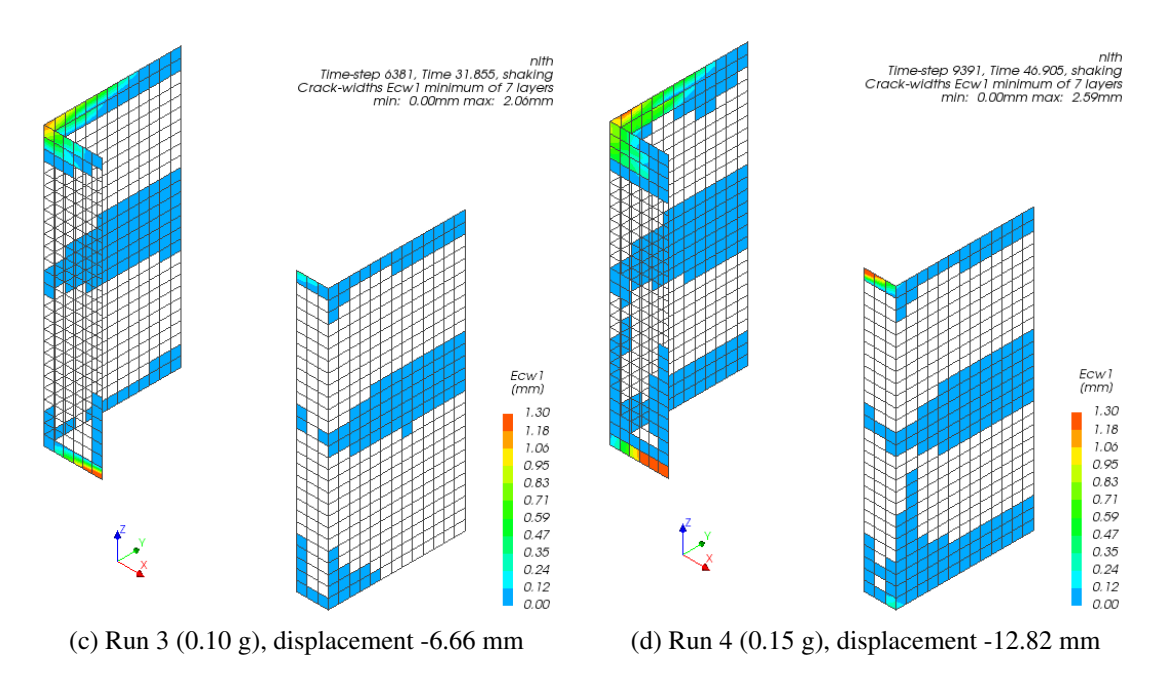


Figure 6.16: Crack width at the maximum displacement of run 1 to run 4

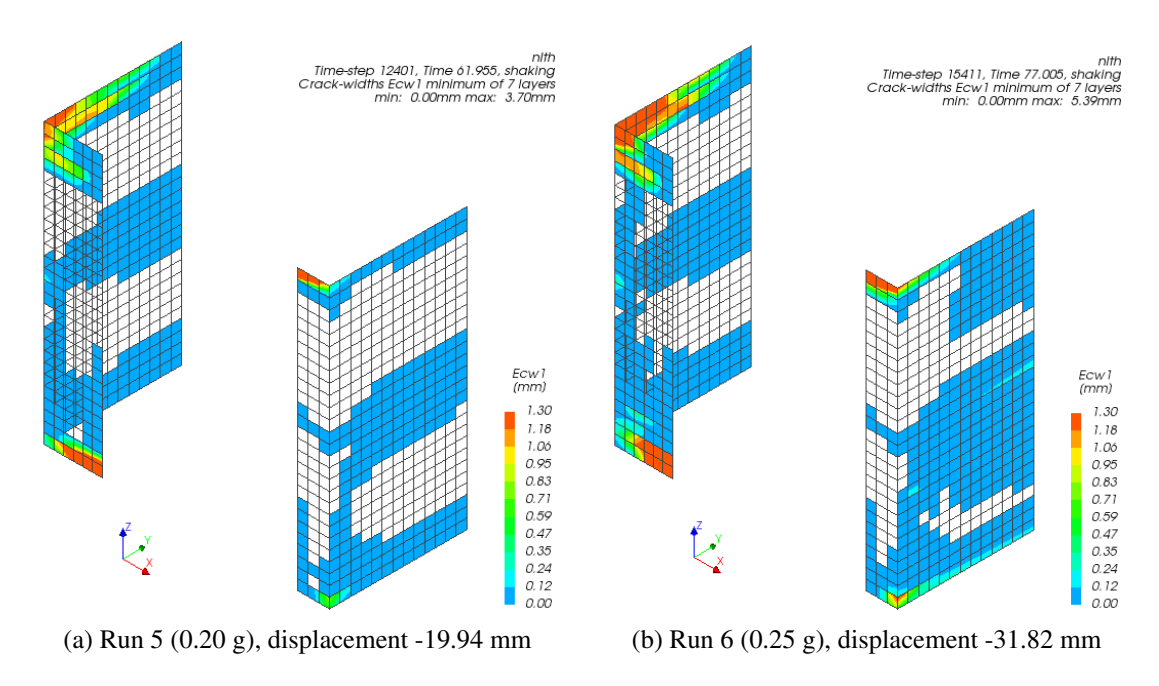


Figure 6.17: Crack width at the maximum displacement of run 5 and run 6

Run 7 (0.30 g), Run 8 (0.35 g)

Figure 6.18 (a) and (b) show the crack patterns at the maximum displacements under the seismic load run 7 and run 8, respectively.

The main damages are still localized at the bottom of the wide pier. The cracks at the top of the piers also develop further. The cracks in the transversal walls are mostly located at the intermediate height and the bottom of the walls, especially at the maximum layer of element thickness (Figure D.18 and D.19 in Appendix D). However, cracks are also observed developing from the edges to the center of the wall, which indicates a two-way out-of-plane crack pattern.

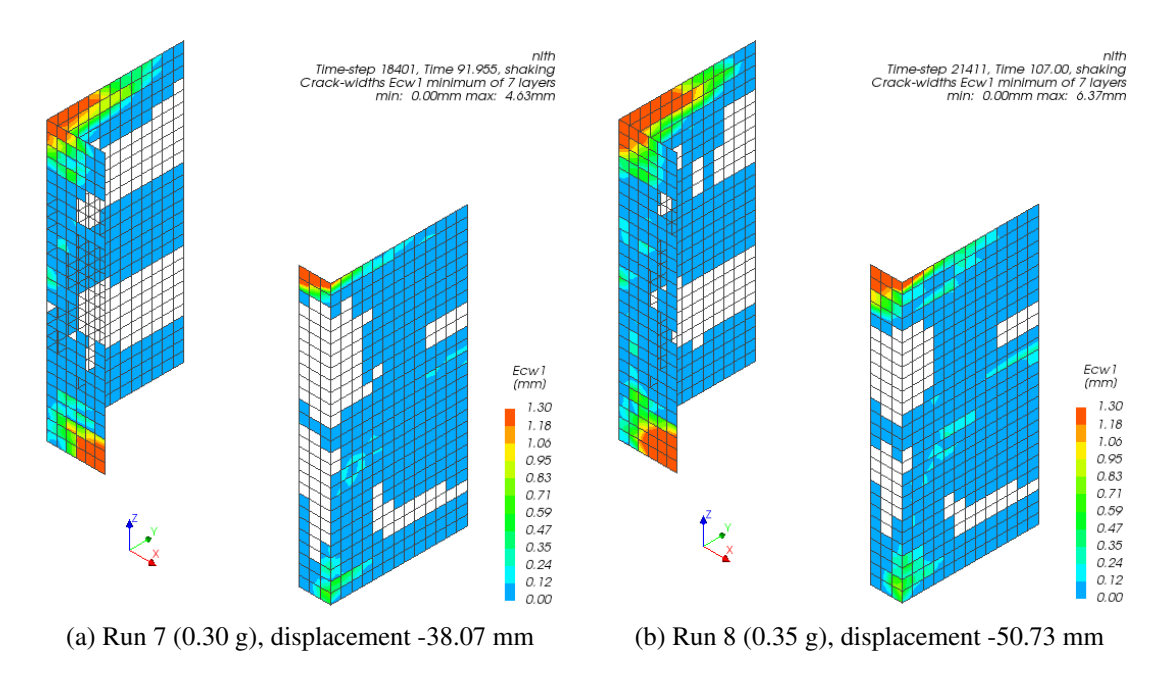


Figure 6.18: Crack width at the maximum displacement of run 7 and run 8

Run 9 (0.40 g)

Figure 6.19 presents the crack patterns at the maximum displacement under seismic load run 9.

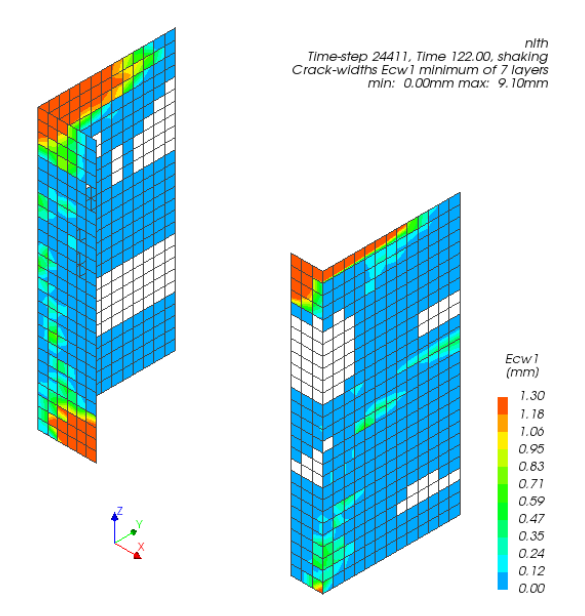


Figure 6.19: Crack width at the maximum displacement of run 9 (0.40 g), displacement -77.50 mm

More cracks are observed over the height of the wide pier, which leads to a reduction in its cross-section. The development of these cracks agrees with the decrease in base shear capacity in run 9.

Flexural cracks on the transversal wall connected to the narrow pier also develop further.

6.4.3 Drifts

The maximum drifts of the two floors in each run are calculated and presented in Figure 6.20.

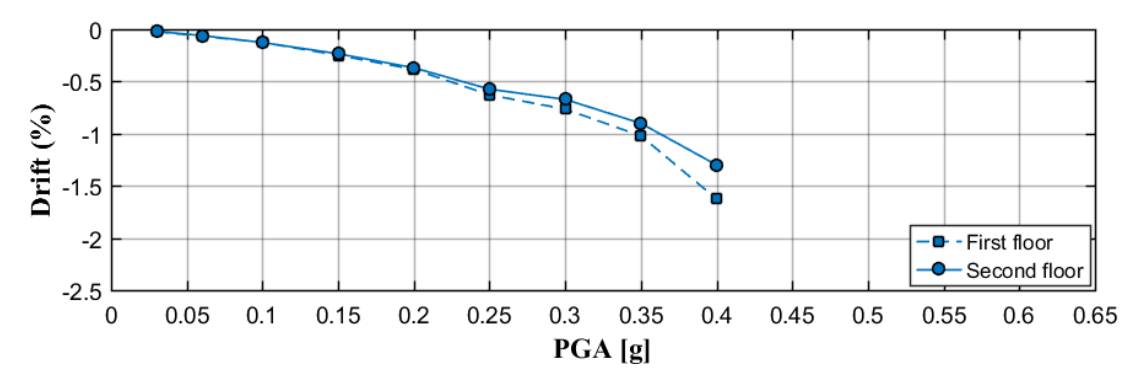


Figure 6.20: Maximum drifts of the two floors in each run

Similar drift results are observed in the negative direction. The drifts of the two floors are almost identical in the first five runs. A larger first floor drift is found since run 6 (0.25 g) due to severe damage of the wide pier and crack formation in the transversal wall.

A maximum drift value of 1.6% at the first floor and 1.3% at the second floor are reached in run 9 (0.40 g). These values are compared to the calculated drift limits per Eurocode 8 in Table 6.4, showing that the first floor is near the limit state of severe damage.

Case		Drift (%)	
		Wide piers	Narrow piers
Numerical	First floor - negative	1.6 1.3	
(0.40 g)	Second floor - negative		
Eurocode 8	Limit state of severe damage	1.9	3.6
	Limit state of near collapse	2.6	4.8

Table 6.4: Comparison of the drifts in Run 9 (negative direction)

Chapter 7

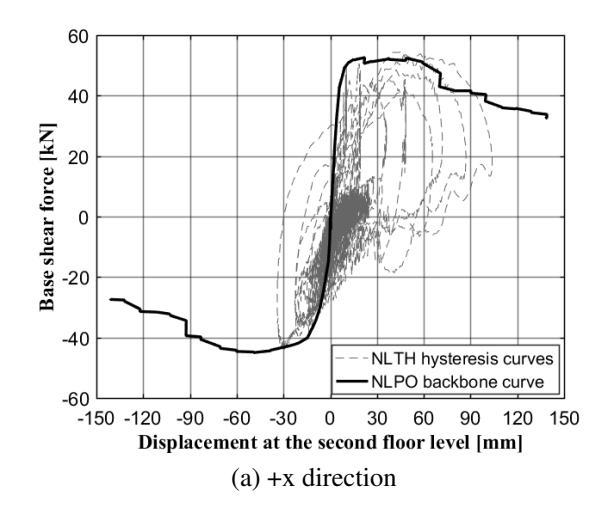
COMPARISON AND DISCUSSION

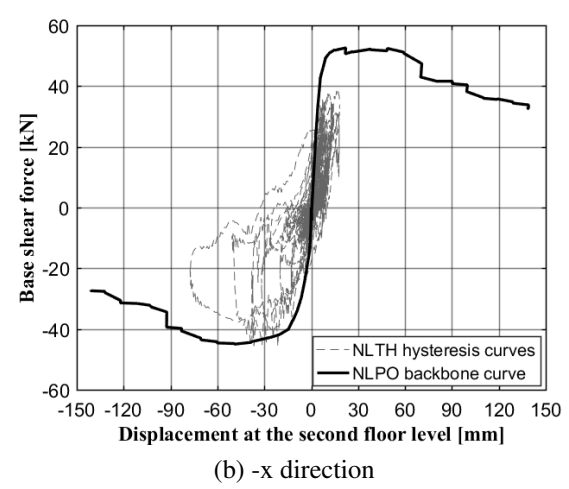
This chapter presents the comparison between the nonlinear pushover and nonlinear time-history analyses results of the studied masonry house. The results are mainly compared in terms of structural capacities and failure mechanisms. Section 7.1 compares the capacity curves of the house model obtained in these two analyses. Section 7.2 discusses the failure modes based on the crack patterns presented in Chapter 5 (nonlinear pushover analysis) and Chapter 6 (nonlinear time-history analysis).

7.1 Structural Capacity

First, the hysteresis curves from the nonlinear time-history analyses are plotted together with the pushover backbone curve in Figure 7.1. The results are also presented separately for the positive and negative loading directions (Figure 7.1 (a) and (b)). The asymmetric behavior of the house model for positive and negative loading is captured in the dynamic analysis.

In order to clearly compare the structural capacity of the masonry house under the performed quasi-static and dynamic loading, an interpretation of the IDA results is necessary to get the representative base shear-second floor displacement relationship. Generally, two different criteria can be employed: a) maximum displacement in each IDA run versus the corresponding base shear force and b) maximum base shear force reached in each run versus the corresponding displacement.





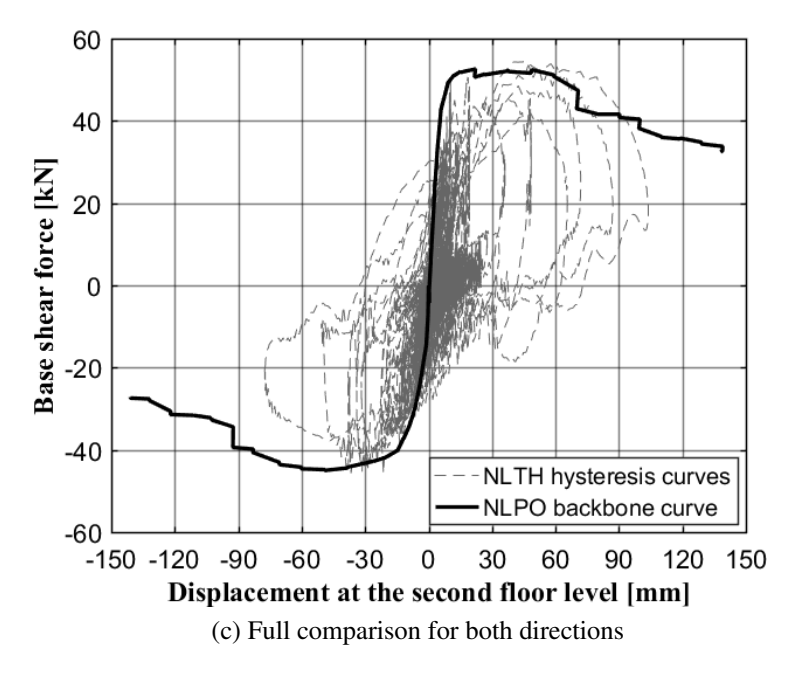


Figure 7.1: Time-history hysteresis curves vs. Pushover backbone curve

Here, the goal is to compare the dynamic response to the pushover backbone curve, where the deformation capacity is an important assessment criterion. For this comparison, it is customary to match the maximum displacement in each IDA run with its associated base shear force. However, it is observed that in the last few runs of the IDA with a high amplitude signal, the base shear force at the maximum displacement of each run is much lower than the actual maximum force that has been reached.

To obtain a more realistic dynamic capacity curve, Ferracuti, Pinho, Savoia, and Francia (2009)

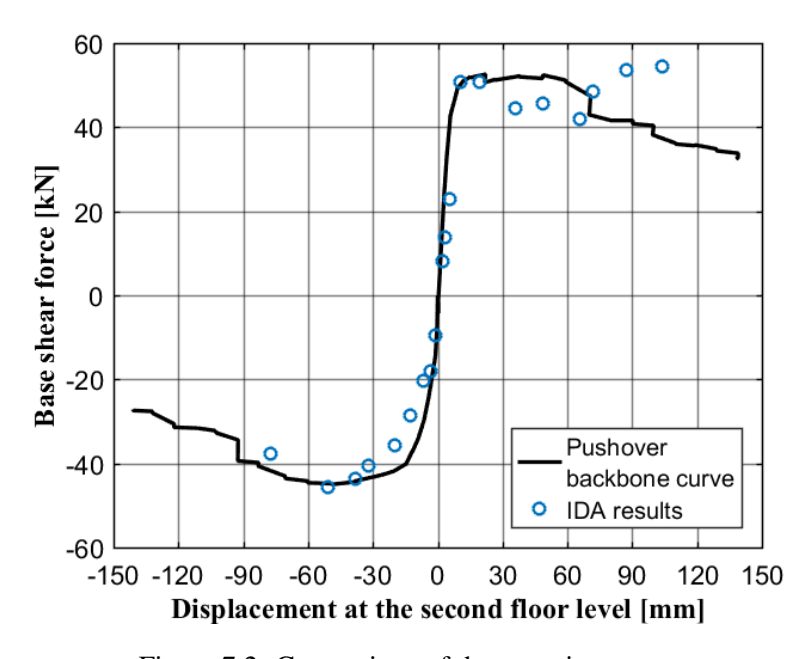


Figure 7.2: Comparison of the capacity curves

proposed a method by selecting the maximum displacement attained during a given dynamic analysis and the corresponding maximum base shear found inside a time-window of ± 0.25 s. Under this methodology, the base shear-second floor displacement relationship of the masonry house under dynamic loading is obtained and compared to the pushover curve in Figure 7.2.

Figure 7.2 shows very close agreement between the base shear-second floor displacement relations in both analyses. A maximum base shear force of +54.4 kN is reached in positive loading in the dynamic time-history analysis, which is only 3% higher than the value obtained in the pushover analysis. In the negative loading direction, the same peak base shear force of -45 kN is obtained. However, a smaller maximum displacement is found in the dynamic analysis for both directions. It is noted that the smaller displacement capacity may be affected by the accumulation of the damages in the IDA.

Overall, for the studied masonry house under this earthquake loading, the nonlinear pushover analysis is capable of properly estimating the base shear capacity but overestimating the deformation capacity.

7.2 Failure Mechanism

Generally, the same rocking and toe crushing failure mechanism is observed in both quasi-static pushover and dynamic time-history analyses.

The rocking mechanism leads to horizontal cracks in both masonry piers. These cracks develop further under the increased horizontal load, leading to a degradation of the stiffness and capacity of the house model in both positive and negative loading directions. In both analyses, the failure of the structure is governed by the damages of the wide piers, especially for the negative loading. Moreover, they both capture the flange effects of the transversal walls caused by the use of running bond. The two-way out-of-plane mechanism of the transversal walls is triggered by the running bond as well. However, the corresponding diagonal crack patterns are not clearly shown in both analyses. To further investigate this behavior, a finite element house model using 3D solid elements or micro-modeling method can be employed.

On the other hand, differences in the crack patterns are still observed. The damages in the nonlinear pushover analysis are more concentrated along the top and bottom of the masonry piers, while in the nonlinear time-history analysis, although the main damage is still localized at the top and bottom of the piers, more distributed cracks can be found in the wide pier and transversal walls. Therefore, a very large maximum crack width is observed in the last few loading cycles of the nonlinear pushover analysis. Figure 7.3 provides the crack patterns at the same displacement from both pushover and time-history analyses. The main crack with a maximum crack width of 38.88 mm is observed along the bottom of the pier in the pushover analysis. While in the time-history analysis the maximum crack width is 12.63 mm, and more sub-cracks are found over the masonry piers and walls.

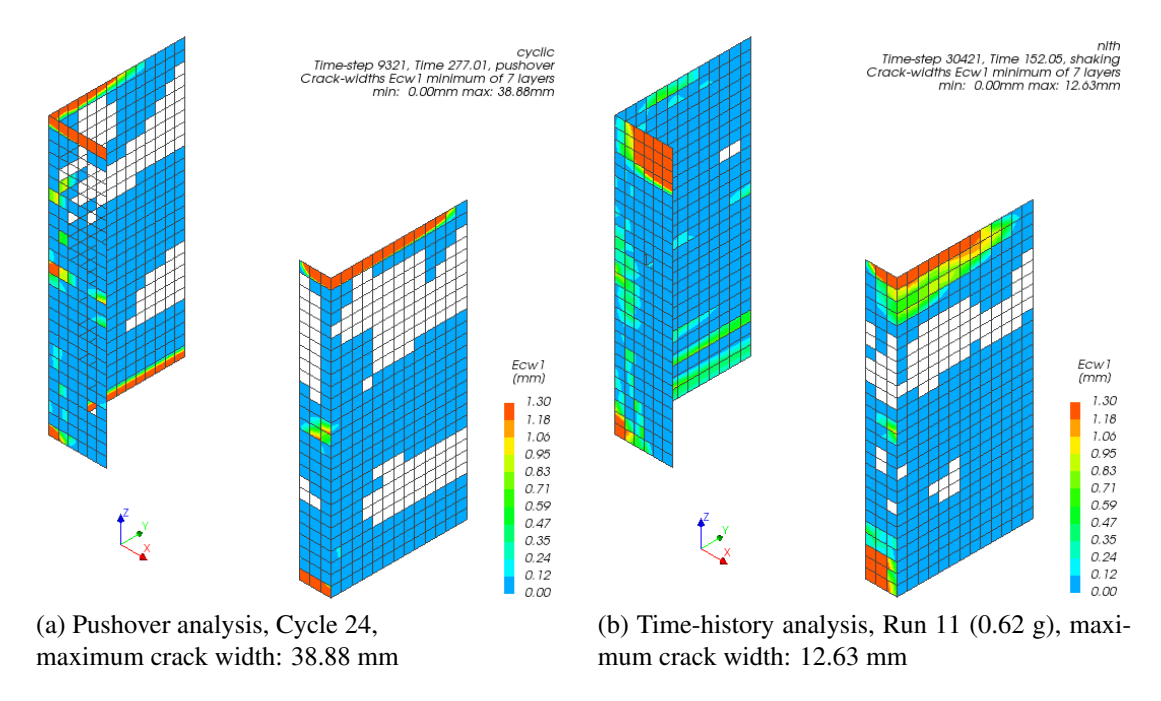


Figure 7.3: Comparison of crack patterns (same scale) at displacement +104 mm

Chapter 8

CONCLUSIONS AND RECOMMENDATIONS

8.1 Conclusions

Prior to this research, a quasi-static cyclic pushover test was carried out on a full-scale CS brick masonry assemblage at TU Delft. The specimen is representative of a typical terraced house built with unreinforced masonry in the northern part of the Netherlands. In this research, the masonry assemblage was modeled numerically and analyzed via nonlinear pushover and time-history analyses in DIANA FEA 10.2, to investigate its seismic response and to evaluate the efficiency of using pushover method for this structure.

The recently developed Engineering Masonry model implemented in DIANA FEA 10.2 was used for modeling masonry. First, a single masonry pier was modeled to assess the suitability of this constitutive model to replicate the experimental behavior of calcium silicate masonry walls.

Then, the finite element model of the masonry assemblage was built. Both monotonic and cyclic nonlinear pushover analysis were performed on the model. The seismic response of the house model under cyclic pushover load is discussed and compared thoroughly with the experimental results. A sensitivity study based on the monotonic pushover analysis was further completed to investigate the influence of the most relevant masonry properties on the structural behavior.

Finally, a nonlinear time-history analysis was performed on the model using the incremental dynamic analysis method. The time-history analysis results are compared to the nonlinear pushover analysis results to validate the accuracy and applicability of the pushover method to evaluate the seismic behavior for this type of masonry structure.

From the aforementioned studies, the following conclusions are drawn:

• The engineering masonry model can simulate the masonry flexural behavior better than the total strain crack model. In the pushover analysis of the single masonry pier, the total strain crack model leads to divergence problems at an early stage. The engineering masonry model is capable of capturing its structural behavior more comprehensively, especially under cyclic loading conditions.

- The test results of the masonry assemblage were properly reproduced by the nonlinear pushover analysis in terms of:
 - The capacity curve. Both results exhibit similar peak base shear forces and an asymmetric capacity curve. However, the numerical results display higher ductility (slower softening) along the positive loading direction.
 - An accumulation of inelastic deformation in the positive direction, observed both numerically and experimentally.
 - The rocking mechanism and associated horizontal cracks at the top and bottom of both masonry piers.
 - The damages of the wide piers govern the failure of the structure.
 - Flange effects of the transversal walls are found due to the use of running bond.
 - On the other hand, some discrepancies are still observed in the numerical analysis, which are mainly the non-clear diagonal crack failure in the wide pier and the nonclear crack pattern in the transversal walls associated with the two-way out-of-plane mechanism.
- The sensitivity study shows that the softening behavior of the house model is directly related to the masonry compressive strength f_c . The occurrence of crushing damage of the piers leads to the redistribution of compressive stress within the pier and therefore reduces the level arm and the base shear capacity of the model. The initial shear strength $f_{\nu 0}$ also has an influence on the model behavior. However, no direct relation between the masonry compressive fracture energy G_{fc} and its post-peak behavior was observed.
- The incremental dynamic analysis provides similar base shear capacity and failure mechanism as the nonlinear pushover analysis. However, the obtained maximum displacement is smaller in both loading directions. Overall, for the studied masonry house, the pushover method is capable of properly estimating the base shear capacity but the deformation capacity might be overestimated.

8.2 Recommendations

On the basis of the presented conclusions and the assumptions made previously in this project, the following recommendations are of interest for further research on the topic:

- Further sensitivity studies can be conducted to investigate the influence of material parameters on the seismic response of the masonry structure.
- A more detailed modeling strategy (e.g. using 3D solid elements and micro-modeling) can be considered to better reproduce the crack patterns and to further investigate the effects of the structural details (e.g. running bond, shear connectors) on the house behavior.
- Because the studied masonry house is built in the Netherlands, where the soil conditions are
 often poor, it is recommended to include soil-structure interaction in the model.
- Other variations could be performed for the nonlinear time-history analysis, for instance applying the scaled earthquake signals separately without damage accumulation.

- The incremental dynamic analysis is conducted with a single earthquake signal in this project. As the earthquake characteristics may influence the seismic responses of the structure, it is recommended to apply IDA with multiple different earthquake signals to get the average IDA results.
- Other pushover analyses can be performed on this model as well, e.g. mode proportional pushover analysis and adaptive pushover analysis. The efficiencies of different pushover analyses on studying the seismic behavior for this type of masonry structure can be evaluated through comparisons with the IDA results.
- A similar procedure can be adopted to study other building typologies, or for the same typologies with different details (e.g. connection at corners or type of masonry).

Bibliography

- EN-1996-1-1. (2005). Eurocode 6 design of masonry structures part 1-1: general rules for reinforced and unreinforced masonry structures.
- EN-1998-3. (2005). Design of structures for earthquake resistance part 3: assessment and retrofitting of buildings.
- Backes, H. (1985). On the behavior of masonry under tension in the direction of the bed joints. *Dissertation, Aachen University of Technology, Aachen, Germany.*
- Binda, L., Fontana, A., & Frigerio, G. (1988). Mechanical behaviour of brick masonries derived from unit and mortar characteristics. *Brick and Block Masonry*(8 th IBMAC) London, Elsevier Applied Science, 1, 205–216.
- Bracci, J. M., Kunnath, S. K., & Reinhorn, A. M. (1997). Seismic performance and retrofit evaluation of reinforced concrete structures. *Journal of Structural Engineering*, 123(1), 3–10.
- Brincker, R. (1984). Yield-line theory and material properties of laterally loaded masonry walls. *MASONRY INT. Masonry Int.* (1), 8.
- Calderini, C., Cattari, S., & Lagomarsino, S. (2009). In-plane strength of unreinforced masonry piers. *Earthquake Engineering & Structural Dynamics*, 38(2), 243–267.
- D'Ayala, D. & Speranza, E. (2003). Definition of collapse mechanisms and seismic vulnerability of historic masonry buildings. *Earthquake Spectra*, 19(3), 479–509.
- Dhanasekar, M., Page, A., & Kleeman, P. (1985). The failure of brick masonry under biaxial stresses. *Proceedings of the Institution of Civil Engineers*, 79(2), 295–313.
- Esposito, R., Jafari, S., Ravenshorst, G., Schipper, H., & Rots, J. (2018, February). Influence of the behaviour of calcium silicate brick and element masonry on the lateral capacity of structures. In *In proceedings of 10th australiasian masonry conference (amc)* (pp. 11–14). Sydney, Australia.
- Esposito, R., Messali, F., & Rots, J. G. (2016). *Material characterisation of replicated masonry and wall ties*. Delft University of Technology. Final report, 18 April 2016.
- Esposito, R. & Ravenshorst, G. (2017). *Quasi-static cyclic in-plane tests on masonry components* 2016/1017 (tech. rep. No. C31B67WP3-4). Delft University of Technology. Version 1, 10 August 2017.
- Fajfar, P. [P.]. (1999). Capacity spectrum method based on inelastic demand spectra. *Earthquake Engineering and Structural Dynamics*, 28, 979–993.
- Fajfar, P. [Peter]. (2000). A nonlinear analysis method for performance-based seismic design. *Earthquake spectra*, 16(3), 573–592.
- Feenstra, P., Rots, J., Arnesen, A., Teigen, J., & Hoiseth, K. (1998). A 3d constitutive model for concrete based on a co-rotational concept.
- Ferracuti, B., Pinho, R., Savoia, M., & Francia, R. (2009). Verification of displacement-based adaptive pushover through multi-ground motion incremental dynamic analyses. *Engineering Structures*, 31(8), 1789–1799.

108 BIBLIOGRAPHY

Graziotti, F., Tomassetti, U., Kallioras, S., Penna, A., & Magenes, G. (2017). Shaking table test on a full scale urm cavity wall building. *Bulletin of earthquake engineering*, *15*(12), 5329–5364.

- Krawinkler, H. & Seneviratna, G. (1998). Pros and cons of a pushover analysis of seismic performance evaluation. *Engineering structures*, 20(4-6), 452–464.
- Lourenco, P. B. (1996). *Computational strategies for masonry structures* (Doctoral dissertation, Delft University of Technology).
- Lourenço, P. B. (2002). Computations on historic masonry structures. *Progress in Structural Engineering and Materials*, 4(3), 301–319.
- Manie, J. (2017). User's manual release 10.2. DIANA FEA B.V.
- Meisl, C., Elwood, K., & Ventura, C. (2007). Shake table tests on the out-of-plane response of unreinforced masonry walls. *Canadian Journal of Civil Engineering*, *34*(11), 1381–1392.
- Groningen gasfield. (2016). Retrieved June 8, 2018, from http://www.nlog.nl/en/groningen-gasfield
- Types of Masonry Wall. (2017). Retrieved October 19, 2018, from http://www.acivilengineer.com/2017/04/Masonry-Wall-Types.html
- Panyakapo, P. (2014). Cyclic pushover analysis procedure to estimate seismic demands for buildings. *Engineering Structures*, 66, 10–23.
- Ravenshorst, G., Esposito, R., Schipper, R., Messali, F., Tsouvalas, A., Louren, E., & Rots, J. (2016). *Structural behaviour of a calcium silicate brick masonry assemblage: quasi-static cyclic pushover and dynamic identification test*. Delft University of Technology. Version 5, 21 October 2016.
- Rots, J. (1991). Numerical simulation of cracking in structural masonry. Heron, 36(2), 49-63.
- Rots, J., Messali, F., Esposito, R., Jafari, S., & Mariani, V. (2016). Computational modeling of masonry with a view to groningen induced seismicity. In *10th international conference on structural analysis of historical constructions*, *sahc* (pp. 13–15).
- Schreppers, G., Garofano, A., Messali, F., & Rots, J. (2017). *Diana validation report of masonry modelling* (tech. rep. No. CM-2016-17). Delft University of Technology. 15 February 2017.
- Stockl, S., Bierwirth, H., & Kupfer, H. (1994). The influence of test method on the results of compression tests on mortar. In *Proc. 10th int. brick and block masonry conf* (pp. 1397–1406).
- Vamvatsikos, D. & Cornell, C. A. (2002). Incremental dynamic analysis. *Earthquake Engineering & Structural Dynamics*, 31(3), 491–514.
- Van der Pluijm, R. [R.]. (1992). Material properties of masonry and its components under tension and shear. In *Proceedings 6th canadian masonry symposium*, 15-17 june 1992, saskatoon, canada (pp. 675–686). University of Saskatchewan.
- Van der Pluijm, R. [Rob], Hamid, A. A., & Harris, H. G. (1993). Shear behaviour of bed joints. In 6th north american masonry conference, 6-9 june 1993, philadelphia, pennsylvania, usa (pp. 125–136). Technomic Publ. Co.
- Wesche, K. & Ilantzis, A. (1980). General recommendations for methods of testing loadbearing walls. *Mater. Struct./Res. Test.* 13(78), 433.

Appendices

Appendix A

Results of the Masonry Pier

This chapter presents the pushover curves of the masonry pier models which are built in Engineering Masonry model with different head-joint options.

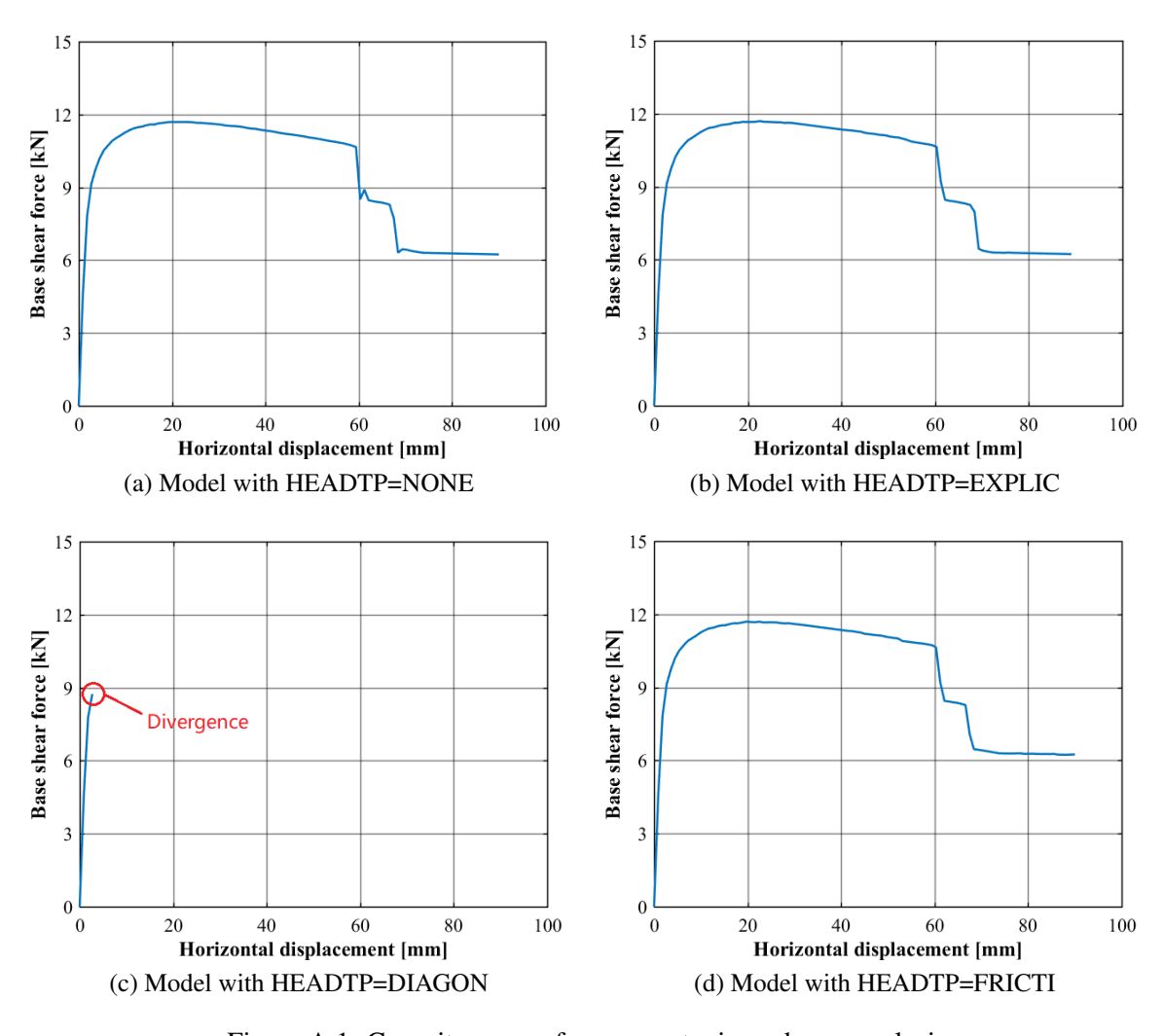


Figure A.1: Capacity curves from monotonic pushover analysis

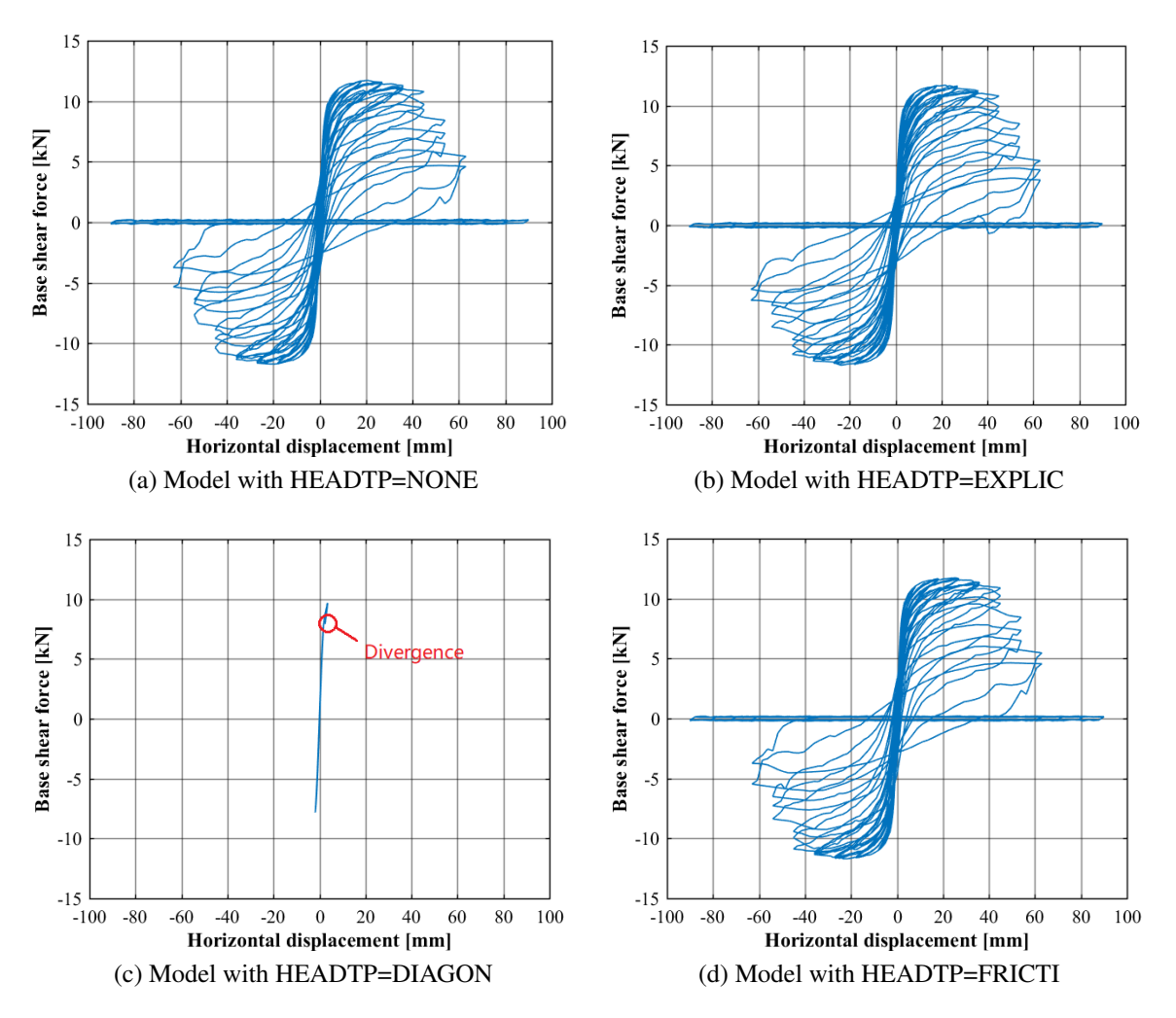


Figure A.2: Capacity curves from cyclic pushover analysis

Appendix B

Geometrically Nonlinear Effect on Pushover Results

The geometrically nonlinear effect on the pushover results of the house model is discussed here. As described in Chapter 5, a monotonic pushover analysis including the geometrically nonlinear effect was performed on the built house model. Similarly, a monotonic pushover analysis excluding the geometrically nonlinear effect is carried out, and all other analysis parameters remain unchanged.

Figure B.1 provides the obtained capacity curves for both cases.

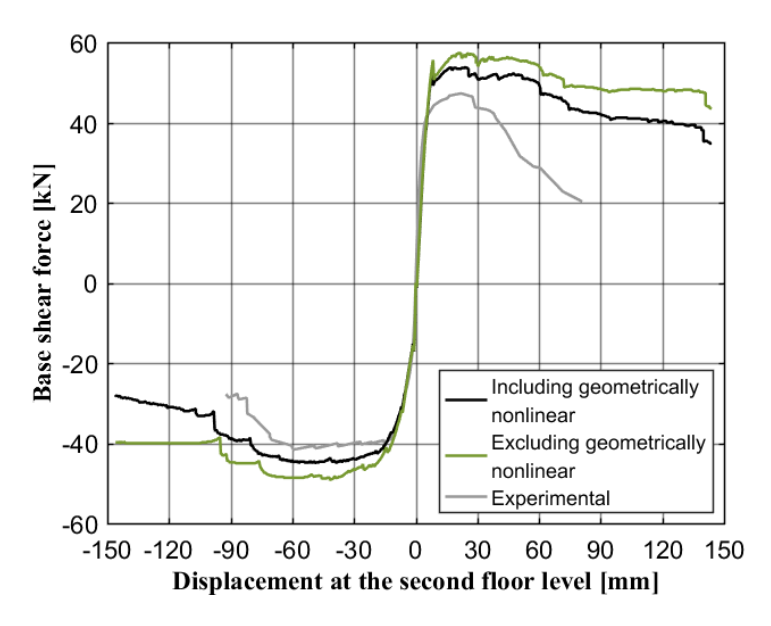


Figure B.1: Capacity curves

Figure B.1 shows that including the geometrically nonlinear effect leads to an obvious decrease in the base shear force for both loading directions. The difference between including and excluding geometrically nonlinear effect becomes larger with the increase of applied displacement loading. Thus, it is validated that the second effect plays an important role in the house behavior and the geometrically nonlinear effect should be included in the nonlinear pushover analysis.

114	APPENDIX B.	GEOMETRICALLY NONLINEAR EFFECT ON PUSHOVER RESULTS	

Appendix C

Results of Nonlinear Pushover Analysis

The detailed damage patterns and stress/strain distributions of the house model in the cyclic pushover analysis are presented. The crack widths and crushing pattern of the masonry are shown at both the minimum and maximum layer over element thickness.

Like in the section 5.3, results are presented at the end of the pseudo-linear stage (Cycle 8), at the positions of the peak base shear forces (Cycle 15 and 18)¹, at the position after 20% reduction of base forces has been reached (Cycle 22) and at the last loading cycle (Cycle 27) in both directions.

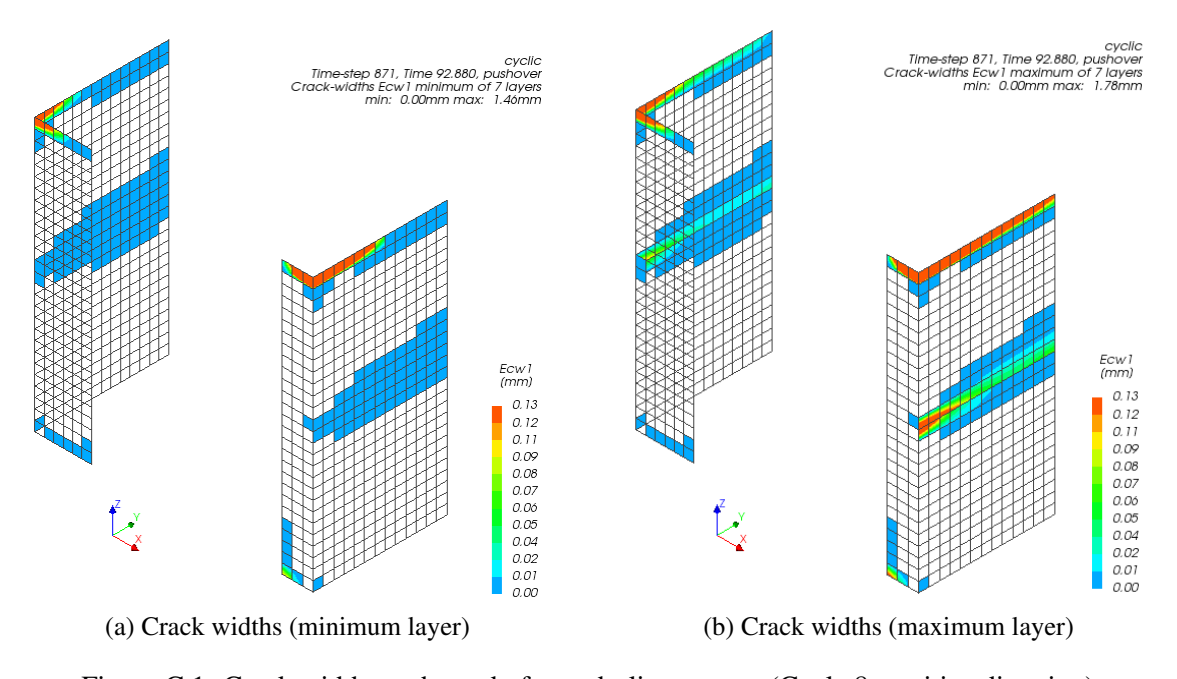


Figure C.1: Crack widths at the end of pseudo-linear stage (Cycle 8, positive direction)

¹Cycle 15 in the positive loading direction, and Cycle 18 in the negative loading direction.

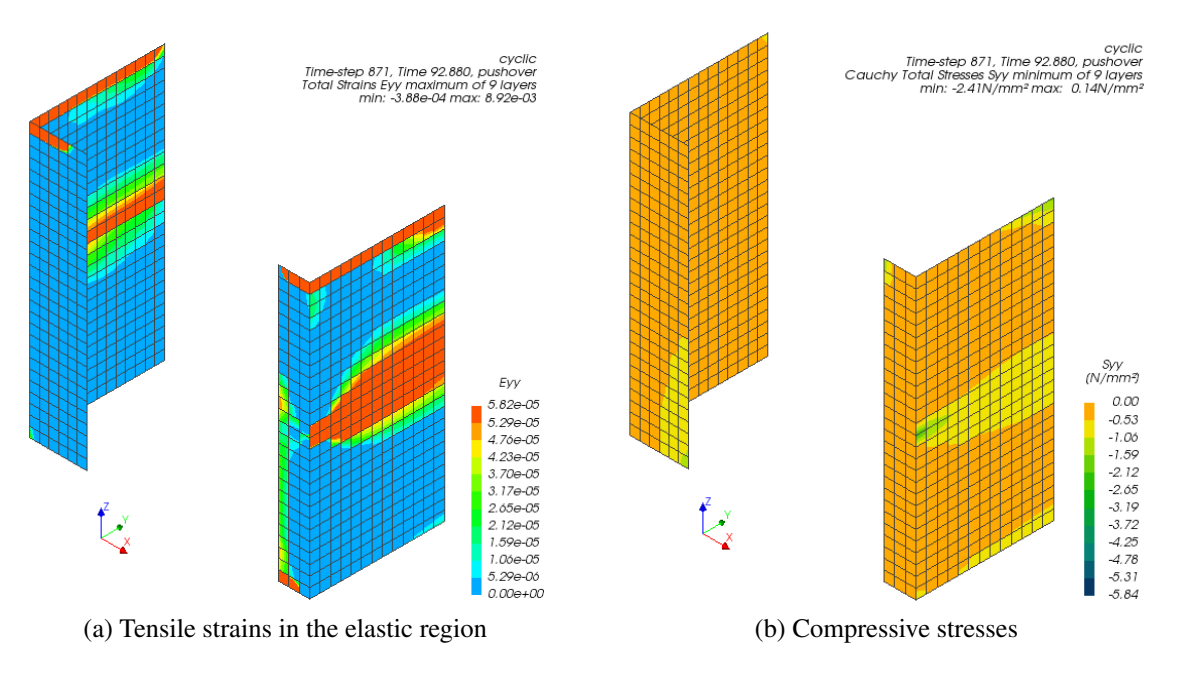


Figure C.2: Stress/strain at the end of pseudo-linear stage (Cycle 8, positive direction)

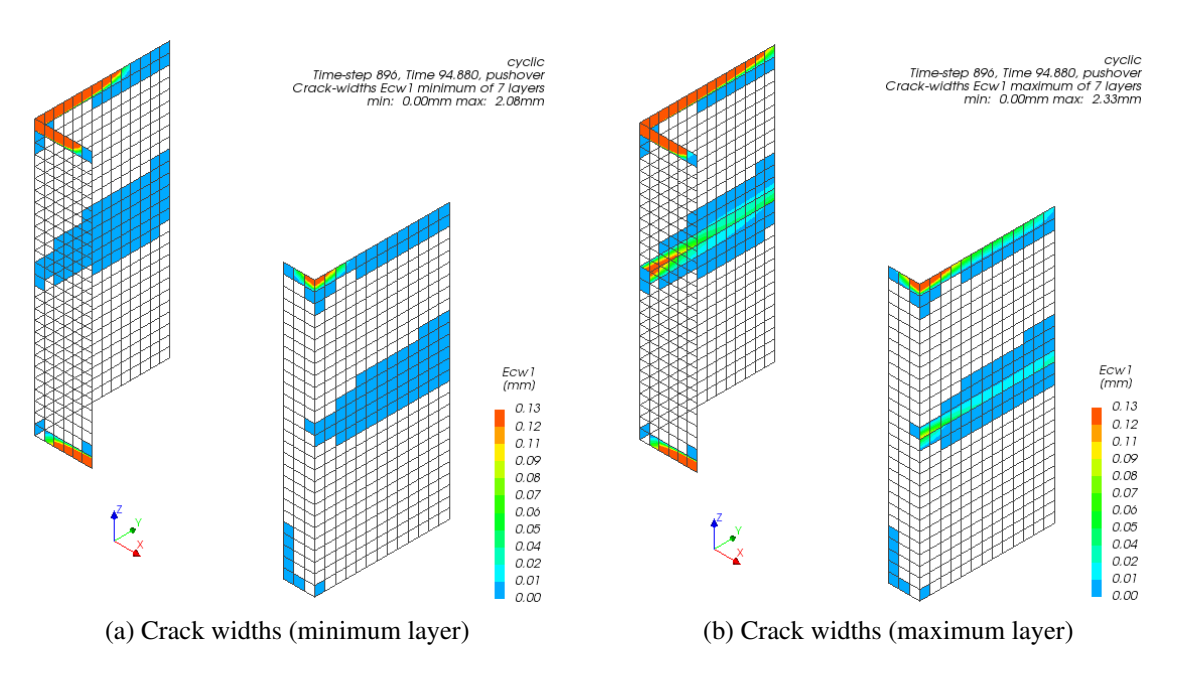


Figure C.3: Crack widths at the end of pseudo-linear stage (Cycle 8, negative direction)

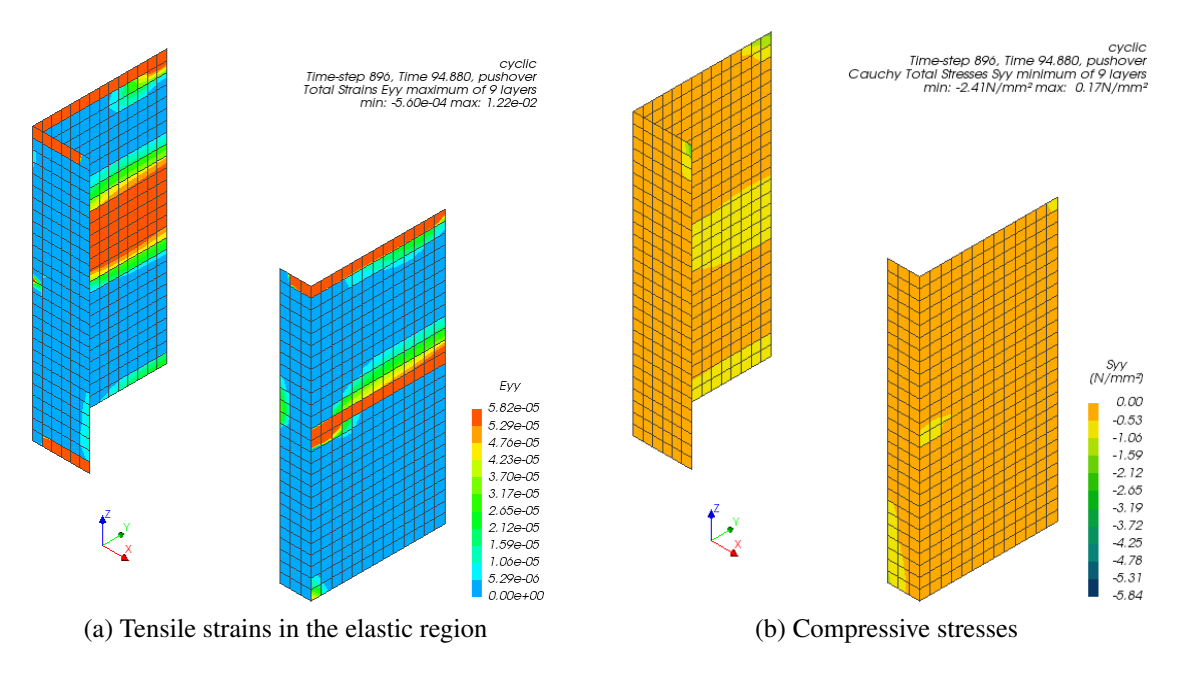


Figure C.4: Stress/strain at the end of pseudo-linear stage (Cycle 8, negative direction)

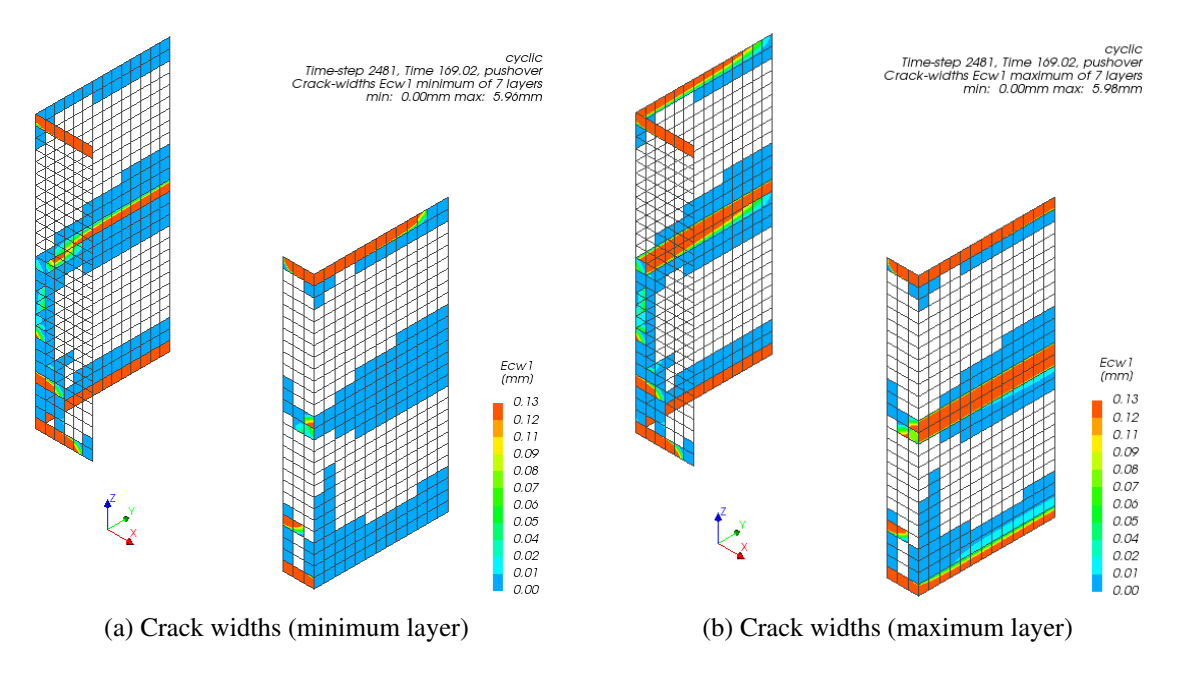


Figure C.5: Crack widths at the peak base shear capacity (Cycle 15, positive direction)

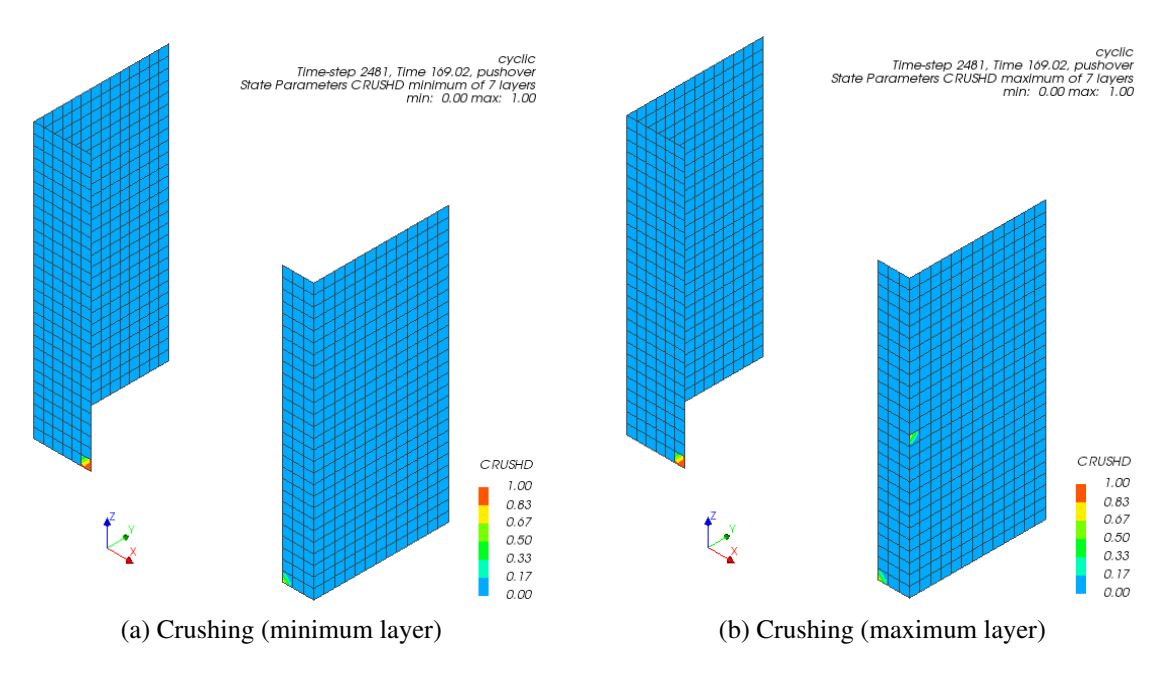


Figure C.6: Crushing at the peak base shear capacity (Cycle 15, positive direction)

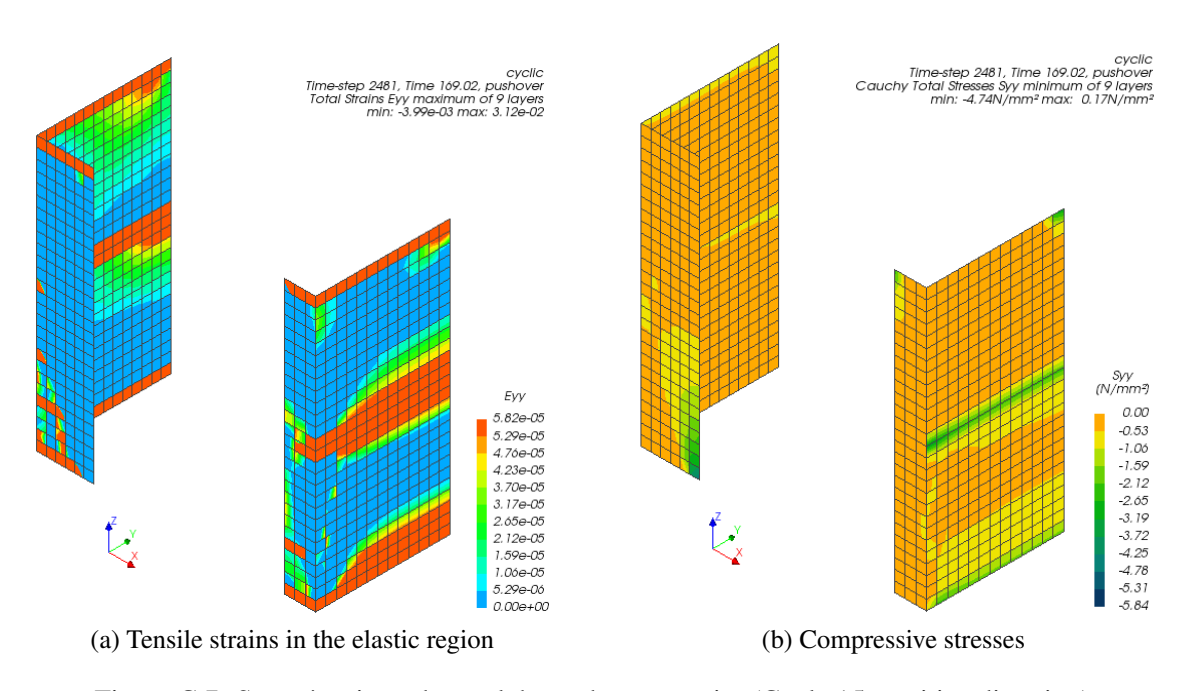


Figure C.7: Stress/strain at the peak base shear capacity (Cycle 15, positive direction)

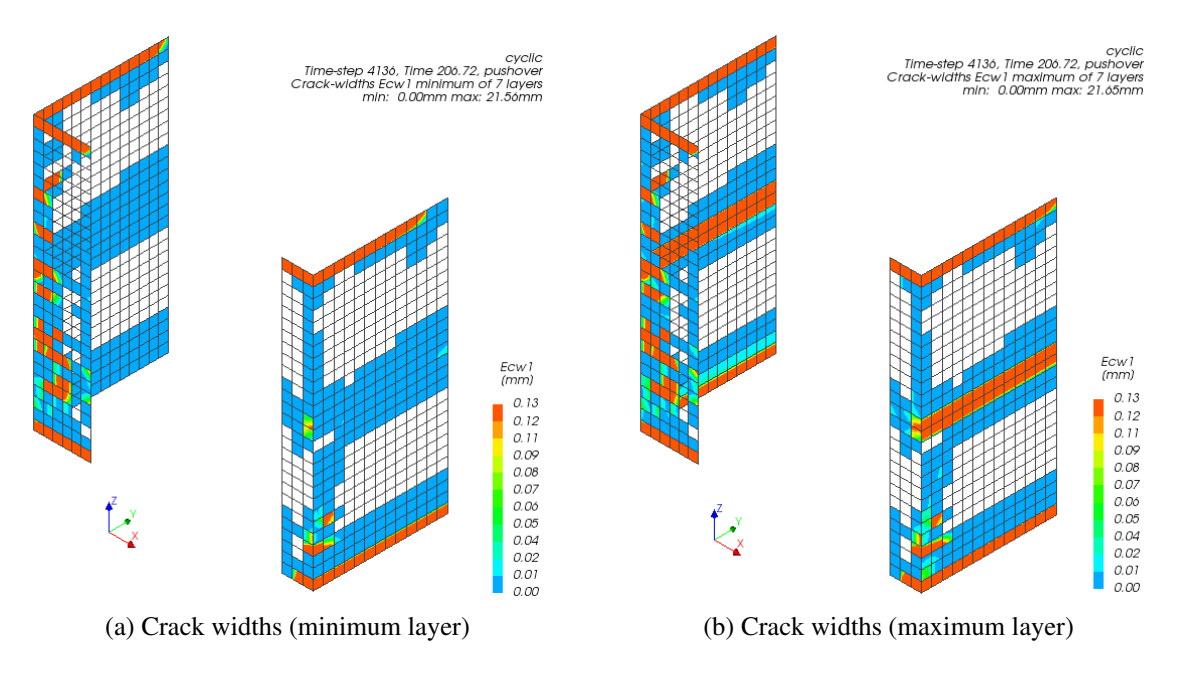


Figure C.8: Crack widths at the peak base shear capacity (Cycle 18, negative direction)

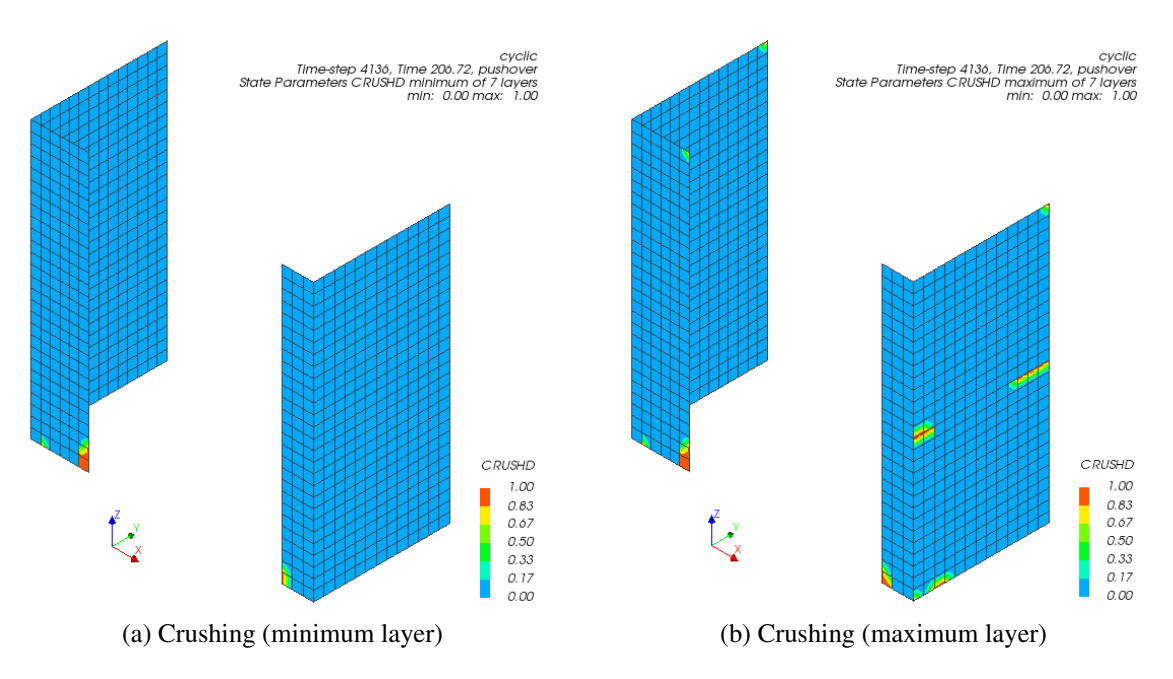


Figure C.9: Crushing at the peak base shear capacity (Cycle 18, negative direction)

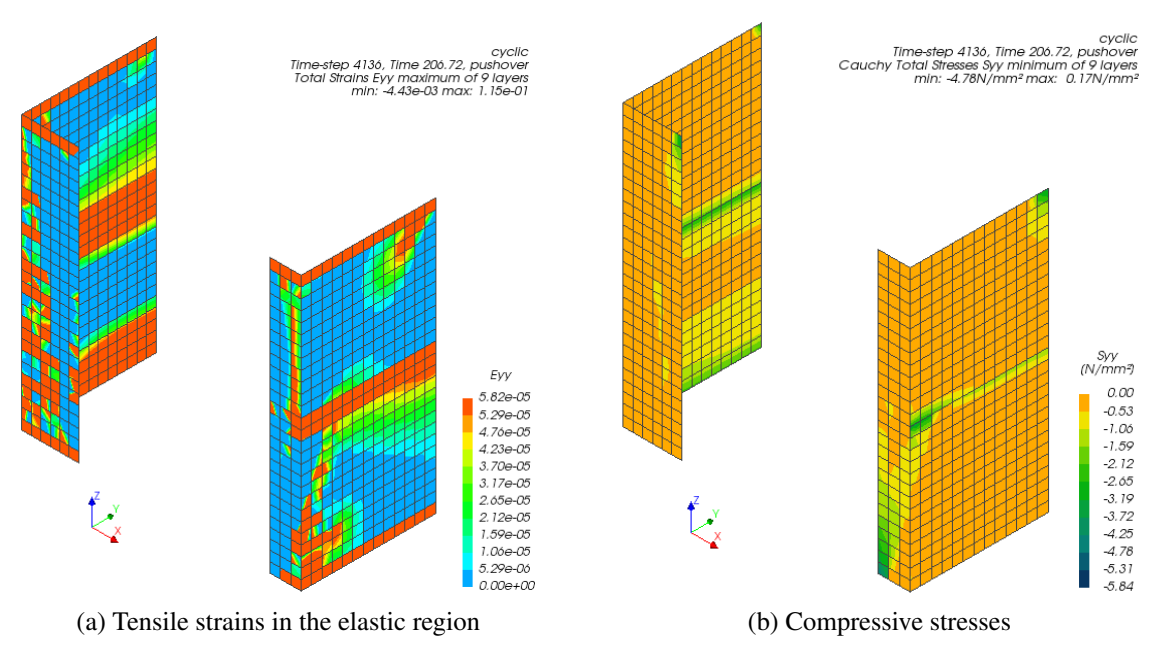


Figure C.10: Stress/strain at the peak base shear capacity (Cycle 18, negative direction)

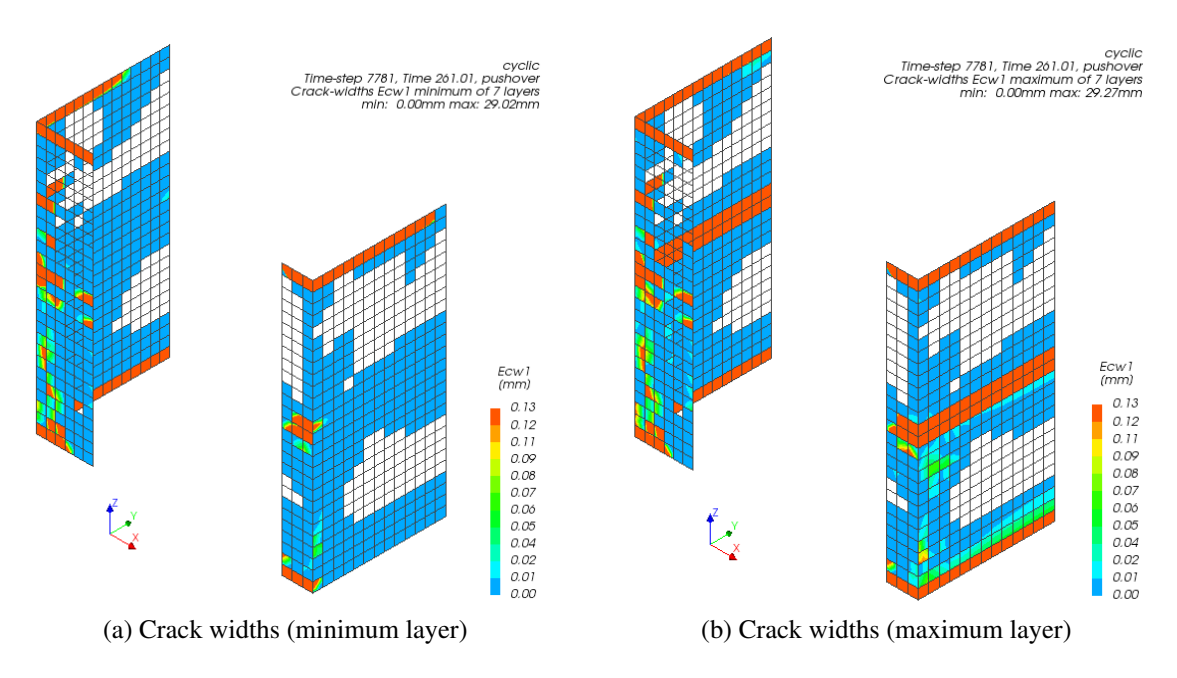


Figure C.11: Crack widths at post-peak stage (Cycle 22, positive direction)

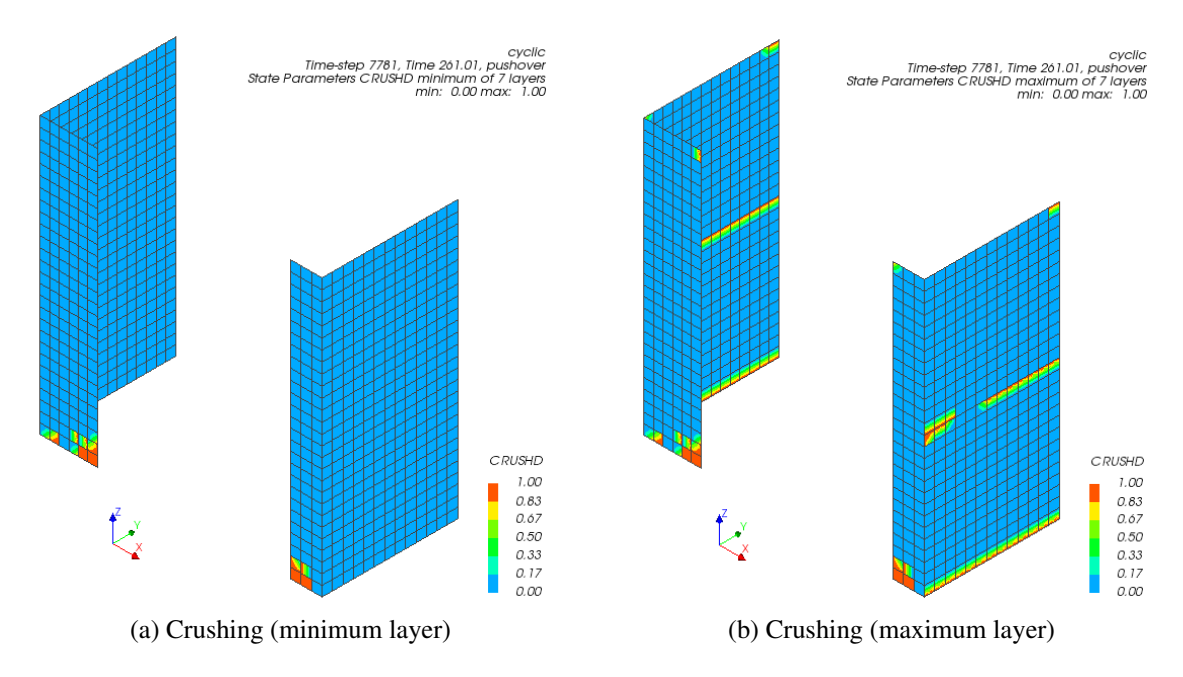


Figure C.12: Crushing at post-peak stage (Cycle 22, positive direction)

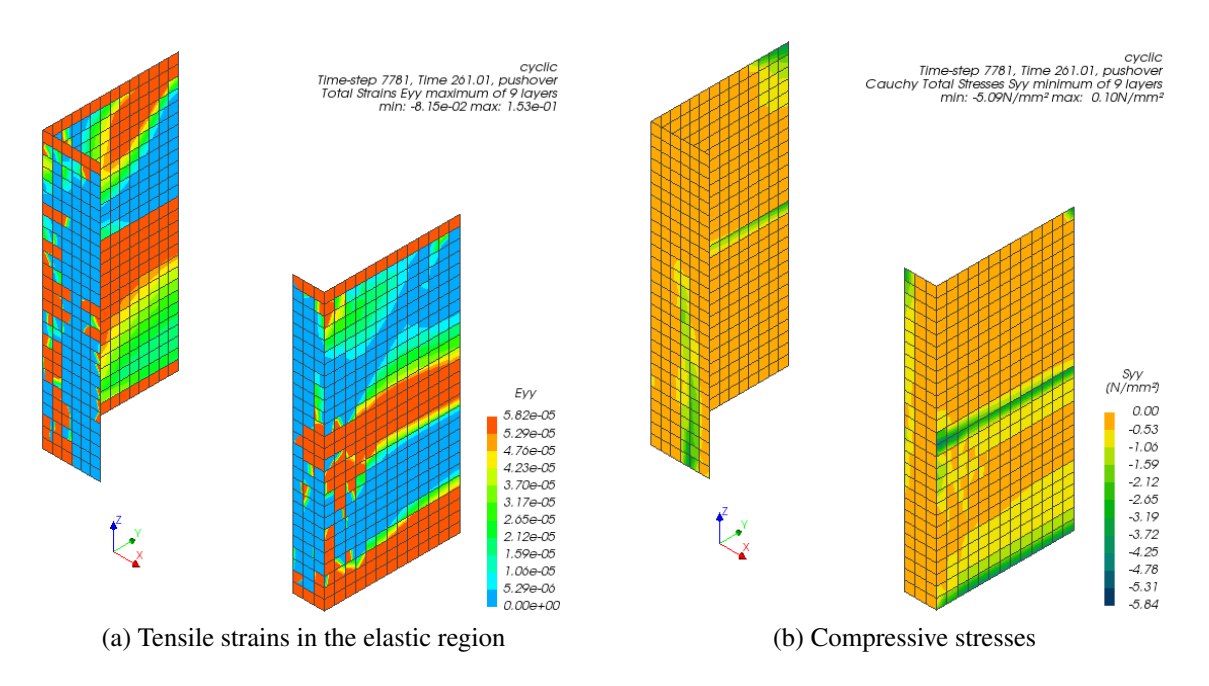


Figure C.13: Stress/strain at post-peak stage (Cycle 22, positive direction)

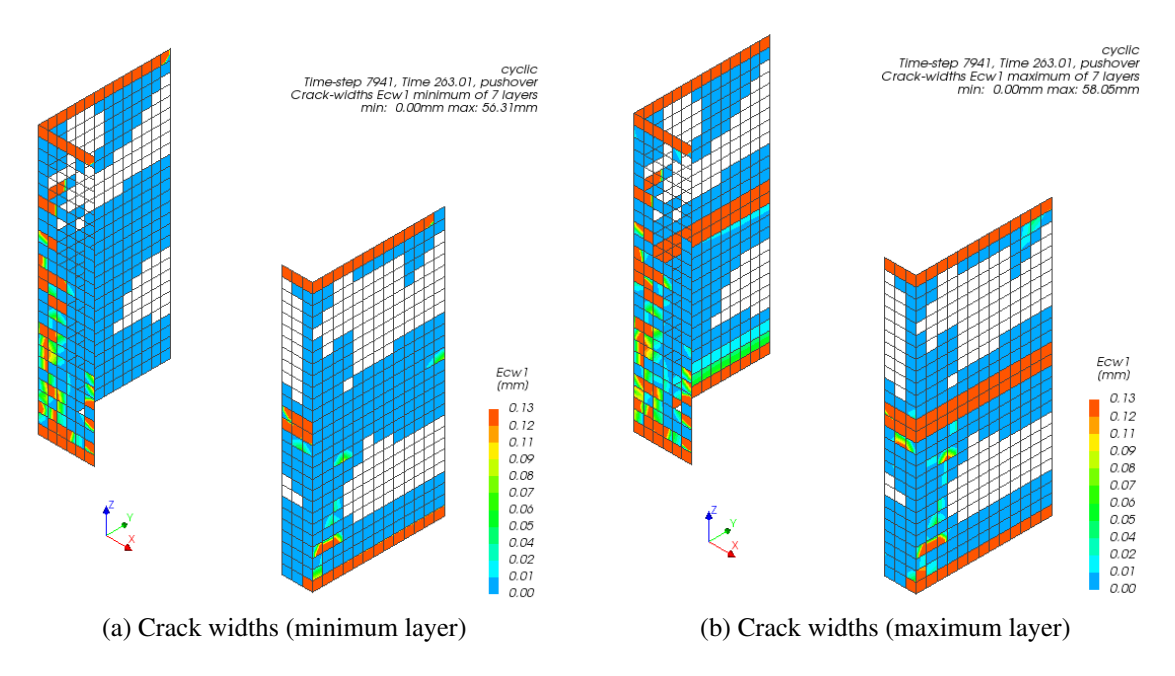


Figure C.14: Crack widths at post-peak stage (Cycle 22, negative direction)

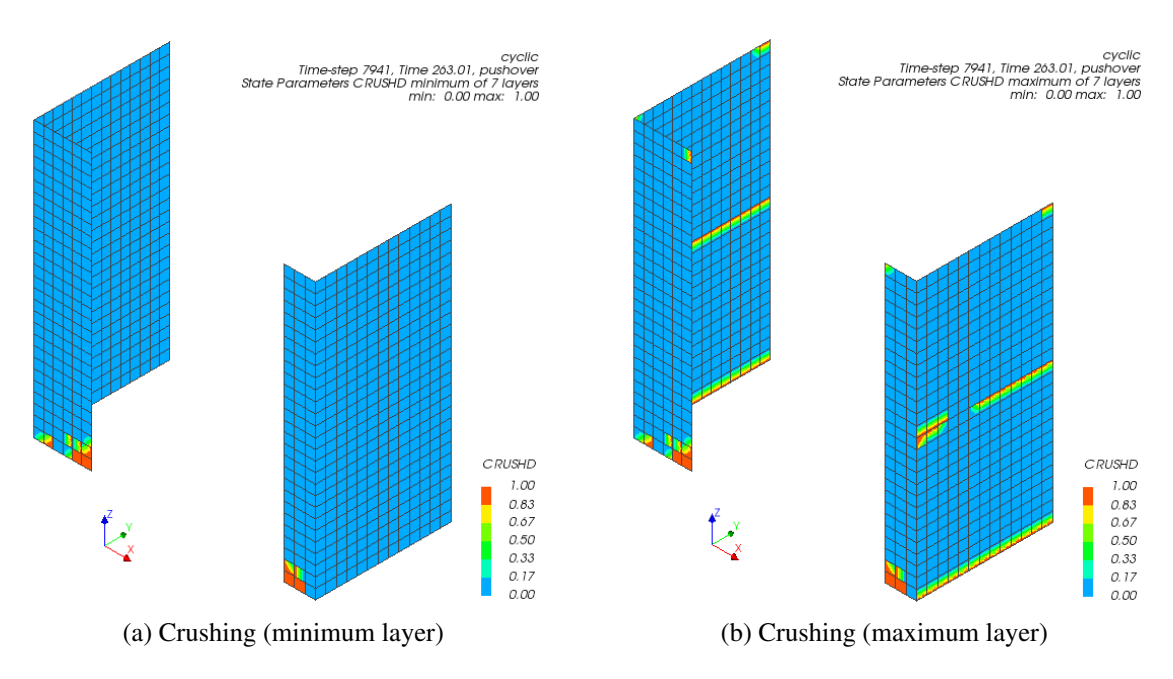


Figure C.15: Crushing at post-peak stage (Cycle 22, negative direction)

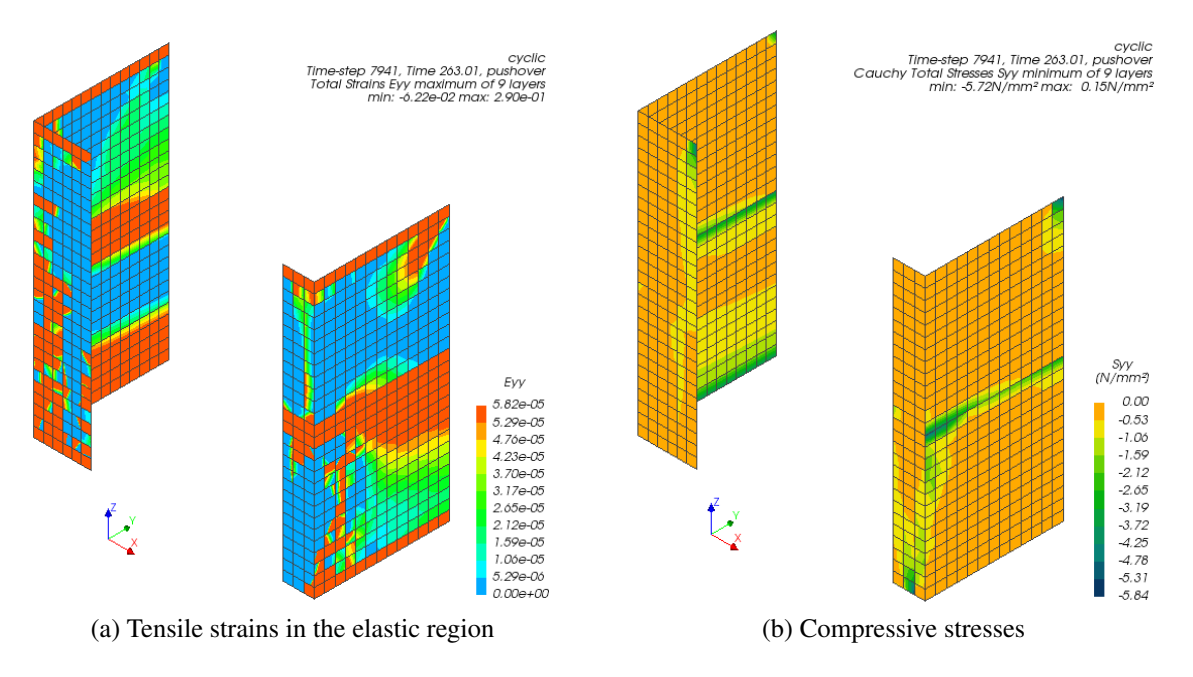


Figure C.16: Stress/strain at post-peak stage (Cycle 22, negative direction)

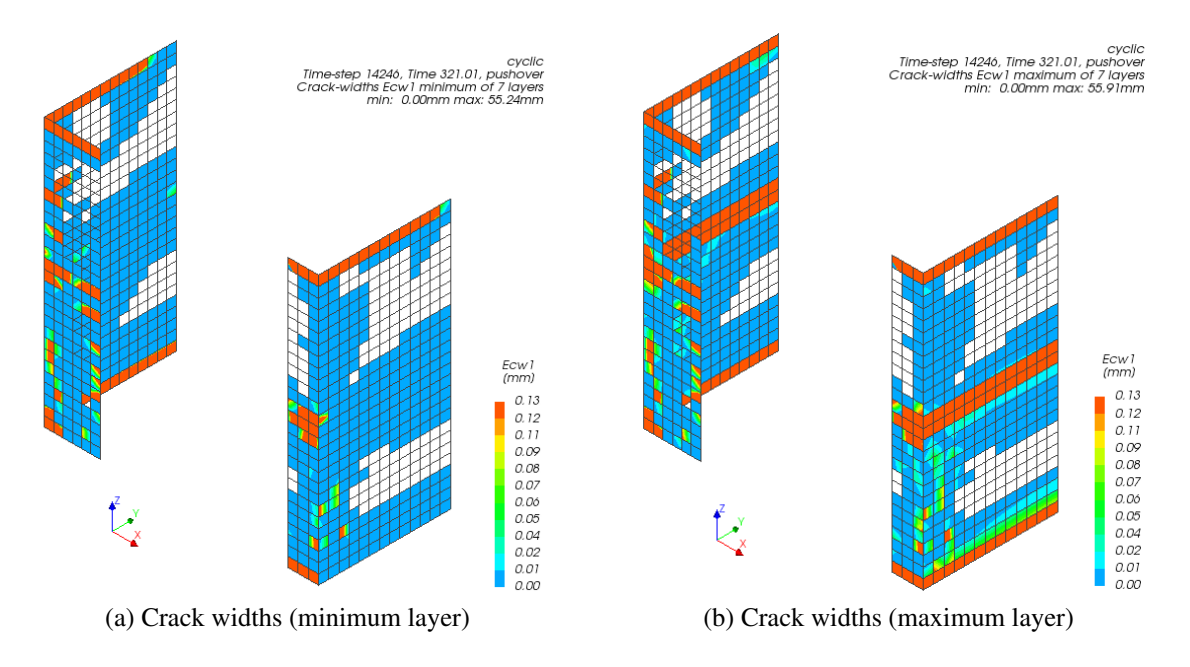


Figure C.17: Crack widths at the last loading cycle (Cycle 27, positive direction)

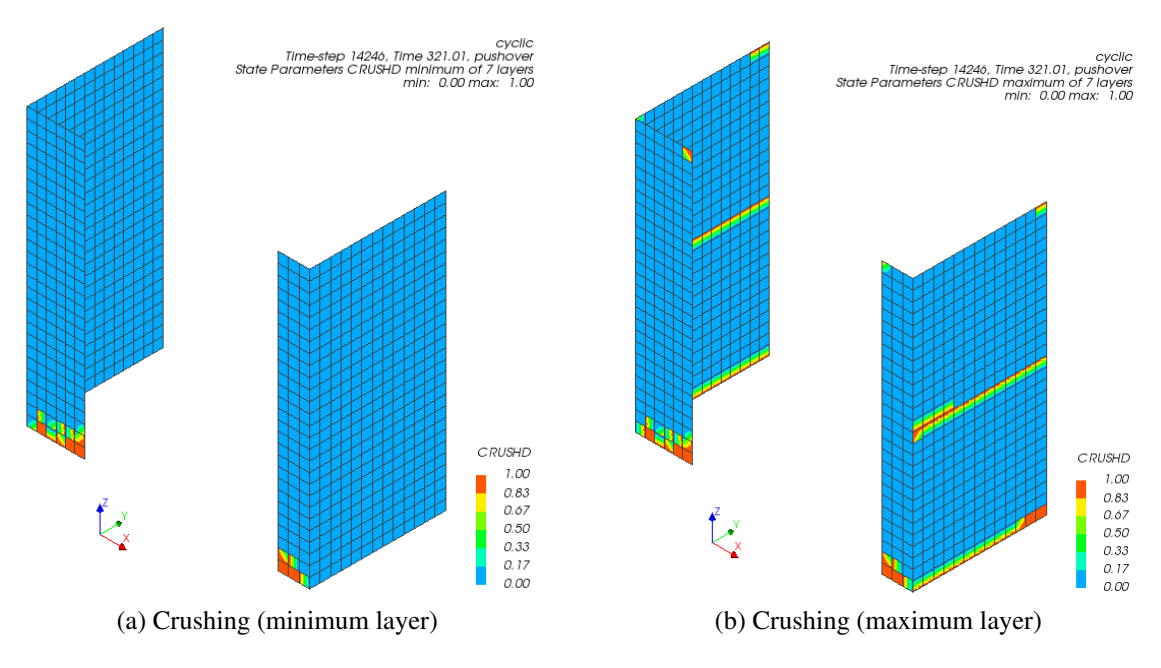


Figure C.18: Crushing at the last loading cycle (Cycle 27, positive direction)

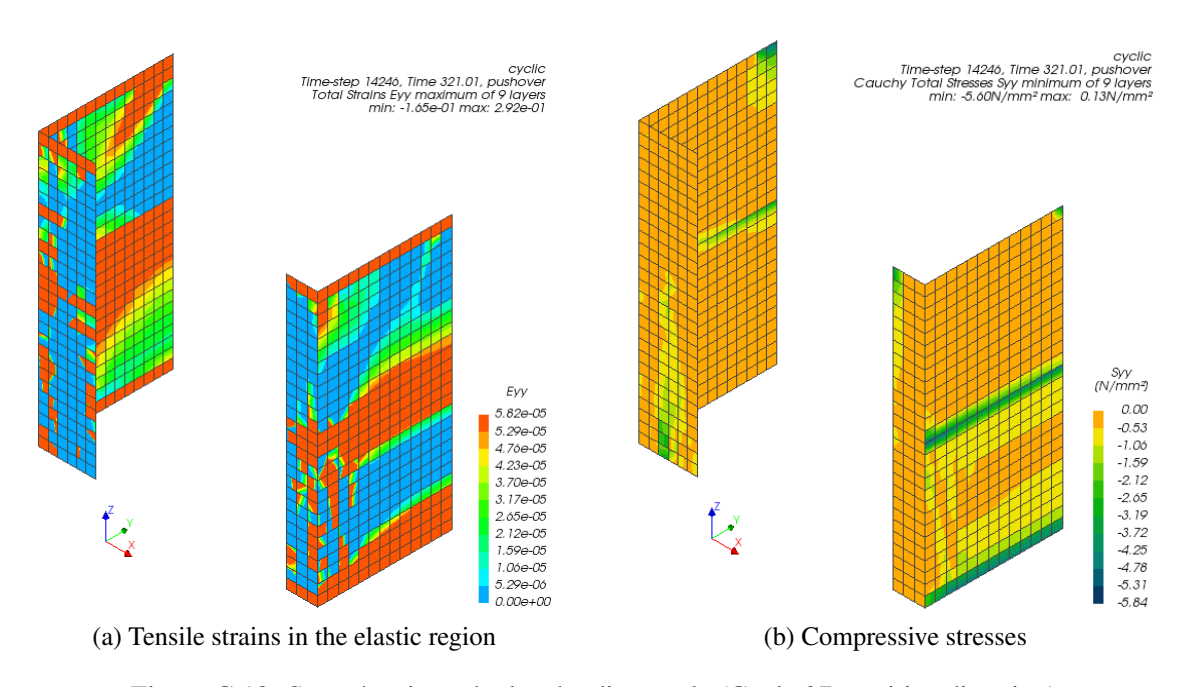


Figure C.19: Stress/strain at the last loading cycle (Cycle 27, positive direction)

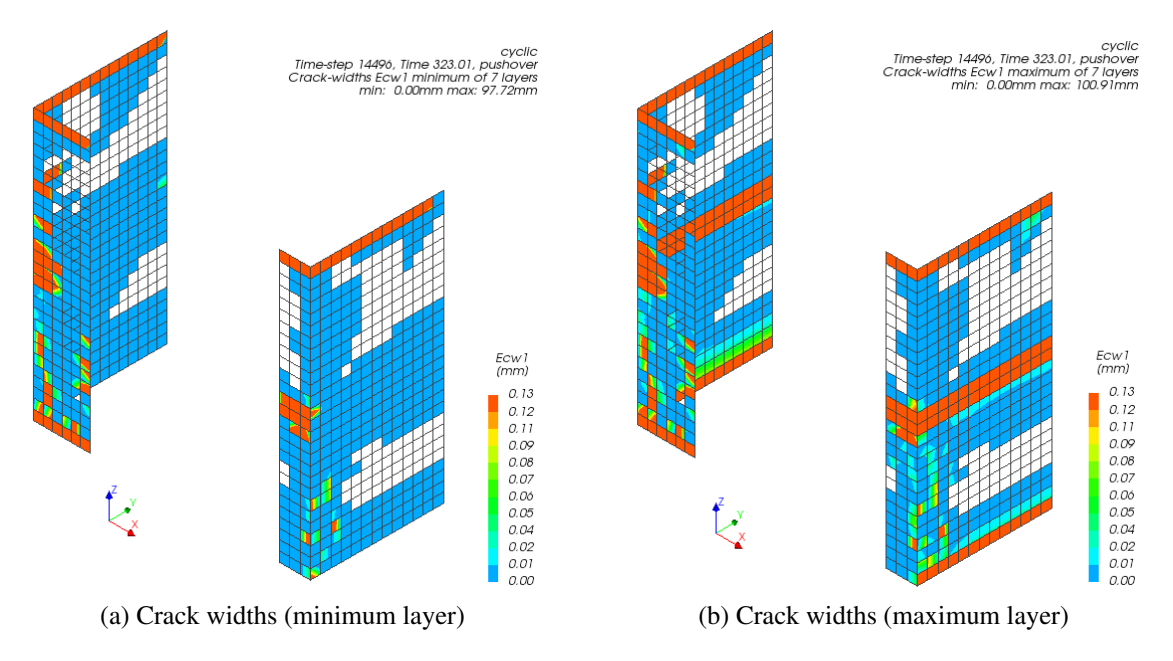


Figure C.20: Crack widths at the last loading cycle (Cycle 27, negative direction)

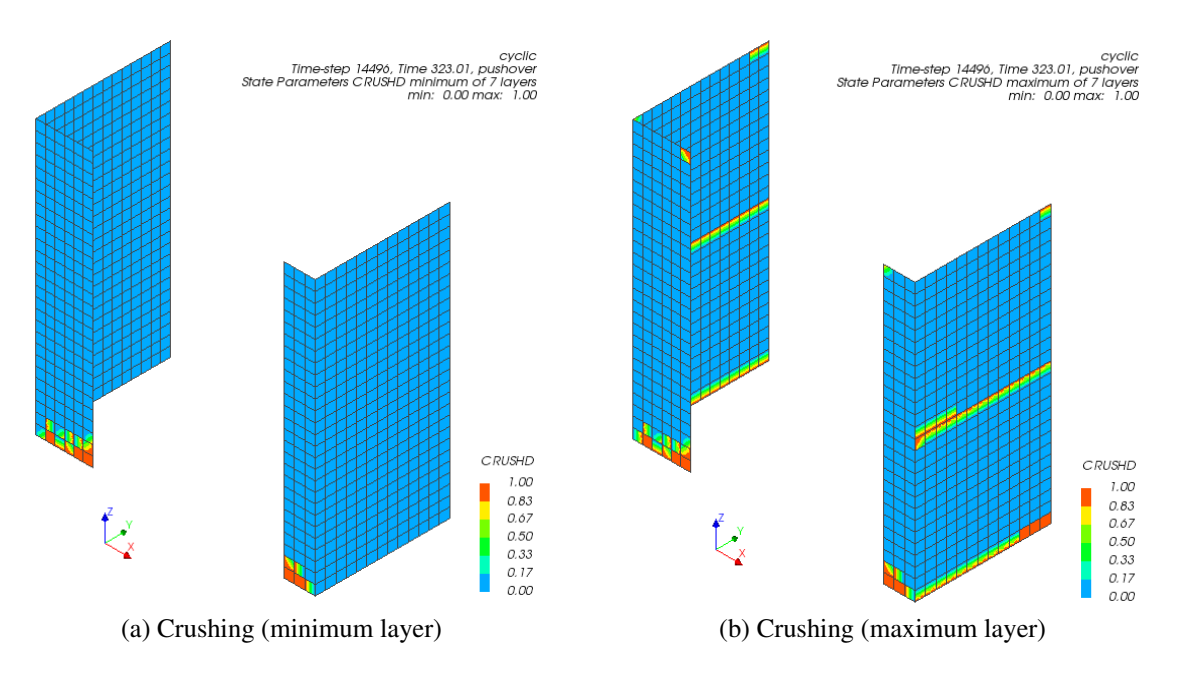


Figure C.21: Crushing at the last loading cycle (Cycle 27, negative direction)

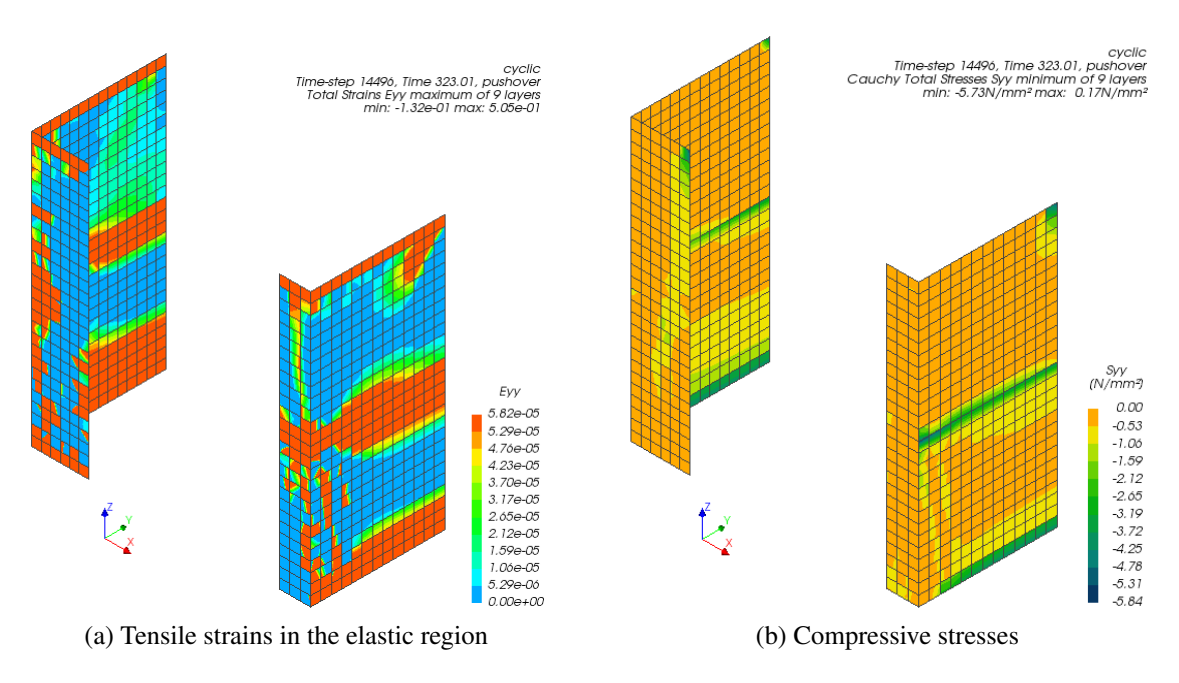


Figure C.22: Stress/strain at the last loading cycle (Cycle 27, negative direction)

Appendix D

Results of Nonlinear Time-history Analysis

The detailed damage patterns of the house model in the time-history analysis are presented. The crack widths of the masonry are shown at both the minimum and maximum layer over element thickness.

D.1 +x direction

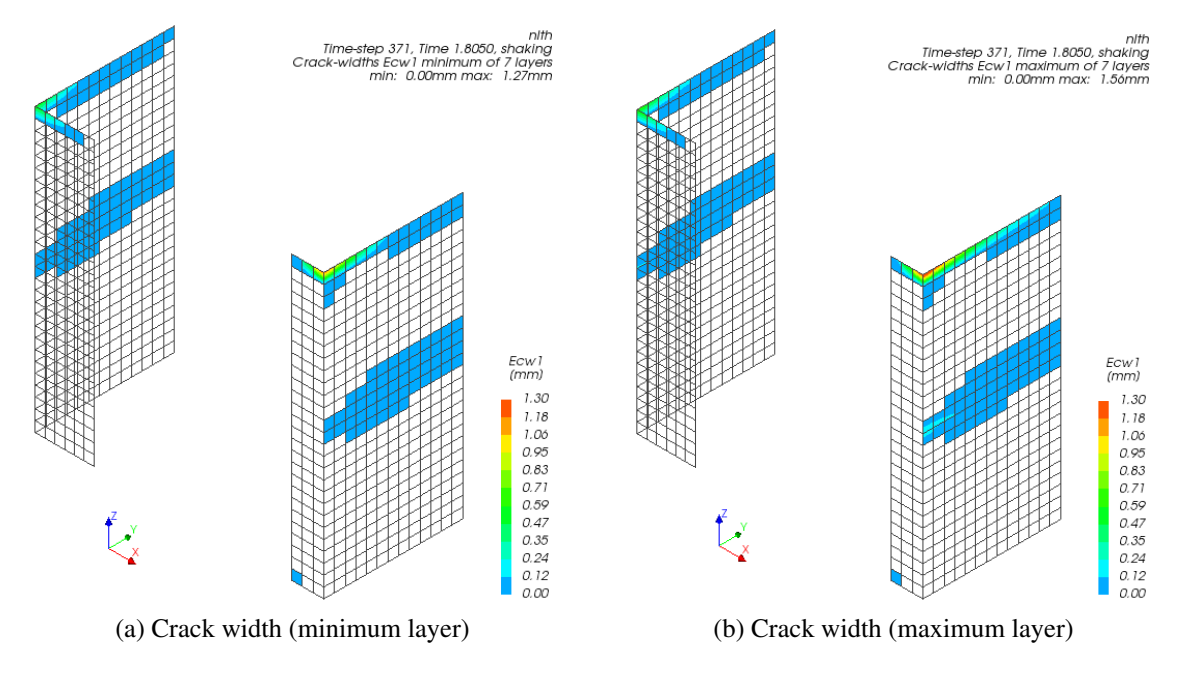


Figure D.1: Results at run 1 (0.03 g, +2.16 mm)

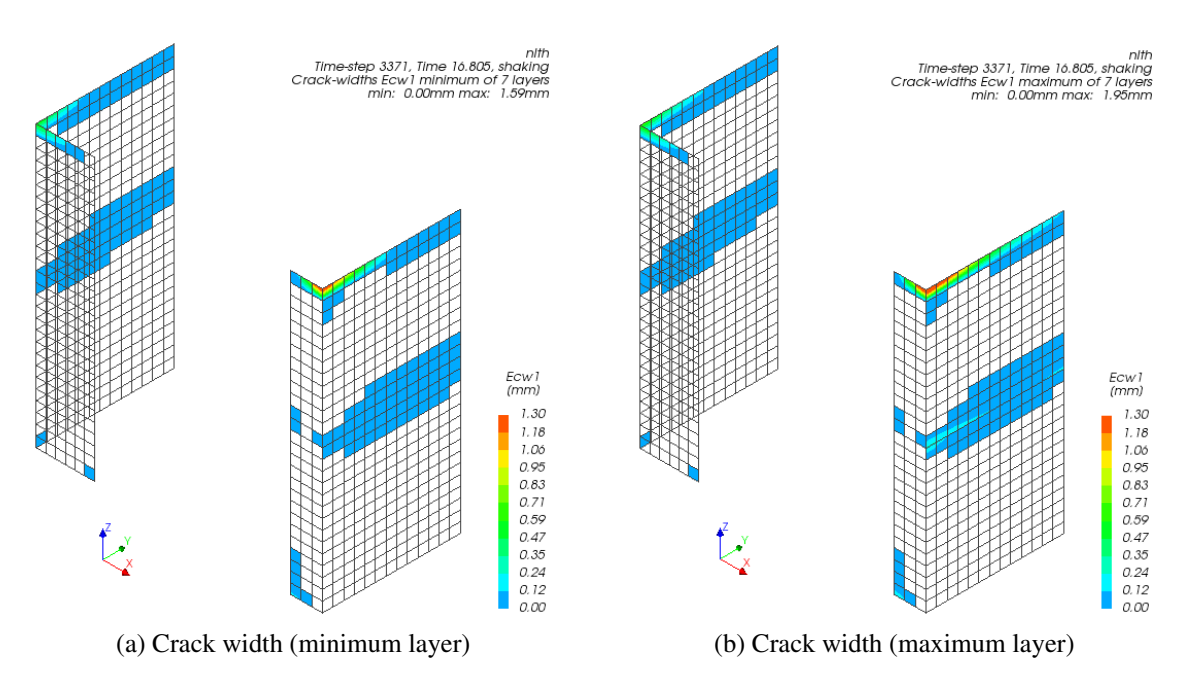


Figure D.2: Results at run 2 (0.06 g, +3.51 mm)

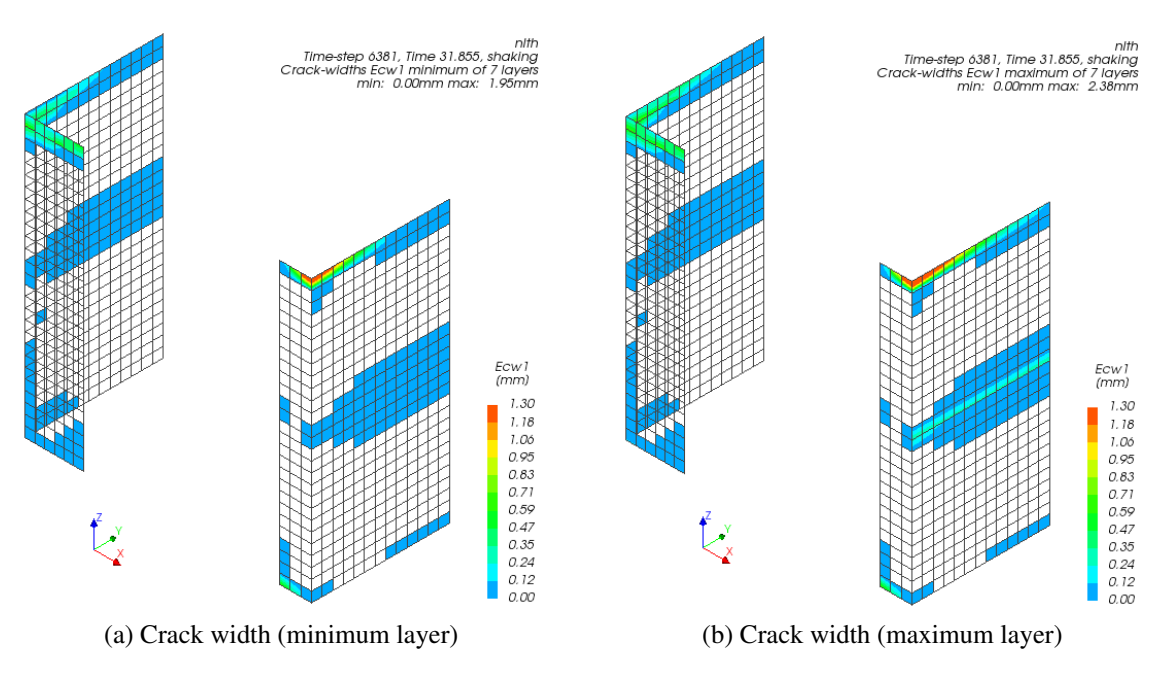


Figure D.3: Results at run 3 (0.10 g, +5.27 mm)

D.1. +X DIRECTION 129

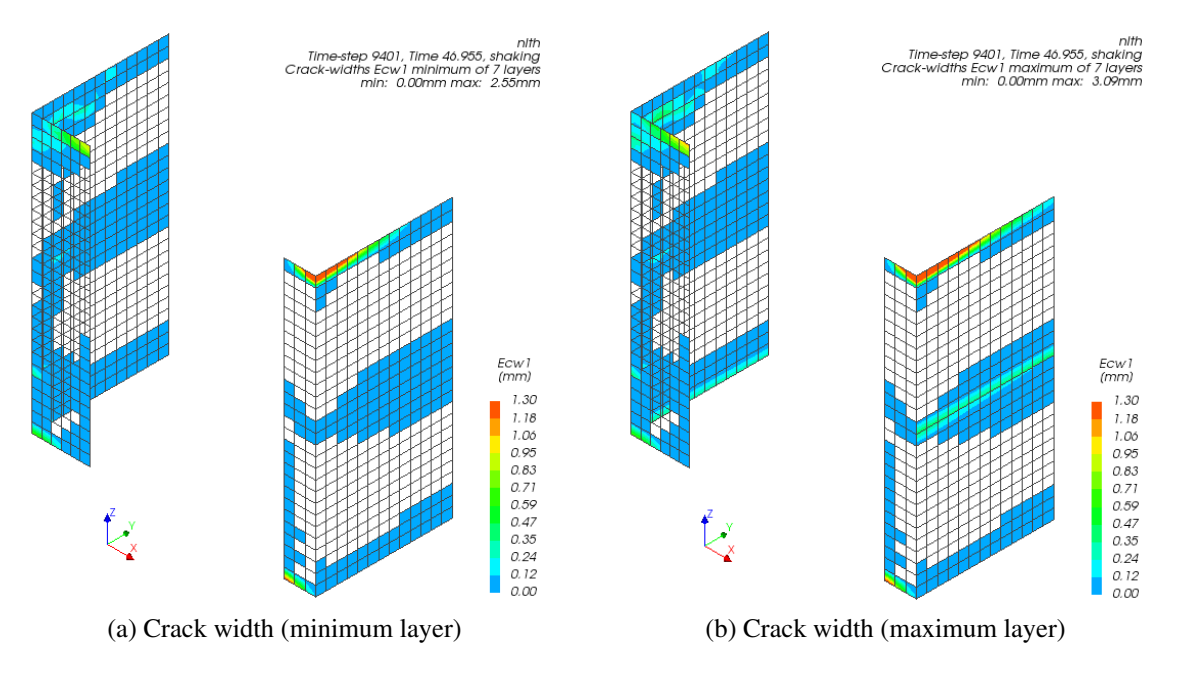


Figure D.4: Results at run 4 (0.15 g, +10.40 mm)

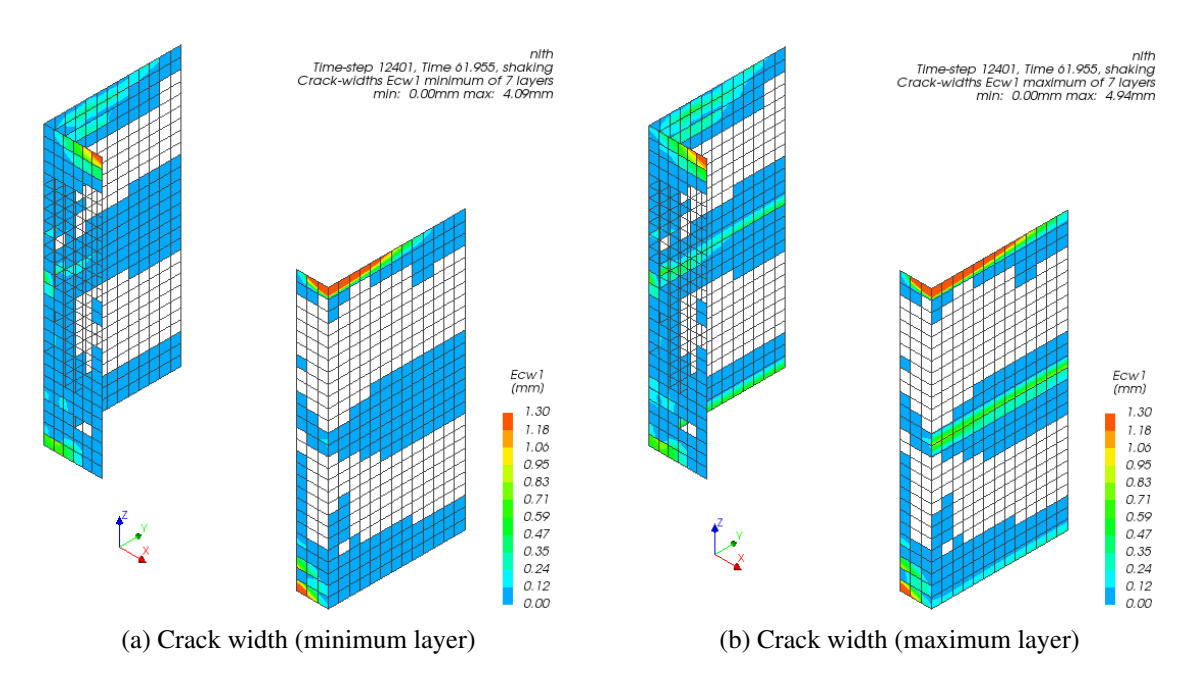


Figure D.5: Results at run 5 (0.20 g, +19.32 mm)

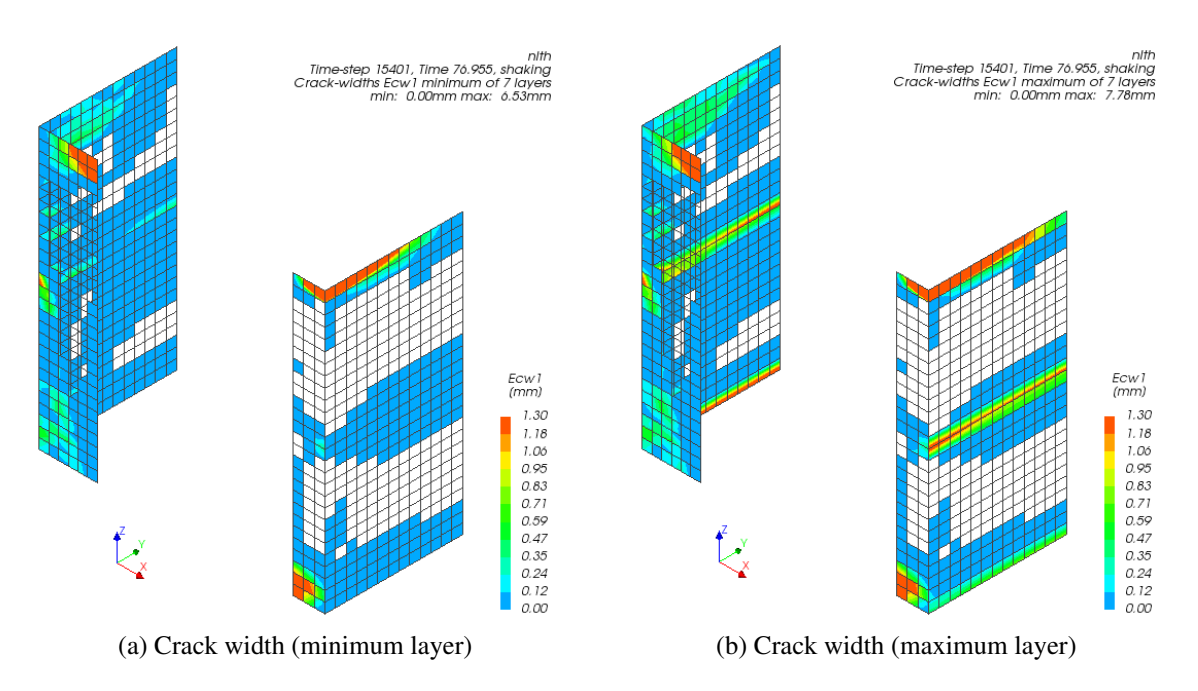


Figure D.6: Results at run 6 (0.25 g, +36.11 mm)

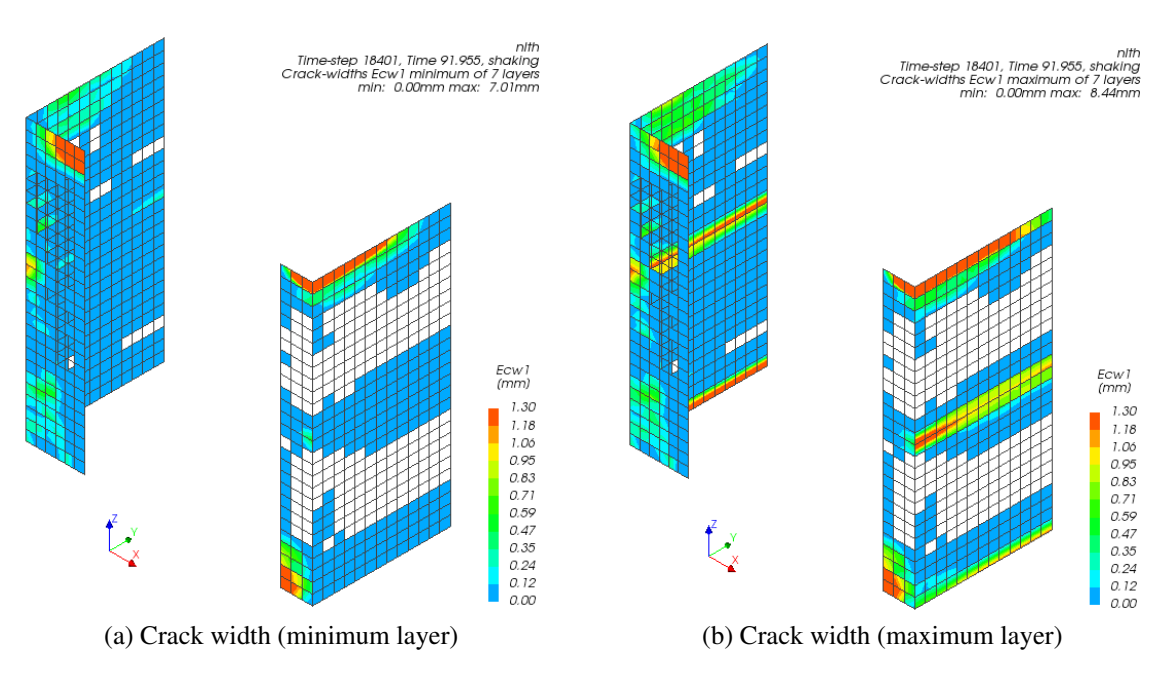


Figure D.7: Results at run 7 (0.30 g, +48.48 mm)

D.1. +X DIRECTION 131

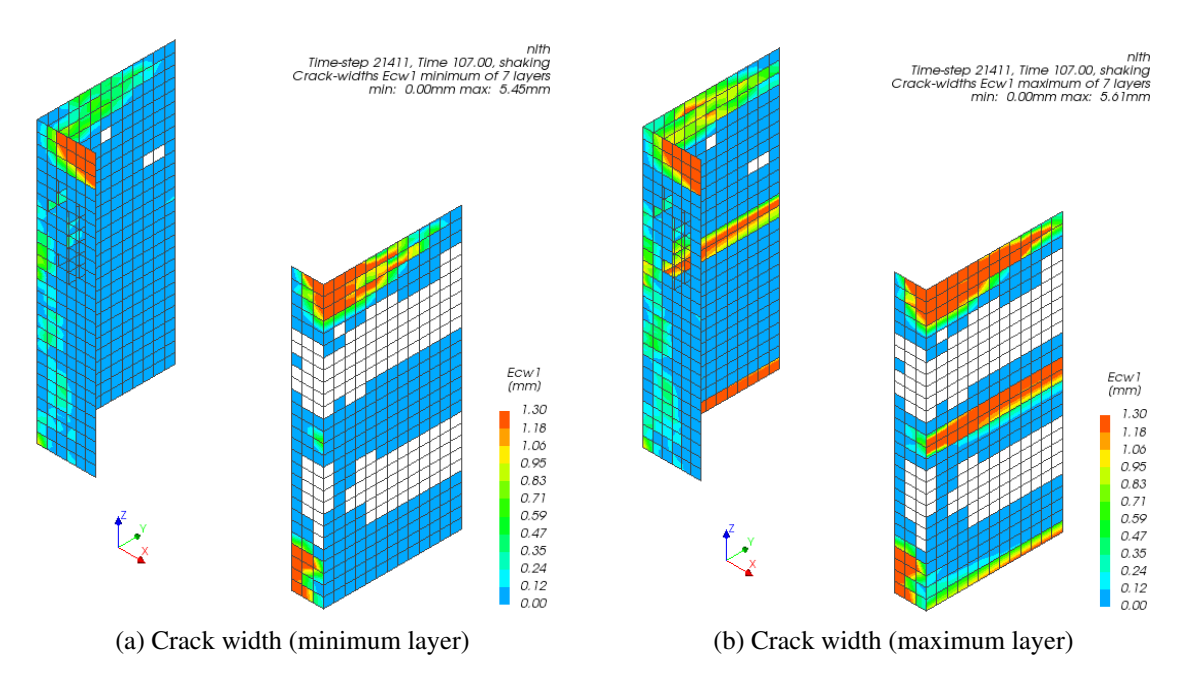


Figure D.8: Results at run 8 (0.35 g, +65.60 mm)

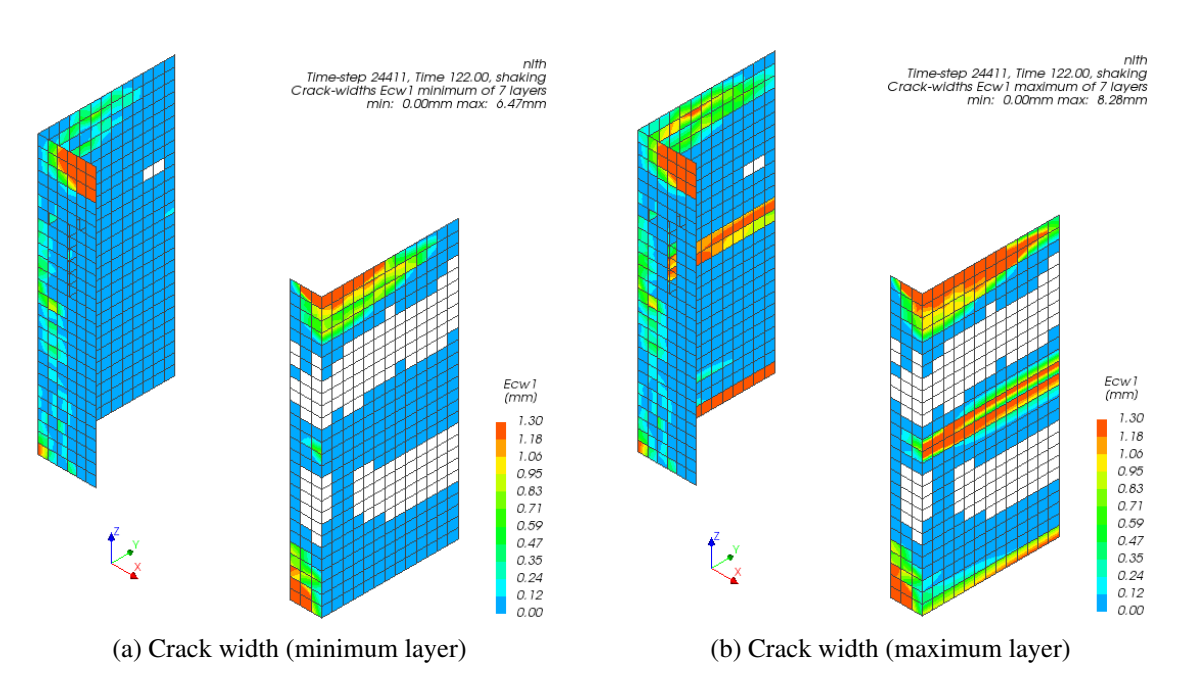


Figure D.9: Results at run 9 (0.40 g, +71.90 mm)

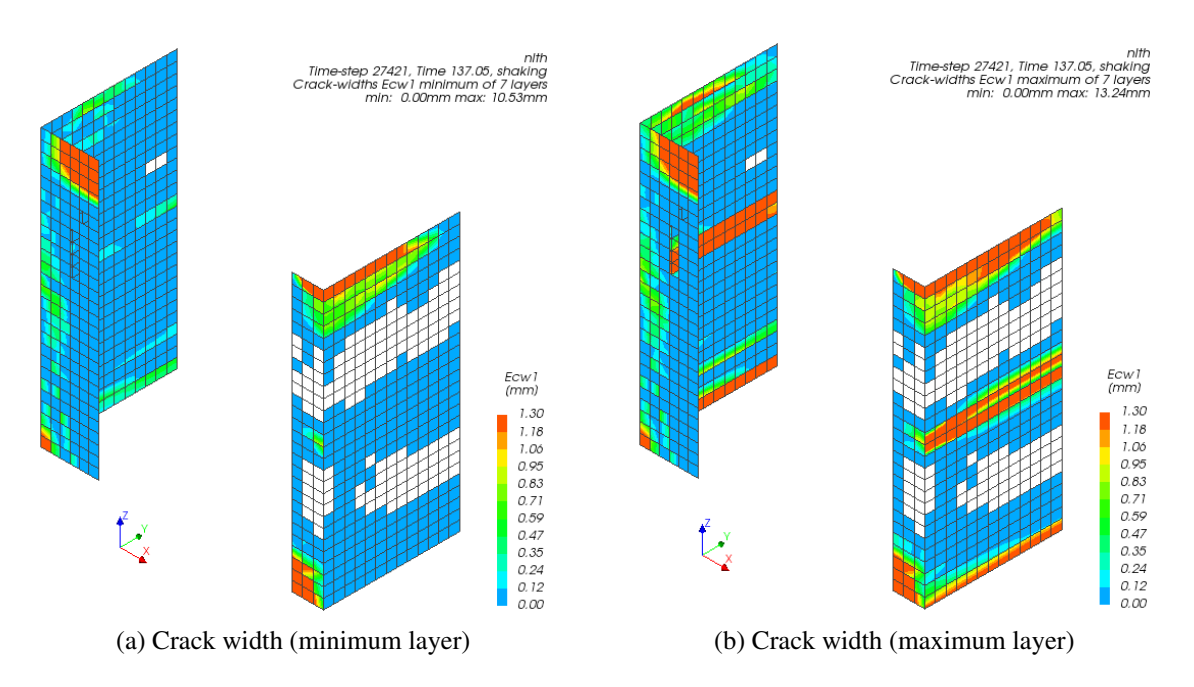


Figure D.10: Results at run 10 (0.50 g, +87.10 mm)

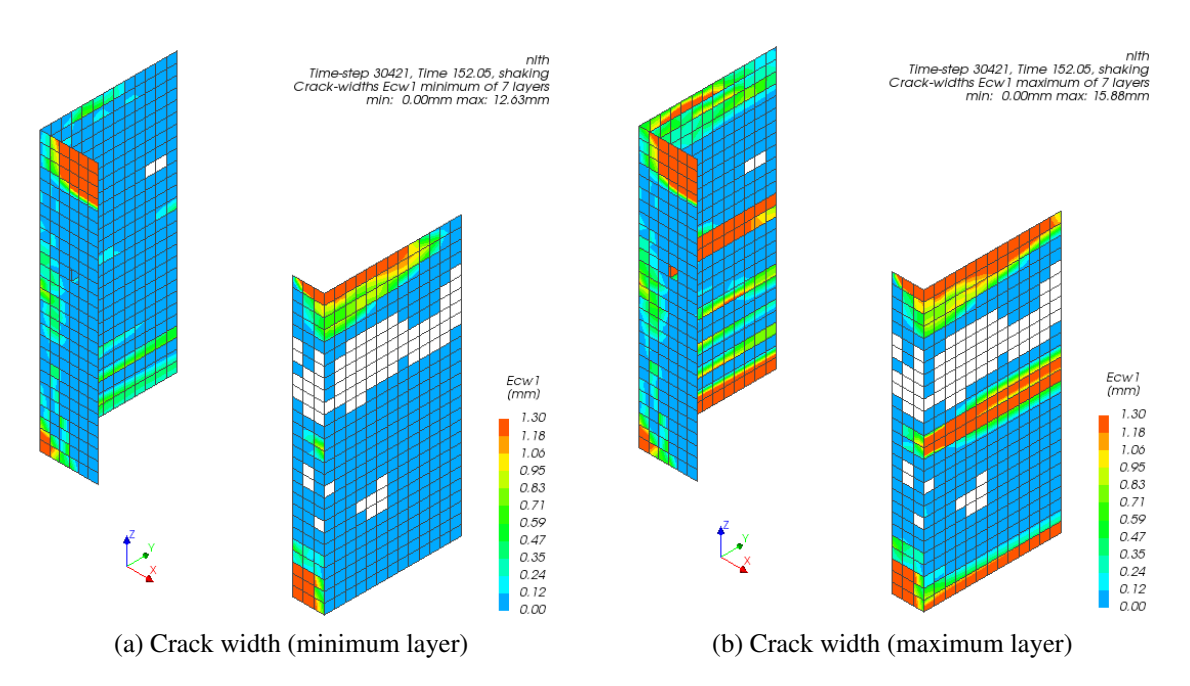


Figure D.11: Results at run 11 (0.62 g, +103.90 mm)

D.2. -X DIRECTION 133

D.2 -x direction

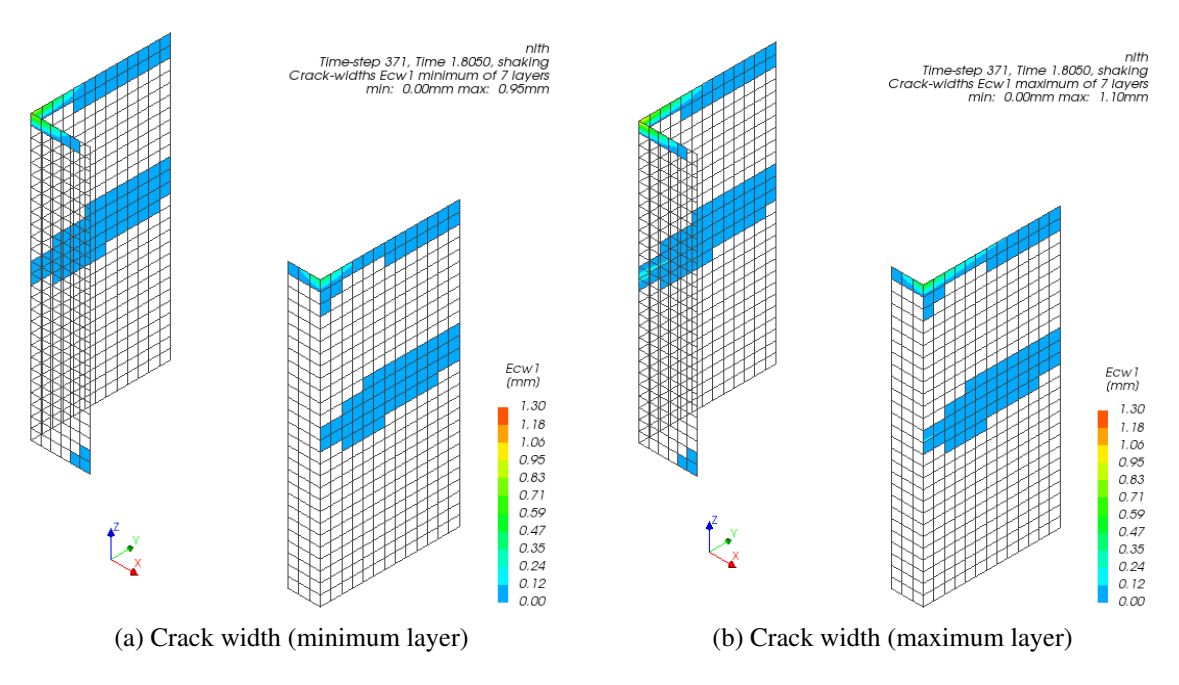


Figure D.12: Results at run 1 (0.03 g, -1.15 mm)

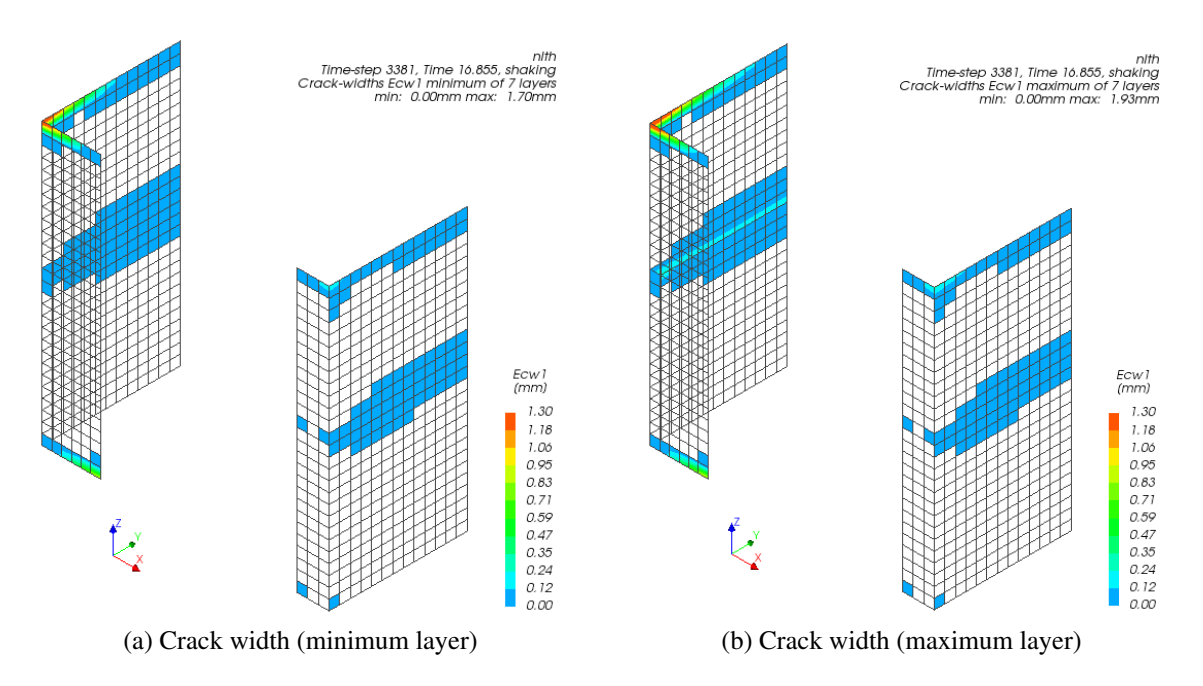


Figure D.13: Results at run 2 (0.06 g, -3.29 mm)

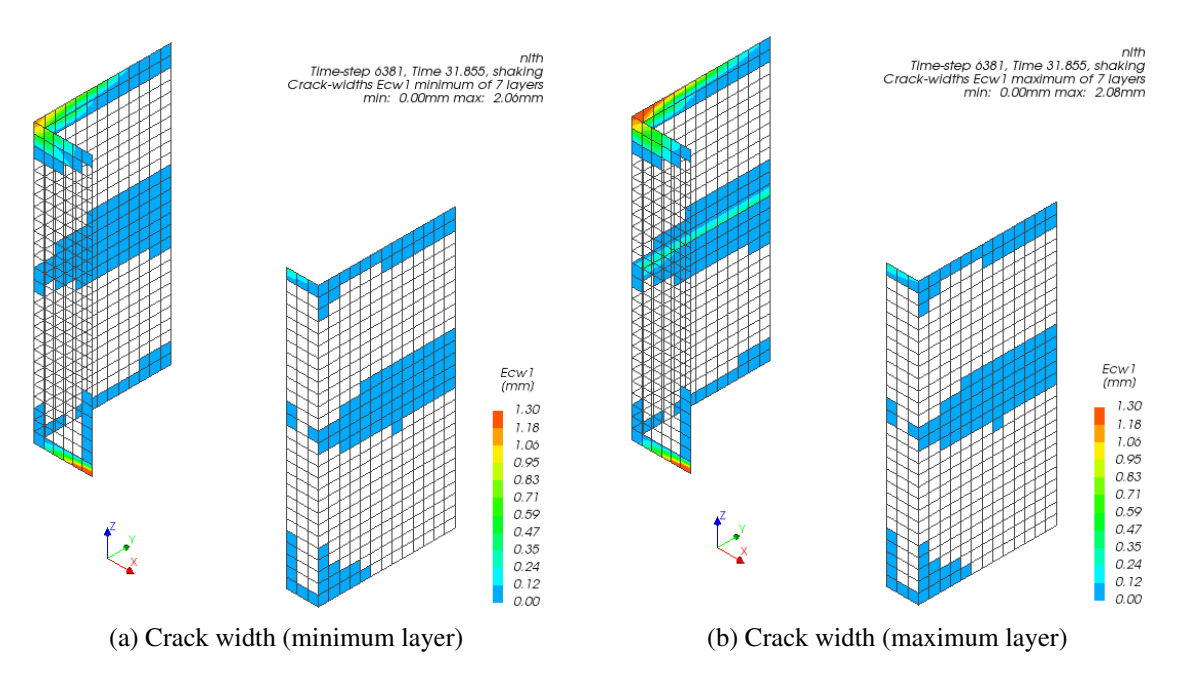


Figure D.14: Results at run 3 (0.10 g, -6.66 mm)

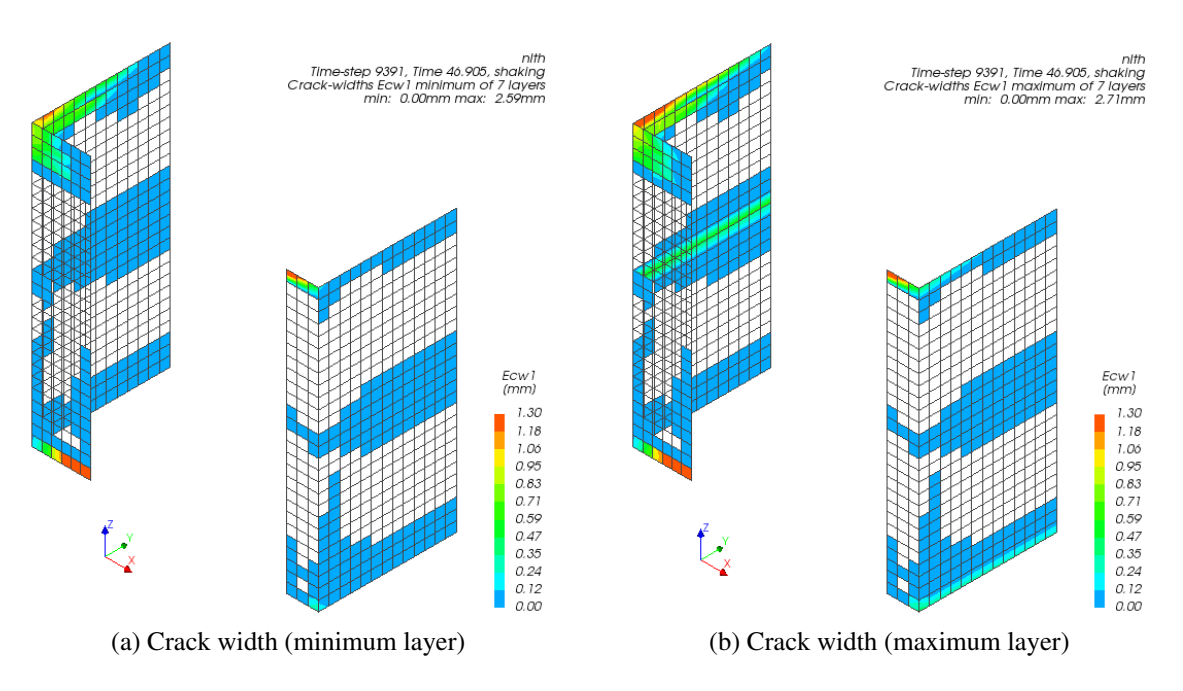


Figure D.15: Results at run 4 (0.15 g, -12.82 mm)

D.2. -X DIRECTION 135

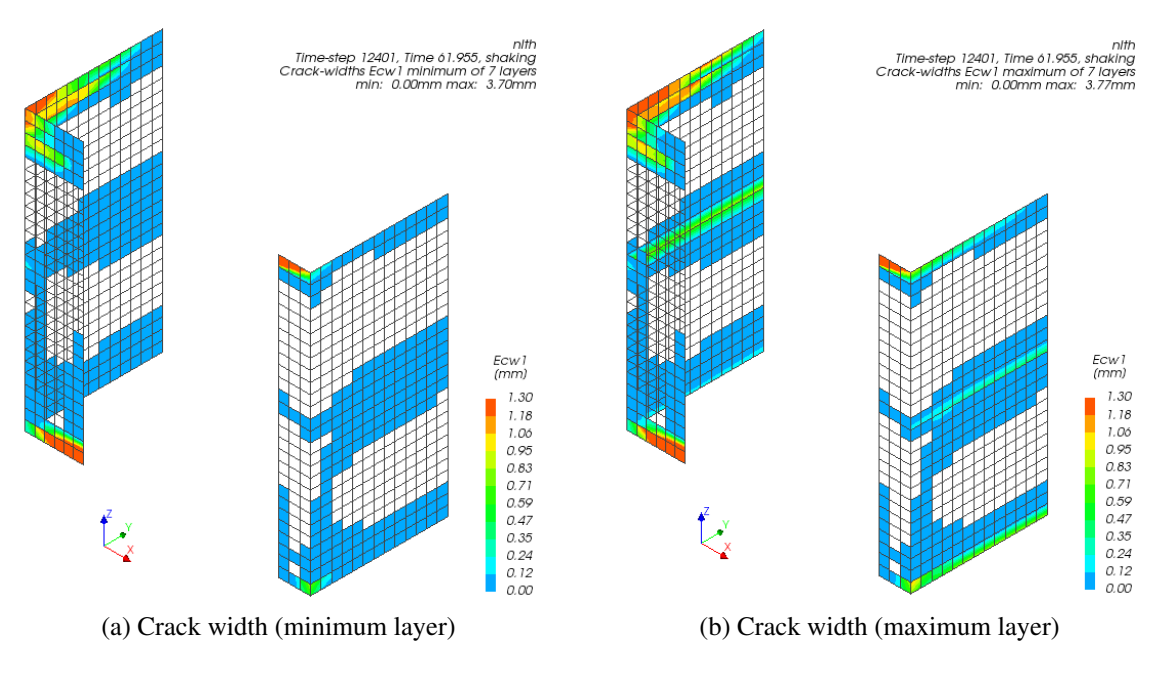


Figure D.16: Results at run 5 (0.20 g, -19.94 mm)

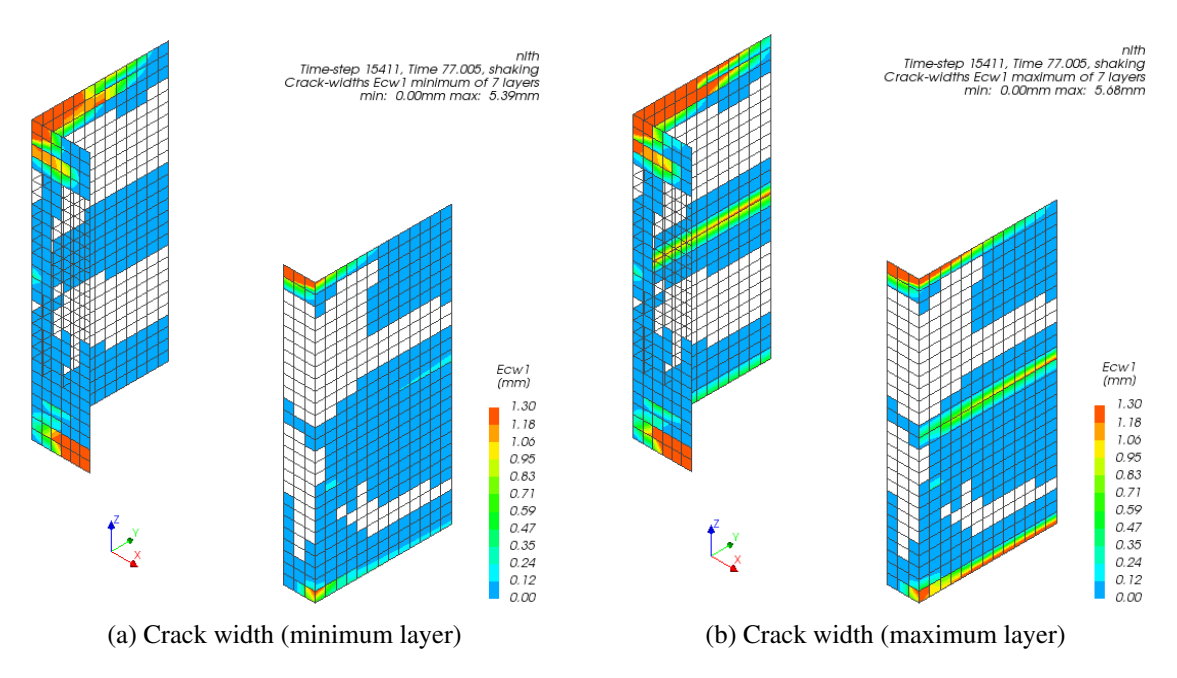


Figure D.17: Results at run 6 (0.25 g, -31.82 mm)

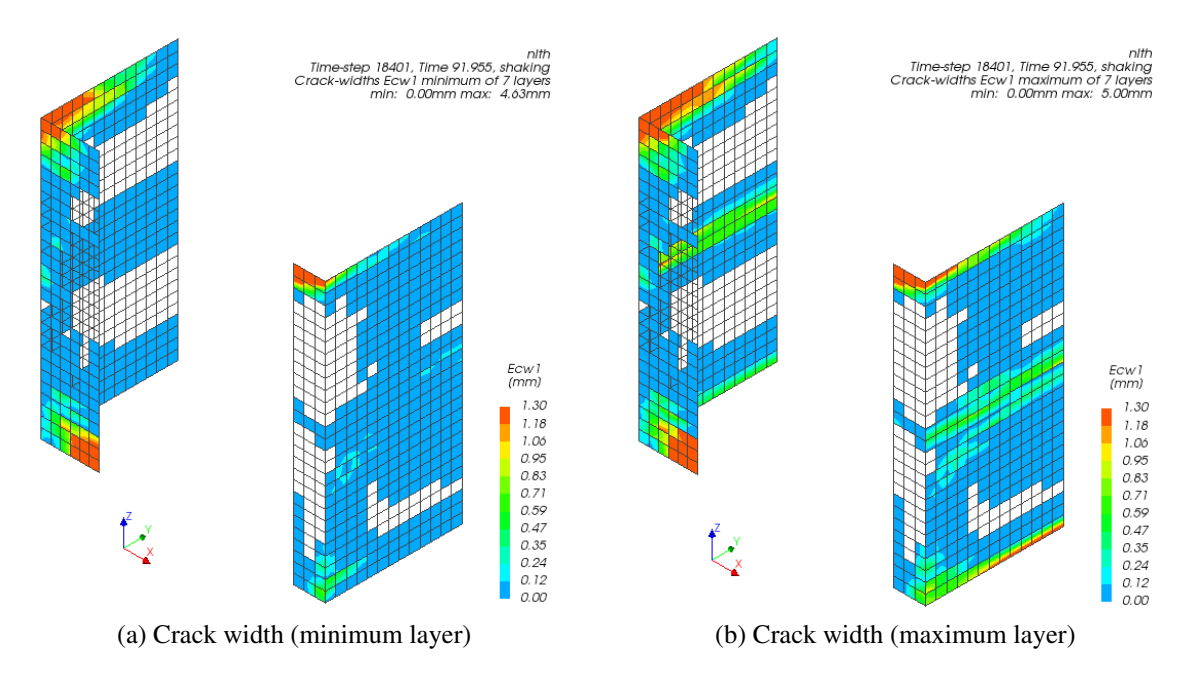


Figure D.18: Results at run 7 (0.30 g, -38.07 mm)

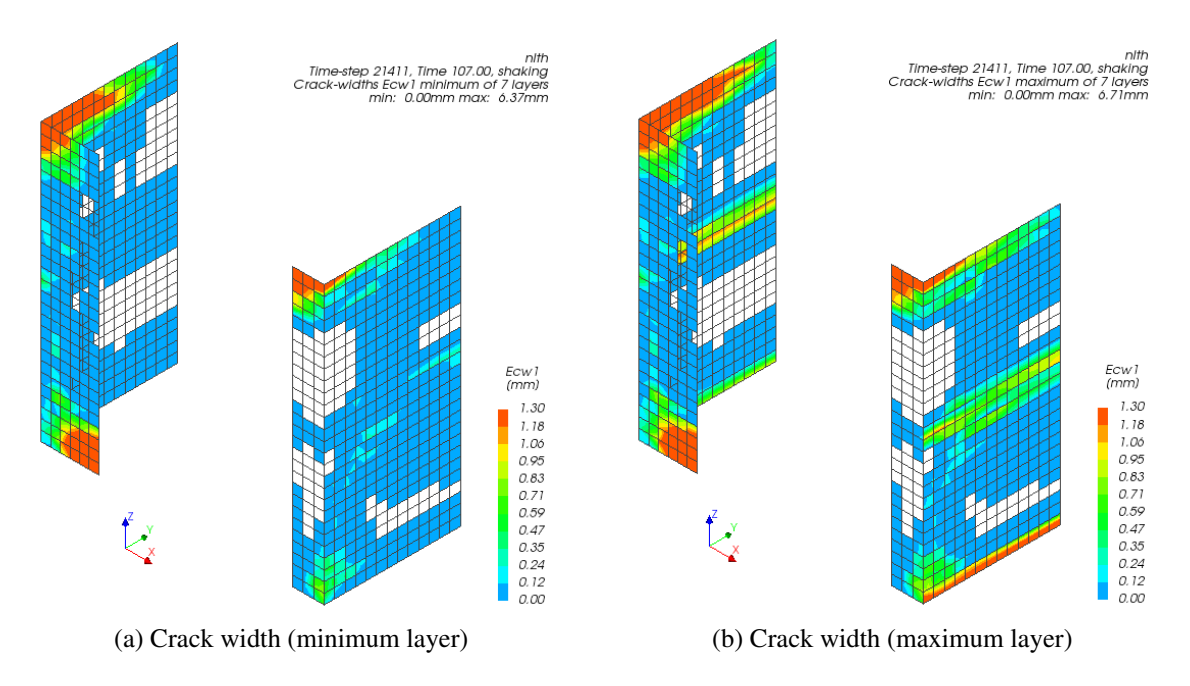


Figure D.19: Results at run 8 (0.35 g, -50.73 mm)

D.2. -X DIRECTION

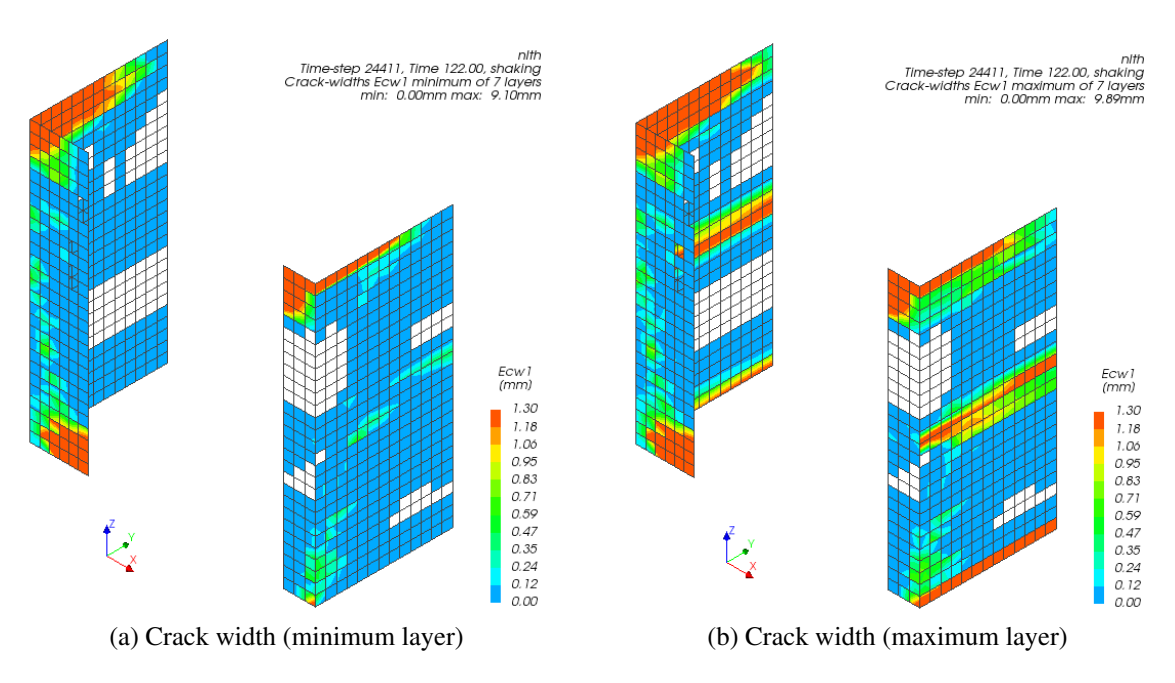


Figure D.20: Results at run 9 (0.40 g, -77.50 mm)